SYNTHESIS, CHARACTERIZATION AND SELECTED APPLICATIONS OF QUASI ONE DIMENSIONAL NANO-ARCHITECTURES OF TiO_2

By

RAJINI P ANTONY

Enrolment No: CHEM02200704011
Thin Films and Coatings Section, Surface and Nanoscience Division,
Material Science Group,
Indira Gandhi Centre for Atomic Research, Kalpakkam

A thesis submitted to the

Board of Studies in Chemical Sciences

In partial fulfillment of requirements

for the Degree of

DOCTOR OF PHILOSOPHY
of
HOMI BHABHA NATIONAL INSTITUTE

October - 2012

Homi Bhabha National Institute

Recommendations of the Viva Voce Board

As members of the Viva Voce Board, we certify that we have read the dissertation prepared by Rajini P Antony entitled **"Synthesis, Characterization and Selected Applications of Quasi One Dimensional Nano-architectures of TiO_2"** and recommend that it may be accepted as fulfilling the dissertation requirement for the Degree of Doctor of Philosophy.

Date: 21/5/2013

Chairman – Prof. Dr. B. V. R. Tata

Date: 21-5-2013

Guide / Convener – Prof. Dr. Sitaram Dash

Date: 21/5/2013

Member 1- Prof. Dr. A. K. Shukla (External Examiner)

V. Jayaraman **Date:** 21.05.2013.

Member 2 – Prof. Dr. V. Jayaraman

K. Viswanathan **Date:** 21/05/2013

Member 3 – Prof. Dr. K. S. Viswanathan

Date: 21/5/2013

Member 4 – Prof. Dr. A. K. Tyagi (Permanent Invitee)

Final approval and acceptance of this dissertation is contingent upon the candidate's submission of the final copies of the dissertation to HBNI.

I hereby certify that I have read this dissertation prepared under my direction and recommend that it may be accepted as fulfilling the dissertation requirement.

Date: 21-5-2013

Place: IGCAR, kalpakkam

(SITARAM DASH
Guide-Convener)

STATEMENT BY AUTHOR

This dissertation has been submitted in partial fulfillment of requirements for an advanced degree at Homi Bhabha National Institute (HBNI) and is deposited in the Library to be made available to borrowers under rules of the HBNI.

Brief quotations from this dissertation are allowable without special permission, provided that accurate acknowledgement of source is made. Requests for permission for extended quotation from or reproduction of this manuscript in whole or in part may be granted by the Competent Authority of HBNI when in his or her judgment the proposed use of the material is in the interests of scholarship. In all other instances, however, permission must be obtained from the author.

Rajini P Antony

Kalpakkam

October, 2012

CERTIFICATE

I here by certify that I have read this Doctoral Dissertation documented by Miss Rajini P. Antony under my supervision and recommend that it may be accepted towards fulfillment of the dissertation requirement of HBNI

Date: 21-05-2013

Place: MSG, IGCAR, KALPAKKAM

Prof. Sitaram Dash (Guide)

DECLARATION

I, hereby declare that the investigation presented in the thesis has been carried out by me. The work is original and has not been submitted earlier as a whole or in part for a degree / diploma at this or any other Institution / University.

Rajini P Antony

Kalpakkam

October, 2012

Dedicated to my

Pappa, Mummy,

Achan chettan

Josemon, Jeesuttan & Jerommon

Acknowledgement

It would not have been possible for me to prepare my doctoral thesis without the help and support of a number of wonderful people, who have shaped my ideas and helped in my research.

I express with great pleasure my deep sense of appreciation and gratitude to my supervisor ***Dr Sitaram Dash*** *for giving me an opportunity to work in his lab and I am grateful to him for his support and guidance, throughout the course of this work. I specially thank him for providing me the necessary infrastructure and resources to accomplish my research work.*

I am immensely indebted to my research coordinator ***Dr Tom Mathews*** *for the stimulating discussions, constructive criticisms and tutelage that put me always on my toes. I will ever ruminate with joy the association with Dr Tom that marked consistent encouragement and dutiful guidance interspersed with warmth and sublimity. The passion for fine research kindled by him will be commemorated forever. All above, I thank him for his systematic guidance, constant encouragement, great effort and patience which have given a solid shape to the work in this thesis. I deem it as my privilege to work under his able guidance.*

I would like to extend my heartfelt thanks to ***Dr Baldev Raj****, former director of IGCAR, for allowing me to pursue research in this prestigious institution. I express my sincere gratitude to him for allowing me to choose the project of my interest, for his moral support and inspirational talks. Had it not been for him I would not have done my doctoral research in the emerging area of nanomaterials. I also thank* **Shri. S C Chetal,** *director, IGCAR, for allowing me to continue my research here.*

I thank ***Dr A. K Tyagi,*** *Head, Surface and Nanoscience Division, for support, motivation and interest during the course of research. I take this opportunity to register my thanks to* **Dr C S Sundar***, Director, Material Science Group for his interest and motivation.*

The road to my PhD started with the one year course work which helped me in understanding some of the basic aspects of science with deep insight. This enthused me a lot in my research to approach the problems in a systematic way. I thank all my teachers who conducted classes during course work.

My sincere thanks to the doctoral committee Chairman ***Dr B V R Tata*** *and members* ***Dr V Jayaraman, Dr K S Viswanathan*** *for the time to time evaluation, constant encouragement and useful suggestions throughout my research work. I am much grateful to* ***Dr K S Viswanathan*** *who picked me up and brought me back as a student during my critical stage in research.*

The inspiration, help and suggestions received from ***Dr. T Gnanasekharan****,* ***Dr K I Gnanasekharan****,* ***Dr K V Govindankutty, , Dr V Balamurugan, Dr Niranjan Kumar, Dr Arindam Das, Dr Arun K Prasad, Dr R Vishwanathan, Shri Manoj Kumar, Dr R Bhaskaran, Dr Seshadri, Mr N Sanil, Dr M T Jose, Dr Madhosoodhanan*** *and* ***Mrs O Annalakshmi*** *are beyond evaluation and the facilities extended by them were of great help and solace and is acknowledged with gratitude. The guidance, care, encouragement and affection given during the past five years by* ***Dr S Rajagopalan****,* ***Dr, R Ramaseshan, Dr R Krishnan, Dr S Tripurasundari, Dr S Ilango*** *is acknowledged with gratitude.*

I would like to thank ***Mrs & Mr M C Valsakumar*** *for their parent like concern and care. I express my sincere thanks to* ***Dr John Philip*** *for his valuable suggestions, advices and help.*

I am thankful to ***Dr M Saibaba****, for support and advices in the initial stage of my life in Kalpakkam and for facilitating a nice and enjoyable stay in JRF enclave.*

I wish to thank, ***Dr Arupdas Gupta, Mr C Ramesh, Mr N Murugesan, Dr Rani P George, Mr P K Ajikumar, Dr R V Subbarao, Mrs S Kalavati, Dr Sandip Kumar Dhara*** *and* ***Dr Sundaravel****, for extending their technical help during my research work. A special thanks to my friend* ***Mr Nandagopal Krishna*** *for his keen involvement in the XPS characterization, analyses and fruitful technical discussions. I thank my friend* ***Mr Kalpataru Panda*** *for helping me in field emission studies. I wish to thank* ***Mrs Vijayakumari, Sunita, Sheela*** *and* ***Mr Kannabiran*** *for their kind cooperation during my research work. Thanks to* ***Anoop, Ajithachechi, Rasmi, Shima, Jyothirmayee,*** *and* ***Dayana*** *for sending research articles needed for my research during the past five years*

My Sincere thanks to my seniors, ***Dr Feby Jose, Dr Baban P Donge, Dr Nirmal Chandra Raut, Mr Kamalakannan*** *for the help and support. I also thank* ***Avinash, Bonu, Ashok, Shyamala Rao, Suresh, Subhroto, Preethi*** *for their help and nice companionship during my research in this group. Special thanks go to* ***Ms Madhusmita Sahoo*** *whose presence made the lab lively. Her timely help during my research work will remain green in my mind for ever.*

I wish to express my appreciation to all my colleagues and friends in MSG, especially ***Prasana Kumar Sahoo, Soumee, Gayathri, Mahendra Kumar, Tulasi Satya, Prabhakar, Herojit, Kamali, Saravanan, Deepak, Manan, Gurpreet, Radhakrishnan, Karthik, Namrata, Sorb, Shilpam Sharma, Vinod chettan, Neha, Sumita, Remya, Sivadasan*** *and* ***Lekshmichechi*** *for their valuable suggestions, help, support, consideration and love.*

A large Quantum of thanks goes to ***Mrs Assa and family****, who considered me as their family member and extended a sisterly love towards me. The affectionate smile and face of her daughter "****Chinmayee****" made my life in Kalpakkam hopeful. I really miss her in this moment and their memories will linger in my mind for ever.*

I would ever cherish the memorable companionship of my friends and batchmates especially ***Subhra, Ruth, Madhusmita, Kuheli, Bishnu, Kalpataru, Prasana, Bharat, Joy, Girish, Rahul, Karanakara Misra****,* ***Haribabu*** *and their memories will stay behind in my mind for ever. Special thanks to* ***Thrinad*** *and* ***Varghese*** *who helped and encouraged me in my early stages of course work and research. The camaraderie developed between me, Ruth and Subhra is treasured.*

I am indebted to many of my friends and their family especially ***Mrs Sajimol & Reni, Mrs Neethu & Ribu, Mrs Brijitta & Amit, Mrs Sini & Satya, Mr Praveen & Sreeranjini,*** *who used to visit my house frequently. I thank them for their care and support. Special thanks to my friend* ***Clinsha*** *for her encouraging technical discussions and help during my research work in IGCAR*

The bustling company of many friends made the stay in Kalpakkam vivacious. ***Shima, Divya, Priyada, Juby, Suja, Anishia, Reshmi, Arun chandran, Sabeena, Rasmi C K, Rasmi K R, Soja, Meera, Hemlin, Venkat, Joby, Mebin, Joel, Jovin, Anuraj, Sreejith, Nishad, Navas, Jaffar, Jayarajettan, Haneef, Sandeepan, Linet,*** *__Vineetha, Greeshma, Deba, Arun Babu, Devidas, Aishwarya, Shaswat and Uma and all members in enclave__ and many others need a special mention at this juncture. I thank all of them for the interesting discussions other than research and fun filled moments we had together. Thanks to all for being with me in adverse stages of my life. Special thanks go to __Jobha__ and __Annu__ for being my sister like friends here in Kalpakkam and have a great pleasure to thank __Annu & family__ who have given a place for me in their prayers.*

I would like to express huge, warm thanks to __Arun__ whose brotherly concern supported me in Kalpakkam in various stages of my research life.

It is my fortune to gratefully express the support of some special individuals who are special in my life and shaped me to the present stage.

Words fail me to express my appreciation to my achan chettan, __Fr Seby Kanjirathingal__ for his spiritual and material support, generous care and concern during the inevitable ups and downs in my life. I recall here with reverence his prayers which fortified me in times of despair. He was always with me to motivate and push me forward. He taught me from his deeds to love others as our own irrespective of their nature, to help others and to look deeper into myself to become the person I wanted. I doubt that I ever be able to convey my appreciation fully to him, but I owe him, my eternal gratitude.

"A best friend is like a four leaf clover, hard to find and lucky to have". Thanks to __Anees__ for being my best friend who were always there with me in my toughest moments. Thanks for making me smile in my miserable situations. Your friendly advice, soothing words, being at the needful moments, your big heart, helped me to overcome the obstacles I faced and continue my work. You had a faith in my ability, anchored me when I was adrift, and stood by me when I felt alone. Words cannot express my heartfelt thanks to you.

My sincere thanks to all my teachers who taught me in my schooling and college life, especially __Mrs Usha, Mrs Nandini, Miss Deena, Miss Mary, Miss Lissy, Dr . E A Jose, Dr. Joby Thomas, Dr. P A Jose.__

I recall at this juncture with reverence, my parents __Mr P V Antony__ (Late) & __Mrs Kathrina Antony__ whose selfless sacrificial life, great efforts with pain and tears, unceasing prayers and immense concern, enabled me make this thesis possible. __Josemon, Jeesuttan & Jerom mon…..__ thanks for being supportive and caring siblings which were always my confidence. I remember thankfully my __ammamma__, __vellyammachi__, __kunjachan__ and __kochachan__ for their care and prayers.

Finally I thank one and all who have helped me directly or indirectly for the successful completion of my thesis.

…Rajini

Contents

SYNOPSIS

Sustainable energy and environment are the two important concerns of our modern society. Innovations on new materials and material architectures embodying novel functions expand the scope of their application for assisting global sustainability. In this context, titanium dioxide (TiO_2) based materials have proven to be the most promising candidate material because of their low cost, non-toxicity, high stability and wide range of applications in the field of energy conversion and storage (photovoltaic cells, green-energy hydrogen generation by splitting of water, hydrogen storage), electronics (large area electron field emitters, sensors), self cleaning surfaces (fog-proof and self cleaning glass) and environmental photocatalysis (photocatalytic decomposition of organic pollutants in water and air, anti-bacterial, anti-viral, fungicidal, anti-soiling). Various nano-architectures of TiO_2, like nano-tubes, nano-wires, nano-rods, nano-fibers and nano-platelets with tailored geometry and surface complexity, in thin film and powder forms, are being investigated for various functional applications in energy, electronics and environment. In all the cases the advantages of tailored geometry combined with the intrinsic properties of nano-crystalline TiO_2 can be gainfully exploited.

For applications in dye sensitized solar cells, large area electron field emitters and wetting – de-wetting coatings, where nanoarchitectures of high aspect ratio, large surface area, directional electron transport properties, thin tube edges and surface roughness with long trapped air columns are expected to enhance the efficiency, vertically aligned nanotube arrays as thin films / coatings are of high interest. In applications like green-energy hydrogen generation by splitting of water and photocatalytic decomposition of organic pollutants in water, suspensions of large surface area particles like nanotubes are preferred as the configuration has better light harvesting ability and hence better efficiency. The aim of the present study is to explore the effect of the relevant properties of electrochemically synthesized pristine and N-doped TiO_2 nanotube arrays and powders in photovoltaics, field emission, self-cleaning surfaces, green energy hydrogen generation and degradation of organic pollutants.

Synthesis of vertically aligned pristine and N-doped TiO_2 nanotube array thin films / coatings, their characterization, studies pertaining to their application in DSSCs, large area electron field emitters and hydrophobic ↔hydrophilic switching surfaces as well as synthesis of pristine, Pt loaded and C & N - co-doped TiO_2 nanotube powders, their characterization and their application in photocatalytic hydrogen generation by splitting of water and photocatalytic decomposition of organic pollutants in water are the highlights of this thesis.

Outline of the research work

Chapter 1:

The chapter gives a brief history of the progress of the development of TiO_2 nanotubular architectures and its present status. The physical and chemical properties of TiO_2 are also deliberated. Based on these unique physical and chemical properties of TiO_2, discussions on selected applications of TiO_2 are incorporated. This is followed by statement of objectives.

Chapter 2:

The chapter briefly discusses the various experimental tools employed for the synthesis and characterization of TiO_2 nanotubular structures. In addition, description on the design and fabrication of the experimental facilities used for photovoltaic, field emission, wetting – de-wetting, hydrogen generation and photocatalytic studies are furnished.

Chapter 3:

It is expected that one dimensional nanostructures of TiO_2, having large surface area, high aspect ratio, vectorial electron transport and surface roughness with long trapped air columns, when used for fabricating devices such as dye sensitized solar cells, electron filed emitters and hydrophobic ↔ hydrophilic switching surfaces, will enhance their overall efficiencies. Vertically aligned TiO_2 nanotube arrays are one dimensional nanostructures that exhibit the above characteristics. At the outset, studies were undertaken to understand the improvement in the efficiencies of the devices when self organized nanotube arrays are incorporated instead of other common nanostructures like particulates. To aid this step, synthesis of vertically aligned nanotube arrays of pristine and N-doped TiO_2 was undertaken.

This chapter mainly deals with the synthesis of TiO_2 Nanotube Arrays (TNTA) on foils and Fluorine doped Tin Oxide coated (FTO) glasses by potentiostatic anodization technique. The electrolyte used for anodization was ethylene glycol containing ammonium fluoride and water. The process parameters like applied voltage, anodization time and electrolyte compositions were varied in the synthesis process to study their effect on surface morphology and aspect ratio of TiO_2 nanotubes. From the potentiostatic transients the mechanism of formation of TiO_2 nanotubes, during anodization, was formulated. Correlating with reported results, it was confirmed that field assisted chemical oxidation of Ti along with field assisted chemical dissolution of Ti and TiO_2 by fluoride ions played the key role in nanotube formation. The subsequent steady state equilibrium between field assisted chemical dissolution and field assisted chemical oxidation led to continuous growth. The process parameters for obtaining smooth walled high aspect ratio nanotube arrays were optimized by carrying out anodization at different experimental conditions. From the morphological analyses of samples synthesized under various electrochemical conditions, the minimum required potential for the formation of nanotubes as well as the maximum potential under which tube formation occur were found to be 40 and 60 V, respectively. The diameter as well as the length of the TiO_2 nanotubes were found to increase with applied potential and anodization time. In addition, surface morphology of individual tubes was found to vary with electrolyte composition. The appropriate process parameters for attaining highly ordered, debris free TiO_2 nanotube arrays of sufficient lengths (~8 microns), were found to be applied potential of 30 to 50 V, 2 to 3 hours of anodization time and electrolyte composition of 0.25 to 0.5 wt% of NH_4F + 2 to 3 wt% of H_2O in ethylene glycol. All the nanotubes in the as prepared stage were amorphous. These underwent transformation to anatase phase on annealing at 400 ^oC. The anatase to rutile phase transition occurred above 500 ^oC. It was also observed that the samples annealed at 400 and 500^oC retained their tubular structure. Whereas those annealed at 600 and 700 ^oC exhibited tubes with closed mouth, formed due to wall thickening. The presence of different surface and subsurface defect states, such as bridging oxygen vacancies (Ti - V_O – Ti), Ti – OH – Ti / Ti-$(OH)_2$-Ti bridge and surface terminating Ti – OH, in the nanotubes were confirmed from XPS and FTIR studies. The defect state detection of XPS analysis supports the enhanced photo catalytic activity of TiO_2 nanotube arrays. The band gap of the pristine TiO_2 nanotube array calculated from diffuse reflectance spectra was 3.27eV.

The TNTA fabricated on foils possessed certain limitations in specific applications such as DSSCs as it requires back side illumination which reduces light to electrical energy conversion efficiency. In addition, when used in electronic devices like sensors, the Ti metal substrates on which the TiO_2 nanotubes are formed causes short circuits. To resolve these issues, efforts were initiated to fabricate TNTA on FTO coated glasses. TiO_2 nanotube thin films on FTO coated glasses were synthesized by electrochemical anodization of Ti film deposited on FTO coated glasses by RF magnetron sputtering. The electrochemical process parameters were fixed based on the results obtained in the case of synthesis of TNTA on foils. Anatase nanotube arrays with homogeneous tube diameters, wall thicknesses and inter-tubular spacings were obtained when anodization was carried out at 40V for 2 hours in 0.5wt% NH_4F + 2.5 wt% water in ethylene glycol medium, followed by annealing at 400 ^oC. As in the case of TNTA on foils, the nonstoichiometry of the TNTA films on the FTO coated glasses due to the presence of bridging oxygen vacancies and hydroxyl groups were proved by X-ray photoelectron spectroscopy. The band gap of the annealed samples obtained from diffuse reflectance spectroscopy was 3.36 eV which indicated absorption in the ultra violet region.

The major drawback of TiO_2 is that its band-gap is rather large, 3.0–3.2 eV, and thus only 5% of the solar spectrum ($\lambda < 380$ nm, corresponding to the UV region) is absorbed. To lower the threshold energy for photoexcitation, a great deal of research has been focused on doping TiO_2 with both transition metal cations and anions. Among these, N-doping was found to be more promising. Substitution of O^{2-} ions by N^{3-} ions is more effective due to their similar size. Because of the comparable ionic size, the lattice distortion will be less and hence large numbers of recombination centres are not generated. Single step electrochemical synthesis of N-doped TNTA was carried out using urea as the nitrogen source in the electrolyte. Urea was chosen as the nitrogen source, as electrolysis of aqueous solutions containing urea decomposes to N_2 and CO_2 at high anodic potentials. Since nitrogen formed at the anode surface will be nascent, before being liberated as N_2, there exists the possibility of nitrogen incorporation in to the anion lattice of TiO_2 during the formation of TNTA. Also one can expect a variation in the amount of nitrogen substituted for oxygen in the anion sub lattice with nitrogen precursor (urea) concentration. Anatase N-doped TNTA was prepared by anodizing Ti foils, in 0.5wt% NH_4F + 2.5 wt% water in ethylene glycol medium containing various wt% of urea at 40V for 2 hours, followed by annealing at 400 °C. XPS analysis revealed substitutional N- doping of about 3.88, 4.74 and 4.12 atom percent corresponding to formulae $TiO_{1.85}N_{0.115}$, $TiO_{1.813}N_{0.14}$ and $TiO_{1.84}N_{0.121}$ respectively. The optical band gap values were found to shift to lower values with N-doping. The band gap values obtained are 3.22, 2.75 and 2.77 eV for $TiO_{1.85}N_{0.115}$, $TiO_{1.813}N_{0.14}$ and

$TiO_{1.84}N_{0.121}$, respectively. In the case of $TiO_{1.813}N_{0.14}$, introduction of inter-band state could be easily discerned from the absorption spectrum.

Chapter 4:

The fabricated TNTA on foils and FTO coated glasses can be used in various applications such as DSSCs, field emission, photocatalysis, self cleaning surfaces and sensors depending upon their aspect ratio, crystallinity, composition and electronic energy band structure. The present chapter therefore discusses the selective applications of TNTA on foils and FTO glasses. The chapter is divided into three sections. The first part deals with the photovoltaic characteristics of the DSSCs fabricated using TNTA on foils and FTO glasses, this is then followed by studies on enhancement of field emission properties with N-doping of TNTA and hydrophobic ↔ super hydrophilic switching behaviour of pristine and N-doped TNTA.

Dye sensitized solar cells were fabricated using TNTA on Ti foil and FTO coated glass working electrodes, ruthenium I pyridyl dye, N-719 sensitizer, iodolyte (Solaronix, Switzerland) electrolyte and Pt coated glass counter electrode. The solar cell performance of these cells was investigated at $1.6 mW/cm^2$ light intensity. The efficiency of the DSSCs fabricated using TNTA on foils and TNTA on FTO coated glasses were very low with values 0.65% and 0.11%, respectively. The lower efficiency can be attributed to the low fill factors and low incident to photon conversion efficiencies (IPCE) of the respective cells. The reasons for low fill factor and IPCE can be ascribed to the deterioration of the FTO film upon anodization, the limited transmittance of the anodized thin films and improper dye attachment. The limited length of the nanotubes on FTO coated glass (~1 μm) is another reason. To ascertain the above said limitations, DSSCs were fabricated using TiO_2 coated FTO glasses and Pt counter electrodes procured from Solaronix, Switzerland, with the same dye and electrolyte as employed before.

The efficiency of the corresponding cell was higher with an value of 7.8%. In addition, the high electrochemical impedance obtained for the cells fabricated using TNTA compared to the cell fabricated using procured TiO_2 and Pt electrode confirmed the identified drawbacks. Transparent TNTA on conducting glass will be a promising candidate for the third generation solar cells if the above mentioned limitations are properly addressed and overcome.

Since TNTA possess vertical alignment, high aspect ratio, small wall thickness and sharp edges, these become potential candidates for large area field emitters. In addition, as N-doping is reported to modify the electronic energy band structure of TiO_2 leading to reduction in work function, N-doping of TNTA is expected to enhance electron field emission properties. Hence electron field emission properties of pristine and N-doped TNTA were explored. Field emission properties of pristine and N-doped TNTA corresponding to various concentrations of nitrogen were measured and compared. In the case of N-doped TNTA, the electron field emission was detected at much lower turn on fields viz., 12.5, 10.4 and 7.1 V / μm at 3.88, 4.12 and 4.74 at% of nitrogen doping, respectively. Systematic variation in electron emission with increase in N-doping confirmed the role played by substitutional nitrogen towards FE enhancement. The enhancement of FE properties on N-doping occurs because of the presence of localized donor states, with higher band width, placed at energy levels close to CBM compared to that of $TiO_{2-\delta}$ and N-2p states above the VBM, leading to a shift in the Fermi level to higher energies. In the present study, the Fowler Nordheim (FN) plot of the N doped TNTA revealed nonlinearity, with three regimes of distinctly different slopes (high field, intermediate field and low field). The low field region corresponds to surface states dominated FE. In the high field regime the field penetration caused breakdown of the surface potential barrier which enhances FE. In the intermediate field regime both the mechanisms competed and a different slope appeared. The results of the present investigations formed the basis for future research in developing large surface area field emitters using N-doped TNTA.

The last part of the chapter deals with near superhydrophobic to superhydrophilic conversion of the nanotube arrays under UV (1.4mW/cm^2) as well as sun light (44 mW/cm^2) illumination. Near super hydrophobic states were observed for both pristine and the N doped TNTA. The N-doped samples were less hydrophobic compared to the pristine samples, as expected. The hydrophobic to super hydrophilic conversion was faster and the reverse process slower for N-doped samples. Under sun light irradiation, complete superhydrophilicity was observed only for N-doped TNTA and this was achieved within 90 minutes. The recovery, when kept under dark was attained within two and half days. Since no single mechanism could explain all the observed experimental results, a combination of mechanisms (photocatalytic decomposition of adsorbed organics and photo induced surface reconstruction) has been proposed. The observed near super hydrophobic ↔ super hydrophilic switching behaviour indicated the potential of TNTA coated surfaces for application as smart surfaces.

Chapter 5:

For applications such as photocatalytic hydrogen generation and organic pollutant destruction, TiO_2 nanotubes in the powder form will be more efficient as these can be suspended in the media thereby facilitating better light harvesting and exhibiting superior kinetics. The chapter discusses the synthesis and characterization of TiO_2 nanotube powders by the rapid break down anodization technique. The tubular morphology was confirmed by FESEM and TEM analysis. The tubes were of uniform diameter (15 to 18 nm) and wall thickness (~5 nm). The SAED patterns and XRD analysis revealed as prepared nanotubes to be of anatase phase. Their band gap values varied from 2.95 to 3.07 eV indicating near UV and visible light absorption capabilities. The samples in the as prepared state had surface area as high as $155m^2/g$. FTIR and PL spectroscopic studies revealed presence of defect states which is crucial for the photo catalytic applications. Compared to TNTA, these nanotubes were found to be visible light absorbing and consisted of smaller diameter and wall thickness.

The preparation of N-doped nanotube powders were tried by anodizing Ti foils in perchloric acid media containing urea as the nitrogen source. The anodization resulted in C and N- co-doped TiO_2 nanotube powders. X-ray photoelectron spectroscopic analysis revealed interstitial N-doping and substitutional C-doping. Similar to the pristine TiO_2 nanotube powders, the C and N- co-doped samples were of anatase phase in the as prepared condition. These powders possessed high surface area ($124m^2/g$) although their value is marginally lower than that of pristine ones. The FESEM and TEM analysis revealed destruction of tubular architecture upon doping. The diffuse reflectance spectroscopic studies did not show any significant reduction in band gap. Hence an enhancement in photocatalytic properties cannot be expected. In turn, deterioration in photocatalytic property is possible due to the generation of defect states, arising from doping, and these states can act as electron-hole recombination centres. Indeed, the same was observed.

Chapter 6:

Since, the as prepared pristine as well as N and C co-doped TiO_2 nanotube powders possess high surface area, these are potential candidates for photocatalytic applications such as green energy hydrogen generation and organic pollutant destruction. The present chapter deals with the photocatalytic studies on TiO_2 nanotube powders and is divided into two parts. The first part deals with studies on hydrogen generation by water photolysis using Pt loaded TiO_2 nanotube powder catalyst and is followed by organic pollutant destruction studies under sunlight illumination using pristine and C and N- co-doped TiO_2.

Noble metals such as Pt, Au, and Pd have been reported to be very effective in enhancing the photocatalytic efficiency, when loaded on TiO_2. Since the Fermi levels of the noble metals are lower than the TiO_2 conduction band, when loaded on to TiO_2, the photo excited TiO_2 electrons move to the noble metal Fermi levels leaving the holes in the valence band, reducing the electron – hole recombination and thereby enhancing the photocatalytic efficiency. Among these noble metals Pt is reported to be the most efficient.

TiO_2 nanotube powders were loaded with Pt at different weight percentages (varying from 1 to 10) by chemical reduction technique using sodium borohydride. A phase transformation from anatase to rutile structure was also observed at high Pt loadings (> 5wt %). The decrease in PL intensity of the Pt loaded TiO_2 compared to TiO_2 without Pt, revealed reduction in electron hole recombination on Pt loading. The active area (chemisorption surface area) of Pt was measured by temperature programmed desorption reduction oxidation technique (TPDRO) and was found to be high at low Pt loadings (1 to 2.5wt% of Pt). The H_2 gas generated from 1:3 water – ethanol reaction mixture was measured using a polymer electrolyte membrane based H_2 sensor (PEMHS). Hydrogen generation efficiency was found to decrease with increase in Pt loading. The highest H_2 generation rate, under near UV light (~380 nm and 120 W), was observed at 1.25 and 2.5 wt% Pt loadings and are 777.3 and 927.9 μ moles of H_2 / h for 1 g of Pt-TiO_2 catalyst, respectively. For an incident light of 254 nm wave length (64 W) and with 1.25 wt% Pt loading, the hydrogen generation rate obtained was 0.030 moles / hour for 1 g of Pt/TiO_2. The turn over frequencies (TOF) calculated from the chemisorption surface area and hydrogen generation measurements revealed that at low platinum loading more catalytic sites are available for hydrogen generation. Taking into consideration the low amount of Pt loading and the low power of UV sources used, the hydrogen generation rates obtained are the highest among the reported values.

The dye degradation efficiencies of pristine and C and N- co-doped TiO_2 nanotube powders were investigated, using Rhodamine 6 G dye as the model pollutant, under sunlight of 10 mW/cm^2 intensity. The change in dye concentration with irradiation time was measured using UV-visible absorption spectroscopy. It was observed that the degradation kinetics followed apparent first order kinetics and the calculated rate constants are 4.99×10^{-5} s^{-1} (2.99×10^{-3} min^{-1}) and 3.99×10^{-5} s^{-1}(2.4×10^{-3} min^{-1}) for pristine and doped samples, respectively. The dye destruction efficiencies of pristine and doped samples were 40% in 150 minutes and 42% in 240 minutes, respectively. Even though a slight decrease in the band gap on doping was observed, the photocatalytic efficiency of doped samples was low. This can be attributed to generation of charge recombination centres on doping.

Chapter 7

This chapter summarizes major research findings, implications and recommendations for future work.

List of Figures

List Tables

List of Publications

1. **Rajini P. Antony**, Tom Mathews, Arup Dasgupta, S. Dash, A. K. Tyagi, and Baldev Raj, "Rapid breakdown anodization technique for the synthesis of high aspect ratio and high surface area anatase TiO_2 nanotube powders," Journal of Solid State Chemistry **184** (3), 624-632 (2011).
2. **Rajini P. Antony**, Tom Mathews, Sitaram Dash, Ashok K. Tyagi, and Baldev Raj, "X-ray photoelectron spectroscopic studies of anodically synthesized self aligned TiO_2 nanotube arrays and the effect of electrochemical parameters on tube morphology," Materials Chemistry and Physics **132** (2–3), 957-966 (2012).
3. **Rajini P. Antony**, Tom Mathews, C. Ramesh, N. Murugesan, Arup Dasgupta, S. Dhara, S. Dash, and A. K. Tyagi, "Efficient photocatalytic hydrogen generation by Pt modified TiO_2 nanotubes fabricated by rapid breakdown anodization," International Journal of Hydrogen Energy **37** (10), 8268-8276 (2012).
4. **Rajini P. Antony**, Tom Mathews, Kalpataru Panda, B. Sundaravel, S. Dash, and A. K. Tyagi, "Enhanced Field Emission Properties of Electrochemically Synthesized Self-Aligned Nitrogen-Doped TiO_2 Nanotube Array Thin Films," The Journal of Physical Chemistry C **116** (31), 16740-16746 (2012).
5. **Rajini P Antony**, Tom Mathews, P. K Ajikumar, D Nandagopal Krishna, S. Dash and A. K Tyagi, "Electrochemically synthesized visible light absorbing vertically aligned N-doped TiO_2 nanotube array films" , Material Research Bulletin **47**, 4491-97 (2012)
6. **Rajini P Antony**, Tom Mathews, Jobha C Johnson, S. Dash and A. K. Tyagi, "Visible light photocatalytic degradation of Rhodamine 6 G by pure and C and N co- doped TiO_2 nanotube powders", (Energy and Environment Focus- Just accepted)
7. **Rajini P Antony**, Tom Mathews, S. Dash and A. K. Tyagi, "Kinetics and Physico-Chemical Process of Photo-Induced Hydrophobic ↔ Super-Hydrophilic Switching of Pristine and N-doped TiO_2 Nanotube Arrays" (Journal of physical chemistry C, *J. Phys. Chem. C*, **2013**, *117* (13), pp 6851–6860)
8. **Rajini P Antony**, Tom Mathews, S. Dash and A. K. Tyagi, " Effect of tube diameter on the photo-induced antibacterial properties of TiO_2 nanotube arrays" (Communicated- RSc advances)
9. **Rajini P Antony**, Tom Mathews, S. Dash and A. K. Tyagi, "Photovoltaic characteristics of Dye sensitized solar cells fabricated using TiO_2 nanotube arrays." (Communicated - Solar Energy Materials & Solar Cells)

Conference Presentations

1. **Rajini P Antony**, Tom Mathews, C Ramesh, N Murukesan, S Dash, A K Tyagi, Photo-assisted Hydrogen generation from ethanol-water mixtures by Platinum loaded Titania nanotube catalyst, Third International Conference on Frontiers in Nanoscience and Technology (Cochin Nano 2011, August 14-17, Cochin, India). (Oral presentation)
2. **Rajini P Antony**, Tom Mathews, Sitaram Dash and A K Tyagi. "Effect of annealing temperature on structural and morphological stability of TiO_2 nanotube arrays." ICONSET-2011, 28th-30th Nov, 2011, Satyabhama University, Chennai. (Oral presentation- Best presentation award), IEEE Xplore, Proc. of ICONSET-2011, pp. 326-330, DOI:10.1109/ICONSET.2011.6167974.
3. Tom Mathews, **Rajini P Antony**, P. K Ajikumar, B. Robert, S. Chakraborty, S. Dash and A. K Tyagi. "Fabrication of TiO_2 nanofibers by electrospinning technique" ICONSET-2011, 28th-30th Nov, 2011, Satyabhama University, Chennai. IEEE Xplore, Proc. of ICONSET-2011, pp. 540-542, DOI:10.1109/ICONSET.2011.6168026.
4. **Rajini P Antony**, Tom Mathews, Sitaram Dash, A. K. Tyagi and Baldev Raj, "Transparent Self Aligned TiO_{2-X} Nanotube Array Thin Films for Solar Cell Applications: Synthesis and Characterization". ICAM 2011, Dec 11-15, PSG Tech Coimbatore. (Oral Presentation)
5. **Rajini P Antony**, Tom Mathews, S. Dash and A .K .Tyagi, Synthesis and Characterization of TiO_2 Nanotube 1 Arrays and Powders by Electrochemical Anodization: Impact of Solution Conditions, 4th ISEAC Triennial International Conference on Electro Analytical Chemistry and Allied Topics (ELAC-2010) at Toshali Sands, Puri, Orissa, India during March 16-18, 2010 organized by Indian Society for Electro Analytical Chemistry (ISEAC). Published in conference proceedings.
6. **Rajini P Antony**, Tom Mathews, S. Dash and A .K .Tyagi , Synthesis of self organized TiO_2 nanotubes by electrochemical method, The International Workshop On Nanotechnology and Advanced Functional Materials during 09-11 July, 2009 (NTAFM-09) organized by NCL, IISER and University of Pune
7. **Rajini P Antony**, Tom Mathews, Arup Dasgupta, S. Dash and A .K .Tyagi, Formation of TiO_2 nanotubes by anodization of Titanium foils and thin films, IBSA Nanotechnology School on Advanced Materials at Hotel Chariot Beach Resort, Mamallapuram, India during February 22-26, 2010 conducted by India-Brazil- South Africa Nanotechnology Initiative.
8. **Rajini P Antony**, Tom Mathews, S Dash and A K Tyagi, Quasi-one dimensional nano-architectures of TiO_2 for sustainable energy, 24th Annual General Meeting of Materials Research Society of India, 2013 held at the Indira Gandhi Centre for Atomic Research, Kalpakkam, during February 11-13, 2013

Chapter 1

Introduction

The chapter addresses the issues involved in identification of suitable one dimensional nano-architecture of TiO_2 *for selected applications pertaining to energy, electronics and environment. The first part of the chapter provides a brief overview of the structure, properties and various methods employed for modification of the electronic energy band structure of* TiO_2*. The subsequent section describes the synthesis of different one-dimensional nano-architectures of* TiO_2 *and their selected applications in the area of energy, environment and electronics. In addition, role of titania nanotubular architectures in alternative energy generation processes and environmental cleaning is deliberated. This is followed by a statement of motivations and objective behind the present research work.*

Semiconducting materials have been the subject of intense research because of their practical applications. They also provide fundamental insight into the electronic processes involved when used in various applications. Within the class of inorganic semiconducting materials, oxide semiconductors display diverse range of properties, due to their dependence on the nature of metal – oxygen bonding. Among semiconducting oxides, wide band gap oxide materials are of high interest as these exhibit wide ranges of electrical and optical properties. Among the wide band gap oxide materials, titanium (IV) oxide has attracted much attention due to its application in various fields ranging from paint to sunscreen to food coloring to photocatalyst, hydrogen production, storage medium, solar cells and biology. For example TiO_2 powder is commonly used as a pigment in paints, coatings, plastics, inks, fibers, nutrients, toothpaste, and cosmetics.[1,2] Due to its high refractive index, it is applied as antireflection coatings, optical wave guide and narrow-band filters.[3-5] Because of its interesting photocatalytic properties, it finds use in various applications such as environmental remediation, hydrogen generation by photolysis of water, photovoltaic cells, electrochromic devices, photoelectrochemical anticorrosion coatings, self cleaning and antifogging coatings.[6-15] The two commonly available stable phases of TiO_2 are rutile and anatase. Rutile is preferred to anatase for optical and dielectric applications because of its high refractive index and dielectricity.[16] Whereas, anatase is preferred for all applications related to photocatalytic activity due to its higher charge carrier mobility.[10, 11, 17,18] Several excellent reviews are found in literature which deals with the synthesis, properties and applications of TiO_2.[19-23]

Ever since the discovery of size quantization effect in semiconductor nanomaterials, research in nanostructured materials has generated considerable interest.[24,25] The properties of interest viz. optical, electronic and catalytic are found to be related to size in the nanoscale regime and drastically differ from those of bulk counterparts. With respect to photo-activity,

TiO_2 nanoparticles have specific advantages in enhancing light absorption due to the presence of large fraction of atoms in surfaces and interfaces. The primary mechanism of light absorption in semiconductors is the direct valance band to conduction band electronic transition, which is low in case of semiconducting materials like TiO_2 as direct transition, is forbidden by crystal symmetry. However, when light absorption takes place at the crystal boundaries such as surfaces and interfaces interspersed among crystallites, the momentum is not conserved and an indirect transition occurs leading to enhancement in light absorption. Hence, it can be expected that, nanocrystals with high surface to volume ratio and large surface atom fraction will have enhanced light absorption. The particle size at which enhancement becomes significant is around 20 nm. When the particle size is confined, at least in one dimension, to a scale below the de Broglie wavelength, the wave function is spread over the particle and the charge carriers need not diffuse to the surface to take part in surface/interface processes. This makes possible the timely utilization of photo-generated charge carriers. In addition, due to quantum confinement, the energy band structure becomes discrete thereby rendering the ensuing photophysical, photochemical and surface properties different from those of bulk.[26-28] Since the properties of nanostructured TiO_2, relevant to the various applications, are significantly different from those of the bulk, recent research has been concentrated on controlling the size, shape, composition and surface morphologies as well as surface properties for tailoring them to be utilized for specific applications.

Over the past decade, one dimensional nano-architectures of TiO_2 such as nanotubes, nanowires, nanorods and nanobelts have attracted wide spread attention due to the unique physical and chemical properties associated with their size confinement in one dimension. Relatively simple preparation techniques used to achieve the requirements for various applications have made them quite attractive.[29-34] In nanostructured semiconductors the mobility of charge carriers is governed by quantum confinement and hence the electron and hole transport properties are influenced by their one dimensional architecture.[35] The properties of one dimensional nano-architectures of TiO_2 are comparable to that of nanoparticles but with high surface to volume ratio as well. The high specific surface area of one dimensional nanostructured TiO_2 facilitates interaction between surfaces / interfaces and reactive species.[36-38] In addition, they have enhanced photoactivity and charge transfer at the interface due to better charge transport, higher surface defect density and aspect ratio. These properties along with the exotic surface geometry render the one dimensional nanostructured TiO_2 based materials excellent candidates for application in photocatalysis, sensors, hydrogen generation by water splitting, photovoltaics and biology. Among the one dimensional nano-architectures, nanotubes are promising because of larger active surface area.[39-42] Nanoarchitectures like self aligned nanotube arrays in thin film form provide enhancement in the performance of devices as well as expand the field of applications. For example, vertically aligned thin walled TiO_2 nanotube arrays are expected to find application in large area field emitting devices because of their high aspect ratio and large amount of surface states.

The present chapter focuses on synthesis, modification and selected application of one-dimensional nanoarchitectures of TiO_2 in energy, environment and electronics. Emphasis is given to self aligned nanotube arrays and nanotube powders of TiO_2. A brief review on structure, properties and modification of electronic band structure by doping are given at the outset.

1.1. Structure

Titanium dioxide (TiO_2) exists in nature mainly in three forms, namely, anatase, rutile and brookite.[19],[43]. This transition metal oxide is highly stable and has a melting point of 1855°C. The most common polymorphs of TiO_2 are anatase and rutile and their structure can be expressed in terms of chains of octahedra in which Ti^{4+} ion is surrounded by an octahedron of six

O^{2-} anions. The TiO_6 octahedra in both these phases are orthorhombically distorted. The distortion is significant in anatase whereas it is marginal in rutile. Hence anatase is of lower symmetry. Compared to rutile, the Ti-Ti distances are larger in anatase (3.79 and 3.04 A^o vs 3.57 and 2.96 A^o), whereas the Ti-O distances are shorter (the Ti-O distance 1.934 and 1.98 A^o vs 1.949 and 1.98 A^o in rutile). In rutile, each octahedron is in contact with 10 other octahedra (two sharing edge oxygen pairs and eight sharing corner oxygen atoms) whereas in anatase, each octahedron is in contact with eight neighbors (four sharing edge and four sharing a corner).[20, 44] The rutile unit cell contains two Ti atoms and four oxygen atoms. The anatase unit cell contains four Ti atoms and eight oxygen atoms.[45] These differences in lattice arrangements cause difference in mass densities and electron band structures of rutile and anatase TiO_2. The lattice structures of anatase and rutile are shown in Figure1.1.[46] The crystal faces with lowest energy are (110) and (100) for rutile[47,48] and (101) and (001) for anatase.[19] The crystal structure data of both anatase and rutile phases are given in Table 1.1.[49] Between these two phases, rutile is the thermodynamically stable one. However, in the nano-size samples occurrence of anatase phase is quite common.[50,51] On heating, concomitant with coarsening, anatase is transformed to rutile in the temperature range 400 – 700 ^oC. Enthalpy of anatase to rutile phase transformation is low with values ranging from -1.3 to -6 ±0.8 kJ/mol.[52,53] The phase transitions depend upon several factors such as strain, presence of impurities, particle size, applied pressure and texture.[54,55] Due to these differences, anatase and rutile phases find different applications.

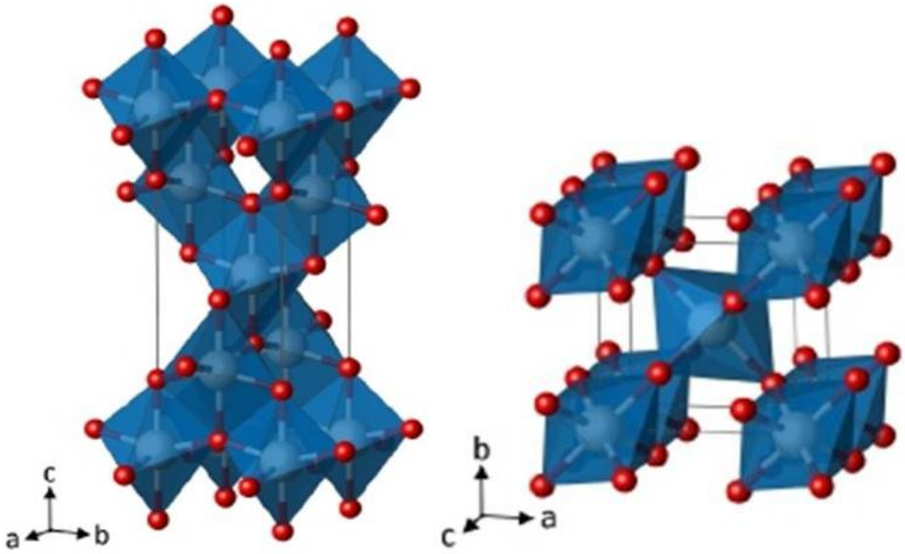

Figure 1.1: Crystal structure of anatase and rutile phase of TiO_2[46]

	Rutile	Anatase
Crystal structure	tetragonal	tetragonal
Lattice constants (A^o)	a= 4.5936	a=3.784
	c=2.9587	c=9.515
Space group	P4$_2$/mnm	I4$_1$/amd
Molecule/cell	2	4
Volume/molecule (A^{o3})	31.2160	34.061
Density (g/cm^3)	4.13	3.79
Ti-O bond Length (A^o)	1.949(4)	1.965(4)
	1.980(2)	1.965(2)
O-Ti-O bond angle	81.2^o	77.7^o
	90.0^o	92.6^o

Table 1.1: Crystal structure data of anatase and rutile TiO_2

1.2. Electrical and electronic properties

Titanium dioxide is an n-type semiconductor having a band gap of 3.2 and 3 eV respectively for anatase and rutile phases. Electronic structure of TiO_2 has been determined experimentally by various groups.[56-60] The valence bands of TiO_2 can be split into three main regions: the σ bonding in the lower energy region mainly due to O-p σ bonds; the π bonding in the middle energy region; and O-p π states in the higher energy region due to O-p π nonbonding states where the hybridization with d states of Ti is almost negligible. The conduction band is split into Ti e_g (>5 eV) and t_{2g} bands (<5 eV). The d_{xy} states of t_{2g} are dominantly located at the bottom of the conduction band. The rest of the t_{2g} bands are anti-bonding with p states of oxygen. The main peaks of the t_{2g} bands are identified to be constituted by mostly d_{yz} and d_{zx} states. The conductivity of TiO_2 is mainly dependent upon the presence of oxygen vacancies and Ti^{3+} cation, which makes TiO_2 an n-type semiconductor.[61] The oxygen vacancies formed can be represented using Kroger-Vink notation by the equation,

$$O_O^x(TiO_2) \rightarrow V_O^{\cdot\cdot} + 2e^- + \frac{1}{2}O_2 \qquad (1)$$

A color center at 3 eV due to the oxygen vacancy has been identified as the reason for the observed yellow color.[62] The nonstoichiometry of TiO_2 depends on the synthesis conditions and history of the samples. The anatase TiO_2 shows Arrhenius type thermally activated conduction, with higher carrier mobility, in comparison conduction in rutile TiO_2 is rather low, stemming mainly from small polaron hopping. However, in both these crystal structures, high concentrations of donors lead to the formation of impurity bands.[63] The band gap of TiO_2 (3 - 3.2eV corresponding to ~ 390 to 410 nm wavelength) implies excitation of electrons from VB to CB only under UV irradiation.

1.3. Photocatalytic properties

Photo catalysis term is generally used when light energy is used to activate the material which modifies the rate of a reaction without changing its chemical structure. The process can occur homogenously or heterogeneously. Heterogeneous photocatalysis is a rapidly emerging research field in Green chemistry. The process is termed as advanced oxidation processes (AOP) for the organic destruction, waste water treatment, generation of renewable energy sources and organic synthesis.[64] Heterogeneous photocatalysis mainly involves an interface between the photocatalyst (semiconductors) and the liquid which contains the reactant. When the semiconductor is excited by photons of appropriate energy, electrons are excited from the VB to the CB creating holes and electrons in the VB and CB, respectively. These photogenerated charge carriers migrate to the TiO_2 crystallite surface, where they reduce and oxidize adsorbed electron acceptors and donors by interfacial charge transfer. This is the principle behind the photocatalytic organic degradation and generation of H_2 by water splitting. The electron-hole pair have lifetime of the order of 10^{-9} s to react with the adsorbed species.[65] In TiO_2 based photocatalysis, usually the photogenerated electrons are trapped as Ti^{3+} at the surface and are transferred to the adsorbed molecular oxygen yielding peroxyl radical anions (O_2^-). In a suspension, depending on the pH value, these peroxyl radical anions can combine with H^+ ions to form superoxide radicals ($HO_2^{\cdot}$). In the gas phase, the peroxyl radical anions directly attack the organic molecules. The holes participate in organic destruction either by directly oxidizing the organics (before being trapped either within the particle or at the particle surface) or by combining with hydroxyl anions to give hydroxyl radicals. The hydroxyl radicals then degrade the adsorbed organic species.

The probability and rate of the charge transfer processes for electrons and holes depend upon the respective positions of conduction and valence band edges and the redox potential levels of the adsorbate species. The schematic of the photoexcitation and its reaction pathway is shown in Figure 1.2. For efficient reaction, the potential of the electron acceptor should be positioned below (more positive) the CB of the semiconductor and the potential of the electron donor should be above the VB of the semiconductor[66]. The former case applies to photocatalytic hydrogen generation and the latter applies to organic destruction. Therefore, assuming absence of any kinetic limitations, photoinduced interfacial redox reaction takes place with acceptors and donors whose respective reduction potential are located between the CB and VB positions of the semiconductor. The photo generated valence band holes are powerful oxidants (+1 to +3.5V Vs NHE depending on the semiconductor) whereas the CB electrons are strong reductants (0.5 to -1.5V vs NHE).[67] The schematic of CB and VB positions of various semiconductors vs NHE is given in Figure 1.3.

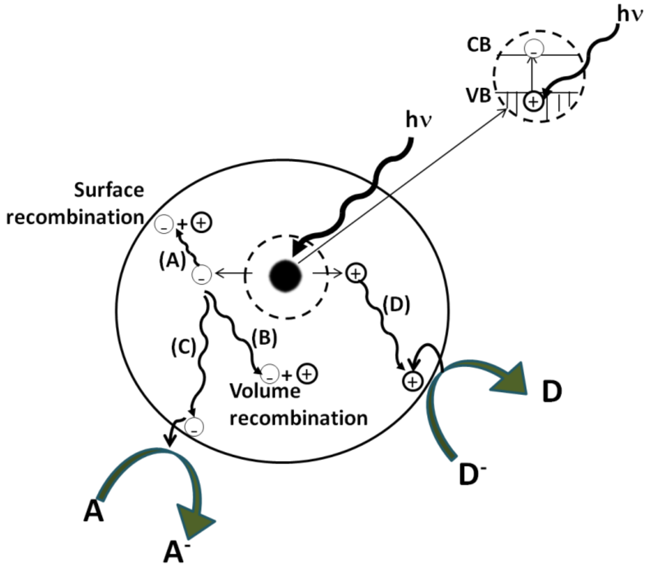

Figure1.2: Schematic of Photoexcitation process and its reaction pathway

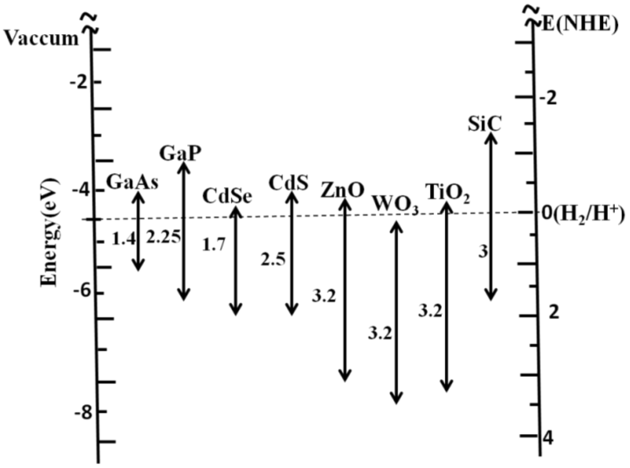

Figure 1.3: Schematic of CB and VB positions of various semiconductors vs NHE

Theoretically, all the semiconductors which satisfy the above mentioned conditions exhibit photocatalytic activity. But the semiconductors such as CdS and SiC undergo photocorrosion and are not suitable for photocatalysis/water splitting applications. Limited numbers of photocatalysts are available which satisfies the criteria, among which TiO_2 is best suited[9]. Ever since the publication of photo-assisted electrolysis of water using TiO_2 photo-electrode, by Honda and Fujishima[68] in 1972, lot of research on photocatalytic action of TiO_2 have been going on which includes, water purification, organic destruction and hydrogen generation. The schematic of the TiO_2 photocatalytic process is represented in Figure 1.4.

The photocatalytic efficiency of TiO_2 is limited due to the fast electron-hole recombination and relatively large band gap (3.2 eV) which need photons of energy greater than or equal to UV radiations (which constitutes only ~5% of total solar energy) for VB to CB electronic excitation.[66] The limitations can be surmounted by surface and electronic band structure modification of the semiconductor such that the charge carrier recombination is inhibited and wavelength response range is increased.

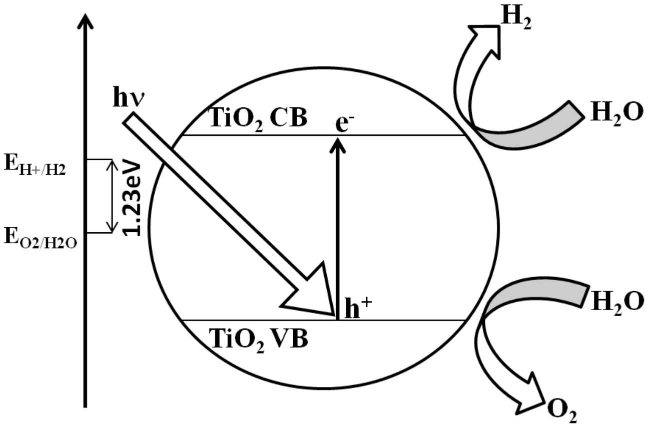

Figure 1.4: Schematic of the TiO_2 photocatalytic process

1.4. Modification of pristine TiO_2

In order to increase the charge separation as well as to tune the band gap to make TiO_2 visible light active, surface modifications by noble metal loading,[20,69-71] dye sensitization,[72-76] coupling with lesser band gap semiconductors[77-79] and electronic band structure modification by cation,[80-83] or anion doping,[84-87] are generally employed.

1.4.1. Noble metal loading

Transition metals, especially noble metals are widely used as cocatalysts for photocatalytic hydrogen generation. As the Fermi level of noble metals are lower than that of the TiO_2 conduction band, the photogenerated electrons in the CB of TiO_2 can easily migrate to the noble metal thereby enhancing charge separation and hence efficient photocatalysis. Figure 1.5a shows the schematic of the electron capture by noble metal from the CB of TiO_2 thereby achieving efficient charge carrier separation. The enhancement in the photo conversion of H_2O to H_2 and O_2 was first observed by loading TiO_2 with Pt.[70] Therefore, as of now, it is the most studied system. The metal (Pt) itself is important because of its specific catalytic activity towards hydrogen. Increase in hydrogen production due to platinum loading can be attributed to the trapping of photogenerated electrons on the metal sites yielding efficient charge carrier separation. It has been reported that there is an optimum size and loading for maximum generation of hydrogen.[9] Efficient hydrogen generations have also been reported for other metal loaded TiO_2 such as Ag/TiO_2 and Au/TiO_2.[71]

1.4.2. Semiconductor coupling

Visible light utilization for the purpose of photocatalysis can be achieved by coupling TiO_2 with other semiconductors of lower band gap with conduction band placed at more negative level compared to that of TiO_2 (Figure 1.5b). On exposing the couple to visible light, the VB electrons of the small band gap semiconductor is excited to the CB. The excited electrons then move to the CB of TiO_2 thereby reducing electron-hole recombination. Thus the couple acts as a visible light active photocatalyst with efficient charge carrier separation. The process is similar to dye sensitization. The conditions for efficient use of TiO_2-semiconductor composite are; the semiconductor should be resistant to photo-corrosion and should have band gap corresponding to visible light excitation. Figure 1.5b depicts a schematic of electron injection process observed in composite semiconductors.

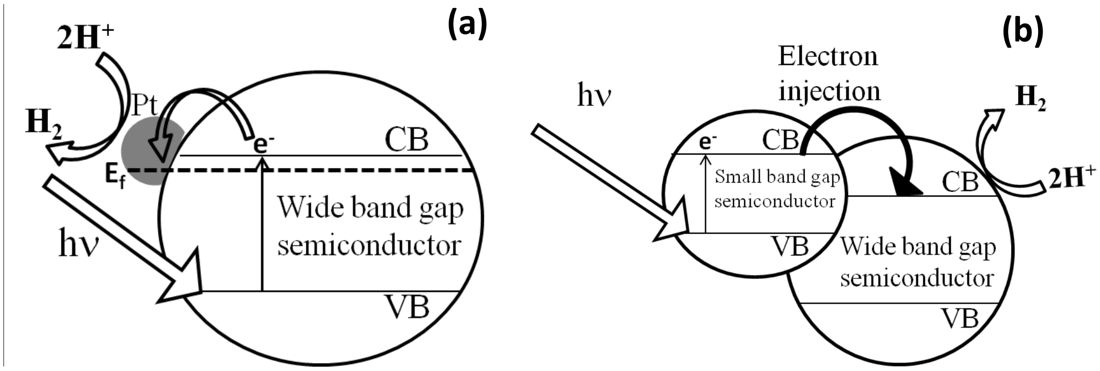

Figure 1.5: Schematic of (a) of the electron capture by noble metal from the CB of TiO_2 (b) Electron injection and prevention of electron hole recombination in semiconductor combination.

Among the composite semiconductor systems, CdS/TiO_2 has been the focal point of extensive research activity and has been investigated in detail.[88-90] However, the fabrication of CdS/TiO_2 composite is a challenging task as oxygen intercalation to chalcogenite (CdS) lattice can alter the band gap of the same and deteriorate the photocatalytic activity. In addition it is photo-corrosive. Therefore alternative small band gap semiconductors such as CuO, Cu_2O, ZnO, SnO_2 and Fe_2O_3 have been used to couple with TiO_2. Recently composite of TiO_2/ single walled carbon nanotubes has been reported to show reduced recombination rate, in turn exhibiting enhanced photocatalytic activity.[91]

1.4.3. Dye sensitization

Sensitization by chemisorbed or physisorbed dyes on semiconductors increase the efficiency of the excitation process, thereby enhancing the photocatalytic activity. Under visible light illumination, the dye electrons undergo excitation and the excited electrons are injected to the conduction band of TiO_2 by virtue of the position of the lowest unoccupied molecular orbital (LUMO) and highest occupied molecular orbital (HOMO) of the dye molecule. The electrons in the CB of TiO_2 can be utilized for H_2 production by the decomposition of organic species as well as to send current through an external circuit (Dye sensitized solar cells). The process occurs only when the oxidative energy level of the excited dye molecule with respect to the conduction band energy level of TiO_2 is higher. Thus sensitization expands the wavelength range of excitation for the photocatalyst through the sensitizer, followed by the charge transfer to the semiconductor. Figure 1.6 shows the schematic of the dye sensitization process. Since electron injection rates differ for various dyes, a variation in photocatalytic rates occur. This necessitates further studies are required to understand and compare the dynamics of charge excitation, recombination and electron injection rates in different dyes.

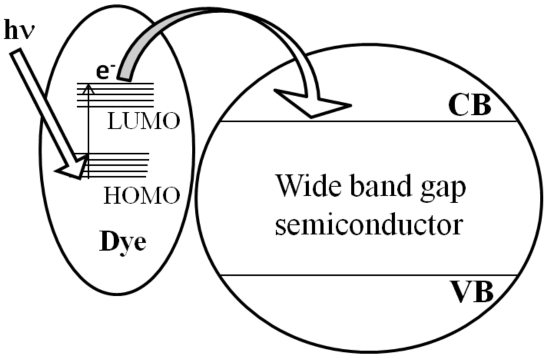

Figure 1.6: Schematic of Dye sensitization in TiO_2

1.4.4. Cation doping

Modification of electronic energy band structure by introducing impurity levels in a band gap semiconductor is another way of making TiO_2 visible light active. This can be easily achieved by metal ion doping. Numerous reports on the modification of the band gap of the materials by cation doping lists a wide range of metals such as Cu, Ni, Au, Cr, Mn, Fe, V.[80-83] Even though it was reported that cation doping decreases the photo threshold energy of TiO_2, several drawbacks such as thermal instability and shorter electron-hole lifetime were observed for the same, thus reducing the overall photocatalytic efficiency.[92] Only a few metals like Fe^{3+} and Cu^{2+} were found to inhibit the electron-hole recombination. The concentration of beneficial transition metals dopants needs to be kept low and large concentrations are detrimental. Therefore, the photocatalytic activity is highly sensitive to the cation dopant concentration. In addition, it has been observed that many of the cations do not result in free charge carriers but in bound excitons and has a tendency to generate charge carrier recombination centers, thereby rendering them impractical for photocatalytic applications.

1.4.5. Anion doping

Another approach to make TiO_2 visible light active is by nonmetal doping. The band gap of the semiconducting material can be narrowed down by introducing donor and acceptor levels below and above the conduction and valence bands, respectively. Doping with anions like C, N, F, B and S is likely to reduce the recombination centers and shift the absorbance of TiO_2 to visible light region.[84-86] Asahi et al have studied the substitution effects of N, C, S, F and P for O in TiO_2. Using full potential linearised augmented plane wave method (FLAPW)[93], they calculated the electronic structures of anatase TiO_2 with the above mentioned dopants. It was observed that both sulfur and nitrogen creates a band gap narrowing in TiO_2. But the size of S is too large to be incorporated into the oxygen sub lattice of TiO_2. From the results of FLAPW studies, it was found that the mixing of 2p states of nitrogen atom with 2p state of oxygen could shifts VB edge upwards leading to narrowing of band gap of TiO_2. Later Chen et al found that the degree of nitrogen doping is an important factor in enhancing the photocatalytic activity of doped

TiO_2.[94] Since then, N-doping of TiO_2 and its photocatalytic activity has been widely investigated both theoretically and experimentally.[94-96] The synthesis of N-doped TiO_2 can be done by various methods which include both physical and chemical techniques such as vapor deposition, heating with nitrogen precursors and treatment under ammonia gas flow etc. X-ray photoelectron spectroscopy is the major tool used for the confirmation of nitrogen incorporation into the oxygen sub-lattice. Theoretical work by Valentine et al revealed that nitrogen can be incorporated into the crystal lattice both interstitially and substitutionally.[95] The model structures for substitutional and interstitial N doped anatase TiO_2 is depicted in Figure 1.7.

Reports on the photocatalytic activity on N doped TiO_2 reveal that both substitutional and interstitial nitrogen doping yields enhanced photocatalytic activity.[93,97-99] However most of the researchers believe that substitutional nitrogen doping is the major factor responsible for enhancement in photocatalytic activity. Density functional theory calculations have addressed the variances in the photoactivity measurements taking both anatase and rutile TiO_2 that have been substitutionally doped with nitrogen.[100] For anatase samples, substitutional N doping results in a decrease in the photon energy necessary to excite the material whereas for rutile TiO_2 materials, the opposite effect is observed and is attributed to the contraction of the valence band and the stabilization of the N 2p state, thus causing an overall increase in the effective band gap[100] which is in agreement with the work of Diwald et al.[97] For anatase TiO_2, substitutionally bound nitrogen atoms create localized occupied electronic states (N 2p in character) above the top of the O 2p valence band. The creation of this occupied electronic state has also been shown experimentally.[95,101]As a result, the mechanism for photoexcitation of N-doped anatase most probably results from direct excitation of electrons from the N 2p state located within the band gap of the TiO_2 into the conduction band. The measured inter-band-gap density of states has been postulated to reduce the rate of electron-hole pair generation, which otherwise readily occurs without the presence of localized N 2p states.[95] A schematic diagram explaining this effect for anatase and rutile structures is shown in Figure 1.8. For rutile TiO_2 the suppression of the top of the valence band is observed upon N doping.[102,103]

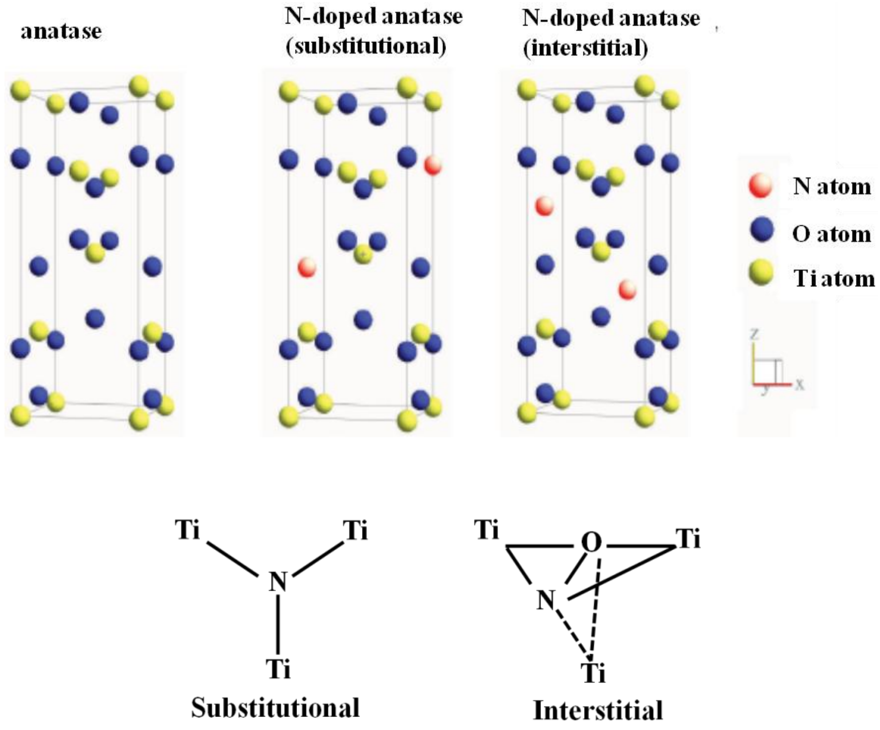

Figure 1.7: The structure anatase TiO_2 in which the nitrogen is occupied substitutionally as well as interstitially[103]

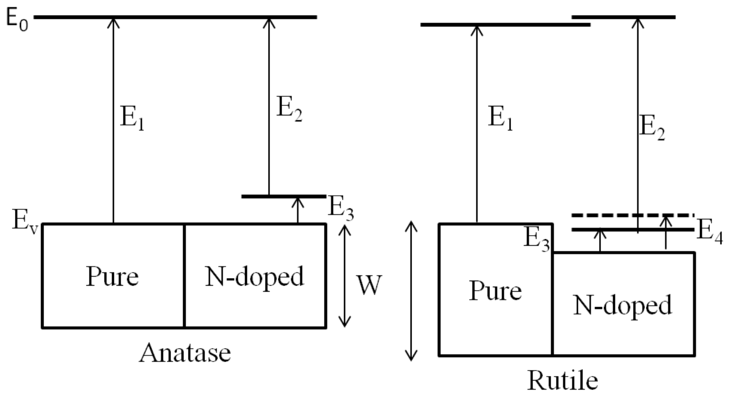

Figure 1.8: Schematic representation electronic band structure of Pure and N-doped anatase and rutile[100]

The substitutional and interstitial type impurities in anatase TiO_2 crystal is investigated experimentally (electron paramagnetic resonance spectroscopy and XPS) and theoretically (DFT calculations). Both types of impurities are found to add localized states within the band gap. For substitutional type nitrogen, these states are located 0.14 eV above the valence band, and for interstitial type nitrogen species (referred to as N-O), the localized states are calculated to lie 0.73 eV above the valence band. In addition, these calculations have also found that there is a large decrease in the formation energy of oxygen vacancies. Therefore, oxygen vacancies are most probably induced by N doping of TiO_2.[99] Figure 1.9 shows the schematic representation of substitutionally and interstitially N-doped anatase TiO_2.

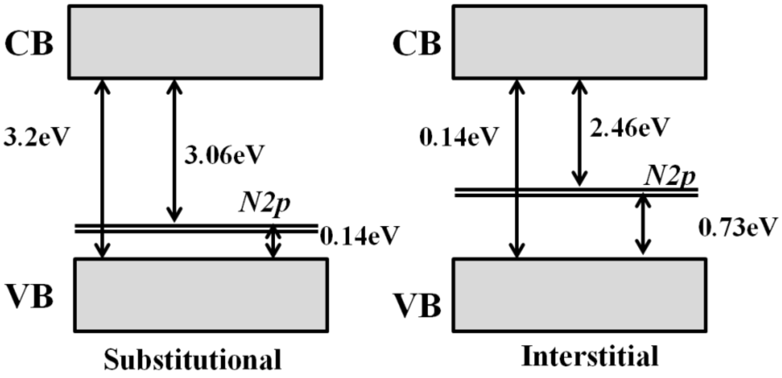

Figure 1.9: Schematic representation electronic band structure of substitutionally and interstitially doped anatase TiO_2

1.5. Synthesis of one dimensional TiO_2 nanoarchitectures

Among the various nanoarchitectures of TiO_2, one dimensional nanostructure are preferred for various applications due to their high aspect ratio and enhanced electron transport properties compared to that of nanoparticles[29,31,32]. There exist various methods for the synthesis of disordered TiO_2 nanotubes in the form of powders and suspensions, which include sol-gel, hydrothermal, chemical vapor deposition, electro deposition and template assisted growth.[104-115] Even though these techniques have several advantages, none of these can produce self organized nanostructures on suitable substrates in a simple and cost effective route, which can be used directly for device fabrication. Also these techniques cannot control the nanotube dimensions precisely. Electrochemical anodization has found to be a cost effective and efficient technique to produce self organized TiO_2 nanotube arrays.[116] The following section briefly discusses different techniques which produce disordered one dimensional TiO_2 nano-architectures. This is followed by description of anodic oxidation technique which produces highly ordered self organized TiO_2 nanotubular arrays. Using the same anodization technique, one can synthesize high surface area TiO_2 nanotubes in the powder form by altering the electrolyte composition.

TiO_2 in the nanotubular form can be synthesized by different methods. Among those, a selected few are discussed in the following section.

1.5.1. Sol-gel assisted synthesis

Sol gel synthesis of TiO_2 is a wet chemical technique in which a colloidal suspension is formed from the acid catalyzed hydrolysis of Ti alkoxide or Ti salts followed by gelation.[117] This technique employs gels derived from low to moderate molecular weight organic compounds for the synthesis of metal oxide nanotubes.[118,119] The driving forces behind such physical gelation involve hydrogen bonding, Vander Waals force, π-π interaction and electrostatic interaction through cooperating noncovalent interactions of gelator molecules. The outstanding feature responsible for gelation is thought to rely on the formation of three-dimensional networks composed of highly intertwined fibers. The first stage of physical gelation is the self assembly of gelator molecules, with the self-assembled bundle organogelator acting as a template in the sol-gel polymerization process. Oxide nanotubes are thus synthesized by coating these templates with oxide precursors followed by gel dissolution in a suitable solvent and subsequent calcination. By this reconstructive synthesis, hierarchical morphologies can be obtained, with the gelators acting as the structure-directing agents. Closely packed 3 dimensional polymeric Ti-O-Ti chains formed by hydrolysis can also be converted to one dimensional form by electrospinning the viscous precursor along with the co-solvent (generally high molecular weight polymer) or by electrophoretic deposition of TiO_2 suspensions into the pores of anodic alumina membrane and its subsequent removal.

1.5.2. Hydrothermal synthesis

It is generally conducted in Teflon coated steel pressure vessel known as autoclaves, and it assist in crystallizing the compound from high temperature aqueous solutions at high vapor pressures. TiO_2 nanoparticles, nanotubes and nanorods are synthesized by hydrothermal treatment of Ti precursor with water. Hydrothermal treatment temperatures and conditions determine the extent of precursor conversions, which influences the geometrical features of the resulting nanostructures.[104,106] Highly concentrated NaOH solutions and temperature in the range of 120-130^{o}C were found to be more appropriate for the formation of TiO_2 nanotubes by hydrothermal method. Formation of TiO_2 nanotubes by hydrothermal technique were proposed by several groups.[106,120, 121] Wang et al[120] proposed that during the reaction with NaOH, the Ti-O-Ti bonding existing between the basic building blocks of the anatase phase, the octahedron, was broken and a zigzag structure was formed when the free octahedra shared edges between the Ti ions with the formation of hydroxy bridges, leading to the growth along the [100] direction of the anatase phase. Two-dimensional crystalline sheets were formed from the lateral growth of the oxo bridges between the Ti centers (Ti-O-Ti bonds) in the [001] direction. These sheets rolled up to saturate the dangling bonds emerging from the surface subsequently lowering the total energy and resulting in the formation of TiO_2 nanotubes.

Other techniques such as chemical vapor deposition, electrospinning, physical vapor deposition are less commonly used techniques for the fabrication of TiO_2 nanotubes.

1.5.3. Electrochemical oxidation

Electrochemical anodization is a cost effective technique, generally used for the corrosion protection of metals. Metals, generally valve metals (Al, Ta, Hf, Zr, and Ti) have a thin native oxide layer coating, measuring to few nanometers in thickness, on its surface due to interaction with atmospheric oxidation. Thickness of this native oxide layer can be further increased by thermal and anodic oxidation. The thin oxide films can be grown to thick oxide coatings by anodization. Conversely, a number of approaches are there to dissolve the oxide layers from the metal surface, which includes surface etching and polishing. Taking the idea of both oxidation and etching, in 1995 Masuda and Fukuda have developed porous alumina coating by anodizing aluminum metal.[122] These porous structures possess high surface area and the pores have a narrow size distribution. The aspect ratio of the porous structures can be varied easily by varying the electrochemical parameters. By optimizing the electrochemical process parameters one can obtain ordered porous structures. The highly ordered porous anodic alumina has significant use as template for the synthesis of one-dimensional nanoarchitectures. This includes synthesis of one dimensional structure like nanofibrils as well as nanowire arrays of semiconductors, metals and polymers which find important applications in optical and magnetic devices, photonic crystal based devices and biocompatible equipments.[123-126] The idea has been extended to fabricate porous structures of TiO_2 by anodizing Ti metal. In 1999, Zwilling et al successfully developed porous TiO_2 structure by anodizing Ti in fluoride based acidic electrolytes.[127] Following this, extensive studies on anodization of Ti metal in various electrolytes have been done by several research groups and is widely accepted that fluoride ion containing electrolytes results in the formation of highly ordered self organized nanostructures of TiO_2.[128, 129]

1.5.3.1. Mechanistic aspect of formation of TiO_2 nanotube arrays

Pourbiax diagram of Ti-H_2O system at 25°C reveals that TiO_2 layer on Ti has excellent corrosion resistance.[130, 131] Valve metals possess wide passivation region in the range of few tens of volts.[132] When an external voltage is applied, this stable oxide layer thickness increases linearly, and the passivation region increases. The trend shows a deviation when the anodization is carried out in fluoride ion containing electrolytes. This is because the stable oxide layer is attacked by the fluoride ions yielding soluble fluoride complexes. The behaviour of fluoride ion in the passivation of Ti metal has been extensively studied.[133-135] It is widely accepted that formation of oxide layer on Ti in the presence of fluoride ion is the result of competition between anodic oxidation and chemical dissolution of the oxide layer (by F^- ions leading to the formation of $[TiF_6]^{2-}$ complexes in solution) which is in contact with the electrolyte. The dissolution of oxide by fluoride ions occur initially at the surface defects or cracks and further penetrate towards the metal to form pores in nanometer scale. Further anodization leads to the formation of ordered porous nanostructures followed by separation to isolated nanotubes.

The key processes involved in the anodic formation of TiO_2 nanotubes, in a fluoride ion containing electrolyte, are initial oxidation at the metal electrolyte interface due to OH^- and O^{2-} ions, field assisted oxidation of Ti metal (ie; migration of oxide ion through oxide layer to the oxide-metal interface and oxidation of the metal resulting in increased oxide layer thickness), and field assisted dissolution of metal oxide as well as metal, by fluoride ion at the metal oxide/ electrolyte interface and metal/ metal oxide interface respectively. The second process results in a thick oxide layer on Ti surface whereas the third process results in the dissolution of the metal and metal oxide forming nanopores and pit. At the initial stage the pores formed by reaction with fluoride ions are of irregular shape and produce unequal local current densities. At a later stage the current densities will be shared equally by the pores and they start growing uniformly. This indicates equilibrium between the field assisted chemical oxidation and field assisted chemical dissolution. Further, steady state equilibrium leads to growth of ordered porous nanostructures and finally to well separated self organized nanotubes. The schematic of the formations steps are depicted in Figure 1.10. A qualitative picture regarding formation of TiO_2 nanotube arrays during anodization can be obtained from the current density transient recorded in situ and is discussed in chapter 3. The aspect ratio of the nanotubes can be varied by varying the process parameters such as applied voltage, time of anodization, electrolyte composition and temperature.[20,128, 129,136-138]

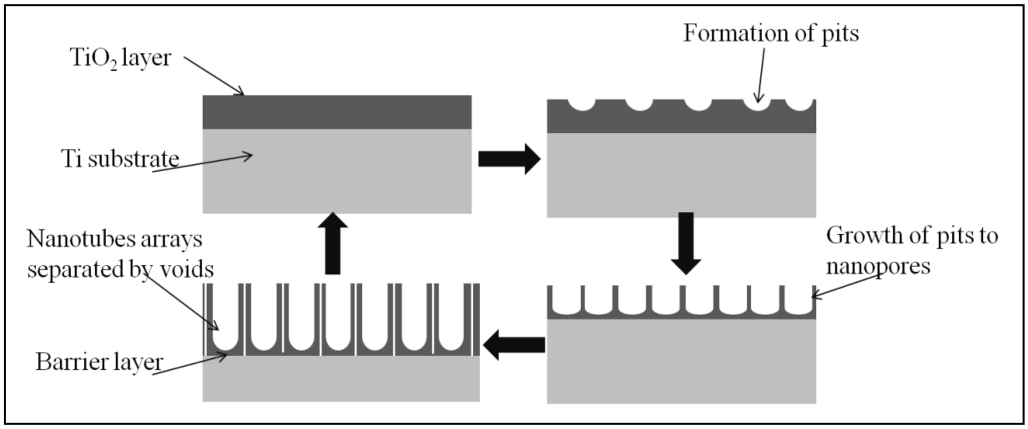

Figure 1.10: Schematic of the formations steps of self organized TiO_2 nanotubular structures.

The history TiO_2 nanotube fabrication by anodization technique can be classified into different generations depending upon the selection of process parameters. The first generation nanotubes were synthesized in HF containing aqueous electrolytes.[116,139,140] In this case the lengths of the nanotubes were limited to few hundreds of nanometers due to high chemical dissolution rate.[139,140] The synthesis of second generation nanotubes of several micrometer lengths were achieved by replacing HF with fluoride salts such as KF, NaF and NH_4F, and varying the electrolyte pH.[141] But no nanotube formation occurred when the alkaline electrolyte medium was employed.[141] One of the limiting factors of second generation nanotubes is the formation of unwanted precipitates. In the third generation nanotubes, ammonium fluoride containing polar organic electrolytes such as formamide or dimethyl sulfoxide with less than 5 wt% of water were employed for anodizing Ti metal. The reduction in water content in the electrolyte decreases the rate of chemical oxidation and dissolution in fluoride containing electrolyte and therefore longer nanotube formation could be achieved.[142,143] When fluoride ion containing ethylene glycol was used as an electrolyte, smooth walled long TiO_2 nanotubes were obtained. It was reported that double side anodization of Ti foils resulted in nanotubes having 1mm length which is the highest achieved length.[143] Attempts were also made by various research groups, to anodize Ti thin films on different substrates like glass, silicon, quartz and conducting glasses with aim of using the same in applications such as dye sensitized solar cells (DSSC). In order to get high aspect ratio titania nanotube arrays (TNTA) on different substrates, the process parameters such as thin film deposition conditions, electrolyte composition, time of anodization and temperature were varied and investigated.[144-146] Depending upon the aspect ratio and crystallinity of the nanotubes, these can be employed for various applications such as DSSC, field emission and photocatalysis. The subsequent section discusses the basic principle involved in some of the selected applications of TiO_2 nanotube arrays.

1.6. Selected Application of TiO_2 nanotube arrays

1.6.1. Dye Sensitized Solar cell:

Dye sensitized solar cells (DSSC) belong to the class of third generation solar cells which includes liquid based solar cells, Forster resonance energy transfer based solar cells and organic solar cells. Since the original report on the fabrication of DSSCs by O'regan and Graetzel,[147] DSSCs continued to be an exciting field of research because of its regenerative low cost, ease of fabrication and possibility of large scale production. In DSSCs, the electrons in the dyes are excited by light absorption and injected to the conduction band of the semiconducting material (generally TiO_2). The injected electrons then diffuse through the semiconducting matrix and reach the conducting electrode, subsequently to the counter electrode through the external circuit. At the counter electrode (Pt coated conducting glass) the electrons react with the tri-iodide ions to generate iodide ions ($I_3^- + 2e^- \leftrightarrow 3I^-$). The iodide ions in contact with the dye supply the electrons to the HOMO of the dye molecules regenerating triodide ions ($3I^- \leftrightarrow I_3^- + 2e^-$). The $I_3^- + 2e^- \leftrightarrow 3I^-$ reaction is catalyzed by the Pt nanoparticles of the counter electrode. Titanium dioxide acts as the photo anode and the nanostructure increases the available surface area for the dye attachment. The light harvesting component of the DSSC is the dye, generally a ruthenium bi-pyridyl dye, adsorbed on TiO_2.[148, 149] The enhanced visible light absorption and power conversion efficiencies have made DSSCs a strong competitor to solar cell based on other approaches. The schematic of the working principle of the DSSC is depicted in Figure 1.11.

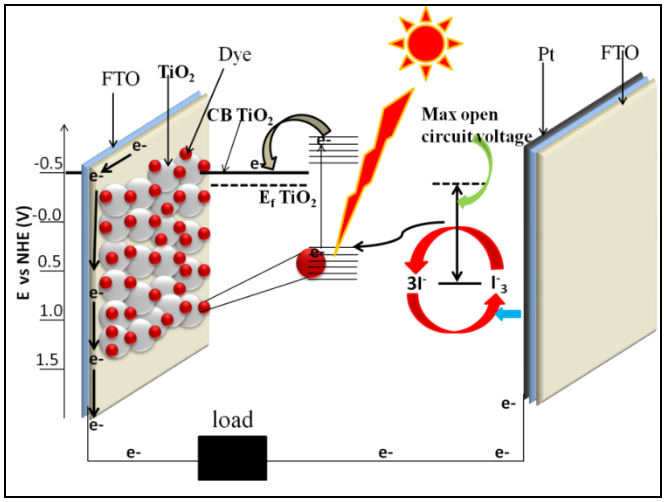

Figure 1.11: Schematic representation of working principle of Dye sensitized solar cell.

The efficiency can be calculated from the I-V characteristics of the DSSC which is discussed in chapter 4. The photocurrent produced in a DSSC is directly influenced by the properties of the sensitizer. The energy gap between the HOMO and LUMO of the sensitizer (Which corresponds to the band gap, E_g, for inorganic semiconductor materials) determines the photoresponse range of the DSSC. Absorption over a wide range of wavelengths, extending into the near-IR region due to a small HOMO-LUMO energy gap, helps in harvesting a large fraction of the solar spectrum. This in turn produces large photocurrent which enhances the device performance. In addition, the energy levels of the HOMO and LUMO must match the I_3^-/I^- redox potential and the CB of the TiO_2 electrode (Figure 1.6 and 1.11). For efficient electron injection, the LUMO must be sufficiently more negative (higher energy) than the TiO_2 CB, which is the driving force for electron injection. Thus, the molecular structure of the sensitizer must be strategically designed so that its properties are optimal for efficient DSSC performance. Traditionally used sensitizing dyes are made from ruthenium based complexes (N3, N719, C106 and CYB11) which possess broad absorption spectra ($\Delta\lambda$=350 nm) but low molar extinction coefficient.[148,149] These are generally packed with a density of 0.5-1 dye molecules per square nanometer. Due to the low molar extinction coefficient of ruthenium based complexes, great strides have been made during the past decade, to understand and design new dyes. The HOMO of the dye molecule must be sufficiently more positive (lower energy) than the redox potential of $I_3^-/3I^-$ to accept electrons effectively.[150,151] The open circuit potential of the DSSC corresponds to the difference between the redox potential of the mediator and the fermilevel of TiO_2. The iodide/triodide system has been particularly used in DSSC because of the slow recombination kinetics between electrons in TiO_2 with the oxidized dye and tri iodide in the electrolyte thereby increasing the electron life time between 1ms to 1s.[152,153] The small size of the I^-/I_3^- redox component allows fast diffusion, and provides two electrons per molecule to the counter electrode. Unfortunately the redox system is corrosive and dissolves sealants and contact materials in the long run. Alternative redox system such as Co^{2+}/Co^{3+} and Fc/ Fc^+ based electrolytes have found to give good performance.[154,155]

The carrier recombination at grain boundaries and long carrier diffusion path in the case of nanoparticulate TiO_2 restricts the performance efficiency and this could be overcome using TNTA. The major issues and strategies for using TNTA in DSSC's have been reviewed and discussed.[146,156,157] According to the reported studies, the specific surface area of TiO_2 and specific dye loading are the efficiency limiting factors in the case of TNTA based DSSCs. Therefore modification of the tube geometry is necessary to increase device performance.

1.6.2. Field Emission

Field emission, also called Fowler-Nordheim tunneling, is the process whereby electrons tunnel through a barrier in the presence of high electric field. The process is also referred as cold cathode emission. The current generated in the field emitter is mainly governed by Fowler Nordheim equation. The quantum mechanical tunneling process is an important mechanism for thin barriers as those in metal-semiconductor junctions or highly-doped semiconductors. The typical field emission model for metallic conductors with the potential barriers and the corresponding field emission energy distribution (with the energy on the vertical axis and current on the horizontal logarithmic axis) is shown in Figure 1.12.[158]

The FN model has shown that the emitted current from the surface of the material directly depends on the local electric field at the emitting surface and on its work function, and varies exponentially. Therefore a change in the morphology of the emitter (geometrical field enhancement by shape and sharpness of the tip) and the chemical state of the surface has a strong effect on the emission current. As the radius of the emitting surface decreases the electron emission increases. Also increasing the number of surface states per unit area enhances the field emission and therefore it is always preferred to fabricate organized/patterned one dimensional architectures having sharp tips. High aspect ratio carbon nanotubes are found to be promising candidates as field emitter with low turn field and high current densities. For future applications,

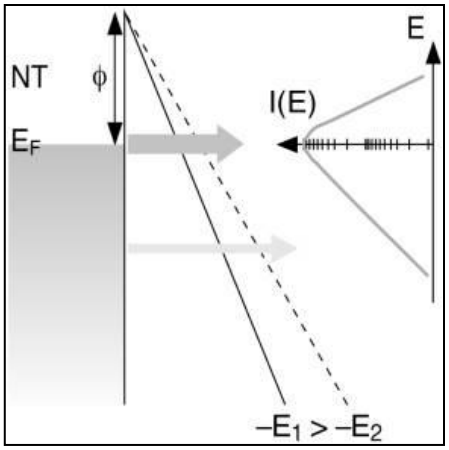

Figure 1.12: Schematic of typical field emission model for metallic conductors with the potential barriers and the corresponding field emission energy distribution[158]

the long term stability of the field emitter is a prerequisite. Even the residual gases present in the field emission chamber affects the stability of the materials like carbon nanotubes. The chemical stability can be achieved by using modified semiconducting materials especially one dimensional nanoarchitectures of TiO_2. Among the one dimensional nanoarchitectures of TiO_2, TNTA on Ti foils is a promising candidate for field emission application due to its high aspect ratio, good chemical stability, guaranteed electrical contact between TiO_2 nanotube thin films and Ti foil, low work function, high degree array uniformity and its simple and cost effective fabrication process.[159] Since the field emission density and the field enhancement are dependent on the diameter, height, wall thickness and density of the nanotubes. The field emission process can be tuned by changing the above mentioned parameters. Several reports on the field emission properties of TNTA and modified TNTA can be found in the literature.[159-163]

1.6.3. Photocatalytic Hydrogen Generation:

Hydrogen is a desired candidate for energy production, having high calorific value and producing only water upon oxidation. Hence the term hydrogen economy is a proposed system for delivering energy by generation of hydrogen, efficiently and inexpensively on a renewable basis. Hydrogen generation by photocatalysis reaction employing semiconducting materials is an efficient and cost effective route in hydrogen economy. As mentioned earlier in this chapter, nanoarchitectures of TiO_2 are appropriate for photocatalytic hydrogen production.

Water splitting into H_2 and O_2 is an uphill reaction. It needs the standard Gibb's free energy change (ΔG^0) of 237 kJ / mol or 1.23 V[20], as represented in equation,

$$H_2O \rightarrow \frac{1}{2}O_2 + H_2\,;\ \ \Delta G^0 = +237kJ/mol \qquad (2)$$

Therefore, in order to achieve water splitting, the band gap of the semiconducting material should be greater than 1.23 eV. As mentioned previously the reduction and oxidation potential of H_2O should lie within the band gap of the material (figure 1.4). Thus band gap structure of the material is a thermodynamic requirement for photocatalytic hydrogen generation. Life time of the photogenerated electrons, charge separation and mobility are the other factors which affect the efficiency of photocatalytic hydrogen generation.[20] The processes in the photocatalytic hydrogen generation includes absorption of light by semiconductor, generation of charge carriers, separation, migration and transfer of the charge carriers to water or other molecule. Recombination of charge carriers is a competing process which reduces the hydrogen generation efficiency[9]. Any other processes which consume the excited electrons should be avoided to increase the efficiency. Effective charge separation and migration is essential requirement for efficient hydrogen generation. This can be achieved by surface modification of the semiconducting material. As discussed earlier, noble metal (Pt) loading is a widely adopted method for efficient charge separation and generation of active sites for hydrogen production.[70] The efficient hydrogen generation due to noble metal loading is attributed to the formation of

Schottky barriers which enable easy flow of photogenerated electrons from semiconductor to metal.[164, 165]

1.6.4. Surface wetting:

When a liquid drop is in contact with a surface, at the interface three phases coexist (gas, liquid and solid). The wettability of a solid surface by a liquid can be quantified by measuring the contact angle (CA) which can be defined as the angle between the solid surface and the tangent line of the liquid at the contact point between these three phases. Thomas Young, in 1805 explained the phenomenon of the interfacial energy, which is proportional to the number molecules present in the surface and thus proportional to the surface area, which can be represented by the equation[166],

$$\gamma_{sv} = \gamma_{sl} + \gamma_{lv} \cos\theta \qquad (3)$$

The equation can also be written as

$$\cos\theta = \frac{\gamma_{sv} - \gamma_{sl}}{\gamma_{lv}} \qquad (4)$$

Where θ is the CA, γ_{sv}, γ_{sl} and γ_{lv} are the interfacial energy per unit area of the solid-vapor interface (surface energy per unit area of the solid), the solid-liquid interface, and the liquid-vapor interface (surface energy (tension) per unit area of the liquid), respectively. When $(\gamma_{sv} - \gamma_{sl}) > \gamma_{lv}$, the drop will completely wet the surface, indicating high surface energy. The term is referred as superhydrophilicity, ie; the CA will be ~ 0^o ($<10^o$). There exist surfaces, in which the CA will be more than 10^o but less than 90^o. This condition is known as hydrophilicity. When the condition is $(\gamma_{sv} - \gamma_{sl}) > \gamma_{lv}$ the surface turns to be non-wetting and the CA will be ~180^0 and the state is called superhydrophobic state. When the CA ranges occur in between 90 to 150^o the state is referred to hydrophobic.[167] The schematic of the different wetting states are represented in Figure 1.13.

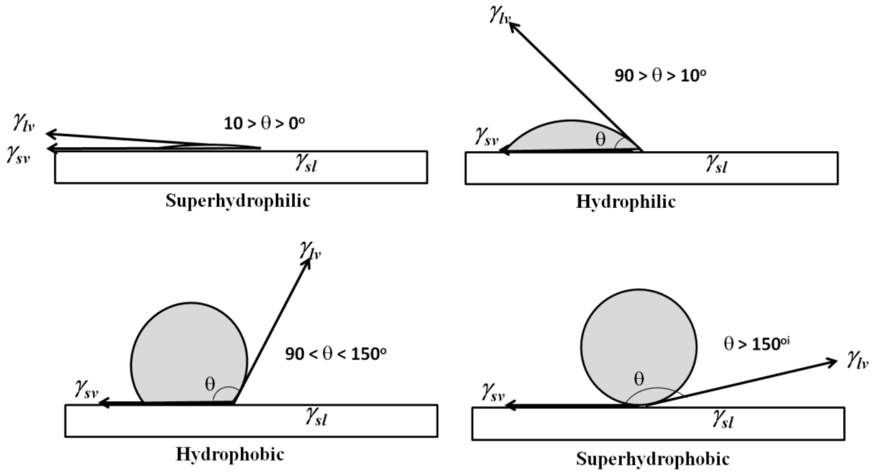

Figure 1.13: Different wetting states derived on the basis of Young's equation

The Young's equation is valid only for smooth surfaces. When the surface roughness and chemical nature comes into picture, the non ideal behavior can be observed and two extreme cases can happen, ie; either total wetting or non-wetting. The correlation of the surface roughness with the former case has been derived by Wenzel[168] and the latter by Cassie and Baxter[169]. The fundamental assumption in the Wenzel theory is that the liquid penetrates into the grooves of the rough surface. He suggested a linear relationship between the observed CA and the surface roughness

$$\cos\theta_r = r\cos\theta_s \qquad (5)$$

Where θ_r and θ_s are the observed (apparent) and actual CA (on a smooth surface) and r is the surface roughness or else the ratio between the actual surface area and the geometrical surface area. If the CA on a smooth surface is smaller than 90^o, then the apparent CA on the corresponding rough surface will be smaller than 90^o and vice versa. But the theory shows violation, by showing hydrophobicity, when large fraction of air is present in the pores of the material. In the Cassie Baxter model, the apparent CA is be given as follows,

$$\cos\theta_r = f_s\cos\theta_s + f_v\cos\theta_v \qquad (6)$$

Where f_s and f_{sv} are the area fractions of the solid and vapor on the surface, respectively. Since $f_s + f_{vs} = 1$ and $\theta_v = 180^o$, the equation can be written as

$$\cos\theta_r = -1 + f_s\,(\cos\theta_s + 1) \qquad (7)$$

Figure 1.14 shows the schematic representation of the surface liquid interaction in Wenzel and Cassie Baxter models. Wettability on the surface here is regulated by the fraction of air trapped on the rough surface. When f_v tend towards '1' the surface becomes superhydrophobic. Thus the wettability of the surface can be adjusted by tuning the surface roughness of the material.

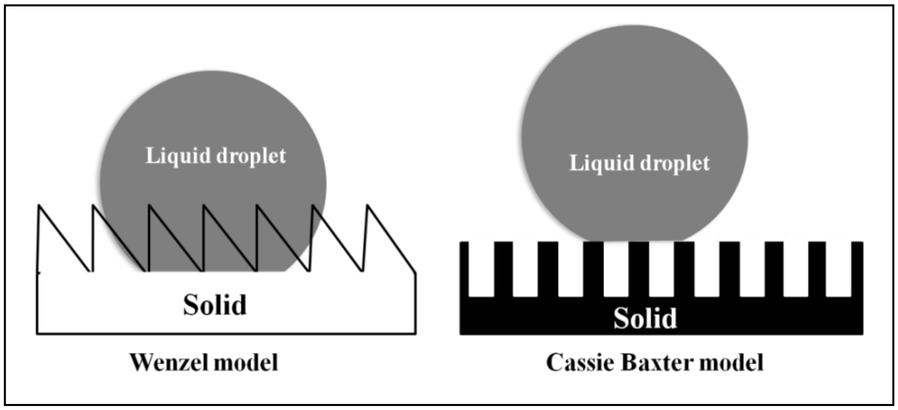

Figure 1.14: Schematic representation of Wenzel and Cassie Baxter model of surface wetting due to surface roughness.

Photoinduced changes of the chemical states on the surface can cause changes in the wetting behaviour of the material and this makes it possible to create an intelligent surface with controllable wettability. Superhydrophilicity is an important property that can endow materials with self cleaning property. Among the various semiconductors, TiO_2 is one of the most important candidate material, which exhibit this phenomenon under light irradiation.[170] Because of this unique phenomenon, TiO_2 is a promising candidate for self cleaning and antifogging-coating applications.

1.7. Objective of the thesis

The research programme pertaining to this thesis is targeted towards, synthesis and characterization of one dimensional nanoarchitectures of pristine and doped TiO_2 as well as to study their properties pertaining to selected applications in energy, environment and electronics. Among the various one dimensional nanostructures viz nanotubes, nanobelts, nanorods, nanowires and fibers, nanotubes are of importance because of their high active surface area and electron transport properties. The TiO_2 nanotubular architectures considered in the present study are vertically aligned nanotube arrays in thin film form and nanotube powders. These structures are in general synthesized by various techniques viz hydrothermal, template assisted sol-gel, template assisted PVD and CVD, electrospinning and electrochemical techniques. Among these, electrochemical anodization is the most cost effective, easy to adopt (for large scale production) and environmentally friendly. In addition, the technique provides accurate method for tuning the aspect ratio and surface morphology of the nanotubes as these can be modified by controlling the applied potential which in turn can be controlled accurately in nanovolt levels.

An important drawback of TiO_2 for selected applications is that its band gap is rather large, 3.0–3.2 eV, and thus only 5% of the solar spectrum ($\lambda < 380$ nm, corresponding to the UV region) is absorbed. To extend the photo-absorption into the visible region, doping with cations and anions are adopted. Among the various dopants, nitrogen is found to be more promising. Hence, it is of paramount importance to synthesize N-doped TiO_2 nanotubular arrays for enhancing the efficiency of the devices based on their architectures.

The application studies were chosen based on the enhanced properties of pristine and N-doped TiO_2 nanotube arrays and powders which are expected to improve the efficiency of devices when fabricated using them. The specific objectives, for which present thesis work was undertaken, are the following,

- Synthesis of pristine and N-doped vertically aligned TiO_2 nanotube arrays in thin film form by electrochemical anodization technique and their morphological, structural, compositional and optical characterization. Delineation of dopant nature (interstitial or substitutional in TiO_2) by XPS and determination of change in electronic band gap and interband defect states by UV-vis and photoluminescence spectroscopies were part of the objective.
- Fabrication of dye sensitized solar cells (DSSC) using vertically aligned TiO_2 nanotube arrays and their I-V characteristic studies, and field emission and wetting characteristics of pristine and N-doped TiO_2 nanotube arrays. The rationale behind choosing application studies pertaining to DSSCs and field emission is that the alignment, high aspect ratio, thin edges and directional electron transport properties of vertically aligned TiO_2 nanotube arrays are expected to play a major role in enhancing the efficiency of the respective devices fabricated using them. Another important recently proposed application of vertically aligned TiO_2 nanotube arrays on Ti is controlled drug release because of its expected hydrophobic nature due to the presence of long air trapped columns. Since it is possible to fabricate vertically aligned TiO_2 nanotube arrays of varying tube diameter and length by changing applied potential as well as duration of anodization one can expect preparation of samples of varying hydrophobicity. The hydrophobic surfaces can be made superhydrophilic by photo irradiation and the same can be reverted back to initial hydrophobic state by keeping it in dark. Hence, it is possible to make controlled drug delivery systems by loading the vertically aligned TiO_2 nanotube arrays with appropriate drug after making it hydrophilic by light irradiation and then reverting it back to hydrophobic state by keeping in the dark. The same can then be used in orthopedic implants for controlled drug delivery. However, care should be taken not to expose the

implant to light before implantation as it could become hydrophilic leading to uncontrolled drug release. With this application in mind the studies on kinetics of hydrophobic ↔ superhydrophilic transitions were considered.

- Synthesis and characterization of pristine and N-doped TiO_2 nanotube powders using rapid break down (RBA) anodization technique. The study was undertaken because in certain applications like hydrogen generation by photolysis of water, destruction of organics and microbes in water, nanotubes in powder form are advantageous as they can be suspended in the media to yield uniform dispersion thereby facilitating better light harvesting with better kinetics.
- Investigations on hydrogen generation efficiency of platinum loaded TiO_2 nanotube powders from ethanol/water mixtures under different wavelength photo irradiation as well as dye degradation kinetics using pristine and doped TiO_2 nanotube powders.

References

---

[1] Banerjee, A. N., *Nanotech. Sci. App.* **2011**, 4, 35-65

[2] Weir, A.; Westerhoff, P.; Fabricius, L.; Hristovski, K.; von Goetz, N., *Environ. Sci. Technol.* **2012,** *46* (4), 2242-2250.

[3] Clark, W.; Broadhead, P., *J. Phys. C: Solid St. Phys* **1970,** *3* (5), 1047.

[4] Layman, P., *Chemical & Engineering News Archive* **1996,** *74* (4), 13-14.

[5] Harris, A. W.; Ludden, B. P.; Blaikley, D. C. W., *Vacuum* **1992,** *43* (1–2), 143-147.

[6] Frank, S. N.; Bard, A. J., *J. Am. Chem. Soc* **1977,** *99* (1), 303-304.

[7] Ohko, Y.; Hashimoto, K.; Fujishima, A., *J. Phys. Chem A* **1997,** *101* (43), 8057-8062.

[8] Sakata, T.; Kawai, T., *Chem. Phys. Lett.* **1981,** *80* (2), 341-344.

[9] Linsebigler, A. L.; Lu, G.; Yates, J. T., *Chem. Rev.* **1995,** *95* (3), 735-758.

[10] Brian O'Regan & Michael Gratzel, *Nature,* **1991,** 353, 737-740

[11] Gratzel, M.; Kalyanasundaram, K., *Curr. Sci*. **1994**, 66, 706-714

[12] Bonhote, P.; Moser, J. E.; Vlachopoulos, N.; Walder, L.; Zakeeruddin, S. M.; Humphry-Baker, R.; Pechy, P.; Gratzel, M., *Chem.Comm.* **1996,** (10), 1163-1164.

[13] Wang, R.; Hashimoto, K.; Fujishima, A.; Chikuni, M,; Kojima, E.; Kitamura, A.; Shimohigoshi, M.; and Watanabe, T., *Nature,* **1997**, 388, 431-432

[14] Al-Homoudi, I. A.; Thakur, J. S.; Naik, R.; Auner, G. W.; Newaz, G., *App. Surf. Sci.* **2007,** *253* (21), 8607-8614.

[15] Mor, G. K.; Carvalho, M. A.; Varghese, O. K.; Pishko, M. V.; Grimes, C. A., *J. Mater. Res.* **2004,** *19* (02), 628-634.

[16] Bally, A. R.; Prasad, K.; Sanjinés, R.; Schmid, P. E.; Lévy, F.; Benoit, J.; Barthou, C.; Benalloul, P., *MRS Online Proceedings Library* **1996,** *424*, 471-475.

[17] Nishikiori, H.; Qian, W.; El-Sayed, M. A.; Tanaka, N.; Fujii, T., *J. Phys. Chem. C* **2007,** *111* (26), 9008-9011.

[18] Kondo, J. N.; Domen, K., *Chem. Mater.* **2007,** *20* (3), 835-847.

[19] Diebold, U., *Surf. Sci. Rep.* **2003,** *48* (5–8), 53-229.

[20] Chen, X.; Mao, S. S., *Chem. Rev.* **2007,** *107* (7), 2891-2959.

[21] Fujishima, A.; Zhang, X.; Tryk, D. A., *Surf. Sci. Rep.* **2008,** *63* (12), 515-582.

[22] Patzke, G. R.; Krumeich, F.; Nesper, R., *Ang. Chem. Int. Ed.* **2002,** *41* (14), 2446-2461.

[23] Tang, H.; Prasad, K.; Sanjinés, R.; Lévy, F., *Sens. Act. B: Chem* **1995,** *26* (1–3), 71-75.

[24] Brus, L. E., *The Journal of Chemical Physics* **1984,** *80* (9), 4403-4409.

[25] Efros, A. I. L., Efros, A. L. *Sov. Phys. Semicond.* **1982,** 16, 772- 775.

[26] Enright, B.; Fitzmaurice, D., *J. Phys. Chem.* **1996,** *100* (3), 1027-1035.

[27] Nozik, A. J.; Memming, R., *J. Phys. Chem.* **1996,** *100* (31), 13061-13078.

[28] Grela, M. A.; Brusa, M. A.; Colussi, A. J., *J. Phys. Chem. B* **1997,** *101* (51), 10986-10989.

---

[29] Zhou, W.; Liu, H.; Boughton, R. I.; Du, G.; Lin, J.; Wang, J.; Liu, D., *Journal of Materials Chemistry* **2010,** *20* (29), 5993-6008.

[30] Tsai, C.-C.; Teng, H., *Chem. Mater.* **2005,** *18* (2), 367-373.

[31] Wang, J.; Tafen, D. N.; Lewis, J. P.; Hong, Z.; Manivannan, A.; Zhi, M.; Li, M.; Wu, N., *J.Am. Chem. Soc.* **2009,** *131* (34), 12290-12297.

[32] Joo, J.; Kwon, S. G.; Yu, T.; Cho, M.; Lee, J.; Yoon, J.; Hyeon, T., *J. Phys. Chem. B* **2005,** *109* (32), 15297-15302.

[33] Lin, Y.; Wu, G. S.; Yuan, X. Y.; Xie, T.; Zhang, L. D., *. Phys.: Condesns. Mat.* **2003,** *15* (17), 2917.

[34] Joo, J.; Kwon, S. G.; Yu, T.; Cho, M.; Lee, J.; Yoon, J.; Hyeon, T., *J. Phys. Chem. B* **2005,** *109* (32), 15297-15302.

[35] Burda, C.; Chen, X.; Narayanan, R.; El-Sayed, M. A., *Chem. Rev.* **2005,** *105* (4), 1025-1102.

[36] Tsai, C.-C.; Teng, H., *Chem. Mater.* **2004,** *16* (22), 4352-4358.

[37] Riss, A.; Elser, M. J.; Bernardi, J.; Diwald, O., *J. Am. Chem.l Soc.* **2009,** *131* (17), 6198-6206.

[38] Xia, Y.; Yang, P.; Sun, Y.; Wu, Y.; Mayers, B.; Gates, B.; Yin, Y.; Kim, F.; Yan, H., *Adv. Mater.* **2003,** *15* (5), 353-389.

[39] Adachi, M.; Murata, Y.; Harada, M.; Yoshikawa, S., *Chem. Lett.* **2000,** *29* (8), 942-943.

[40] Quan, X.; Yang, S.; Ruan, X.; Zhao, H., *Env. Sci. Tech.* **2005,** *39* (10), 3770-3775.

[41] Uchida, S.; Chiba, R.; Tomiha, M.; Masaki, N.; Shirai, M., *Electrochemistry*, **2002**, 70, 418-420.

[42] Adachi, M.; Okada, I.; Ngamsinlapasathian, S.; Murata, Y.; Yoshikawa, S., *Electrochemistry*, **2002**, 70, 449-452.

[43] Hasiguti, R. R., *Ann. Rev. Mater. Sci.* **1972,** *2* (1), 69-92.

[44] Cronemeyer, D. C., E, *Phys. Rev.* **1952,** *87* (5), 876-886.

[45] Wycoff, R. W. G. *The Structure of Crystals*; The Chemical Catalog Company Inc.: New York, 1931

[46] Landmann, M.; Rauls, E.; Schmidt, W. G., *J. Phys: Conden. Matt.* **2012,** *24* (19), 195503.

[47] Henrich, V. E., *Rep. Prog. Phys.* **1985,** *48* (11), 1481.

[48] Thiên-Nga, L.; Paxton, A. T., *Phys. Rev. B* **1998,** *58* (19), 13233-13241.

[49] Landmann, M.; Rauls, E.; Schmidt, W. G., *J. Phys: Condens. Mattter.* **2012,** *24* (19), 195503.

[50] Navrotsky, A.; Jamieson, J. C.; Kleppa, O. J., *Science* **1967,** *158* (3799), 388-389.

[51] Jamieson, J.C.; Olinger, B.; *Am Min*. **1969**, 54,1447.

[52] Dabler, A.; Feltz, A.; Jung, J.; Ludwig, W.; Kaisersberger, E., *J. Therm. Anal. Cal.* **1988,** *33* (3), 803-809.

[53] Hanaor, D. H.; Sorrell, C., *J Mater Sci* **2011,** *46* (4), 855-874.

[54] Horn, M.; Schwerdtfeger, C. F.; and Meagher, E. P.; *Z. Kristallogr*, **1972,** 136, 273-281

[55] Carp, O.; Huisman, C. L.; Reller, A., *Prog. Sol. St. Chem.* **2004,** *32* (1–2), 33-177.

[56] Asahi, R.; Taga, Y.; Mannstadt, W.; Freeman, A. J. *Phys. Re*V. *B* **2000**, *61*, 7459.

[57] Wu, Z. Y.; Ouvrared, G.; Gressier, P.; Natoli, C. R. *Phys. Re*V. *B***1997**, *55*, 10382.

[58] Brydson, R.; Sauer, H.; Engel, W.; Thomas, J. M.; Zeitler, E.; Kosugi,N.; Kuroda, H. *J. Phys.: Condens. Matter* **1989**, *1*, 797.

---

[59] Brydson, R.; Williams, B. G.; Engel, W.; Sauer, H.; Zeitler, E.;Thomas, J. M. *Sol. St. Commun.* **1987**, *64*, 609.

[60] Choi, H. C.; Ahn, H. J.; Jung, Y. M.; Lee, M. K.; Shin, H. J.; Kim,S. B.; Sung, Y. E. *Appl. Spectrosc.* **2004**, *58*, 598.

[61] Balachandran, U.; Eror, N. G., *J Mater Sci* **1988,** *23* (8), 2676-2682.

[62] Sekiya, T.; Ichimura, K.; Igarashi, M.; Kurita, S., *J. Phys. Chem. Sol.* **2000,** *61* (8), 1237-1242.

[63] Hasiguti, R. R.; Yagi, E., *Phys. Rev. B* **1994,** *49* (11), 7251-7256.

[64] Herrmann, J.-M., *Cat. Today* **1999,** *53* (1), 115-129.

[65] Nosaka, Y.; Fox, M. A., *J. Phys. Chem.* **1988,** *92* (7), 1893-1897.

[66] Ni, M.; Leung, M. K. H.; Leung, D. Y. C.; Sumathy, K., *Renew. Sust. Ener. Rev.* **2007,** *11* (3), 401-425.

[67] (a) Munter, R., , *Proc. Estonian Acad. Sci. Chem*. **2001,**50, 59-80, 2001; (b) CRC Handbook, **1985**.(c)Dean, J. A.; *Lange's Handbook of Chemistry*, 11ed, New York, McGraw-Hill **1973.**(d) Gratzel,M. *Heterogeneous Electron Transfer*; CRC Press: Boca Raton, FL, **1989** (e) Hoffmann, M. R.; Martin, S. T.; Choi, W.; Bahnemann, D. W., *Chem. Rev.* **1995,** *95* (1), 69-96.

[68] Fujishima, A.; Honda, K., *Nature*, **1972**, 238, 37-38.

[69] Wu, G.; Chen, T.; Zhou, G.; Zong, X.; Li, C., *Sci. Chin. B: Chem.* **2008,** *51* (2), 97-100.

[70] Sato, S.; White, J. M., *Chem. Phys. Lett.* **1980,** *72* (1), 83-86.

[71] Idakiev, V.; Yuan, Z. Y.; Tabakova, T.; Su, B. L., *App. Catal.s A: General* **2005,** *281* (1–2), 149-155.

[72] Gerischer, H.; Willig, F.; Meier, H.; Jahnke, H.; Schönborn, M.; Zimmermann, G., Eds. Springer Berlin / Heidelberg: 1976; Vol. 61, pp 31-84.

[73] Vlachopoulos, N.; Liska, P.; Augustynski, J.; Graetzel, M., *J. Am. Chem. Soc.* **1988,** *110* (4), 1216-1220.

[74] Kamat, P. V.; Fox, M. A., *Chem. Phys. Lett.* **1983,** *102* (4), 379-384.

[75] Desilvestro, J.; Graetzel, M.; Kavan, L.; Moser, J.; Augustynski, J., *J. Am. Chem. Soc.* **1985,** *107* (10), 2988-2990.

[76] Peng, T.; Dai, K.; Yi, H.; Ke, D.; Cai, P.; Zan, L., *Chem. Phy. Lett.* **2008,** *460* (1–3), 216-219.

[77] Jang, J. S.; Li, W.; Oh, S. H.; Lee, J. S., *Chem. Phys. Lett.* **2006,** *425* (4–6), 278-282.

[78] Sasikala, R.; Shirole, A.; Sudarsan, V.; Sakuntala, T.; Sudakar, C.; Naik, R.; Bharadwaj, S. R., *Int. J. Hyd. Ener.* **2009,** *34* (9), 3621-3630.

[79] Hirai, T.; Suzuki, K.; Komasawa, I., *J. Coll. Inter. Sci.* **2001,** *244* (2), 262-265.

[80] Kato, H.; Kudo, A., *J. Phys. Chem. B* **2002,** *106* (19), 5029-5034.

[81] Liu, J. W.; Chen, G.; Li, Z. H.; Zhang, Z. G., *J. Solid. Stat. Chem.* **2006,** *179* (12), 3704-3708.

[82] Hwang, D. W.; Kim, H. G.; Lee, J. S.; Kim, J.; Li, W.; Oh, S. H., *J. Phys. Chem. B* **2004,** *109* (6), 2093-2102.

[83] Borgarello, E.; Kiwi, J.; Graetzel, M.; Pelizzetti, E.; Visca, M., *J. Am. Chem. Soc.* **1982,** *104* (11), 2996-3002.

[84] Lindgren, T.; Mwabora, J. M.; Avendaño, E.; Jonsson, J.; Hoel, A.; Granqvist, C.-G.; Lindquist, S.-E., *J. Phys. Chem. B* **2003,** *107* (24), 5709-5716.

[85] Chen, X.; Burda, C., *J. Am. Chem. Soc.* **2008,** *130* (15), 5018-5019.

[86] Ohno, T.; Mitsui, T.; Matsumura, M., *Chem. Lett.* **2003,** *32* (4), 364-365.

[87] Le Paven-Thivet, C.; Ishikawa, A.; Ziani, A.; Le Gendre, L.; Yoshida, M.; Kubota, J.; Tessier, F.; Domen, K., *J. Phys. Chem. C* **2009,** *113* (15), 6156-6162.

---

[88] Sant, P. A.; Kamat, P. V., *Phys. Chem. Chem. Phys.* **2002,** *4* (2), 198-203.

[89] Baker, D. R.; Kamat, P. V., *Adv. Func. Mater.* **2009,** *19* (5), 805-811.

[90] Evans, J. E.; Springer, K. W.; Zhang, J. Z., *J. Chem. Phys.s* **1994,** *101* (7), 6222-6225.

[91] Yao, Y.; Li, G.; Ciston, S.; Lueptow, R. M.; Gray, K. A., *Env. Sci. Tech.* **2008,** *42* (13), 4952-4957.

[92] Choi, W.; Termin, A.; Hoffmann, M. R., *J. Phys. Chem.* **1994,** *98* (51), 13669-13679.

[93] Asahi, R.; Morikawa, T.; Ohwaki, T.; Aoki, K.; Taga, Y., *Science* **2001,** *293* (5528), 269-271.

[94] Chen, X.; Lou, Y. B.; Samia, A. C. S.; Burda, C.; Gole, J. L., *Adv. Func. Mater.* **2005,** *15* (1), 41-49.

[95] Nakamura, R.; Tanaka, T.; Nakato, Y., *J. Phys. Chem. B* **2004,** *108* (30), 10617-10620.

[96] Di Valentin, C.; Finazzi, E.; Pacchioni, G.; Selloni, A.; Livraghi, S.; Paganini, M. C.; Giamello, E., *Chem. Phys.* **2007,** *339* (1–3), 44-56.

[97] Diwald, O.; Thompson, T. L.; Goralski, E. G.; Walck, S. D.; Yates, J. T., *J. Phys.Chem. B* **2003,** *108* (1), 52-57.

[98] Chen, X.; Burda, C., *J. Phys. Chem. B* **2004,** *108* (40), 15446-15449.

[99] Di Valentin, C.; Pacchioni, G.; Selloni, A.; Livraghi, S.; Giamello, E., *J. Phys. Chem. B* **2005,** *109* (23), 11414-11419.

[100] Di Valentin, C.; Pacchioni, G.; Selloni, A., *Phys. Rev. B* **2004,** *70* (8), 085116.

[101] Miyauchi, M.; Ikezawa, A.; Tobimatsu, H.; Irie, H.; Hashimoto, K., *Phys. Chem. Chem. Phys.* **2004,** *6* (4), 865-870.

[102] Thompson, T. L.; Yates, J. T., *Chem. Rev.* **2006,** *106* (10), 4428-4453.

[103] Dunnill, C. W.; Parkin, I. P., *Dalt. Trans.* **2011,** *40* (8), 1635-1640.

[104] Kasuga, T.; Hiramatsu, M.; Hoson, A.; Sekino, T.; Niihara, K., *Langmuir* **1998,** *14* (12), 3160-3163.

[105] Zhu, Y.; Li, H.; Koltypin, Y.; Hacohen, Y. R.; Gedanken, A., *Chem. Comm.* **2001,** (24), 2616-2617.

[106] Kasuga, T.; Hiramatsu, M.; Hoson, A.; Sekino, T.; Niihara, K., *Adv. Mater.* **1999,** *11* (15), 1307-1311.

[107] Jung, J. H.; Kobayashi, H.; van Bommel, K. J. C.; Shinkai, S.; Shimizu, T., *Chem. Mater.* **2002,** *14,* 1445-1447.

[108] Zhang, Q.; Gao, L., *Langmuir* **2002,** *19* (3), 967-971.

[109] Feng, X.; Shankar, K.; Varghese, O. K.; Paulose, M.; Latempa, T. J.; Grimes, C. A., *Nano Lett.* **2008,** *8* (11), 3781-3786.

[110] Feng, X.; Zhai, J.; Jiang, L., *Ang. Chem. Int. Ed.* **2005,** *44* (32), 5115-5118.

[111] Pradhan, S. K.; Reucroft, P. J.; Yang, F.; Dozier, A., *J. Cryst. Growth* **2003,** *256* (1–2), 83-88.

[112] Wu, J.-J.; Yu, C.-C., *J. Phys. Chem. B* **2004,** *108* (11), 3377-3379.

[113] Wu, J.-M.; Shih, H. C.; Wu, W.-T.; Tseng, Y.-K.; Chen, I. C., *J. Cryst. Growth* **2005,** *281* (2–4), 384-390.

[114] Lei, Y.; Zhang, L. D.; Fan, J. C., *Chem. Phys. Letters* **2001,** *338* (4–6), 231-236.

[115] Liu, S.; Huang, K., *Sol. Ener. Mater. Solar Cells* **2005,** *85* (1), 125-131.

[116] Gong, D.; Grimes, C. A.; Varghese, O. K.; Hu, W.; Singh, R. S.; Chen, Z.; Dickey, E. C., *J. Mater. Res.* **2001,** *16* (12), 3331-3334.

[117] Bessekhouad, Y.; Robert, D.; Weber, J. V., *J. Photochem. Photobio. A: Chem.* **2003,** *157* (1), 47-53.

---

[118] Chen, Y.; Crittenden, J. C.; Hackney, S.; Sutter, L.; Hand, D. W., *Environ. Sci. Tech.* **2005,** *39* (5), 1201-1208.

[119] Jung, J. H.; Kobayashi, H.; van Bommel, K. J. C.; Shinkai, S.; Shimizu, T., *Chem. Mater.* **2002,** *14* (4), 1445-1447.

[120] Wang, W.; Varghese, O. K.; Paulose, M.; Grimes, C. A.; Wang, Q.; Dickey, E. C., *J. Mater. Res.* **2004,** *19* (02), 417-422.

[121] Yao, B. D.; Chan, Y. F.; Zhang, X. Y.; Zhang, W. F.; Yang, Z. Y.; Wang, N., *App. Phys. Lett.* **2003,** *82* (2), 281-283.

[122] Masuda, H.; Fukuda, K., *Science* **1995,** *268* (5216), 1466-1468.

[123] Possin, G. E., *Rev. Sci. Inst.* **1970,** *41* (5), 772-774.

[124] AlMawlawi, D.; Coombs, N.; Moskovits, M., *J. App. Phys.* **1991,** *70* (8), 4421-4425.

[125] Kawai, S.; Ueda, R., *J. Electrochem. Soc.* **1975,** *122* (1), 32-36.

[126] McGarvey, C. E.; Holden, D. A., *Langmuir* **1990,** *6* (6), 1123-1132.

[127] Zwilling, V.; Darque-Ceretti, E.; Boutry-Forveille, A.; David, D.; Perrin, M. Y.; Aucouturier, M., *Surf. Inter. Anal.* **1999,** *27* (7), 629-637.

[128] Grimes, C. A., *J. Mater. Chem.* **2007,** *17* (15), 1451-1457.

[129] Mor, G. K.; Varghese, O. K.; Paulose, M.; Shankar, K.; Grimes, C. A., *Sol. Ener. Mater. Solar Cells* **2006,** *90* (14), 2011-2075.

[130] Schultze, J. W.; Lohrengel, M. M., *Electrochim. Acta* **2000,** *45* (15–16), 2499-2513.

[131] Pourbaix, M. Atlas d’Equilibres Electrochimiques; GauthierVillars: Paris, 1963; pp 644.

[132] Carter, V. E., *Metallic Coatings for Corrosion Control*, Hants (Butterworth), 1977,27.

[133] Caprani, A.; Epelboin, I.; Morel, P., *J. Electroanal. Chem. Interfac.Electrochem.* **1973,** *43* (1), A2-A9.

[134] Mandry, M. J.; Rosenblatt, G., *J. Electrochem. Soc.* **1972,** *119* (1), 29-33.

[135] Kelly, J. J., *Electrochim. Acta* **1979,** *24* (12), 1273-1282.

[136] Macak, J. M.; Tsuchiya, H.; Ghicov, A.; Yasuda, K.; Hahn, R.; Bauer, S.; Schmuki, P., *Curr. Op. Solid State. Mater. Sci.* **2007,** *11* (1–2), 3-18.

[137] Prakasam, H. E.; Shankar, K.; Paulose, M.; Varghese, O. K.; Grimes, C. A., *J. Phys.Chem. C* **2007,** *111* (20), 7235-7241.

[138] Narayanan, R.; Kwon, T.-Y.; Kim, K.-H., *Mater. Lett.* **2009,** *63* (23), 2003-2006.

[139] Mor, G. K.; Varghese, O. K.; Paulose, M.; Ong, K. G.; Grimes, C. A., *Thin Solid Films* **2006,** *496* (1), 42-48.

[140] Zhu, Y.; Li, H.; Koltypin, Y.; Hacohen, Y. R.; Gedanken, A., *Chem. Comm.* **2001,** (24), 2616-2617.

[141] Cai, Q.; Paulose, M.; Varghese, O. K.; Grimes, C. A., *J. Mater. Res.* **2005,** *20* (01), 230-236.

[142] Prakasam, H. E.; Shankar, K.; Paulose, M.; Varghese, O. K.; Grimes, C. A., *J. Phys. Chem. C* **2007,** *111* (20), 7235-7241.

[143] Paulose, M.; Shankar, K.; Yoriya, S.; Prakasam, H. E.; Varghese, O. K.; Mor, G. K.; Latempa, T. A.; Fitzgerald, A.; Grimes, C. A., *J. Phys. Chem. B* **2006,** *110* (33), 16179-16184.

[144] Mor, G. K.; Prakasam, H. E.; Varghese, O. K.; Shankar K.; Grimes, C. A., *Nano. Lett*., **2007**, 7, 2356-2364.

---

[145] Macak, J. M.; Tsuchiya, H.; Berger, S.; Bauer, S.; Fujimoto S.; Schmuki, P., *Chem. Phys. Lett.*, **2006**,,428, 421-425.

[146] Varghese, O. K.; Paulose, M.; Grimes, C. A., *Nat. Nano* **2009,** *4* (9), 592-597.

[147] O'Regan, B, Grätzel, M., *Nature,***1991**, 353, 737-740.

[148] Robertson, N., *Angew. Chem. Int. Ed.* **2006,** *45* (15), 2338-2345.

[149] Mishra, A.; Fischer, M. K. R.; Bäuerle, P., *Angew. Chem. Int. Ed.* **2009,** *48* (14), 2474-2499.

[150] Oskam, G.; Bergeron, B. V.; Meyer, G. J.; Searson, P. C., *J. Phys. Chem. B* **2001,** *105* (29), 6867-6873.

[151] Nusbaumer, H.; Moser, J.-E.; Zakeeruddin, S. M.; Nazeeruddin, M. K.; Grätzel, M., *J. Phys. Chem. B* **2001,** *105* (43), 10461-10464.

[152] Huang, S. Y.; Schlichthörl, G.; Nozik, A. J.; Grätzel, M.; Frank, A. J., *J. Phys.Chem. B* **1997,** *101* (14), 2576-2582.

[153] Boschloo, G.; Hagfeldt, A., *Acc. Chem. Res.* **2009,** *42* (11), 1819-1826.

[154] Zhang, Z.; Chen, P.; Murakami, T. N.; Zakeeruddin, S. M.; Grätzel, M., *Adv. Func. Mater.* **2008,** *18* (2), 341-346.

[155] Wang, M.; Chamberland, N.; Breau, L.; Moser, J.; Baker, R. H.; Marsan, B.; Zakeeruddin, S. M.; Gratzel, M., *Nat. Chem*, **2010,** 2, 385- 389.

[156] Roy, P.; Kim, D.; Lee, K.; Spiecker, E.; Schmuki, P., *Nanoscale* **2010,** *2* (1), 45-59.

[157] Ghicov, A.; Albu, S. P.; Hahn, R.; Kim, D.; Stergiopoulos, T.; Kunze, J.; Schiller, C.-A.; Falaras, P.; Schmuki, P., *Chemistry – An Asian Journal* **2009,** *4* (4), 520-525.

[158] Bonard, J. M.; Kind, H.; Stockli, T.; Nilsson, L. O., *Solid State Electron.* **2001,** *45* (6), 893-914.

[159] Yahya, A.; Michael, K.; Sabee, M., *Nanotechnol.* **2010,** *21* (50), 505706.

[160] Miyauchi, M.; Tokudome, H.; Toda, Y.; Kamiya, T.; Hosono, H., *App. Phys. Lett.* **2006,** *89* (4), 043114-3.

[161] Alivov, Y.; Klopfer, M.; Molloi, S., *App. Phys. Lett* **2010,** *96* (24), 243502-3.

[162] Kang, Y.-M.; Wang, C.-W.; Chen, J.-B.; Wang, L.-Q.; Li, D.-S.; Zhu, W.-D.; Zhou, F., *J. Vac. Sci. Tech. B.* **2012,** *30* (4), 041801.

[163] Wang, L.-Q.; Wang, C.-W.; Chen, J.-B.; Guo, R.-S.; Zhou, F.; Liu, W.-M., *Thin Solid Films* **2011,** *519* (22), 8173-8177.

[164] Korzhak, A. V.; Ermokhina, N. I.; Stroyuk, A. L.; Bukhtiyarov, V. K.; Raevskaya, A. E.; Litvin, V. I.; Kuchmiy, S. Y.; Ilyin, V. G.; Manorik, P. A., *J. Photochem. Photobio. A*, **2008,** *198* (2–3), 126-134.

[165] Gurunathan, K., *Int. J. Hydrogen Energy.* **2004,** *29* (9), 933-940.

[166] Young, T., Phil. Trans. R. Soc. Lond, 1805, 95, 65.

[167] Drelich, J.; Chibowski, E., *Langmuir* **2010,** *26* (24), 18621-18623.

[168] Wenzel, R. N., *Ind. Eng. Chem.* **1936,** *28* (8), 988-994.

[169] Cassie, A. B. D.; Baxter, S., *Trans. Faraday Soc.* **1944,** *40*, 546-551.

[170] Wang, R.; Hashimoto, K.; Fujishima, A.; Chikuni, M.; Kojima, E.; Kitamura, A.; Shimohigoshi, M.; Watanabe, T., *Nature* **1997,** *388* (6641), 431-432.

Chapter 2

Experimental Techniques

The chapter provides a brief description of the experimental techniques used for the synthesis, characterization and studies pertaining to application of pristine and doped TiO_2 *nanotube arrays (TNTA) and powders. The synthesis of the pristine and doped nanotube arrays and powders were carried out using an in-house built electrochemical anodization facility whose details are explained. Following the details of anodization facility, the basic principles of electron microscopic techniques, Scanning Electron Microscopy (SEM) and Transmission Electron Microscopy (TEM), used for the morphological characterization of the synthesized samples are discussed. This is followed by discussion of the techniques used for structural characterization (X-Ray Diffraction (XRD) in powder and glancing incidence modes, and Raman spectroscopy) and compositional analyses (X-ray Photoelectron Spectroscopy (XPS)). The basic principles of Photoluminescence (PL) and Ultra violet-visible absorption spectroscopy (UV-Vis) used for studying electronic energy band structure as well as to identify localized excitations or impurities, Fourier Transform Infra Red Spectroscopy (FTIR) utilized to study physisorbed and chemisorbed surface species, Brunauer, Emmett and Teller (BET) and Temperature Programmed Desorption Reduction and Oxidation (TPDRO) methods used for physisorption and chemisorption surface area measurements are also discussed. Further, the details of the experimental facilities used to carry out studies pertaining to selected applications are outlined.*

2.1. Anodization Facility

The schematic of the experimental setup used for anodization is shown in Figure 2.1. Prior to the electrochemical anodization, the Ti foils (10 mm X 10 mm) were cleaned ultrasonically and washed sequentially with distilled water, ethanol and acetone. A two electrode configuration consisting of Ti anode and Pt counter electrode was employed. A programmable DC power supply (Agilent N5700A) and a multimeter (Agilent 34401A) interfaced to a PC were used for DC voltage supply and measurement of current transients respectively. All anodization reactions were performed under potentiostatic conditions in fluoride or chloride ion containing medium. After anodization, the samples were sequentially sonicated in distilled water, ethanol and acetone, followed by drying in N_2 gas stream.

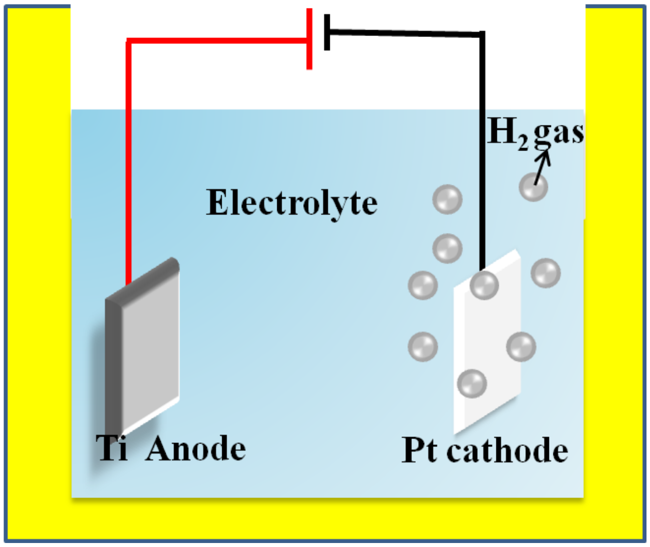

Figure 2.1: Schematic of the potentiostatic anodization set up

2.2. Electron Microscopy

Electron microscopy is a field of science in which electron beam is used to form a magnified image as well as yield diffraction pattern corresponding to the material under inspection. It takes advantage of much shorter wavelength of the electrons and focusing is done through electromagnetic lenses. Electrons accelerated onto a material result in a number of interactions with the atoms of the target sample. Accelerated electrons can pass through the sample without interaction; undergo elastic as well as inelastic scattering thereby resulting in a number of signals that are used for imaging, quantitative and semi-quantitative analyses as well as structure elucidation. The schematic of the processes taking place because of material-electron interaction are depicted in Figure 2.2.

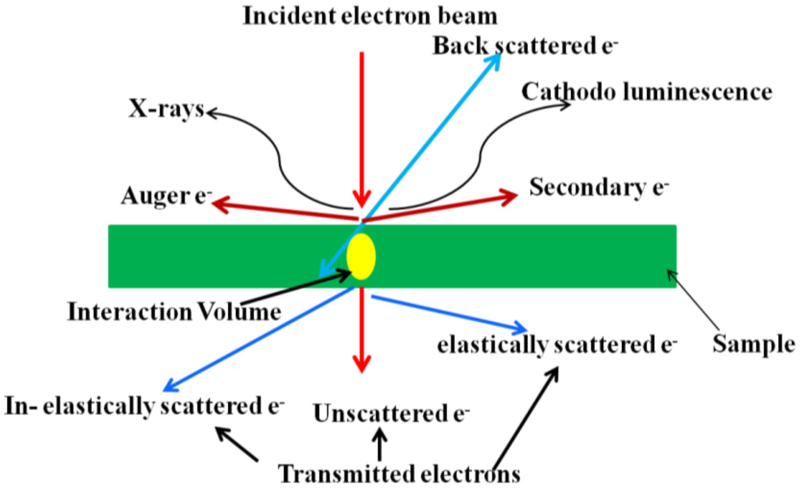

Figure 2.2: Schematic of processes taking place during electron - material interaction.

2.2.1. Scanning Electron Microscopy

Scanning electron microscopy (SEM) is a versatile tool used for surface characterization of materials. The SEM provides the investigator with a highly magnified image of the material surface that is very similar to what one would expect if one could actually "see" the surface visually. The resolution of the SEM can approach a few nm and it can operate at magnifications that are easily adjusted from about 10x to 300,000x**.** In the SEM, a source of high energy electrons (primary electrons) is focused (in vacuum) into a fine probe that is rastered over the surface of the specimen. When the high-energy primary electron interacts with an atom, it undergoes either inelastic scattering with atomic electrons or elastic scattering with the atomic nucleus. This results in secondary electrons (used to produce SEM images), back scattered electrons (used for illustrating contrasts in composition in multiphase samples), diffracted back scattered electrons (used to determine crystal structure and orientation), X-ray photons (used for elemental analysis), visible light and heat. The technique is considered to be non destructive except for the fact that often electron beams can bring about radiation induced surface damage.

During inelastic collision with an electron, some amount of energy is transferred to the electron of the target atom. If the energy transfer is very small, the electron emitted from the atom will probably not have enough energy to exit the surface. If the energy transferred exceeds the work function of the material, the emitted electron can exit the solid surface and are termed as secondary electrons (SE). The energy of these emitted electrons is less than ~50 eV. Most of the emitted SEs are produced within the first few nm of the surface. Secondary electrons produced much deeper in the material suffer additional inelastic collisions, which lower their energy and generally get trapped in the interior of the solid. A fraction of the primary electrons which have undergone elastic scattering with the atomic nucleus (without loss of KE) are back scattered. These backscattered electrons (BSEs) have energies comparable to the primary electron beam. When the energy of the emitted electron is greater than 50 eV**,** by convention, it is referred as BSE. In SEM equipment, the electrons coming out from the specimen surface (SEs and BSEs) are collected by appropriate detectors. The output from the detector is used to modulate the brightness of a cathode ray tube (CRT) whose X- and Y- inputs are driven in synchronism with the X-Y voltages rastering the electron beam. In this way, an image is produced on the CRT. Every point that is struck by the beam on the sample surface is mapped directly onto a corresponding point on the screen. The secondary electrons are the most common signal used in the SEM and have multiple applications e.g. morphological analysis, particles size measurements, fracture analysis, microstructural homogeneity and determination of coating thickness.[1]

In addition to secondary electrons imaging, Energy Dispersive X-ray (EDX) analysis is also a useful tool which is widely used for chemical analysis. The collision of primary electrons with electrons of the atom can cause ejection of core electrons. The excited atom will decay to its ground state by emitting either a characteristic X-ray photon or an Auger electron. The X-ray emission signal can be sorted by energy using an energy dispersive X-ray detector or by wavelength with a wavelength spectrometer (EPMA). These distributions are characteristic of the elements that produced them and can be used to produce elemental images depicting spatial distribution of particular elements in a given field of view. The detectors produce an output signal that is proportional to the number of X-ray photons in the area under electron bombardment. In EDX equipment the output is displayed in the form of a histogram of counts versus X-ray energy. The characteristic X-rays emitted from the sample serve as fingerprints and provide elemental information of the samples permitting semi-quantitative analysis, quantitative analysis, line profiling and spatial distribution imaging. SEM with X-ray analysis is an efficient, inexpensive and non-destructive tool which has become quite essential for the day to day surface analysis.

The essential components of an electron microscope are electron emission gun, electron lenses, sample stage, detectors for all signals of interest, display and data acquisition devices. This equipment also has infrastructure requirements such as power supply, vacuum system, cooling system, vibration free floor and it needs to be installed in a room, free of ambient magnetic and electric fields.

In conventional SEMs, electrons are generated by heating the tungsten filament or lanthanum hexaboride (LaB_6) crystal to high temperatures (~2800^{o}C) (thermionic field emitter). Thermionic sources suffer from relatively low brightness, evaporation of cathode material and thermal drift during operation, which limit electron source life time and low image resolution. Field emission is one way of generating electrons that avoids many of these problems. A Field Emission Source (FES), also known as a cold cathode field emitter, does not need heating of the emitter material. The emission is achieved by placing the emitter in a huge electrical potential gradient (0.5 to 30 KV). The FES is usually a tungsten wire fashioned into a sharp point. The significance of the small tip radius (~ 100 to 10 nm) is that an electric field can be concentrated to an extreme level, becoming so big that the work function of the material is lowered, enabling easy generation of electrons. The electron beam produced by the field emission is 1000 times narrower than that produced in a conventional SEM and produces cleaner images with much less electrostatic distortions and high spatial resolution (< 2 nm). In contrast to a conventional tungsten filament, an FE tip can last, theoretically, for a lifetime provided the vacuum is maintained stable. This high spatial resolution permits one to image nanoscale topography and ultra small scale phenomena.

Field Emission Scanning Electron Microscopes (FEG Quanta, Philips, Netherlands and Zeiss, Germany) having EDX facilities were employed for the morphological analysis in the present study. Semi-quantitative elemental analyses were carried out using the EDX facilities attached to the FESEMs.

2.2.2. Transmission Electron Microscopy

Transmission electron microscopy is an established technique for examining the crystal structure as well as microstructure of materials. It is used to study all varieties of solid materials: metals, ceramics, semiconductors, polymers, and composites. TEM offers two distinct methods of specimen observation, diffraction mode and image mode.[2] A schematic representation of the general image and diffraction modes of TEM is given in Figure 2.3.

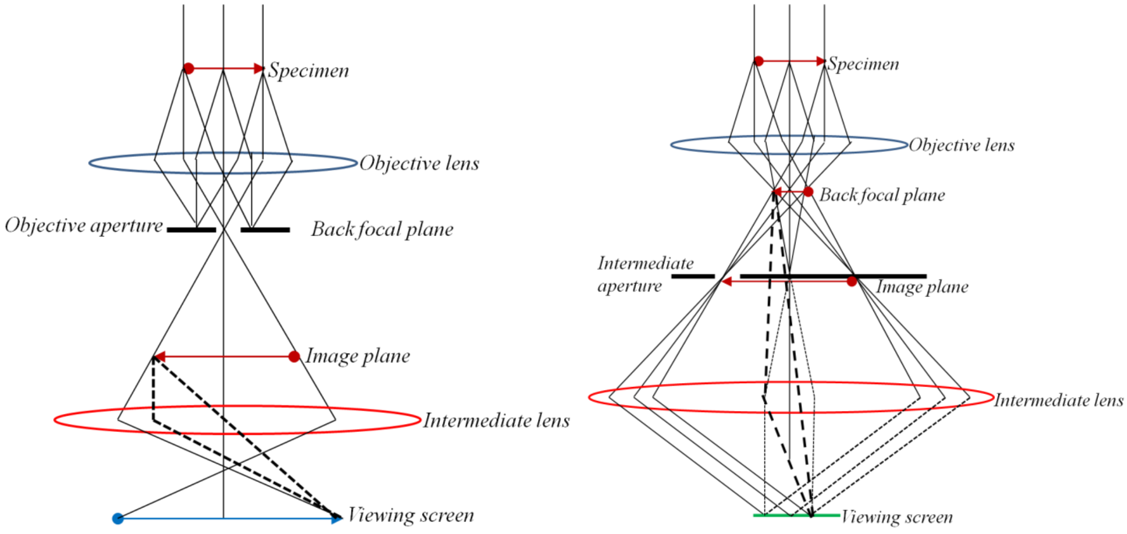

Figure 2.3. Schematic representation of general image and diffraction modes of TEM

In diffraction mode, an electron diffraction pattern originating from the sample area illuminated by the electron beam and formed at the back focal plane of the objective lens, is obtained on the fluorescent screen. The diffraction pattern is obtained by setting the array of magnetic lenses beneath the specimen **(**post-specimen lenses) so as to examine / magnify the information in the transmitted signal at the back focal plane of the objective lens. The diffraction pattern is entirely equivalent to an X-ray diffraction pattern: a single crystal will produce a spot pattern on the screen, a poly-crystal will produce a ring pattern (assuming that the illuminated area includes sufficient number of crystallites). A glassy or amorphous material produces a series of diffuse halos.

In order to obtain diffraction pattern from a desired region of interest (ROI) from a given specimen, selected area electron diffraction (SAED) is carried out. In SAED, the condenser lens is defocused to produce parallel illumination at the specimen and a selected-area aperture is used to limit the diffracting volume. The SAED pattern is a superposition of diffraction patterns originating from crystallites present in an illuminated ROI that possess distinct orientations.

In the imaging mode, a magnified image of the illuminated ROI is produced in the image plane of the objective lens. The image can contain contrast brought about by several mechanisms: mass contrast, due to spatial separations between distinct atomic constituents; thickness contrast, due to non-uniformity in sample thickness; diffraction contrast, which in the case of crystalline materials results from scattering of the incident electron wave by structural defects; and phase contrast. In the imaging mode, there are three types of operations viz. bright field, dark field and high resolution microscopy. In bright-field microscopy, a small objective aperture is used to block all diffracted beams and to pass only the transmitted (undiffracted) electron beam. Whereas, for dark field microscopy all the directly transmitted beams are blocked and only diffracted beams are let by placing the objective aperture around the diffracted beam in the SAED pattern. In case of high-resolution TEM, transmitted beams along with at least one diffracted beam is admitted by using a large-diameter objective diaphragm. All of the beams passing through the objective aperture are then made to recombine in the image-forming process, in such a way that their amplitudes and phases are preserved. When viewed at high-magnification, it is possible to observe contrast in the image in the form of periodic fringes. These fringes represent direct resolution of the Bragg diffracting planes. Thus this mode of contrast is referred to as phase contrast. The fringes that are visible in the high-resolution image originate from those planes that are oriented as Bragg reflecting planes and possess interplanar spacing greater than the lateral spatial resolution limits of the instrument. In addition, the highly energetic beam of electrons used in TEM interacts with sample matter to produce characteristic radiation and particles. From these signals information regarding composition can be extracted.

TEM (Philips, Netherlands) was employed for the morphological and structural characterization of all the samples investigated for the present work.

2.3. X ray Diffraction

When an electromagnetic radiation of wavelength λ impinges on a material having periodic structures with geometrical variations in the length scale ofλ, diffraction effect occurs. Since X-rays have wavelength comparable to interatomic spacing in a crystal, it can interact with the solid and scatter to produce a diffraction pattern[3]. This happens when the interaction satisfies the Braggs diffraction criterion:

$$2dsin\theta = n\lambda \qquad (1)$$

where *d* is the inter-planar spacing (i.e. spacing between adjacent planes in a set of planes, figure 2.4), θ the angle of incidence, *n* the integer representing the order of diffraction, and λ the wavelength of the X-ray (normally Cu Kα =1.54056 A^o). Each peak in the diffraction pattern can be correlated to a set of planes in a crystal lattice. Different set of planes have different inter-planar spacing and according to Bragg condition θ must change as *d* changes. A schematic view of the X-ray Diffraction (XRD) process is shown in Figure 2.4. The X-ray Diffractometer typically uses Bragg-Brentano geometry for recording the diffraction pattern. Generally, the diffraction pattern is plotted as intensity versus diffraction angle 2θ. In powder XRD, the X-rays can penetrate to a material depth in the range of 0.1 to 10 ,mm depending on the material type and the incident X-ray energy.

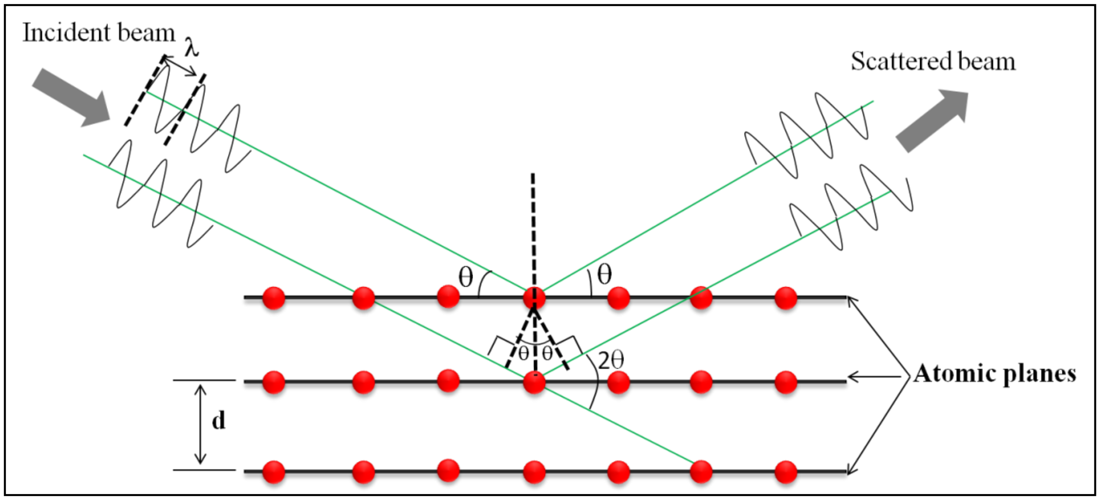

Figure 2.4: Schematic representation of the X-ray diffraction process

Glancing incidence X-ray diffraction (GI-XRD) is a technique used to record the diffraction pattern of thin films, with minimum contribution acquiring from substrate. In this case the penetration depths of the X-rays are restricted to about 10-100 nm by keeping the angle of incidence of X-ray at a very small value (< 5^o). Since the scattering volume is small, high brilliance X-ray sources like rotating anode and synchrotron beams lines are often used. Such surface and subsurface crystallography need fast and efficient detectors to yield significant counts. The crystal structure of the samples are obtained by comparing the pattern with that given in the powder diffraction file collected and maintained by Joint Committee of Powder Diffraction Standards (JCPDS) constituted by International Commission on Diffraction Data (ICDD). The crystallite sizes of the samples are calculated using Scherer formula.[4]

$$t = \frac{K \lambda}{B \, Cos\theta} \qquad (2)$$

where K is a dimensionless constant having value of 0.9, λ is the wave length of the incident X-ray radiation and θ is the diffraction angle in radians. Broadening B is calculated by taking the full width half maximum (FWHM) of the diffraction peak corresponding to each plane in the diffraction pattern.

In the present study, the samples were analyzed in the powder and GIXRD modes using the X-ray diffractometers of make STOI (Germany) and Bruker D8 Discover (Germany) respectively.

2.4. Raman Spectroscopy

Raman spectroscopy is primarily a structural characterization tool. The Raman spectrum arises from the indirect coupling of high frequency radiation (usually visible light, but also ultraviolet and near infrared excitation sources) with the electron clouds that constitute the chemical bonds. Such an interaction is very sensitive to the lengths, strengths, and arrangement of bonds in a material. Elemental chemical composition plays a minor role. A crystalline lattice with nonzero polarization exhibit Raman activity. In the case of crystals, the spectrum responds more to details of defects and disorder than to trace impurities and related chemical imperfections. In addition coupled modes of lattice vibrations ie; optical phonon modes influence the spectral appearance.

When an intense monochromatic light beam impinges on the sample, the electric field of the incident radiation distorts the electron clouds that make up the chemical bonds in the sample, storing some energy. As the wave passes, the field reverses and the distorted electron clouds relax back re-radiating the stored energy. Most of the stored energy is re-radiated at the same frequency as that of the incident excitation source. This component is known as the Rayleigh scattering and gives a strong central line in the scattering spectrum. However, a small portion of the stored energy is transferred to the sample exciting the vibrational modes, resulting in weak side bands in the spectrum at frequencies less than that of the incident beam. These are the Raman lines. Their separation from the Rayleigh line is a direct measure of the vibrational frequencies of the sample and is generally plotted against intensity versus the difference in wave number between the incident beam and scattered beam.[5,6] The reverse process also occurs. Existing vibrations that have been excited by thermal processes can be annihilated by coupling with the incident beam and can add their energies to that of the source. These appear as side bands at higher frequencies. The Raman process that excites molecular and crystal vibrations is called Stokes scattering; the process that annihilates existing vibrations is called anti-Stokes scattering. The two spectra are mirror images on opposite sides of the Rayleigh line. However, because anti-Stokes scattering depends on the existence of thermally activated vibrations, the anti-Stokes intensities are strongly temperature dependent, whereas the Stokes intensities are only weakly temperature dependent. For this reason, anti-Stokes scattering is rarely measured, except for the specialized technique known as coherent anti-Stokes Raman spectroscopy. The schematic of the Raman scattering process is given in figure 2.5.

Due to the small wave vector of the optical phonon, the phonons involved in the Raman scattering of crystalline solids have very small momentum (from the wave vector conservation law) compared with brillouin zone. So only the zone centered phonons participate in the Raman scattering in a normal Raman spectra process. However there are cases where non-zero center phonons ie; phonons originating from beyond Brillouin zone boundary can be excited as is the case with nanostructured materials. The technique is complementary to FTIR and has same energy shifts as infra red absorptions. The main advantages of Raman spectroscopy are its non destructive analysis, high information content, ability to sample through the container and minimal interference from water, as is the case with aqueous suspensions.

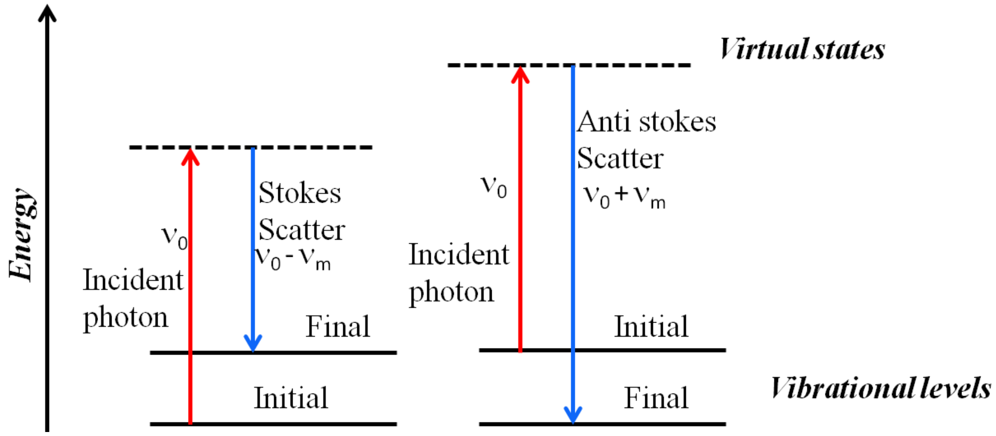

Figure 2.5: Schematic of Raman scattering processes

In the present study Raman spectroscopic tool is utilized to investigate the crystallinity of the samples using Micro Raman Spectrometer (Renishaw, UK), equipped with a confocal microscope with an "argon ion laser" operating at 514.5nm.

2.5. X-ray Photoelectron Spectroscopy

X ray photoelectron spectroscopy is a semi-quantitative technique to determine chemical composition of the material based on photoelectric effect. This is also known as electron spectroscopy for chemical analysis (ESCA). Photoelectron spectroscopy has been developed by the pioneering work of Kai Siegbahn's group in Uppsala in the 1960's. Siegbahn was awarded Nobel Prize in physics in 1981 for this work. His work is the basis for the use of this technique in chemical characterization of materials. The basic principle is that the binding energy of an electron in a molecular orbital of the molecule will be affected by the nature of its chemical environment (chemical shift). X-ray Photoelectron Spectroscopy (XPS) utilizes photo-ionization and analysis of the kinetic energy distribution of the emitted photoelectrons to study the composition and electronic state of the surface region of a sample.[7] The sample is irradiated with soft X-rays (200-2000eV) under ultra high vacuum. The photon is absorbed by an atom or molecule (initial state effects) leading to ejection of core shell electrons (final state effects). The energy spectra of the ejected electrons are then determined by the beta-ray spectrometer. The kinetic energy of the photoelectrons are given by

$$K.E = h\nu - B.E - \phi \tag{3}$$

where *K.E* is the kinetic energy of the photoelectrons, $h\nu$ *the* energy of the incident photon, *B.E* the binding energy of the electron and ϕ the work function of the material. The photon absorption is fast and takes place within 10^{-16} s. If hν is less than B.E + ϕ, no photoemission process will be initiated. As the B.E decreases the KE energy of the photoelectron increases. The intensity of the photoelectron emission is proportional to the intensity of photons. By analyzing the kinetic energies of the photoelectrons, the binding energy of the photoelectrons and corresponding energies of the electronic orbitals can be calculated. Since the energies of various orbitals are characteristic of an element, one can identify the elements present in the material, based on the binding energies of the emitted photo electrons. Binding energy reflects the strength of interaction between the electrons and the nuclear charge and it contains information on the initial and final state of the atoms. The initial state accounts for the core level binding energy shifts and is used for obtaining chemical state information. The chemical surrounding of an atom decides the effective charge on the core electron. With the change in the chemical surrounding, this effective charge is altered. Thus a change in binding energy is caused. This manifests as a chemical shift or surface core level shift and is indicative of the oxidation state of the atom. More the binding energy, more tightly will be the electron bound to the nucleus and therefore in the case of high Z elements, the binding energy will be high. The schematic of the X-ray photo electron emission process is depicted in Figure 2.6.

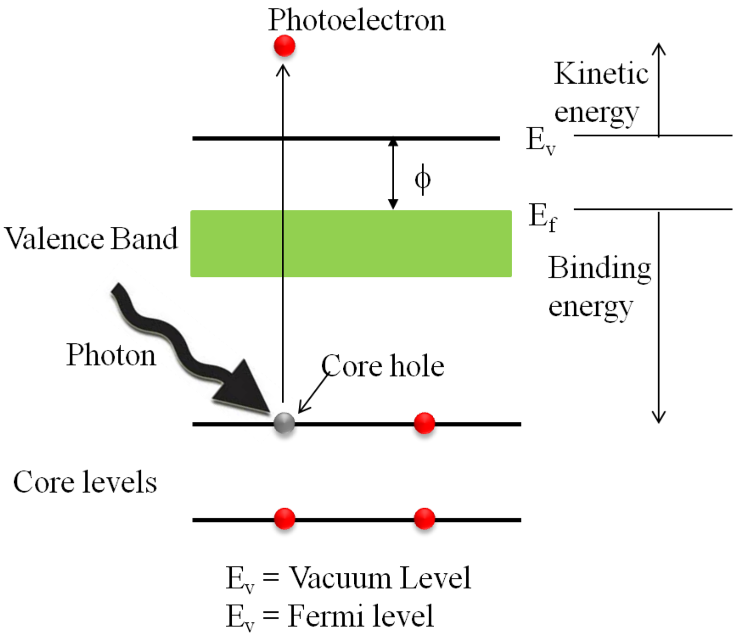

Figure 2.6: The schematic of photoelectron emission process.

For an electron in an orbital which possess orbital angular momentum, coupling between magnetic fields of spin (s) and angular momentum (l) occurs. The level of degeneracy of the spin - orbit splitting will be 2j+1, where j is the total momentum. According to this, no splitting will be observed for the s orbital, whereas the p orbital electron emission will show a doublet keeping the intensity ratio at 1:2 for $p_{1/2}$ and $p_{3/2}$.[8, 9]

The B.E of the electrons not only depends upon the level from which it is ejected, but also on the formal oxidation state and local chemical coordination environment of the atom. Therefore, one can identify the oxidation states as well as the chemical environments from the observed BE values. An approximate composition of the material can be determined by dividing the individual peak areas corresponding to the elements of interest, after appropriate background subtraction, by their respective atomic sensitivity factor (ASF). This was done after appropriate back ground subtraction. The sensitivity factor of the element can be defined by the equation

$$ASF = f \times \sigma \times \theta_i \times y \times \lambda_{mf} \times A \times T_d \qquad (4)$$

where f is the X-ray flux (photons/cm^2-sec), σ the photoelectron cross section of the atomic orbital of interest (cm^2), θ_i is the instrumental angular efficiency factor between photo path and detected electron, y is the efficiency in the photoelectric process for formation of photoelectrons of the normal photoelectron energy and λ_{mf} is the mean free path of the photoelectrons in the sample. A refers to the area of the sample from which emitted photoelectrons are detected and T_d is the detection efficiency for electrons emitted from the specimen of interest. From the peak height or peak areas and atomic sensitivity factor values corresponding to the elements of interest, the stoichiometry of the material can be calculated using the equation,

$$\frac{n_A}{n_B} = \frac{I_A/S_A}{I_B/S_B} \qquad (5)$$

n_A and n_B in this equation refers to the atomic fractions of the elements A and B present in the material. I_A and I_B are the corresponding intensities whereas S_A and S_B are ASF values respectively.

In the present study, the composition and nonstoichiometry of the samples were determined by X-ray photoelectron spectrometer, M/s SPECS, Germany.

2.6. Photoluminescence

Photoluminescence (PL) spectroscopy is a powerful technique for investigating the electronic structure, both intrinsic and extrinsic, of semiconducting and semi-insulating materials from the spectrum of light emitted.[10] It can also be used to monitor the impurity levels or dopants in III-V, II-VI, and group IV compounds, as well as in dilute magnetic and other chalcogenide semiconductors. In PL, material gains energy by absorbing light at a specific wavelength by promoting an electron from a lower to a higher energy level. This may be described as a transition from the ground state to an excited state for an atom or molecule, or from the valence band to the conduction band for a semiconductor crystal (electron-hole pair creation). The system then undergoes a nonradiative internal relaxation involving interaction with crystalline or molecular vibrational and rotational modes, and the excited electron moves to a more stable excited level, such as the bottom of the conduction band or the lowest vibrational molecular state. Applications of PL spectroscopy are quite varied. The technique is very useful in study of semiconducting materials where there is a direct band gap. In such a configuration, extremities of the conduction and valence bands have the same crystal momentum and optical transitions are momentum-allowed. Also one can use this technique semi-quantitatively for compositional analysis, trace impurity detection, spatial mapping, structural determination (crystallinity, bonding, layering), and the study of energy-transfer mechanisms. Photoluminescence spectra often reflect residual stress state of material where peak shifts arise from band movement due to lattice parameter change. Many kinds of defects produce energy states closer to the middle of the band gap than the shallow donor and acceptor states. Recombination processes involving these defect levels result in emission of longer wavelength photons. Because these defect states are localized, they have broad energy spectra. Also, these states tend to be strongly coupled to the lattice and hence have a large number of phonon replicas that often smear together into a single broad band. The PL peak intensity has received widespread attention in the study of interface and recombination. Since the recombination is a non-radiative process and band bending process usually leads to the formation of a depletion layer where PL is quenched leading to decline in intensity.[11] The schematic of the photoluminescence process is given in Figure 2.7.

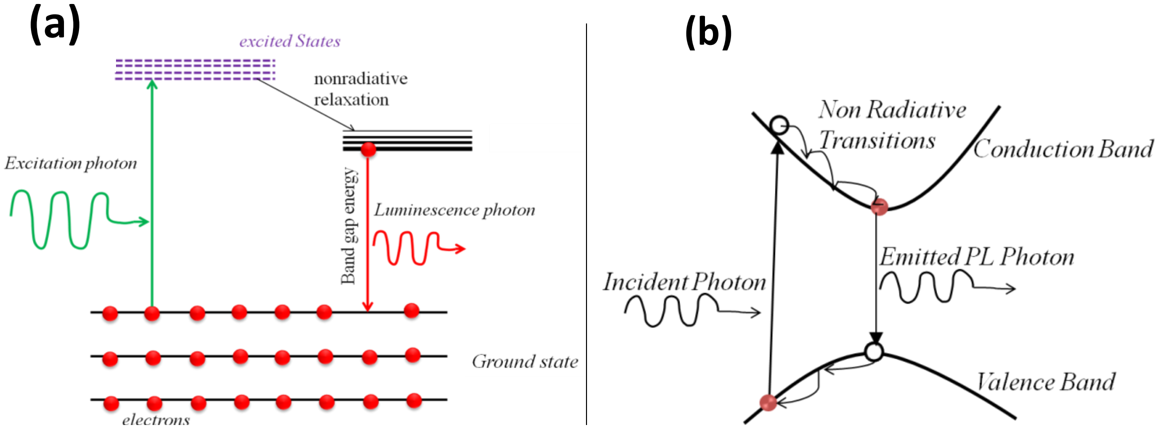

Figure 2.7: The schematic of the photoluminescence process (a) in molecules, (b) in crystals.

In the present study, the PL measurements were carried out using a Jobin Yvon-Spex make Spectrofluorometer (Fluorolog version-3; Model FL3-11) equipped with a 450 W high-pressure xenon arc lamp as an excitation source. PL excitation and emission spectra were acquired at room temperature for a spectral resolution of 0.2 nm and slit width of 0.25 mm.

2.7. Fourier Transform Infra Red Spectroscopy

Infra-red spectroscopy is an important and reliable technique to identify the presence of functional groups in a molecule.[12, 13] Depending on the elements and the type of bonds involved, molecules vibrate at various frequencies. Such molecular vibrations which according to quantum mechanics, corresponds to the ground state (lower frequency) and several excited states (higher frequency). The energy corresponding to these molecular vibrational frequencies (transitions) is around 4184 K joules/mol which matches with the infra-red region of the electromagnetic spectrum. Typically, the molecules are irradiated with the whole range of IR frequencies. The absorption occurs only at the radiation energy of specific frequencies which matches well with the vibrational frequencies of the molecules. An intensity decrease is observed for the transmitted radiation at the vibrational frequencies of the molecule in the spectrum. For a molecule to absorb IR, the vibrations or rotations within a molecule must cause a net change in the dipole moment. Either conventional dispersive infrared analysis or Fourier transform infrared spectroscopy is used for recording the spectra. Compared to the dispersive IR method, Fourier transform is faster and has better signal to noise ratio.[14] The monochromator and the slits in the dispersive IR spectrophotometers are replaced by interferometer fitted with the FTIR spectrophotometer which is mainly Michelson type.[15] The interferogram (plot of light intensity versus optical path difference) obtained from the interferometer is a measure of the temporal coherence of the light. Fourier transformations convert the time domain signal to the frequency domain spectrum and hence the name FTIR spectroscopy. Since the information at all frequency is collected simultaneously, the measurement in FTIR is faster compared to standard IR spectrometer.

In the present study, FTIR spectrophotometer (Bomem, Hartmann & Braun, Canada) was used to study surface adsorbed species and functional groups like OH.

2.8. Ultraviolet and Visible Absorption Spectroscopy

Ultraviolet and visible (UV-Vis) absorption spectroscopy deals with the measurement of the attenuation of a beam of light after it passes through a sample or after reflection from a sample surface. The attenuation can result from processes like absorbance, transmittance, reflectance and interference. The measurements are usually carried out at a single wavelength or over an extended spectral range. The UV-Vis spectral range spans approximately 190 to 900 nm. The short wavelength limit for simple UV-Vis spectrometers is the absorption of UV wavelengths <180 nm by the intervening atmospheric gases. The use of UV-Vis spectroscopy in materials research can be divided into two main categories: (1) quantitative measurements of an analyte in the liquid or solid phase and (2) characterization of the optical and electronic properties of a solid state material. The first category is most useful as a diagnostic tool to quantify various constituents of materials or their precursors or as a process method to monitor the concentrations of reactants or products during the course of a chemical reaction. In quantitative applications, it often becomes a necessity to measure the absorbance or reflectivity at a single specified wavelength. The second, more qualitative application usually requires that at least a portion of the UV-Vis spectrum used for characterization of the optical or electronic properties of materials should be accurately recorded.

For quantitative analysis, the Beer – Lambert law, which allows accurate concentration measurement of the absorbing species, is used and it is given as

$$A = \varepsilon c l \qquad (6)$$

where A is the absorbance, ε the molar absorbance or absorption coefficient (in dm^3 mol^{-1} cm^{-1}), c the concentration of the analyte in the solution (in mol dm^{-3}) and l is the path length of light in the sample (in cm). The relationship between absorbance A and the experimentally measured transmittance T is

$$A = -log\,T = -\log\frac{P}{P_0} \qquad (7)$$

where P is the radiant power (radiant energy on unit area in unit time) after it passes through the sample and P_0 is the initial radiant power, both T and A are unit less. A radiation having wavelength, at which the absorption coefficient is a maximum, is used to determine the concentrations of the solutions. This is because, the change in absorbance for a given concentration change is greater, leading to greater sensitivity and accuracy in measurement. In addition if the relative effect of other substances or impurities is smaller and the rate of change of absorbance with wavelength is lower, then the measurement will not be adversely affected by small errors in the wavelength setting. If the absorbance of a series of sample solutions of known concentrations are measured and plotted against their corresponding concentrations, the plot of absorbance versus concentration should be linear, if the Beer-Lambert Law is obeyed. This graph is known as a calibration graph. A calibration graph can be used to determine the concentration of an unknown sample solution by measuring its spectral absorbance. Since the absorbance of dilute solutions is directly proportional to concentration, this can be gainfully utilized to study reaction kinetics. The rate of change in concentration of reactants or products can be determined by measuring the increase or decrease in absorbance of the solutions with time. Plotting absorbance against time, one can determine the order of reactions with respect to the alteration in combination of reactants. However, the Beer-Lambert Law breaks down for solutions of higher concentration, yielding departure from linear behavior.

In the case of solid materials, the UV-Vis spectrum can measure the band gap and identify any localized excitations or impurities. The measurements are carried out either in the transmittance or reflectance mode. In samples, where light penetrates and initiates different processes such as reflection, refraction and diffraction, and eventually emerges out diffusively (scatters in all directions)[16], UV –Vis spectroscopy in transmission mode becomes difficult to execute. In such cases, diffuse reflectance spectroscopy (DRS), where diffuse reflected light is collected and analyzed, is adopted. This technique is based on the diffuse reflection of light by a powder or a rough sample when the sizes of the particles are comparable to the wavelength of the light. ie; 0.2- 3μm.[17] The diffuse reflectance spectra of the semiconductors can be used to determine the band gap.[18] There are different methods for determining the band gap using DRS.[19- 23] Among the various methods, Tauc plot[22, 23] is widely used to determine the band gap of the materials in which $(\alpha h\nu)^{\gamma}$ is plotted as a function of hν. The values of γ is 2 for the direct allowed transition in the case of semiconductors.[18] In the case of thick samples, the α term called, Kubelka Munk function is used to convert the diffuse reflectance measurements to equivalent absorption coefficient[24, 25] and the equation can be represented as;

$$KM = \frac{(1-R)^2}{2R} = \frac{\alpha}{S} \qquad (8)$$

KM is the Kubelka Munk function, R the ratio of the intensities of radiation reflected in diffuse manner from the sample and from the reference sample, α represents the absorption coefficient of radiation and S is the scattering factor. When the thickness of the sample is much bigger than the individual particle (ie; very small particles), S is approximately unity or it assumes a constant value. Therefore, the KM function will be almost equal to the absorption coefficient.

For different transition mechanisms, it has been proved that along the sharp absorption edge, the energy of incident photons and band gap (E_g) of a semiconductor will have the relation

$$\propto^{n} = A\left(h\vartheta - E_g\right) \quad \text{or} \qquad (9)$$

$$(\propto h\vartheta)^{\gamma} = A(h\vartheta - E_g) \qquad (10)$$

where the value of 'γ' depends on the interband transition mechanism. For indirect band gap materials, the value of γ is 0.5, ν is the frequency and h is the Planks constant.[22] Since the re-emission function (scattering factor S) is equal to the absorption coefficient according to the equation 8, the Tauc plot, (√αhν) versus hν can be replaced by (√KB*hν) versus hν.

In the present study UV visible spectrophotometer (JASCO V-650, Japan) is used for quantitative measurements of dye degradations studies. Absorbance of a series of standard solutions is plotted against respective concentrations. The absorbance of the unknown is then measured and the prepared calibration plot is used for the determination of the analyte concentration. For band gap and doping effect on band structure studies UV-Vis diffuse reflectance spectrophotometer (Shimadzu UV 2401) was used. The reflectance spectra were acquired over the wavelength span range 800 to 200 nm at a scan rate of 100 nm/s. $BaSO_4$ was used as the reference.

2.9. Temperature Programmed Desorption Reduction Oxidation

Counting the number of active metal sites on a supported catalyst surface is of particular importance, because this value is used to obtain turnover rates for reactions. The turnover rates provide an accurate measure for comparing catalytic activity of different catalysts for the same reaction[26]. Temperature programmed desorption reduction oxidation (TPDRO) is an important tool in heterogeneous catalysis to determine the number, type and strength of the active metal sites from the measurement of the amount of the adsorbed gas.[27,28] The analysis involves the sample pretreatment, chemisorption, desorption and reduction which is monitored by a thermal conductivity detector (TCD). Depending upon the type of sample, approximately 0.1 – 1 g of the material is used. The sample is kept in a quartz tube having a heating mantle. The sample is degassed thoroughly and a pulse of known amount of pure active gas is admitted and then flushed with Ar. The amount of active gas adsorbed is calculated by measuring the amount of active gas in the Ar gas coming out of the quartz tube. From the amount of the gas adsorbed, the metal surface area is calculated using the equation

$$A_{sam} = L.N_{ads}.F_s.A_{met}.10^{-23} \qquad (11)$$

where A_{sam} is the metal surface area (m^2/g of the sample), L the Avogadro number, N_{ads} the amount of gas adsorbed in pulse chemisorption (mmole/mVs), F_s the stoichiometric factor (metal mole/gas mole) and A_{met} the metal surface area (m^2/g of metal). The metal surface area can be conveniently expressed in terms of the metal weight in the catalyst (A_{met}) or to the support weight in the catalyst (A_{sup}), as

$$A_{met} = A_{sam}\left(\frac{1}{X_{met}}\right)10^2 \qquad (12)$$

where X_{met} is the metal atom percentage. Referring the metal surface area to the support weight in the catalyst (A_{sup}), the equation will be,

$$A_{sup} = A_{sam}\,\frac{10^2}{10^2 - X_{met}} \qquad (13)$$

The metal dispersion (number of adsorbing metal atoms (or moles), referred to the total number of metal atoms (or moles) that are contained in the catalyst, can be calculated using the equation:

$$D_{met} = \frac{N_{ads}\,.F_S.10.M_{met}}{X_{met}} \qquad (14)$$

where M_{met} is the metallic atomic weight in g/mole.

Hydrogen pulse chemisorption studies were carried out using TPDRO equipment model Thermo Scientific TPD/R/O 1110 (Italy) to find out the active surface area of the Pt loaded on TiO_2 nanotube powders.

2.10. Brunauer Emmet Teller adsorption method

A highly dispersed solid when exposed to a gas or a vapor at a definite pressure in a closed container at a given temperature, adsorbs gas via monolayer adsorption followed by multilayer adsorption and capillary condensation.[29] At a low pressure, a monolayer of the gas is formed on the surface and as the pressure increases, excess gas is adsorbed to form multilayers. The adsorption phenomena follow the following equation:

$$\frac{1}{X[\left({}^{P_0}/_{P}\right)-1]} = \frac{1}{X_m} + \frac{C-1}{X_m C}\left(\frac{P}{P_0}\right) \qquad (15)$$

P/P_0 is the relative gas pressure and C is a constant related to the strength of the interaction between the gas and the solid, X the amount of gas adsorbed and X_m is the monolayer adsorbed gas quantity. This equation is called Brunauer Emmet Teller (BET) adsorption equation[30] and can be plotted as a straight line as $\frac{1}{X[\left(P_0/_P\right)-1]}$ versus $\frac{P}{P_0}$. The value of the slope and the intercept are used to calculate the monolayer adsorbed gas quantity. From this, the total surface area (S_{total}) and specific surface area (S) can be calculated as

$$S_{total} = \frac{X_m.N.s}{M} \qquad (16)$$

$$S = \frac{S_{total}}{w} \qquad (17)$$

where N is the avogadro’s number, s adsorption cross section. M refers to molecular weight of the adsorbate and ‘w’ is the weight of the solid sample.

The surface areas of the samples used in the present study were measured by BET adsorption method using a commercial BET apparatus (Sorptomatic 1990, Thermo Electron Corporation, US), using nitrogen gas as an adsorbate.

2.11. Field Emission Set up

The schematic of the field emission set up used in the present study is given in Figure 2.8. The field emission experiments were carried out in a high vacuum chamber having pressure of about 10^{-7} mbar. The samples under investigation are mounted on a conducting copper plate by means of silver paste (for proper contact). A flat cut mirror polished molybdenum rod of 3.0 mm diameter was used as the anode. The anode is connected to the positive terminal of a high voltage source (~2 kV) and the other terminal to the conducting copper plate. The gap between the cathode and the anode is kept in the range 20 to 100 μm using the micrometer and subsequently measured using a travelling microscope. The FE current derived from a specific surface area is indirectly measured from the voltage drop across the resistor, while applying the voltage to the anode in steps and the corresponding current density versus electric field graph is plotted.

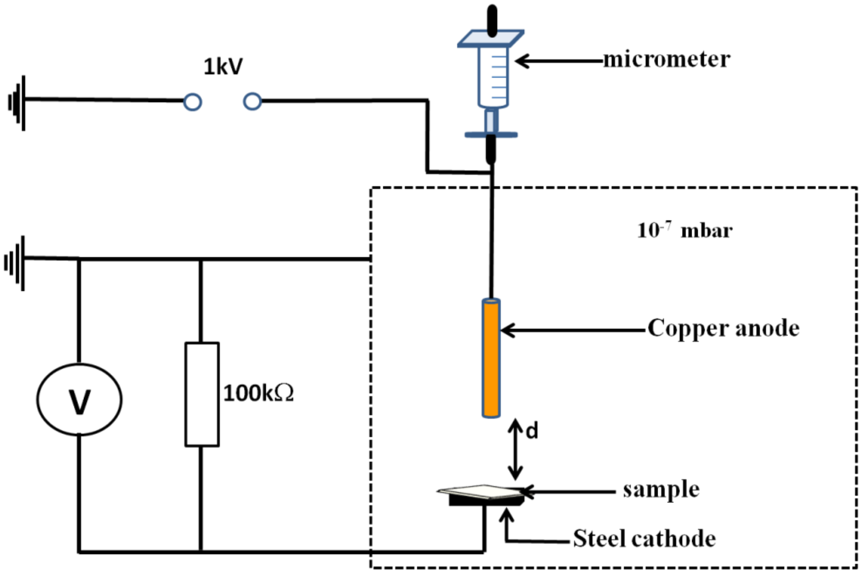

Figure 2.8: Schematic of circuit diagram of field emission set up.

2.12. Contact Angle Set up

Contact angle can be defined as the angle between the tangent to the liquid/air interface and the tangent to the solid/air interface. The measurement can be used for investigating the surface wettability of the material of interest by a specific liquid. Water contact angle experiments of the samples in the present study were carried out in an ambient environment using a contact angle meter equipped with a CCD camera (Holmarc, HO-IAD-CAM-01, India). The sessile drop method was used for the contact angle measurements. Analysis of the shape of a drop of test liquid placed on the sample is the basis for this method. Distilled water was used as the water source and the volume of the water droplets dispensed was approximately 2-3 μl. The image of the droplet which is in contact with the sample surface is captured using the CCD camera. From these images, the contact angles were measured using Image J software.

2.13. Photocatalytic Hydrogen Generation Set up

The photocatalytic hydrogen generation experiments were performed in a 150 ml quartz flask at ambient temperature. Schematic of the experimental set-up is shown in Figure 2.9. A light source, positioned at a specific distance away from the reactor, was used for irradiating the sample during experiments. Before the commencement of the experiment, the catalyst in the quartz flask was properly dispersed by ultrasonication. The quartz flask was then connected to the experimental set-up and argon gas was bubbled through the reaction mixture for 15 minutes to remove dissolved oxygen and to ensure that the reaction system is under anaerobic condition.

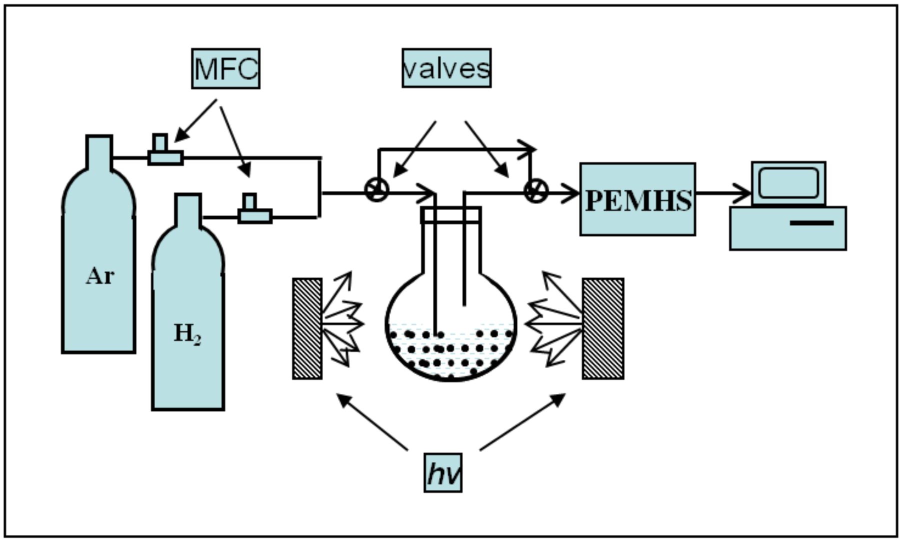

Figure 2.9: Schematic of the experimental setup used for hydrogen generation studies

Argon flow was stopped and the quartz vessel was isolated from the gas flow line by closing the inlet and outlet valves. The reaction mixture was then irradiated with light source of specific wavelength and power for a given time duration and flushed with Ar gas. After this, the quartz vessel was isolated and irradiated for 30 of minutes. After the 30 minutes irradiation, the gas generated over the reaction mixture was carried over to the calibrated polymer electrolyte membrane based H_2 meter (PEMHM) for H_2 analysis.[31, 32] Any H_2 generated produces a peak and the amount of H_2 generated, was estimated from the peak area. The measurements were carried out repeatedly. The sensor was calibrated prior to the measurements using standard Ar + H_2 gas mixtures. The reactor temperature was maintained at 298 ± 2 K by means of a cooling fan.

Conclusion

This chapter provides brief overview of synthesis and characterization techniques adopted for carrying out research on nanotubular arrays and powders of TiO_2 and their doped variants. The microscopic imaging and spectroscopic characterization tools employed are described. The basic principles of the experimental techniques used to demonstrate the application potential of the synthesized nanomaterials are also given.

References

---

[1] Goldstein, J.; Newbury, D.; Joy, D.; Lyman, C.; Echlin, P.; Lifshin, E.; Sawyer, L.; Michael, J., Scanning Electron Microscopy and X-Ray Microanalysis, , Kluwer Academics/ Plenum Publishers, 3rd Ed., New York, 2003

[2] Williams, D. B.; Carter, C. B., Transmission Electron Microscopy**, ,** Plenum Press, New York, 1996

[3] Cullity, B. D.; Stock, S. R., Elements of X-ray Diffraction, Prentice Hall, Upper Saddle River (2001)

[4] Scherrer, 1918 P. Gottinger Nachrichte 2, 98**.**

[5] Harris, D.C.; Bertolucci, M.D.; Symmetry and spectroscopy: an introduction to vibrational and electronic spectroscopy, Oxford University Press (1978)

[6] Herzberg, G, Molecular Spectra and Molecular Structure II: Infrared and Raman Spectra of Polyatomic Molecules, Krieger Publishing (1991)

[7] J. C. Vickerman, Surface analysis – the principal techniques, John Wiley & Sons (1997).

[8] J. F. Moulder, W. F. Stickle, P. E. Sobol and K. Bomben, Handbook of X-ray Photoelectron Spectroscopy, Physical Electronics Inc., Eden Prairie, USA (1992)

[9] D. Briggs and J. T. Grant, *Surface Analysis by Auger and X-ray Photoelectron Spectroscopy*, Eds., IM Publications, Chichester, 2003 ISBN: 1-901019-04-7

[10] Dean, P.J., *Prog. Crystal* Growth *Charact.* 5,89,1982.

[11] Chang, R. R.; Iyer, R.; Lile, D. L., *J. App. Phys.* 1987, *61* (5), 1995-2004.

[12] Barnes, R. B.; Bonner, L. G., *J. Chem. Edu.* **1937,** *14* (12), 564.

[13] Maas, J.H. Vander, (1972), *Basic Infrared Spectroscopy*. Second edition. London: Heyden & Son Ltd.

[14] Smith, B.C., (1996). *Fourier Transform Infrared Spectroscopy*. Boca Raton: CRC Press Inc.

[15] Perkins, W. D., *J. Chem. Edu.* **1986,** *63* (1), A5.

[16] Perkampus, H. H., *UV-VIS spectroscopy and its applications*. Springer-Verlag: Berlin; New York, 1992; p ix, 244 p.

[17] Weckhuysen, B. M., in Spectroscopy of transition metal ions on surfaces, Weckhuysen, B. M., Van Der Voort, P., Catana, G., (Eds.),Leuven University Press, (2000), p. 221.

[18] Radecka, M.; Rekas, M.; Zakrzewska., *Trends. Inorg. Chem.* **2006,** 46, 81-126.

[19] Martínez-Castañón, G. A.; Sánchez-Loredo, M. G.; Dorantes, H. J.; Martínez-Mendoza, J. R.; Ortega-Zarzosa, G.; Ruiz, F., *Mater. Lett.* **2005,** *59* (4), 529-534.

[20] Nowak, M.; Szperlich, P.; Bober, Ł.; Szala, J.; Moskal, G.; Stróż, D., *Ultrason. Sonochem.* **2008,** *15* (5), 709-716.

[21] Macyk, W.; Burgeth, G.; Kisch, H., *Photochem. Photobiol. Sci.* **2003,** *2* (3), 322-328.

[22] Tauc, J., *Materials Research Bulletin* **1970,** *5* (8), 721-729.

[23] Tauc, J.; Grigorovici, R.; Vancu, A., *physica status solidi (b)* **1966,** *15* (2), 627-637.

[24] Murphy, A. B., *Appl. Opt.* **2007,** *46* (16), 3133-3143.

[25] Kubelka, P., Part I. *J. Opt. Soc. Am.* **1948,** *38* (5), 448-448.

[26] Boudart, M.; Mariadassou, G. D.; *Kinetics of Heterogeneous Catalytic Reactions*, 1984, Princeton University Press

---

[27] Baiker, A., Experimental Methods for the Characterization of Catalysts. II. X-Ray Diffraction, Temperature-Programmed Desorption and Reduction, Thermogravimetry and Differential Thermoanalysis, International Chemical Engineering, Vol. 25, No. 1, (1985).

[28] Paul, A. W., Introduction to Chemical Adsorption Analytical Techniques and their Applications to Catalysis, MIC Technical Publications, January 2003, http://www.micromeritics.com/repository/files/intro_to_chemical_adsorption.pdf

[29] Gregg, S. J.; Sing, K. S. W., *Adsorption, surface area, and porosity*. 2nd ed.;
Academic Press: London ; Toronto, 1982; p xi, 303 p.

[30] Brunauer, S.; Emmett, P. H.; Teller, E., *J. Am. Chem. Soc* **1938,** 60, (2), 309-319.

[31] Guo, J. W.; Zhao, T. S.; Prabhuram, J.; Wong, C. W., *Electrochim. Acta* **2005,** *50* (10), 1973-1983.

[32] Ramesh, C.; Murugesan, N.; Krishnaiah, M.; Ganesan, V.; Periaswami, G., *J. Solid State Electrochem.* **2008,** *12* (9), 1109-1116.

Chapter 3

Synthesis and Characterization of Pristine and Nitrogen doped TiO_2 Nanotube Arrays by Potentiostatic Anodization

Titanium dioxide is one of the most studied semiconductor materials because of its unique electronic and photocatalytic properties which lead to its use in photo-electrochemical applications such as dye sensitized solar cells, environmental remediation, hydrogen generation by water photolysis, and antifogging and self cleaning surfaces. As one of the important requirements for efficient photo-catalysis is large surface area, synthesis of nano-scale TiO_2 *has drawn the attention of scientists. For many applications, nano-scale* TiO_2 *is used either as isolated nanoparticles (e.g., suspensions) or as compacted or sintered nanoparticles. Recently, one dimensional nano-structures such as nanorods, nanowires, nanobelts and nanotubes have been shown to achieve enhanced photocatalytic performance. Among the one dimensional nanostructures, nanotubes are preferred because of their large surface area. In applications where alignment, high aspect ratio and directional electron transport properties play a major role, vertically aligned nanotube arrays are of great interest. An important drawback of* TiO_2 *for photocatalysis is that its band-gap is rather large, 3.0–3.2 eV, and thus only 5% of the solar spectrum (*$\lambda < 380$ *nm, corresponding to the UV region) is absorbed. It has been reported by various research groups that the threshold excitation energy can be lowered to the visible light regime by N-doping. The present chapter deals with the synthesis and characterization of vertically aligned pristine and N-doped* TiO_2 *nanotube arrays in thin film form. Of the various techniques available for the synthesis, an electrochemical technique is adopted in the present study as it is easy to use and the tube aspect ratio can be controlled by controlling just one electrochemical parameter, voltage, which can be controlled in nano-volt levels, thereby achieving extremely high control over synthesis.*

3.1. Introduction

Titania is a wide band gap semiconducting functional material which finds application in photo electrolysis, photo catalysis, dye sensitized solar cells (DSSCs), electro chromic devices and gas sensors.[1-5] In DSSCs, TiO_2 nanoparticles, coated on a conducting substrate, on to which suitable organic dyes (sensitizer) were adsorbed, forms the photoactive electrode, which convert solar energy into electrical energy. The TiO_2 nanoparticles act as the electron transporting semiconducting material. However, the low electron diffusion coefficient in TiO_2 nanoparticles due to the presence of defects, surface states and grain boundaries reduces the conversion efficiency[6] . In order to obtain better conversion efficiency, attention have been turned towards synthesis of one dimensional nanostructures like nanotubes[7], nanorods[8] and nanowires[9], as these are expected to have better electron transport properties because of their directional nature. Among the one-dimensional nanostructures, nanotubes are preferred because of their high surface area.

Various techniques such as sol gel[10], hydrothermal[11] and chemical vapor deposition[12] are reported for the synthesis of TiO_2 nanotubes. A limiting factor of these techniques is that, the synthesized nanotubes were not aligned and hence possess different directionality, which limits the efficiency of specific devices fabricated using them. In order to improve the conversion efficiency, efforts were directed towards synthesis of aligned nanotubes. For the first time in 1999, in an attempt to synthesize vertically aligned TiO_2 nanotube arrays (TNTA) by anodizing titanium foil in chromic acid / HF solution, Zwilling et al[13] obtained porous TiO_2 nanostructures. In 2001, Gong et al synthesized self organized TNTA by anodic oxidation of pure titanium foil in an aqueous solution containing 0.5 to 3.5 wt% hydrofluoric acid.[14] It was observed that the tube length, diameter and wall thickness could easily be controlled by varying the electrochemical parameters. Subsequent to this, nanotube arrays were synthesized anodically in acidic electrolytes like H_2SO_4 / HF and acetic acid / HF.[15, 16] But the lengths of the nanotubes obtained were limited to a maximum of ~500 nm. The limiting length was attributed to increase in the electrochemical chemical dissolution of TiO_2 at the low pH of the electrolyte. In order to synthesize nanotubes of higher aspect ratio, effect of electrolyte composition, pH, applied voltage and anodization time on nanotube formation were studied out by several groups[17-19]. From their experimental results, it was found that nanotubes of lengths up to several hundred micrometers were obtained in organic electrolytes such as ethylene glycol, glycerol, formamide or DMSO along with NH_4F, NaF or KF instead of HF.[20-27] Among the various organic electrolytes identified, vertically aligned smooth walled nanotube arrays with maximum length could be obtained when ethylene glycol / H_2O / NH_4F was used as electrolyte. Studies on the effect of potential, time and electrolyte composition on tube morphology in ethylene glycol / H_2O / NH_4F electrolyte are reported by Prakasam et al[18] and Gong et al.[14] aboveSimultaneously studies were carried out to understand the mechanism of nanotube formation during anodization.[28, 29] From their results it was commonly accepted that field assisted chemical oxidation of Ti to TiO_2, field assisted chemical dissolution of Ti and TiO_2 as $[TiF_6]^{2-}$ due to the localized chemical etching of TiO_2 surface by F^- ions are the main processes that takes place during nanotube formation. However, reports on systematic studies elucidating the voltage limits and optimum voltage ranges for tube formation as well as effect of anodization time and electrolyte composition, under optimum voltage are scarce. Taveira et al[25] carried out preliminary studies on stoichiometry of TNTA, obtained in glycol / H_2O / NH_4F medium. However, reports on detailed stoichiometric analysis are not available.

Even though the anodization of Ti foil in glycol / H_2O / NH_4F medium resulted in smooth walled self organized TNTA on Ti foil, these possess certain limitations in specific applications such as DSSCs as it requires back side illumination which reduces light to electrical energy conversion efficiency. In addition, when used in electronic devices like sensors, the Ti metal substrates on which the TiO_2 nanotubes are formed cause short circuits. Therefore, further researches were carried out to develop TNTA by anodizing Ti thin films deposited on various substrates such as conducting glasses and silicon.[30-32] Mor et al developed TNTA thin films of ~20 to 30 nm tube length by anodizing Ti thin films on glass, silicon and alumina, in acetic acid and HF containing media.[33,29] Fabrication of TNTA by anodizing Ti thin films is not an established process as the quality of Ti thin films plays a major role in obtaining nanotube arrays. The morphology and lattice orientations of Ti films are very much dependent on substrate. The deposition process, deposition temperature, stress mismatch between the substrate and the film and film thickness determine the film quality. Once the desired quality films are achieved, the selection of electrolyte for anodization is the important factor for obtaining sufficiently long TiO_2 nanotubes. Earlier studies have used aqueous medium containing HF as an electrolyte, which limited the growth of tubes to few hundred nanometers. In 2009, Oomman et al reported that high aspect ratio well ordered TNTA thin films can be synthesized on FTO coated glasses, using fluoride ion containing organic electrolyte like ethylene glycol.[34]

An important drawback of TiO_2 for photocatalysis is that its band-gap is rather large, 3.0–3.2 eV, and thus only 5% of the solar spectrum ($\lambda < 380$ nm, corresponding to the UV region) is absorbed. To lower the threshold energy for photoexcitation, a great deal of research was focused on doping TiO_2 with both transition metal cations and anions. Doping with transition metal cations has shown both positive and negative effects.[35-39] Indeed, several authors have reported that although cation doping decreases the photo threshold energy of TiO_2, these may also serve as recombination centers for electrons and holes, thus reducing the overall photocatalytic efficiency.[36, 37] Also, cation doping might shift the conduction band below the red-ox potential of the adsorbate, rendering the material inactive for photocatalysis. Hence doping with N, S, C and B anions which introduce p-states above the valence band maximum were considered.[40-44] Among the anions, N is found to be more promising.[45] Substitution of O^{2-} ions by N^{3-} ions is more effective due to their similar sizes and electro negativities.[46] Because of the comparable ion size, the lattice distortion will be less and hence large numbers of recombination centers will not be generated. It has been indicated from theoretical calculations that by N-doping the electronic band structures of TiO_2 are modified by the N-2p – O-2p hybridization and consequent delocalization resulting in the upward shift of the valence band.[47] Density functional theory calculations indicate that substitution of oxygen by nitrogen atoms in TiO_2 can create isolated localized N 2p states above the O 2p dominant valence band.[48-53] Also the mixing of N2p with O2p is less pronounced if N substitutes the O sites. It has been reported that the band structure modification depends on doped nitrogen concentration and band narrowing can occur when doping levels reach a critical concentration of ~20%, as in the case with anatase $TiO_{2.}$ The possible electronic structural changes that occur on N-doping are given in a recent review by Qiu and Burda[54] and the same is given in chapter 1. Various groups have demonstrated the superiority of N-doped TiO_2 from the view point of photocatalytic activity[55-57], surface hydrophilicity[58], and photo induced carrier response [59] under visible light illumination. In view of the above, synthesis of vertically aligned N-doped TNTA thin films is of paramount importance.

N-doped vertically aligned TNTA were synthesized by various techniques viz. annealing in ammonia atmosphere at ≥ 550 ^{o}C[60], plasma nitriding[61], ion implantation followed by annealing[62], wet immersion in ammonia solution followed by annealing under ambient conditions[63] and anodization of Ti foils in electrolytes containing nitrogen precursors.[64,65] Annealing in NH_3 and plasma nitriding of TNTA resulted in N-incorporation as interstitial nitrogen, N_i. Wet immersion followed by annealing led to the formation of both substitutional (N_O) and interstitial nitrogen (N_i), with higher N_i content. Ion implantation was found to lead to amorphization which was overcome by subsequent annealing at 450 °C. The chemical state of nitrogen in ion implanted and annealed samples were primarily N_O. Thus among the above two-step synthesis processes, ion implantation followed by annealing is the one which gave primarily N- substituted TNTA films. However, in view of large scale synthesis, the technique is cost intensive and operationally difficult. The single step, cost effective and easy to operate technique is anodization. Su et al[64] prepared N-incorporated TNTA by anodizing Ti foils in $C_2H_2O_4.2H_2O$ + NH_4F electrolyte. The nanotube arrays upon X-ray photoelectron spectroscopic (XPS) analysis, were found to comprise primarily of interstitial nitrogen, N_i, with very little amount of N_O. Shankar et al[65] synthesized N-doped TNTA, where nitrogen substituted oxygen from the anion sub-lattice. This was achieved by anodizing Ti foils in 0.07 M HF solutions containing varying amount of NH_4NO_3 at a pH of 3.5. However, the tube lengths were limited to 400 nm.

The present chapter deals with synthesis of pristine and N-doped TNTA, by potentiostatic anodization, as well as studies on morphology, structure and composition with respect to various process parameters. The first part of the study include synthesis, mechanism of nanotube formation, effect of temperature on morphology and crystallinity of TNTA, effect of electrolyte composition on tube aspect ratio and detailed compositional analysis by using XPS. This is followed by synthesis of transparent TNTA thin films by anodizing Ti films, grown on FTO coated glasses by RF magnetron sputtering. Anodization was carried out in organic electrolyte medium containing NH_4F. The last part of the chapter discusses the electrochemical synthesis of N-doped TNTA films with different nitrogen concentrations. The N-doping, with different concentration, was achieved by having different concentrations of urea as nitrogen precursor in the electrolyte.

3.2. Experimental

3.2.1. Synthesis

3.2.1.1. Fabrication of Pristine TNTA on Ti foils.

Titanium metal foils (10 mm X 10 mm X 1.5 mm) (Alfa Esar) sonicated in ethanol, acetone and thoroughly washed with distilled water, were anodized in ethylene glycol containing 0.5 wt% ammonium fluoride and 2.5wt% of water, using platinum as the cathode. The electrodes were kept 1.5 cm apart. A potentiostatic anodization was conducted at different voltages viz 5, 10, 20, 30, 40, 50, 60 and 70 V. Anodization was done by ramping up to the specific end potentials with a ramping speed of 1 V/s and holding it for two hours at room temperature. Anodization was also performed as a function of time at constant voltage (40V) at room temperature. The time dependent anodization current was recorded with a computer controlled multimeter (model HP 34401A). The pH of the electrolyte was measured using a pH meter. After each anodization the samples were sonicated in ethanol and then dried in nitrogen stream.

3.2.1.2. Fabrication of transparent TNTA on FTO coated glasses

3.2.1.2.1. Titanium Thin film Deposition:

Titanium thin films, of ~1 micrometer length, on FTO coated glasses were prepared by RF magnetron sputtering (MECA–2000, France). The sheet resistance of the FTO coated glass substrates was 22 Ωcm^{-2}. The chamber was pumped down to a base pressure of 10^{-6} mbar using a turbo molecular pump. Prior to deposition, the substrate was cleaned in situ by Ar^+ ion bombardment and degassed at 300º C. A 4N pure Ti disk with diameter of 50 mm was used as the target, magnetron sputtering was carried out at an operating RF power of 300 W. Target to substrate distance was kept at 100 mm. A constant argon flow of 20 sccm at a constant pressure of 1 x 10^{-2} mbar was maintained throughout deposition. The films were deposited on conducting glass slides at a substrate temperature of 300^0 C. With these conditions, a deposition rate of 20 nm/min could be obtained. The deposited film adherence was checked by scotch tape test.

3.2.1.2.2. Anodization:

The Ti films on FTO glasses were anodized in a two electrode configuration as described in section 3.2.1.1using 0.5wt% of NH_4F, 2.5 wt% of water in ethylene glycol. The samples were anodized at 40 V. The duration of anodization was varied as 1, 2, 3 and 4 hours to check the dissolution of Ti layer during anodization. Anodized thin films were washed in ethanol thoroughly and dried in flowing nitrogen stream.

3.2.1.3. Fabrication of N doped TNTA.

For simultaneous nitrogen doping the Ti foils were anodized in the ethylene glycol / H_2O / NH_4F electrolyte containing 0.1, 0.2 and 0.3 wt% urea under potentiostatic condition as explained in section 3.2.1.1. The effect of anodization voltage on tube morphology was studied for optimizing the process voltage. All the samples were anodized for 2 hours. The variation of current density with anodization time was also recorded.

3.2.2. Characterization

The surface morphology and composition of the anodized foils and thin films were analyzed using Field Emission Scanning Electron Microscope (FESEM) (FEG Quanta, Philips, Netherlands) having EDAX facility. From the partial lift off of the nanotube layer, the cross sectional images were taken and the thickness variations were calculated. To analyze the presence of functional groups like hydroxyl species, FTIR spectra of TiO_2 nanotubes were acquired using FTIR spectrophotometer (Bomem, Hartmann & Braun, Canada). The nanotube arrays were mechanically removed from the Ti substrate and mixed with KBr powder (1% w/w) and pelletized by applying 6 N for 5 minutes. The transparent pellets were introduced into the FTIR spectrophotometer and scanned in the range of 4000 to 400 cm^{-1} with a resolution of $4cm^{-1}$. The composition and non-stoichiometry of the as prepared as well as annealed TNTA were determined by XPS measurements using M/s SPECS (Germany) ESCA instrument. Al Kα was used as the X-ray source at energy of 1486.74 eV. The anode was operated at a voltage of 13kV and source power level was set to 300 W. An Ar^+ ion source is also provided for sputter-etch cleaning of specimens. It was operated at 5 kV and 50 µA. The system sputters approximately at a rate of 10 A^o per minute. This value varies depending on the sample. Spectra were collected using the PHOIBOS 150 MCD-9 analyzer with a resolution of 0.67 eV for 656 kcps at band pass energy of 12 eV. The spectrometer was calibrated using a standard silver sample. Data were processed by Specslab2 software. The binding energy of C 1*s* core level from contaminant C at 285 eV was used as the reference to account for any charging of the sample and the peak positions were compared to standard values for identification of different elements and their respective oxidation states. The crystal structure of the samples was analyzed by X-ray diffraction (XRD). The XRD pattern of the samples were compared with the JCPDS file 21-1272 and 21-1276 corresponding to anatase and rutile phases, respectively. The crystallite sizes of the as prepared samples were calculated using Scherer formula.[66]

$$t = K\lambda \,/\, BCos\theta \qquad (1)$$

K refers to a dimensionless constant having value 0.9. λ=1.5406 A^o and θ is the diffraction angle in radians. Broadening *B* was calculated by taking the full width half maximum of the diffraction peak corresponding to each plane in the diffraction pattern. In the case of N-doped TNTA, in addition to XRD, Raman scattering measurements were carried out using Micro Raman Spectrometer (Renishaw, UK), equipped with a confocal microscope with an "argon ion laser" operating at 514.5nm. This was carried out to confirm the purity of the N-doped sample. Optical characterization of the samples was done by UV-Vis diffuse reflectance spectrophotometer (Shimadzu UV 2401) to obtain the band gap. The reflectance spectra were taken over a range of 800 to 200 nm at a scan rate of 100 nm/s. $BaSO_4$ was used as the reference.

3.3. Results and discussions

3.3.1. Pristine TiO_2 Nanotube Arrays

3.3.1.1. Mechanistic and morphological analysis

From the reported literature on the synthesis of TNTA in aqueous and organic electrolytes, anodization of Ti foils in ethylene glycol / H_2O / NH_4F electrolyte with the composition 2.5 wt% H_2O and 0.3 to 0.5 wt% NH_4F, was found to give smooth walled tubes with maximum growth rate[18]. Hence, in the present study ethylene glycol / H_2O / NH_4F electrolyte of composition 2.5 wt% H_2O and 0.5 wt% NH_4F was chosen and anodization was carried out as a function of applied potential to delineate the optimum potential range for the synthesis of smooth walled nanotube arrays. This was followed by studies on the effect of anodization time, at a selected potential in the optimum potential range, on tube morphology to arrive at optimum time scale. At the selected potential and time, the effect of electrolyte composition was studied, first by changing the concentration of H_2O at fixed NH_4F concentration of 0.5 wt% and then by changing the NH_4F concentration at the observed optimum H_2O

concentration. As the effect of NH_4F concentration below 0.5 wt% is reported, [18] the effect of concentration above 0.5 wt% was studied. Figure 3.1 depicts the typical variation of current density with time which occurs during anodization.

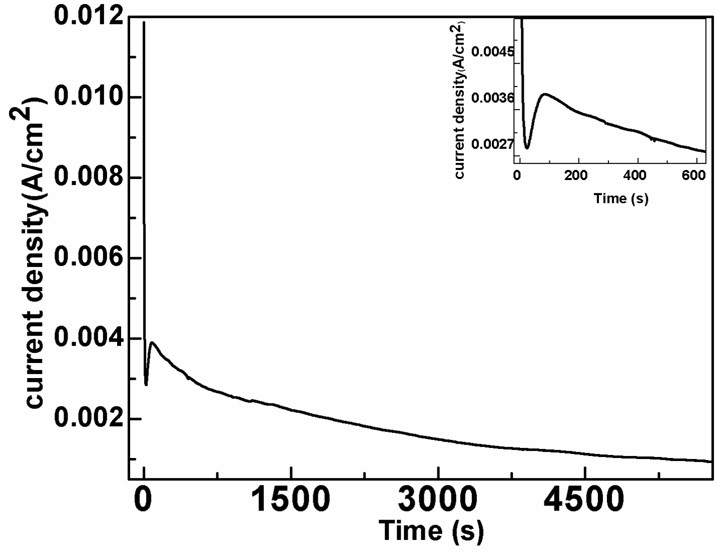

Figure 3.1: Potentiostatic transient obtained during the anodization process, inset shows the variation in the current density at the initial stages of nanotube formation

The transient can be explained as the non ideal case of potentiostatic transient where surface reactions make the deviation from ideal behavior. This deviation explains the formation of nanotube. The main electrochemical reactions taking place during anodization are formation of barrier oxide layer on Ti substrate due to reaction with oxygen generated by electrolysis of water present in the electrolyte, field assisted chemical etching of Ti as well as TiO_2 by fluoride ions to form pits on the substrate, attack of fluoride ions as well as H_3O^+ ions on these pits where the field is very high, and evolution of H_2 at the Pt electrode. Since anodization was carried out in organic medium (ethylene glycol containing 0.5 wt% ammonium fluoride and 2.5 wt% of water) the pH was ~7±0.1.

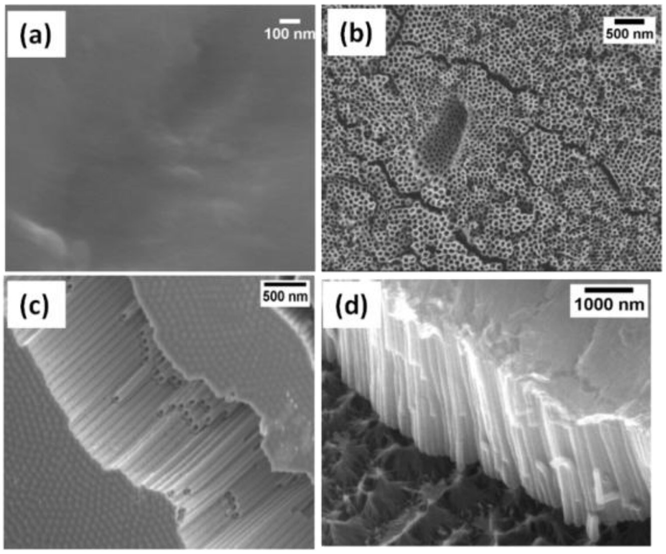

Figure 3.2a-d: (a) SEM image of Ti foil before anodization. (b) SEM image of Ti foil after anodization (reveals the formation of nanotube). (c) and (d) Micrographs showing the closed ends (bottom end) and cross sectional view of nanotubes respectively.

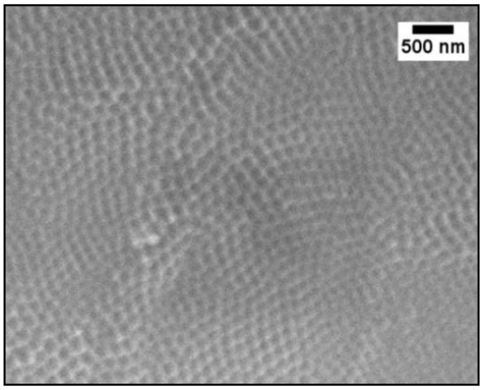

Figure 3.3: Template pattern of Ti Foil after anodization.

It is reported in the literature that in acidic electrolytes like HF or HCl, the rate of chemical dissolution is high and the nanotube length is restricted to a few hundreds of nanometers[15]. The rate of dissolution is determined by the localized concentrations of H^+ and F^- ions nearer to the bottom end of the nanotube, where electrochemical reaction proceeds leading to the continuous growth of the nanotube. Correlating with the current density versus time graph, the mechanism of the nanotube formation can be explained as follows. Initially, when Ti metal is subjected to anodization, a passive oxide layer is formed, according to the reaction:

$$Ti + 2H_2O \longrightarrow TiO_2 + 4H^+ + 4e^- \qquad (2)$$

The initial sharp decrease in the current density is due to the formation of this barrier oxide layer. By this reaction, H^+ ions are generated at the electrolyte / metal oxide interface. At the same time, in the presence of the H^+ ions, the fluoride ions nearer to the substrate will react with TiO_2 as well as Ti metal to form $[TiF_6]^{2-}$ complex according to the reactions:

$$TiO_2 + 6NH_4F + 4H^+ \longrightarrow [TiF_6]^{2-} + 2H_2O + 6NH_4^+ \qquad (3)$$

$$Ti + 6NH_4F \longrightarrow [TiF_6]^{2-} + 6NH_4^+ \qquad (4)$$

Both H^+ and F^- ions enhance the rate of chemical dissolution at the interface resulting in increase in current density. The simultaneous chemical oxidation and chemical dissolution, assisted by the field (E= V/d, where V is the applied voltage and d the thickness of the oxide layer), occurring at the active area, will move the metal oxide/metal interface as well as the electrolyte/metal oxide more inside the metal substrate. After some time the current density approaches a constant value signifying steady state / equilibrium between the competitive oxidation and dissolution reactions. The variation in current density with time is depicted in inset of Figure 3.1. Since the anodization is carried out at constant potential, the field generated should be uniform throughout, i.e.; the active area should have equifield surface. The shape acquired by the active area should be hemispherical in order to satisfy the equifield concept. If the active area would have square or any other geometry the field will not be uniform and will be maximum at the corners thereby increasing the chemical dissolution rate at the corners. This will prevent the continuous growth of nanotubes. The irregularity in the current density observed at the initial stage indicates that the active area is rough and therefore the field is not equivalent everywhere. At steady state the rough surface transforms into an equifield surface (hemispherical shape) because of attainment of equilibrium between the oxidation and dissolution reactions.

Figure 3.2 (a) and (b) shows the SEM image of the Ti foil before and after anodization respectively. From the figure it is clear that anodization process has resulted in nanotube formation. Figure 3.2(c and d) represents the SEM image of the backside (bottom) of the nanotube arrays and the cross section, respectively. The backside view of the nanotube arrays reveals that the nanotubes are having closed ends. Figure 3.3 shows the periodically arranged dimple morphology of Ti substrate after removing the nanotube layers by ultrasonication. The closed ends of the nanotubes and the patterns observed on the titanium sheets after removing the nanotube layers reveal that the bottom end of the nanotube is always hemispherical confirming the equifield mechanism. As illustrated by various researchers,[26,67,68] the nanotube formation is the result of steady state equilibrium between field assisted chemical dissolution and field assisted chemical oxidation reactions.

3.3.1.2. Effect of electrochemical parameters in the aspect ratio of the TNTA.

3.3.1.2.1. Effect of Voltage

The surface topography of Ti foils anodized at different potentials varying from 5 to 70V for 2 hrs, in room temperature is given in Figure 3.4(a-h). When the applied potential was 5V, formation of nanotubes was not observed. At 10 V, porous structures were formed on the Ti surface, but no distinct nanotubes were observed. However, formation of distinct nanotubes having inner diameter ~55nm was observed, from the SEM image, when the applied potential was 20V. The above observation indicates that there is a minimum required potential for the formation of self-organized nanotubes. Under the present experimental conditions, the minimum required potential for the formation of nanotubes is around 20 V. Gong et al reported 10 V as the lowest required potential for the formation of nanotubes in aqueous medium containing HF as an etching agent.[14] The difference in the required minimum potential can be attributed to the low electrical conductivity of the organic electrolyte. In the present study formation of self aligned nanotube arrays were observed up to 60 V. Figure 3.5 shows the cross sectional FESEM images of the nanotube arrays grown at different voltages. The variation of inner diameter of the nanotubes with applied potential is depicted in Figure 3.6a. The increase in tube diameter with voltage can be attributed to the enhanced chemical dissolution of TiO_2 at the pore wall. The variation of tube length with applied potential is shown in Figure 3.6b. When the potential is increased, rate of chemical dissolution and oxidation increases resulting in nanotube growth. When the applied potential was 70 V, the current density increased with time and nano-tubes were not observed on the foil even after two hours of continuous anodization. This is attributed to the enhanced rate of chemical dissolution at high potentials. It has been shown that the break down period or the time for loss of passivation decreases with increase in temperature, electrolyte concentration and the presence of fluoride ions.[69] In the present case, with the increase in voltage, current increased raising the bath temperature leading to enhancement in chemical dissolution rate. From SEM images, it is seen that smooth walled nanotube arrays, ideal for specific applications,[70] are obtained in the range 30 to 50 V.

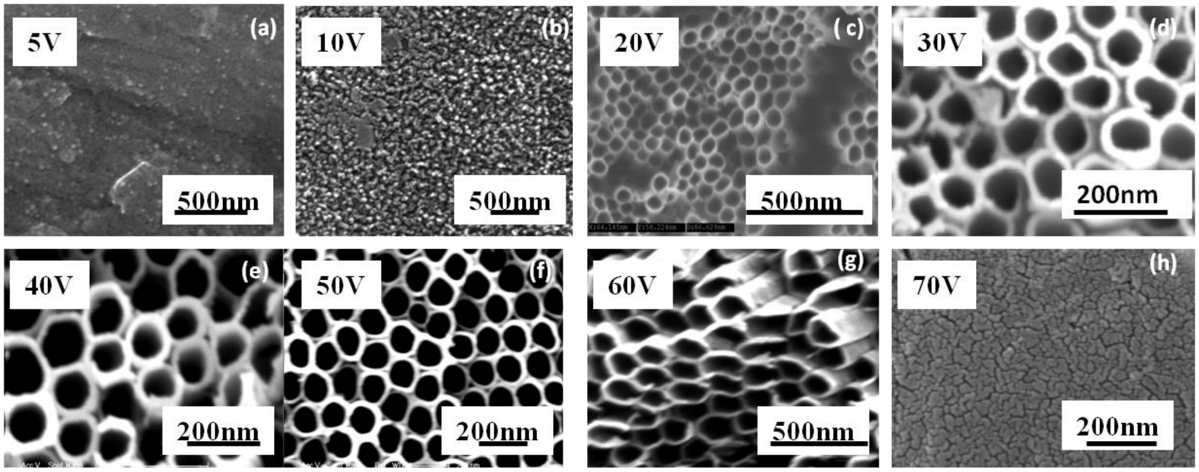

Figure 3.4a-h: FESEM images of nanotube arrays grown at different voltages (a) 5V, (b) 10V, (c) 20V, (d) 30V, (e) 40V, (f) 50V, (g) 60V and (h) 70V.

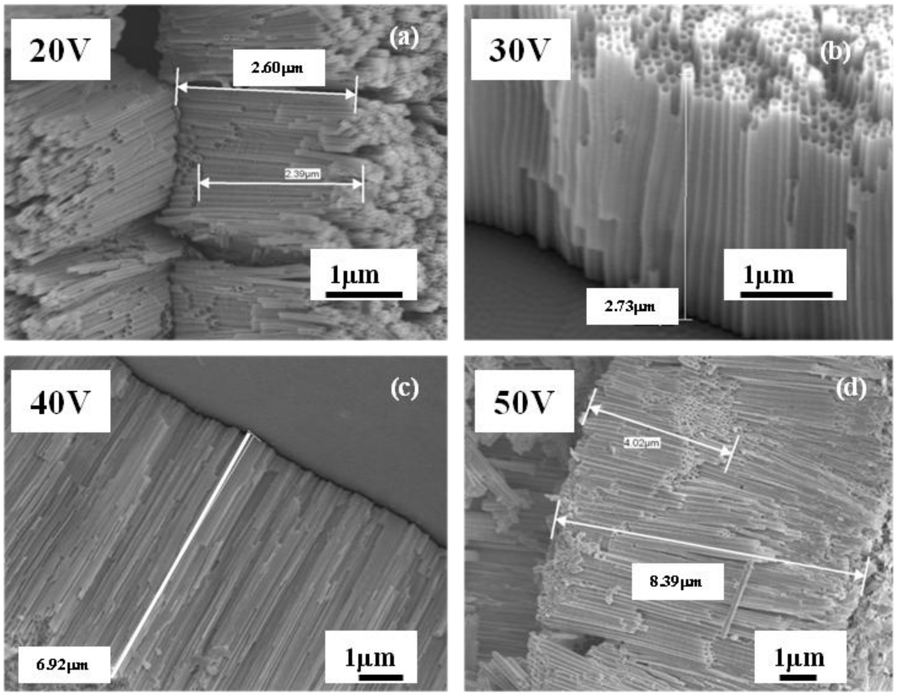

Figure 3.5a-d: Cross section of nanotube arrays grown at different voltages (shows the variation in tube length with the applied voltage). (a) 20V, (b) 30V, (c) 40V and (d) 50V

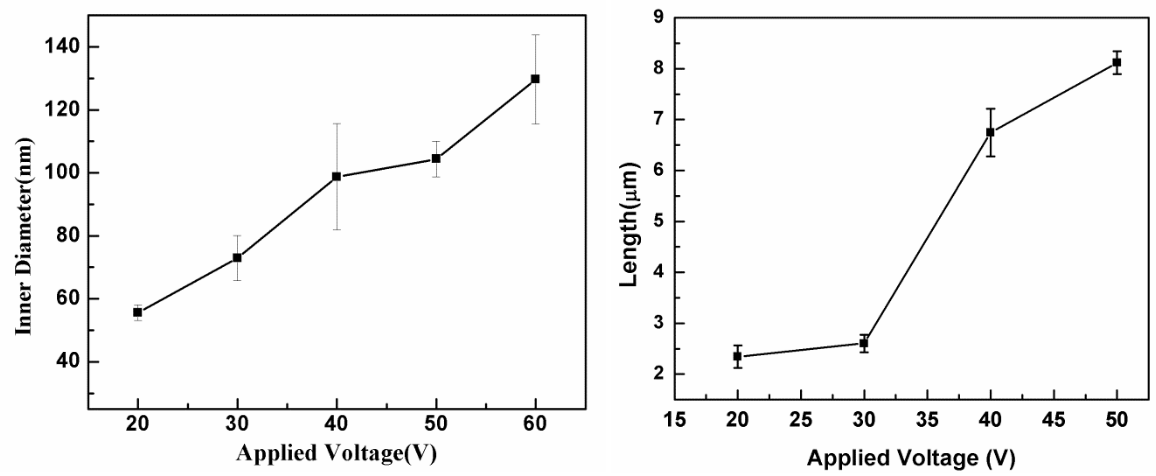

Figure 3.6a-b: (a) Variation of inner pore diameter of the nanotubes with voltage, (b) Variation of nanotube length with applied voltage

3.3.1.2.2. Effect of Anodization Time

The changes in the morphological parameters with anodization time were investigated by anodizing at 40 V at various time intervals, keeping all the other parameters similar. Variation in surface morphology with time can be seen from the FESEM images given in Figure 3.7(a-l). In the initial stages of anodization, the Ti surface transformed to a rough surface which gradually changed to porous like structure and eventually converted to nanotubular morphology. The formation of distinct nanotubular structure of ~1 micro meter length, from the porous structure, occurred at around 20 to 25 minutes. Formation of well separated nanotubes could be discerned after 1 hour of anodization. From the above observations, it is unambiguous that the morphological parameters such tube diameter and length can be tuned by adjusting anodization time, keeping all other parameters same. Compared to anodization in aqueous media, nanotubes of ~1 micro meter length were obtained in the organic media within 25 minutes. This is because of the decrease in the chemical dissolution rate at neutral pH. For application in photo catalysis

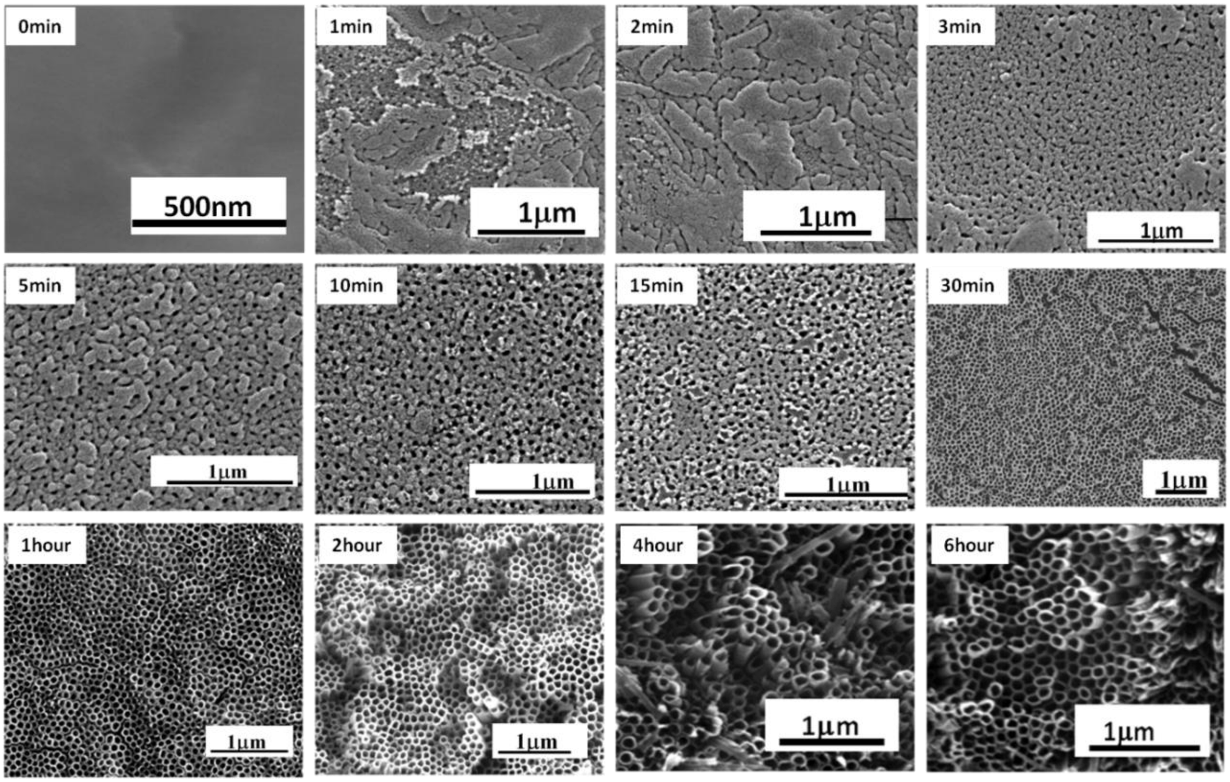

Figure 3.7a-l: FESEM images showing the variation of surface morphology of Ti metal with the anodization time showing the formation of nanotube arrays. (a) 0 minute, (b) 1 minutes, (c) 2 minutes, (d) 3 minutes, (e) 5 minutes, (f) 10 minutes, (g) 15 minutes, (h) 30 minutes, (i) 1 hours, (j) 2 hours, (k) 4 hours and (l) 6 hours

and solar cells, since the diffusion length plays a major role, tuning the length of the nanotubes with time and voltage is of paramount importance.

3.3.1.2.3. Effect of Electrolyte Composition

To study the effects of electrolyte composition on tube formation, anodization was carried out at various water and ammonium fluoride concentrations in ethylene glycol.

3.3.1.2.3.1. Effect of water

Experiments were performed to elucidate the effect of water content keeping the ammonium fluoride concentration a constant (0.5 wt %). The anodization experiments were carried out at 40 V for two hours. Figure 3.8(a-c) depicts the morphology of Ti anodized at water contents of 2.5, 10 and 20 wt%. An increase in tube diameter with increase in water content was observed. As the water content increased, number of H^+ ions per unit area at the electrode increased resulting in higher chemical dissolution rate and hence changes in current density. This resulted in the formation of ripple like structure on the wall of the nanotubes. The observed tube diameters are 77 ±7 nm (2.5wt% water), 97 ±14 nm (10wt%water) and 152 ±16 nm (20wt%water). Formation of ripple like structure on the walls of the nanotubes was observed in excess of 5 wt% of water and that increased with water content. When the water content was 20 wt%, the system behaved almost like an aqueous medium and the rate of chemical dissolution increased leading to nanotube arrays having ripples on the tube walls. The above observations indicate that the water content affect tube wall morphology as well as diameter. When the water content was low, smooth walled TiO_2 nanotubes, ideal for specific applications where the electron transfer efficiency should be higher, could easily be grown.

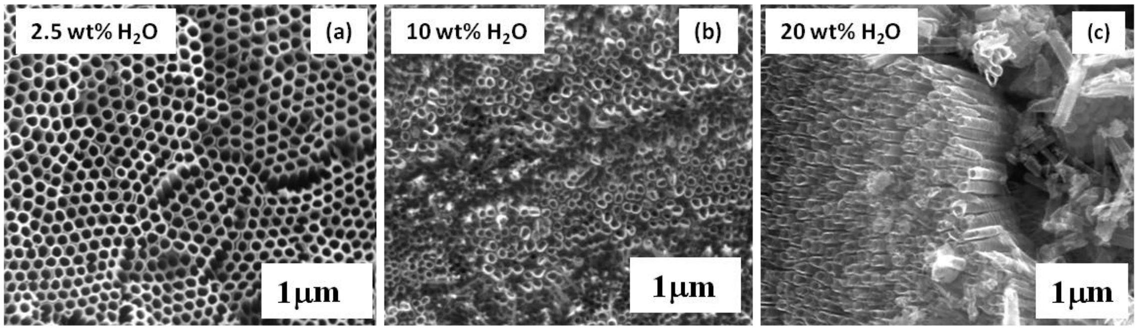

Figure 3.8a - c: Surface morphology of the anodized Ti foils at different weight percent of water. (a) 2.5 wt%, (b) 10 wt% and (c) 20 wt%

3.3.1.2.3.2. Effect of ammonium fluoride

The concentration of ammonium fluoride was varied from 0 wt% to 5 wt% in the electrolytic bath keeping the water content at the optimum level (2.5 wt %) determined from the experiments described in the previous section. The applied potential and anodization time were kept at 40V and 2 hours respectively. Figure 3.9(a-e) shows the SEM images of the surface anodized at different concentrations of NH_4F.

Anodization in fluoride free solutions resulted in the formation of compact oxide layer without nanotubes. When the NH_4F concentrations were 0.5, 1, 2 and 5 wt%, nanotube formation was observed, indicating the need of fluoride ions for the formation of self organized TiO_2 nanotubes. Even though nanotube formation was observed at 0.5, 1 and 2 wt % of NH_4F, homogenous nanotubes were observed only at 0.5 wt%. At higher concentrations of NH_4F, the nanotube arrays were covered with grass like structures which might have formed due to the removal of nanotubes from the substrate. In the case of anodized Ti, where the fluoride ion concentration was 5 wt%, distinct tubular structures were not observed (Figure 3.9e).

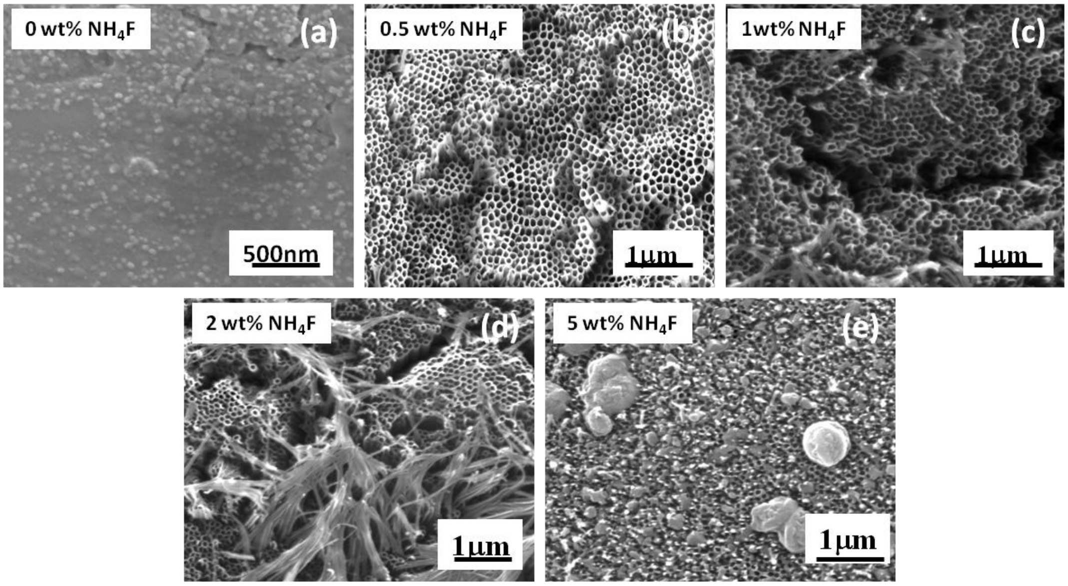

Figure 3.9a-e: Surface morphology of the anodized Titanium samples at different weight percent of NH_4F. (a) Ti surface anodized without adding NH_4F, (b) 0.5 wt%, (c) 1 wt%, (d) 2 wt% and (e) 5 wt% of NH_4F.

No substantial change in tube length or diameter could be discerned with the change in concentration. The observed diameters are, 77 ± 7nm (0.5 wt% NH_4F), 86 ± 9nm (1wt % NH_4F) and 80 ± 7nm (2 wt% NH_4F). Based on these results and those reported in the literature[18], NH_4F content in the range 0.2 to 0.5 wt% can be considered as the optimum range for obtaining smooth walled nanotube arrays.

3.3.1.3. Effect of annealing temperature on crystallinity and morphology:

The as prepared samples, upon XRD analysis, were found to be amorphous and hence annealed at various temperatures to study evolution of phases as different phases of the material are preferred for specific applications. The XRD pattern of the as prepared TNTA as given in Figure 10a shows amorphous nature which is in agreement with the results obtained by Oomman et al.[71] The observed peaks correspond to Ti substrate. In order to study the evolution of phases, the as prepared nanotube arrays were annealed in air at 400, 500, 600 and 700 ^{o}C for 2 hours and the corresponding XRD patterns were recorded. Figure 3.10b shows the XRD pattern of the annealed samples. At 400^{o}C, there were peaks corresponding to tetragonal anatase phase of TiO_2 in addition to the substrate peak. When the samples were annealed at 500^{o}C, the anatase peaks got sharpened and intensified indicating increase in anatase phase crystallinity and crystallite size. The observed low intensity peak (27.4^{o}) corresponding to rutile phase indicates the beginning of phase transformation. The XRD pattern of the sample annealed at 600^{o} C revealed the presence of both rutile and anatase phases. At 700^{o}C, anatase and rutile phases were still present but with higher concentration of rutile phase. The phase transformation behavior observed here was slightly different from those reported by Oomman et al[71], where phase transformations took place at higher temperatures. These changes can be attributed to the difference in the heating rate and annealing duration.

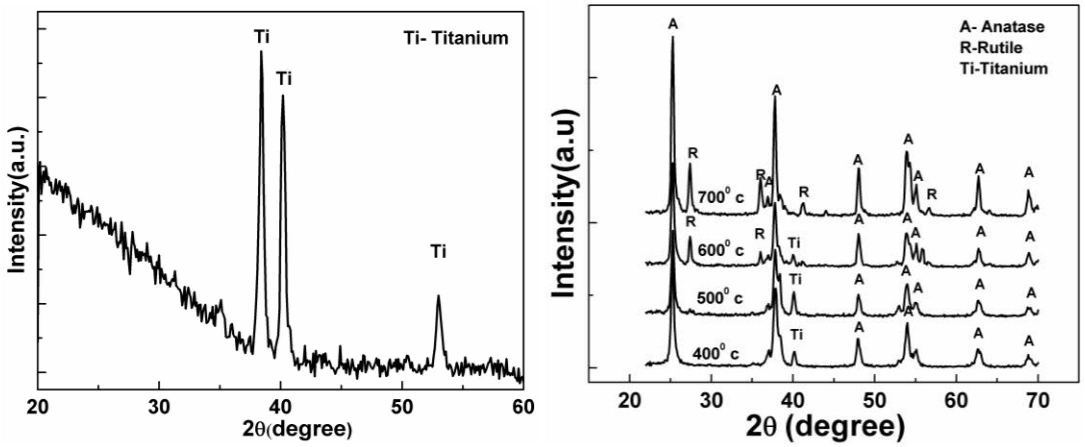

Figure 3.10a-b: (a) XRD pattern of the as prepared TiO_2 nanotubes (shows that the samples are amorphous). b. XRD pattern of TiO_2 nanotubes annealed at different temperature

In order to verify the effect of temperature on tube morphology, FESEM analysis of the nanotube arrays were carried out. Figure 3.11(a-d) and 3.12(a-c) show the surface morphology and cross sectional views, respectively, of the nanotube arrays annealed at different temperatures, clearly depicting the effect of calcination temperature on tube morphology. From the surface topography, it is clear that the samples annealed at 400 and 500 ^{o}C, retains their tubular architecture. Whereas, the samples annealed at 600 and 700^{o}C have tubes with closed mouth, due to wall thickening. However, the cross sectional view clearly indicate retention of tubular morphology even up to 700 ^{o}C.

The occurrence of anatase to rutile phase transformation at 500 to 600 °C as inferred from XRD results and can be correlated with the SEM images. Phase transformation from anatase to rutile requires crystal reorientation and growth[72] and is achieved with increase in temperature. It has been reported that phase stability, crystal growth and nucleation are dependent on crystallite size.[73] Below 14 nm anatase is the stable phase.[73] In our study, the crystallite size of the nanotube arrays annealed at the lowest temperature (400^{o}C) is ~48 nm, and therefore is prone to phase transformation. Gouma et al in 2001 investigated the defect mechanism of phase transformation in vacuum and hydrogen reduced TiO_2 samples.[74] The anatase to rutile transformation involves the breakup of anatase structure with a volume change of about 8%. This collapse occurs by the deformation of the oxygen frame work and shifting of the Ti^{4+} ions by rupturing two of the six Ti-O bonds to form new bonds[73] and hence the phase transformation is affected by the presence of hydroxyl ions chemisorbed on the TiO_2 surface. Figure 12d illustrates the variation of anatase crystallite size with annealing temperature. The 101 diffraction peak of the anatase phase is considered here for the crystallite size calculation. While increasing temperature from 600°C to 700°C there is a drastic change in the crystallite size variation which evidently depicts the increase in crystal growth kinetic rate in this temperature range. Hebrard and Nortier investigated the effect of hydroxyl species in the sintering and crystallite growth of TiO_2 powders and found that surface diffusion of hydroxyl species is the most likely rate limiting step of the particle growth in case of anatase TiO_2 powder.[75]

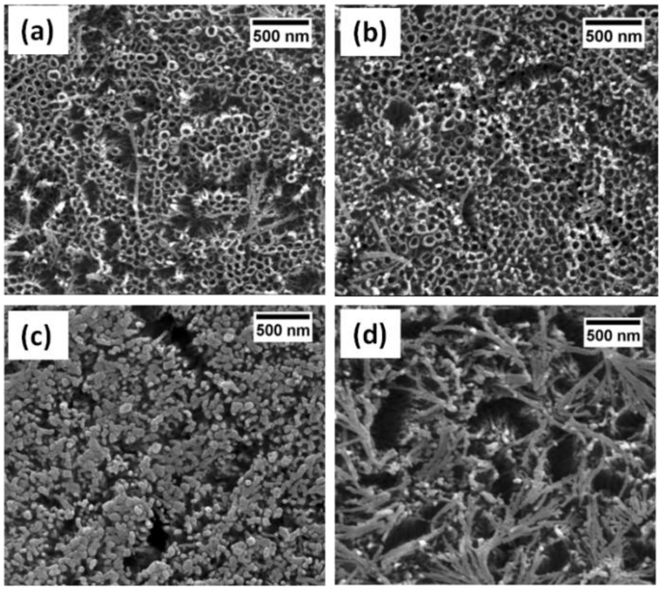

Figure 3.11a-d: SEM images showing the surface morphology of annealed TNTA (a) at 400°C (b) at 500°C (c) at 600°C and (d) at 700°C

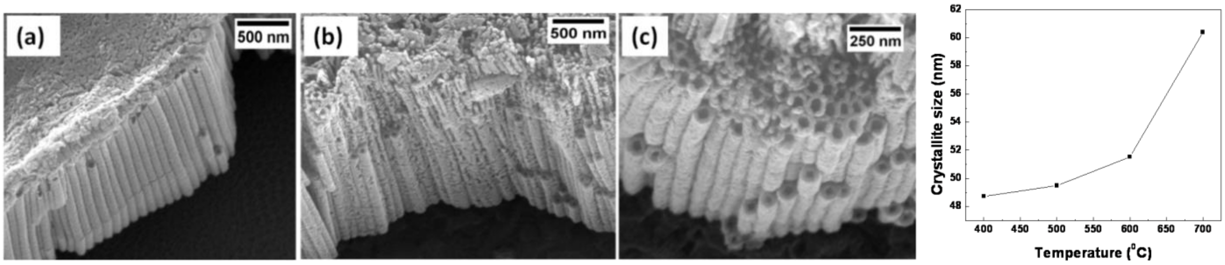

Figure3.12a-d: SEM images showing the cross sectional views of annealed TNTA (a) at 400°C (b) at 600°C and (c) at 700°C and (d) Variation of anatase crystallite size with temperature.

The increase in oxygen and titanium ion diffusion rate is due to the presence of hydroxyl species on the TiO_2 surface. The presence of surface OH groups was clearly identified by XPS measurements which will be discussed in the section 3.3.1.4. The diffusion process creates annihilation of cation and anion vacancies thereby facilitating the crystal growth. An increase in the crystallite size of anatase phase TiO_2 will enhance the rutile phase transformation rate and occurs by consuming the anatase crystallites present at the nanotube walls. As the process continues, complete transformation occurs leading to the destruction of the tubular morphology and there by generating thick rutile films.[71]

Based on the above results, the optimum process parameters for obtaining smooth walled, homogenous vertically aligned TNTA on Ti foils, at room temperature, are 30 – 50 V anodization potential, 2 hours anodization time, electrolyte composition of 0.5 wt% NH_4F and 2.5 wt% H_2O in ethylene glycol. Anatase TNTA are obtained by annealing the samples at 400 °C.

As transparent TNTA films are required for application in devices like DSSCs, for better efficiency, the same were also prepared by anodizing Ti thin films deposited on FTO coated glasses.

Titanium thin films of good adherence were obtained by RF magnetron sputtering at an RF power of 300 W and substrate temperature 300°C. The film adherence was checked with scotch tape test and found to be adherent. The deposition rate and film thickness were found to be 20 nm/min and ~1 micrometer respectively. Based on the obtained optimum process parameters for the synthesis of TNTA on Ti foils, anodization of Ti thin films grown on FTO coated glasses were carried out at 40V in 0.5wt% NH_4F + 2.5wt% water + ethylene glycol. The potentiostatic transients obtained are similar to the one obtained in the case anodization of Ti foils indicating prevalence of similar nanotube formation mechanism. The FESEM images of the samples anodized at different time intervals (2, 3 and 4 hours) are given in Figure 3.13a-c. From figure 3.13 it can be discerned that 2 hours of anodization resulted in comparatively debris free nanotubular architecture having mean tube diameter of 60±7nm.

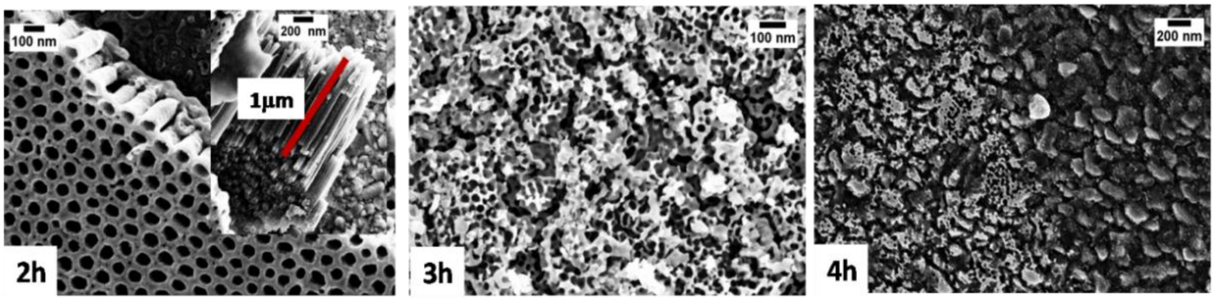

Figure 3.13a-c: FESEM image of the samples anodized at 40V by anodizing at different time intervals ie; (a) 2, (b) 3 and (c) 4 hours.

It is evident from the SEM images that with increase in anodization time precipitates were formed leading to nanotube collapse. At the end of 4h, scales like features were observed (Figure 3.13c). From the above it can be said that under the present experimental conditions transparent TNTA thin films on FTO coated glasses are obtained on anodizing Ti films in ethylene glycol medium containing 0.5wt% NH_4F and 2.5wt% water for duration of 2h. The as prepared TNTA on FTO glasses were amorphous and upon annealing at 400^oC, these samples got crystallized to anatase phase as in the case TiO_2 nanotubes grown on foils.

3.3.1.4. X-ray photoelectron spectroscopic analysis

The composition and the types of oxygen species (lattice O (Ti^{4+}- O), O (Ti^{3+}-O, i.e oxygen near an oxygen vacancy), OH and H_2O) present in the as prepared as well as annealed TNTA were studied by using XPS. Based on the results of FESEM and XRD, TNTA and transparent TNTA films on FTO coated glasses having best morphology were obtained on anodizing Ti foils and Ti films in ethylene glycol medium containing 0.5wt% NH_4F and 2.5wt% water at 40V for 2h. Hence these samples were chosen for XPS studies. Among annealed samples those annealed at 400 ^oC were chosen as they have intact tubular morphology with good anatase phase crystallinity. Stoichiometric TiO_2 consists of Ti^{4+} and O^{2-} ions. It is well understood that TiO_2 synthesized by various techniques exhibits nonstoichiometry and it varies with synthesis technique.[76] Figure14a shows the high resolution XPS spectra of Ti 2p core levels of as prepared TNTA on Ti foil. From the spectra, it can be seen that the core level of Ti $2p_{1/2}$ and Ti $2p_{3/2}$ peak positions are at 465. 3 and 459.4 eV, respectively, and is assigned as Ti^{4+} peak, with a peak separation of 5.9 eV. The peaks are asymmetric indicating the presence of lower valent Ti ions. In order to distinguish the Ti ions of different valancies peak fitting of the spectra were performed using XPS fit software. The electron background correction was carried out using Shirley (nonlinear) background correction method[77] which is commonly accepted and widely used one among the various background correction methods.[77,78,79] For the background correction, the energy window chosen was 468.17 to 452.57eV. The background corrected spectra were fitted by assuming Gaussian profiles for different chemical states. The parameters which define the XPS core level peaks are peak position or binding energy, full width at half maximum (FWHM), peak area and peak intensity. The Ti^{4+} 2p spin orbit components have to confirm the energy difference of 5.7 eV for Ti $2p_{1/2}$ and Ti $2p_{3/2}$ states[80] and intensity ratio of 0.5. The energy difference between the spin orbit components of Ti^0 is fixed as 6.15 eV.[81] By intricate peak fitting process the spectra have been resolved into eight spin orbit components resolved at $2p_{3/2}$ binding energies 459.45, 458.38, 457.44, 454.76 eV and their corresponding $2p_{1/2}$ components (465.28, 464.31, 463.04, 460.72 eV) which are assigned as Ti^{4+} (TiO_2), Ti^{3+} (TiOOH), Ti^{3+} (co-ordinatively unsaturated i.e Ti^{3+} adjacent to oxygen vaccancy) and Ti^0 (Ti), respectively. The binding energy values agree with the reported values.[82-84] Although some studies show the presence of Ti^{2+} in their analysis[82, 84], in the present study, the existence of Ti^{2+} state was not identified. The low intensity peak at 454.76 eV corresponding to Ti^0 is from the Ti substrate as the oxide film formed was highly porous and cracked.

Different types of oxygen species (lattice O, oxygen near an oxygen vacancy, OH and H_2O) present are distinguished by the different O1s binding energies. Figure15a shows the deconvoluted O 1s spectrum of the as prepared TNTA. The asymmetric peak was deconvoluted to three components with minimum chi square by the same peak fitting process, where the window for the peak fitting process was 536 to 526 eV. The peak positions, 530.67 (Ti^{4+}-O), 531.16 (Ti^{3+}-O i.e. oxygen near an oxygen vacancy) and 532.3 eV (Ti-OH/OH^-), agree well with reported literature values.[82] The peak corresponding to the binding energy value of 532.29 reveals the presence of $Ti(OH)_xO_y$ and is supported by FTIR analysis where, the presence of hydroxyl group is revealed.

The XPS analyses were also performed at the Ti/TiO_2 interface. TNTA were peeled off from the Ti substrate and the XPS analysis was carried out at that region. Figure14c shows the deconvoluted XPS spectra at the interface (Ti/TiO_2). The presence of Ti^{2+} at the metal/oxide interface can be attributed to the partial oxidation of Ti metal during electrochemical anodization. Since peak corresponding to Ti^{2+} could not be seen in the deconvoluted Ti 2p spectra of nanotube arrays, it can be inferred that as one moves from metal / oxide to oxide / electrolyte interface, the atomic fraction of Ti^{2+} decreases. The trend is reflected in the O1s spectra too (Figure 3.15c). The amorphous TiO_2 film grows at the Ti/oxide and oxide/electrolyte interfaces by the simultaneous inward and outward migration of anions and cations, respectively. As Ti^{2+} ions migrate towards the film/electrolyte interface, these are oxidized to higher valent states by the incoming oxide ions and therefore Ti^{2+} ions are not observed at the film surface. In view of the above and at any point of time, the TiO_2 films formed will be oxygen deficient and depict nonstoichiometry.

The as prepared amorphous TiO_2 nanotubes, upon annealing at 400 ^{o}C, were transformed to anatase phase. Figure14b shows the deconvoluted Ti2p spectra of annealed nanotube arrays. The spectra were deconvoluted and resolved into six spin orbit components at $2p_{3/2}$ binding energies 459.49, 458.58, 457.44 eV and their corresponding $2p_{1/2}$ components (465.28, 464.09, 463.165) which are assigned as Ti^{4+} (TiO_2), Ti^{3+} (TiOOH) and Ti^{3+}(coordinatively unsaturated i.e Ti^{3+} adjacent to oxygen vacancy). Peak corresponding to Ti^{0} (substrate) was not observed as the substrate got oxidized during annealing. However, peak corresponding to Ti^{3+} state was identified as indicative of the presence of oxygen vacancies. Figure 3.15b shows the deconvoluted oxygen 1s spectra of the annealed TiO_2. The peaks observed are located at 530.73(Ti^{4+}-O), 531.24(Ti^{3+}-O) and 532.10 eV (Ti-OH/OH^{-}). To verify the stoichiometry, the atomic ratios (concentrations) were calculated from the peak areas by taking into account the relative sensitivity factors for individual elements, since the area under the curves doesn't directly give the atomic ratio. From the high resolution Ti-2p, O-1s spectra the atom fractions of Ti and O were calculated using the following equations

$$X_{Ti} = (I_{Ti-2p}/S_{Ti})/\,[(I_{Ti-2p}/S_{Ti}) + (I_{O-1s}/S_{O})] \qquad (5)$$

$$X_{O} = (I_{O-1s}/S_{O})/\,[(I_{Ti-2p}/S_{Ti}) + (I_{O-1s}/S_{O})] \qquad (6)$$

Table 3.1 shows the fraction of different ‘Ti’ and ‘O’ species present at the surface as well as at the metal – oxide interface of the as prepared and annealed TiO_2 nanotubes. An excess of O at the surface compared to the stoichiometric composition of TiO_2, arises due to the presence of $Ti(OH)_xO_y$ species like $Ti(OH)_3$, $Ti(OH)_2O$ and $Ti(OH)_4$.

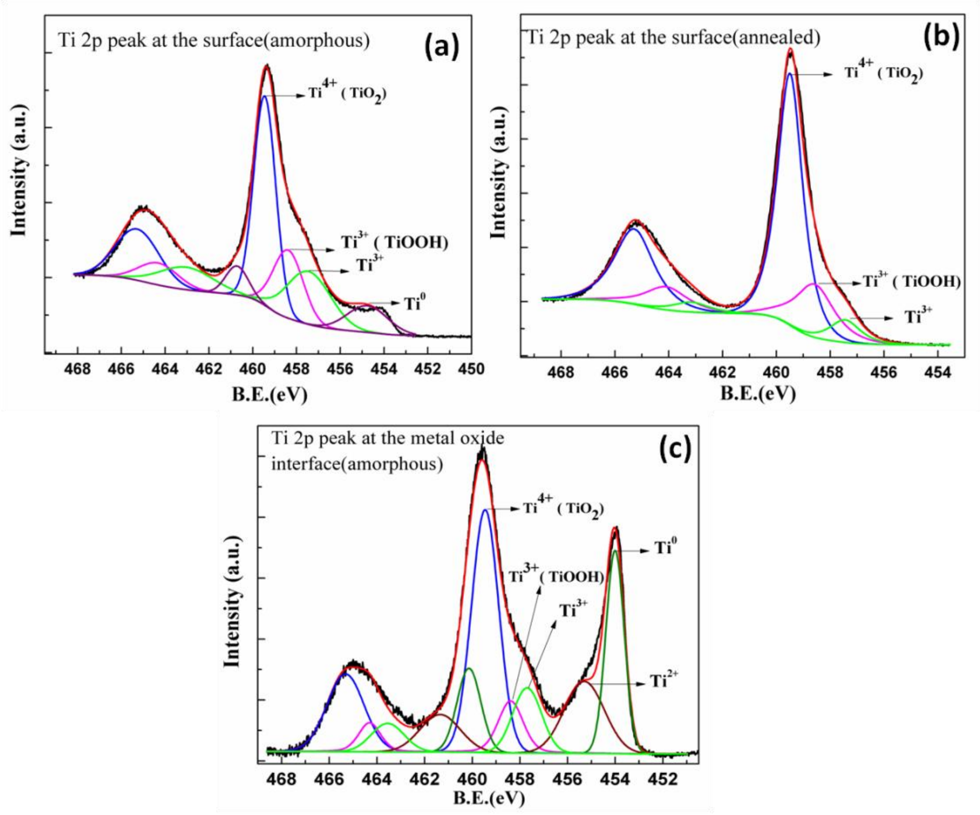

Figure 3.14a-c: Deconvoluted high resolution Ti 2p spectra (a) at the surface, (b) nanotube arrays annealed at 673K and (c) at the interface (Ti/TiO_2), as prepared.

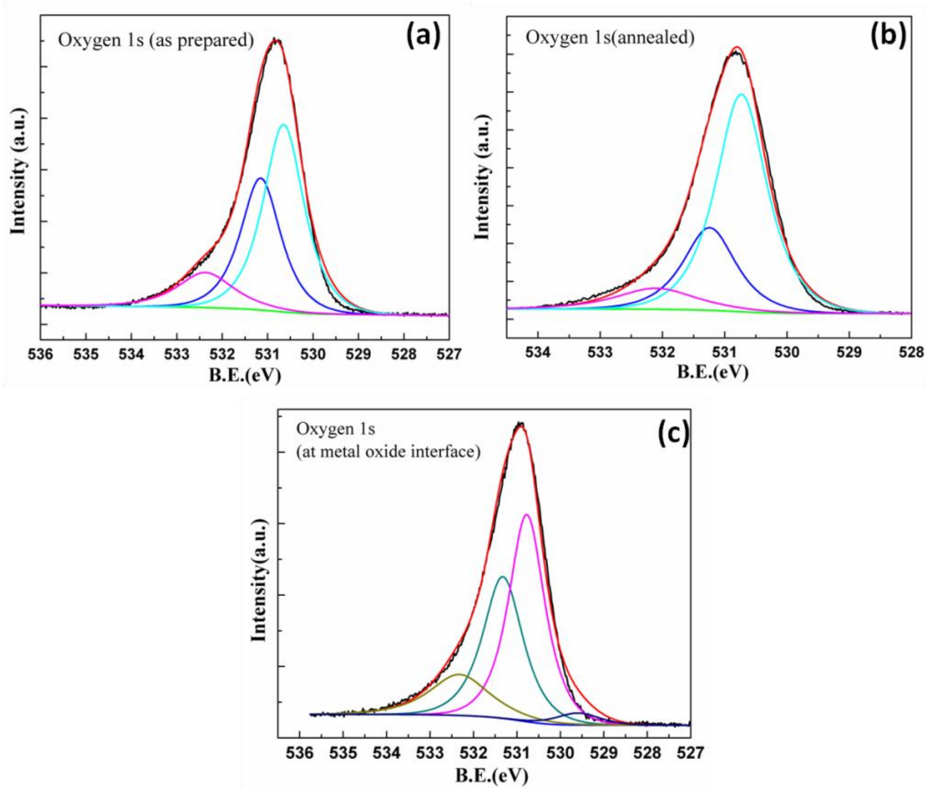

Figure 3.15a-c: Deconvoluted high resolution O1s spectra (a) at the surface (amorphous TiO_2), (b) of nanotube arrays annealed at 673K and (c) at the metal-oxide interface.

Chemical state	Atom fraction at the surface (amorphous)		Atom fraction of Ti at the Interface (amorphous)		Atom fraction of Ti (annealed at 673K)	
	Ti	O	Ti	O	Ti	O
Ti^{4+}	0.154	0.360	0.127	0.355	0.221	0.444
$Ti(OH)_xO_y$	0.065	0.099	0.029	0.098	0.072	0.066
Ti^{3+}	0.079	0.241	0.037	0.272	0.024	0.172
Ti^{2+}	-	-	0.058	0.023	-	-

Table 3.1: Fraction of Ti species and O species present at the surface and the interface of the as prepared and annealed TNTA.

The Ti 2p and O1s spectra of as prepared as well as annealed nanotube arrays confirm the presence of lower valent Ti ions and oxygen vacancies. The oxygen vacancies at the surface take the form of missing oxide ions in the Ti-O-Ti row (oxygen vacancies i.e. Ti^{3+} - V_O – Ti^{3+})

leading to the formation of coordinatively unsaturated Ti^{3+} ions. These Ti^{3+} ions have distorted coordination geometry because of adjacent oxide ion vacancies. They have a tendency to form additional coordination and therefore the oxygen vacancies act as adsorption sites for organic and water molecules thereby playing an important role in the photo-oxidation of organic species.[85] When water molecules come in contact with nanotube surface they are adsorbed at the bridging oxygen vacancies and dissociated into OH and H. The OH group fills the oxygen vacancy to form Ti – OH – Ti / Ti-$(OH)_2$-Ti bridge.[85] The hydrogen atom has two options. It can either form an identical Ti – OH – Ti bridge, by binding to another Ti – O – Ti bridge or, Ti^{3+} - OH by binding to O^{2-} ions terminating at the surface. As anions are easily polarizable by cations they terminate at the surface thereby reducing the surface potential and constitute active sites for reaction with the H atoms to form Ti^{3+} - OH.[60] Hydroxylation at the bridging oxygen vacancies was elucidated by Wendt et al on the basis of results from scanning tunneling microscopic studies on reduced TiO_2 (110) surface and density functional theory calculations.[86] Hence, presence of bridging oxygen vacancies is a necessary condition for water dissociation or organic oxidation and has immense influence on the photocatalytic properties of TiO_2. Based on above observations the expected oxygen species can be enumerated as Ti^{4+} - O, Ti^{4+} - $(OH)_2$, Ti^{3+} - O, $Ti^{3.5+}$ - OH – $Ti^{3.5+}$ and Ti^{3+} - OH. In addition, the presence of H_2O molecules adsorbed on to the OH groups by hydrogen bonding cannot be excluded.[85] Although the surface bridging oxygen vacancies are filled by OH groups still there are O1s peaks corresponding to oxygen near oxygen vacancies and Ti $2p_{3/2}$ peaks corresponding to coordinatively unsaturated Ti^{3+} because of presence of bulk defects.[85] The bridging oxygen vacancies modify the electronic structure by introducing band gap states, ~0.75 eV, below the conduction band and their population increases in direct proportion with the density of bridging oxygen vacancy.[87] This will enhance electronic properties like conduction and field emission.[60] Hence synthesis of oxygen deficient TNTA is vital for application in the area of photocatalytic, photo voltaic and electronic devices.

Presence of fluorine was detected both in the case of as prepared (Figure 3.16a) as well as annealed samples (Figure 3.16c) by XPS analysis. The binding energy value of 685 eV corresponds to adsorbed fluoride ions. Fluoride ions were also observed at the surface and metal-oxide interface (figure 3.16b) before and after sputtering for different time periods.

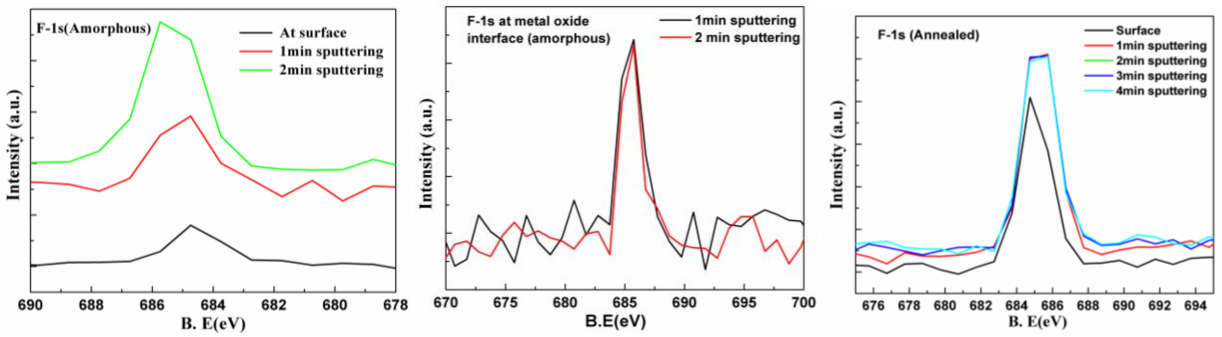

Figure 3.16a-c: (a) Flourine 1s spectra of amorphous TiO_2 sample. Reveals the presence of flourine at different depths. (b) Flourine 1s spectra of amorphous TiO_2 sample (at the interface). From the spectra it is evident that the flouride is present at the metal/oxide interface and reveals that flouride ion is playing an important role in the tubular morphology of Titania and (c) Flourine 1s spectra of annealed TiO_2 sample. Even after annealing at 673K the flourine presence is seen.

From these observations, it can be concluded that fluoride ions migrate along with the oxygen ions to the metal - oxide interface which facilitates the growth of TiO_2 nanotubes. Habazaki et al reported that fluoride ions migrate inward at a rate twice that of O^{2-} ions, developing a thin layer of increased fluoride content between the anodic oxide and the metal substrate.[88] The same is also observed by Albu et al.[89]The observed F 1s binding energy (684.3 eV) corresponds to adsorbed F^- ions. Peaks corresponding to lattice F^- ions (688.5 eV) could not be detected. The incorporated fluoride ions are sensitive to annealing and are eliminated at higher temperatures.[50]

To study the composition of transparent TNTA films on FTO coated glasses, the X-ray photoelectron spectra of annealed samples were required as in the case of TNTA on foils. The Ti 2p spectra of transparent TNTA (Figure 3.17a) were deconvoluted to six spin orbit components ($2p_{3/2}$ and $2p_{1/2}$) at 459.5, 458.7, 457.44, 465.34, 464.39 and463.15 eV. These are assigned as Ti^{4+} (TiO_2), Ti^{3+} (TiOOH), Ti^{3+} (co-ordinatively unsaturated i.e Ti^{3+} adjacent to oxygen vacancy). Different types of oxygen species present are distinguished by different oxygen binding energies observed for O1s spectra. The asymmetric oxygen 1s spectra (Figure 3.17b) were deconvoluted and resolved into three components which are positioned at 530.71, 538.18 and 532.06 eV. The peak positions, 530.67 (Ti^{4+}-O), 531.16 (Ti^{3+}-O i.e. oxygen near an oxygen vacancy) and 532.3 eV (Ti-OH/OH^-), agree well with the results of TNTA on foils. The nonstoichiometry in the TNTA thin film is similar to that of TNTA on foils and it arises due to bridging oxygen vacancies, which modify the electronic structure and enhances the electronic properties.

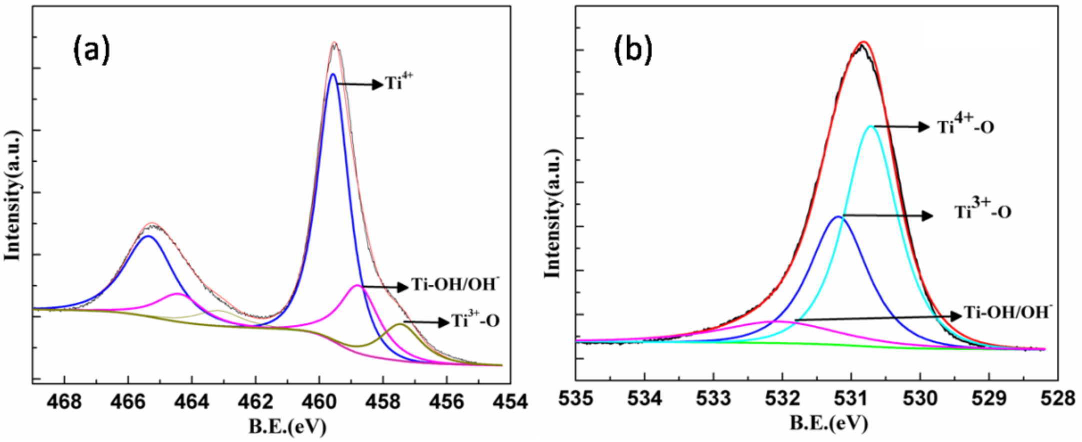

Figure 3.17a-b: (a) the deconvoluted 2p spectra of Ti and (b) the deconvoluted 1s spectra of O

3.3.1.5. FTIR analysis

The FTIR spectra of the pristine TNTA synthesized at 40 V and annealed at 400 ^oC are shown in Figure 3.18. The stretching and bending vibrational peaks of OH groups at 3000-3400 cm^{-1} and 1626.15 cm^{-1} in the spectra confirm the presence of hydroxyl species. The broad peak in the range 400-800 cm^{-1} corresponds to bulk TiO_2. These observations are in agreement with the reported values[11, 82, 90] and confirm the XPS results.

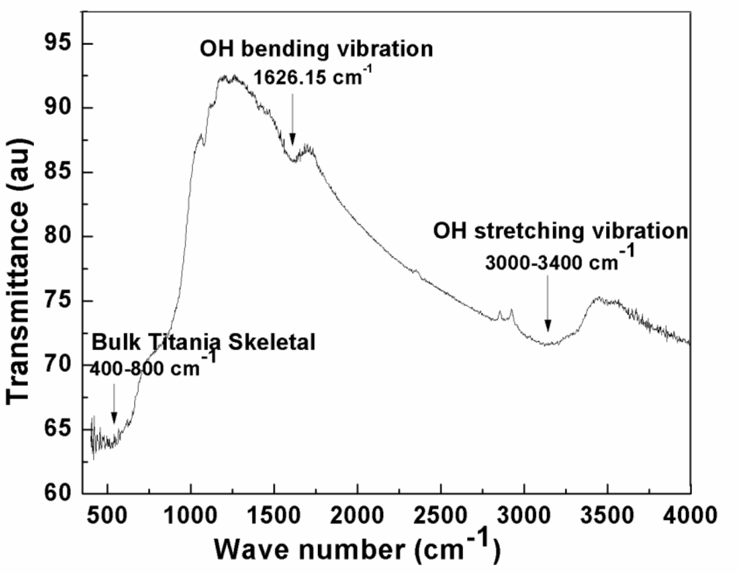

Figure 3.18: FTIR spectra of the as prepared sample anodized at 40V for 2 hours

3.3.1.6. UV-Visible spectroscopic analysis

Figure 3.19a and b shows the DRS and absorbance spectra of the pristine TNTA on foils and on FTO glass, respectively (anodized at 40V for 2 hours and annealed at 400^oC). The optical band gap values are calculated from the Tauc plots obtained from the DRS and absorbance spectra as explained in chapter 2. The optical band gap, obtained by extending the line, from the slope of the linear part of the curve, in the Tauc plot (Figure 3.20a), to x = 0 was calculated and has a value of 3.27. In case of TNTA on FTO glass the band gap calculated turns out to be 2.8

eV and is represented in Figure 3.20b. The analysis reveals that the material absorbs in the ultra violet region.

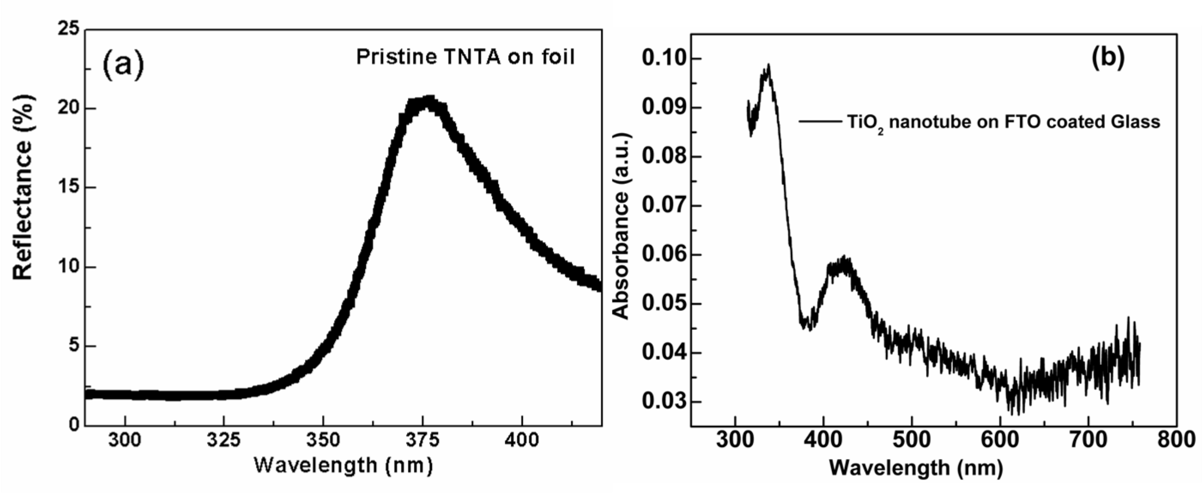

Figure 3.19a-b: (a) DRS spectra of the pristine TNTA on foils, (b) Absorbance spectra of TNTA on FTO glass

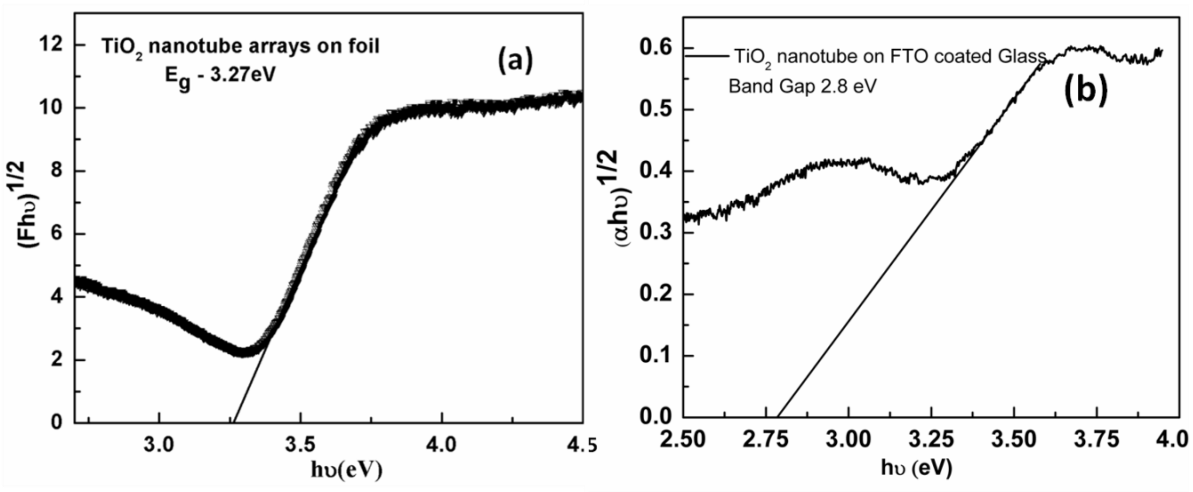

Figure 3.20a-b: Tauc plot of the (a) pristine TNTA on foils, (b) TNTA on FTO glass

3.3.2. Nitrogen Doped TiO_2 nanotube arrays.

3.3.2.1. Mechanism and micro-structural analysis

Based on the earlier results, that anodization of Ti foils in ethylene glycol / H_2O / NH_4F electrolyte, corresponding to the composition 2.5 wt% H_2O and 0.3 to 0.5 wt% NH_4F, yielded smooth walled nanotubes with maximum possible growth rate. Syntheses of N-doped TNTA were carried out in same electrolyte composition with different weight percent of urea (0.1, 0.2 and 0.3) as nitrogen precursor. Urea was chosen as a nitrogen source, as electrolysis of aqueous solutions containing urea decomposes to N_2 and CO_2 at high anodic potentials.[91] Since nitrogen formed at the anode surface will be nascent, before being liberated as N_2, there exists the possibility of nitrogen incorporation into the anion lattice of TiO_2 during the formation of TNTA. Also one can expect a variation in the amount of nitrogen substituted for oxygen in the anion sub lattice with nitrogen precursor (urea) concentration. The potentiostatic transient obtained is quite similar to the conventional one obtained during Ti anodization in the medium without urea. Also the charge (area under the current density Vs time curve) is not much different from that in which anodization has been carried out without urea. This implies similar mechanism prevailing for pristine and N-doped TiO_2 nanotube formation. Anodization was carried out as a function of applied potential to delineate the optimum potential range for the synthesis of smooth walled nanotube arrays. The surface topography of Ti foils anodized at different potentials varying from 20 to 60V for 2 hrs, corresponding to 0.2 wt% urea is shown in Figure 3.21 (a-e). Similar micrographs were obtained for other urea concentrations. Figure 3.21f shows the cross sectional FESEM image of the N-doped TNTA. At 10V, porous structures were formed on the Ti surface, but no distinct nanotubes are observed. However, formation of distinct nanotubes having inner diameter of ~47 nm is observed, when the applied potential was increased to 20V, from the SEM image. The above observation indicates that there is a minimum required potential for the formation of N-doped self-organized nanotubes as in the case of formation of pristine TiO_2 nanotubes. Under the present experimental conditions, the minimum required potential for the formation of N-doped nanotubes is around 20 V. As reported in the case of pristine TNTA, formations of self aligned nanotube arrays were observed up to a potential of 60 V. A careful observation of the SEM pictures shows that the best homogeneous morphology is obtained when synthesis is carried out at 40 V (similar to the case of pristine TNTA). Figure 3.22 shows the variation of inner diameter of the nanotubes with applied potential. The increase in tube diameter with voltage can be attributed to the enhanced chemical dissolution of TiO_2 at the pore wall. No significant variations in wall thickness were observed compared to the pristine samples. The variation in wall thickness with respect to applied voltage is shown in the inset of Figure 3.22.

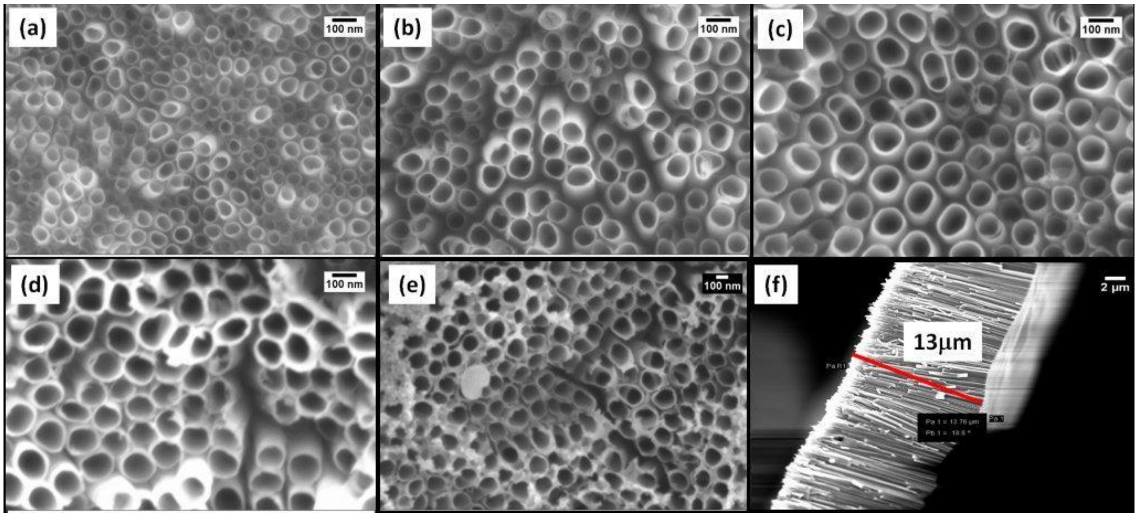

Figure 3.21a-f: Surface morphology of anatase N-doped TNTA synthesized at (a) 20 V, (b) 30 V, (c) 40 V, (d) 50 V, (e) 60 V and (f) cross section of nanotube arrays.

When the potential is increased, rate of chemical dissolution and oxidation increases resulting in nanotube growth. When the applied potential was 80 V, the current density increased with time and nano-tubes were not observed on the foil even after two hours of anodization attempt. This is similar to the case of pristine TNTA. Here too, the electrolyte temperature increased with applied potential enhancing the chemical dissolution.

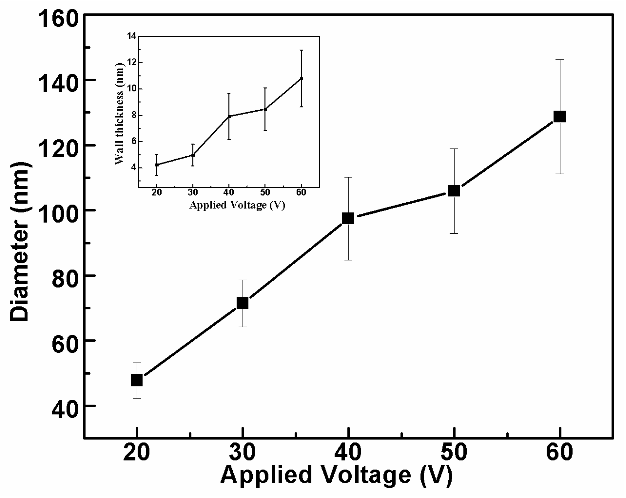

Figure 3.22: Variation of tube diameter of the N-doped TNTA with voltage. The inset shows the change in wall thickness with applied voltage.

3.3.2.2. XRD and Micro Raman analyses

Since the best homogeneous tubular morphology is obtained for samples synthesized at 40 V, the same is considered for the characterization studies. As in the case of pristine samples the as prepared doped samples upon XRD analyses were found to be amorphous, this transformed to anatase phase on annealing at 400 ^{o}C. Figure 3.23a shows the XRD pattern of annealed N-doped TNTA. The XRD pattern of the annealed pristine TNTA is also shown in the figure for comparison. Formation of anatase phase was further confirmed by Raman spectroscopy. Raman spectra corresponding N-doped TNTA synthesized at different conditions and annealed at 400 ^{o}C show an intense peak at 145 cm^{-1} corresponding to the Eg mode of anatase phase. For The weak bands at 199(Eg), 395(B_{1g}), 516(A_{1g}+B_{1g}) and 636 (E_g) are in agreement with the modes exhibited by anatase phase. Figure 3.23b shows the Raman spectra of the N-doped TNTA. The Raman spectra of the pristine sample, synthesized under similar conditions, are also included for comparison. The band positions are in concurrence with the previous results.[92,93] The strongest peak at 145 cm^{-1} arising from the external vibrations of the anatase crystal structure, indicates that long range order pertaining to anatase crystallinity has evolved in the annealed N-doped TNTA. Compared to the pristine one, the highly intense Eg mode (145 cm^{-1}) of the doped TNTA shows a red shift (inset of Figure 3.23 b). This can be ascribed to the change in force constant due to nitrogen doping.

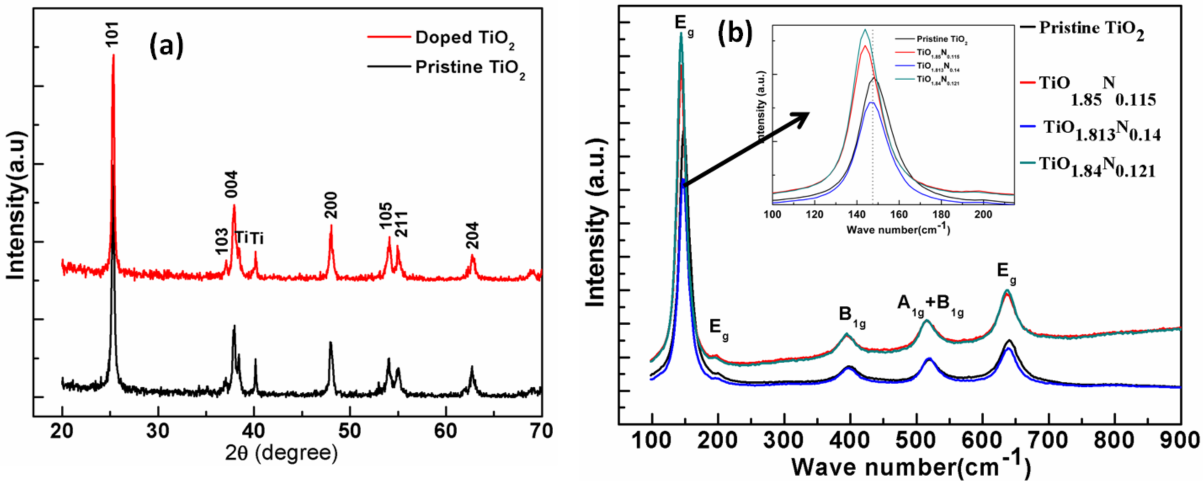

Figure 3.23a-b: (a) XRD pattern of N-doped and pristine TNTA. (b) Visible micro Raman spectra of the N-doped and pristine TiO_2

3.3.2.3. XPS investigations.

As in the case of pristine TNTA, to study the composition as well as nitrogen incorporation to the crystal, XPS studies were carried out. Figure 3.24a-d shows the deconvoluted Ti 2p spectra of TNTA synthesized at different wt% of urea and annealed at 400 ^{o}C. The spectrum of the pristine TiO_2 is also included for comparison. The peaks are deconvoluted into four different peaks. The region shows four doublets: the peaks at 459.4, 458.0, 456.9 and 455.6 eV correspond to the 2p3/2 region suggesting Ti (+4)-O, Ti (+3)-O, Ti (+3)-N or Ti (+3)-OH and Ti (+2)-O, respectively. The other peaks at higher binding energies corresponding to the 2p1/2 core level of the respective states. The O 1s spectra of the corresponding samples are shown in Figure 25 a-d. The deconvoluted peaks positioned at 530.5, 530.9 and 531.9 eV correspond to O-Ti (+3), O-Ti(+4) and HO-Ti(+3,+4), respectively, in agreement with the reported values.[83,85]

The high resolution N-1s spectra of the samples synthesized at different wt% of urea are shown in figures 3.26a (0.1 wt %), 3.26b (0.2 wt %) and 3.26c (0.3 wt %). The data for the analysis are required at a sputter depth arrived after 3 minutes of sputtering (10 nm/min) for all the samples. This was done to obtain a reasonable intensity for nitrogen signal. The high resolution N-1s spectra consist essentially of three peaks viz. one high intensity asymmetric peak around 396.8 eV and two low intensity peaks at 400.2 and 403.1 eV respectively. The high intensity asymmetric peak has been deconvoluted to high and low intensity peaks at 396.8 eV and 397.6 eV, respectively. The different N-1s BE values represent different electron density around nitrogen suggesting various N coordination environments in the lattice. Based on the references given in the introduction, the N-1s peak at 400.2 can be assigned to N_i. The peak observed at 403.1 eV is assigned to surface adsorbed NO_x species.[46,49, 94] The two deconvoluted peaks in the range 396 – 398 eV (396.8 and 397.6 eV) can be ascribed to substitutional nitrogen in the oxide lattice. The structure of anatase TiO_2 consists of corner and edge sharing (TiO_6) octahedra. If the number of oxygen atoms substituted by nitrogen atoms in each octahedron is same (nitrogen substitution is uniformly distributed throughout), one would expect a single N-1s BE value corresponding to N_O (N-Ti-O) species. If the number of N ions in the co-ordination sphere around Ti varies, the observed N-1s values will lie in a range leading to N-1s peak broadening and asymmetry. In such a situation, the asymmetric peak on deconvolution shows up different BE values. In addition, when two oxygen atoms are substituted by nitrogen atoms one oxygen vacancy is generated.

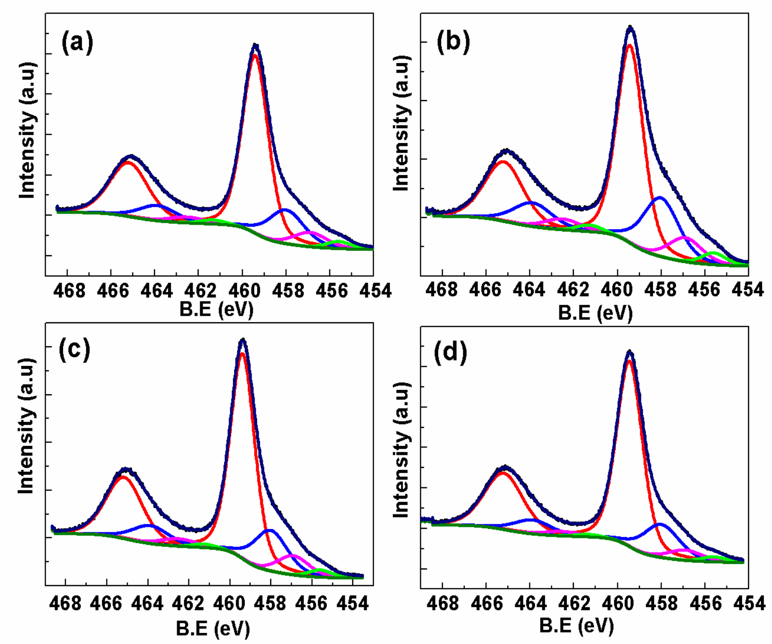

Figure 3.24a-d: High resolution Ti 2p x-ray photoelectron spectra (a) pristine TNTA (b) N doped TNTA anodized 0.1 wt % of urea containing electrolyte(c) 0.2 wt % of urea containing electrolyte and(d) 0.3 wt % of urea containing electrolyte

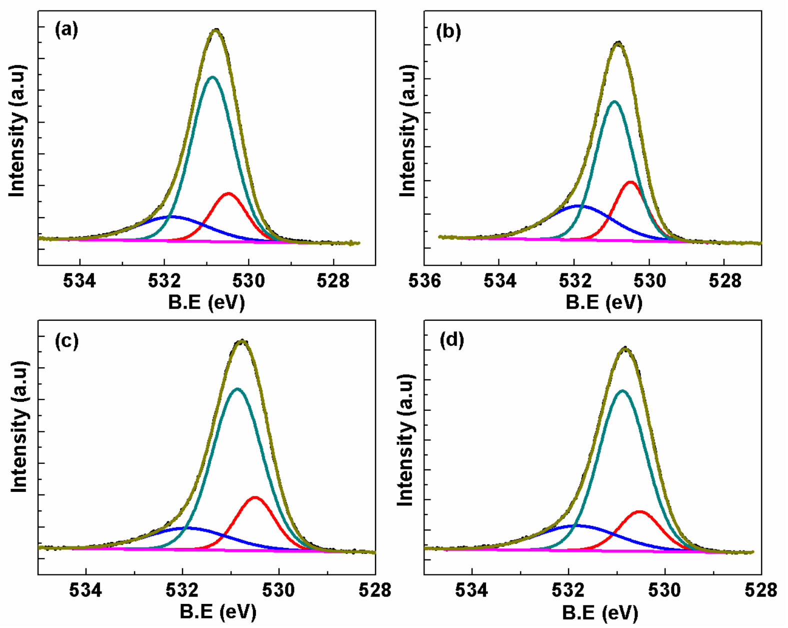

Figure 3.25a-d: High resolution O 1s x-ray photoelectron spectra (a) pristine TNTA (b) N doped TNTA anodized 0.1 wt % of urea containing electrolyte, (c) 0.2 wt % of urea containing electrolyte and (d) 0.3 wt % of urea containing electrolyte

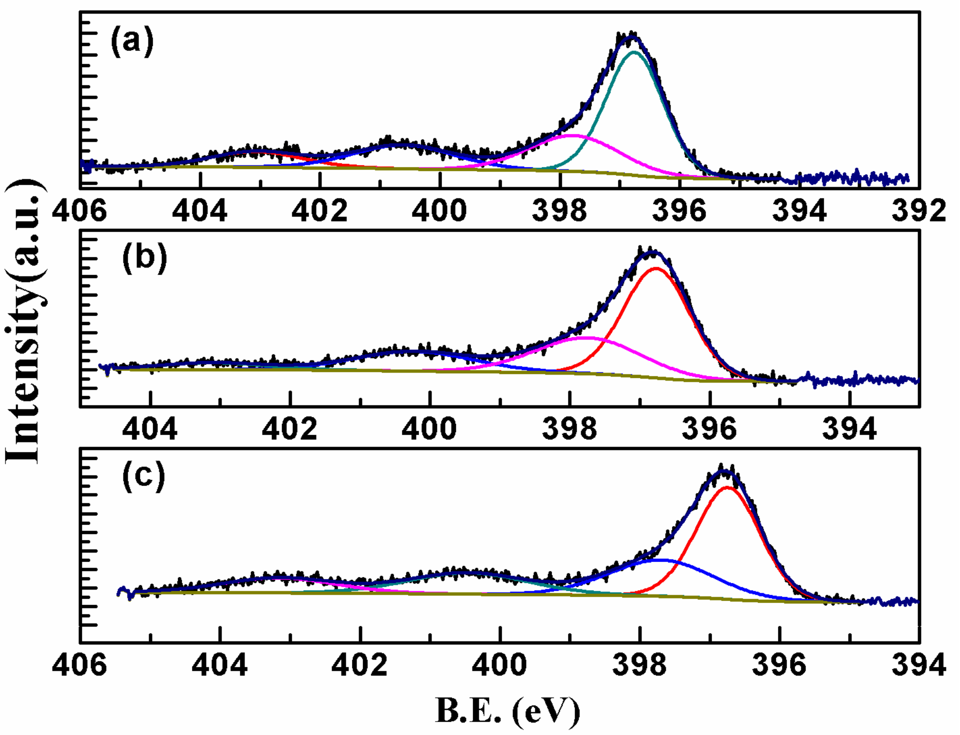

Figure 3.26a-c: High resolution N 1s X-ray photoelectron spectra (a) $TiO_{1.85}N_{0.115}$ (b) $TiO_{1.813}N_{0.14}$ (c) $TiO_{1.84}N_{0.121}$

This will distort the coordination octahedra having vacancies, as neighboring anions relax towards the vacancy, adding small changes to N-1s BE values. Since the electrochemical doping is achieved at ~298 K, equilibrium cannot be expected and therefore there exist the possibility of variation in the number of oxygen atoms substituted by nitrogen atoms in various coordination octahedra present in the lattice. Hence the reason for observing, on deconvolution, N-1s BE values at 396.8 and 397.6 eV, corresponds to substitutional nitrogen in the oxide ion lattice. The atom fractions of Ti, O and N are calculated using the following equations

$$X_{Ti} = (I_{Ti-2p}/S_{Ti})/\,[(I_{Ti-2p}/S_{Ti}) + (I_{O-1s}/S_O) + (I_{N-1s}/S_N)] \quad (7)$$

$$X_O = (I_{O-1s}/S_O)/\,[(I_{Ti-2p}/S_{Ti}) + (I_{O-1s}/S_O) + (I_{N-1s}/S_N)] \quad (8)$$

$$X_N = (I_{N-1s}/S_N)/\,[(I_{Ti-2p}/S_{Ti}) + (I_{O-1s}/S_O) + (I_{N-1s}/S_N)] \quad (9)$$

$I_{N\text{-}1s}$ is the peak area of the N-1s peak corresponding to O-Ti-N, $I_{Ti\text{-}2p}$ is the sum of the areas of the Ti_{2p} deconvoluted peaks (Figure 3.25 (a-d)) and $I_{O\text{-}1s}$ is the area of the O-1s peak (26(a-d)) corresponding to bonded oxygen and S_{Ti}, S_O and S_N corresponding atomic sensitivity factors. Based on the calculated atom fractions, and taking into account the fraction of Ti^{3+} ions, the chemical formula of N-doped TiO_2 is represented as $TiO_{1.85}N_{0.115}$, $TiO_{1.813}N_{0.14}$ and $TiO_{1.84}N_{0.121}$ for the samples synthesized at 0.1, 0.2 and 0.3 wt% of urea in the electrolyte, respectively. The corresponding atom percent of nitrogen are about 3.88, 4.74 and 4.12, respectively.

3.3.2.4. Diffuse reflectance measurements

Figure 3.27a and b shows the Tauc plots of different nitrogen doped samples. Tauc plot of the pristine TNTA is also included for comparison. The optical band gap, obtained by extending the line, from the slope of the linear part of the curve, to x = 0 was calculated and are 3.27. 3.22 2.75 and 2.77 eV for pristine TiO_2, $TiO_{1.85}N_{0.115}$, $TiO_{1.813}N_{0.14}$ and $TiO_{1.84}N_{0.121}$, respectively. In the case of $TiO_{1.813}N_{0.14}$, the Tauc plot show an extra linear part of which intercept at x=0 shows transition state situated at a difference of 2.59 eV.

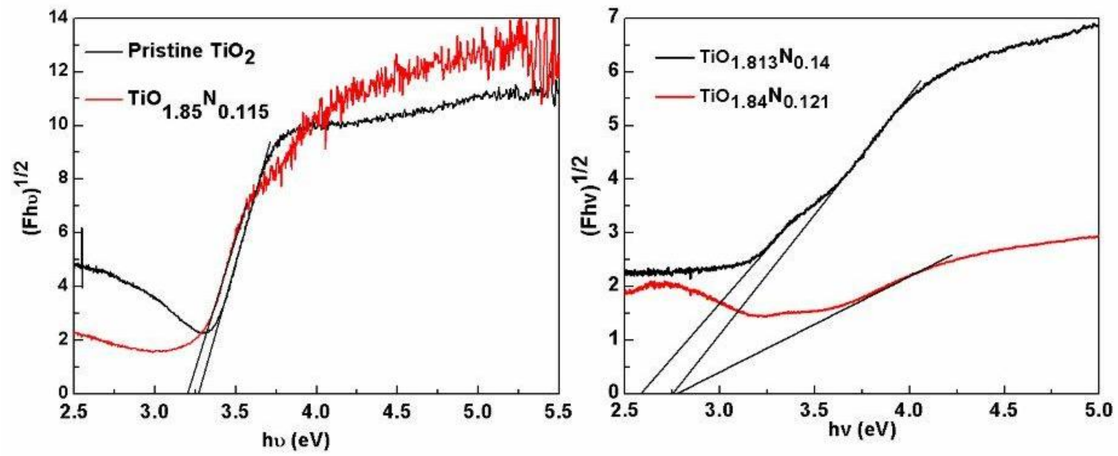

Figure 3.27: Diffuse Reflectance spectra of pristine as well as N-doped TiO_2

This shows that due to nitrogen doping certain interband electronic states have been generated. In the case of N- doped samples, the band gaps have been shifted to lower values than that of the pristine TiO_2. The observed shifts in the band gap energy for $TiO_{1.85}N_{0.115}$, $TiO_{1.813}N_{0.14}$ and $TiO_{1.84}N_{0.121}$ with respect to that of pristine TiO_2 are 0.05, 0.52 and 0.5 eV, respectively. The extra state introduced in the case of $TiO_{1.813}N_{0.14}$ is located 0.68eV above the valence band.

3.4. Conclusion

Self aligned TNTA were synthesized on Ti substrates by electrochemical anodization technique using fluoride ion containing organic electrolyte. Highly ordered nanotubes of about few micrometer lengths were obtained in neutral pH within 1 hour of anodization duration. The potentiostatic transients qualitatively revealed the mechanism of nanotube formation. From the potentiostatic transients, correlating with reported results, it can be said that field assisted chemical oxidation of Ti and field assisted chemical dissolution of TiO_2 and Ti by fluoride ions played a key role in nanotube formation. To understand the mechanism qualitatively, anodization of Ti foils were carried out as a function of voltage, time and electrolyte composition. Desired aspect ratio and wall morphology, depending upon the application, can be achieved by varying the electrochemical parameters. The as prepared amorphous nanotube arrays transformed to anatase phase on annealing at 400 ^{o}C. Anatase to rutile phase transformation was observed with increase in temperature. Although the tubular surface morphology was found to be destroyed at 600 °C and above, the cross sectional SEM micrographs revealed retention of tubular morphology up to a temperature of 700^{o}C. The presence of different surface and subsurface defect states arising from the bridging oxygen vacancies were confirmed from XPS and FTIR measurements. The defect state detection by XPS analysis supports the enhanced photo catalytic activity of TNTA. Existence of fluoride ions at various depths confirms their migration from surface to interface during anodization. The band gap of the annealed TNTA measured by diffuse reflectance analysis was found to be 3.27 eV.

TiO_2 nanotube thin films were synthesized by electrochemical anodization of Ti films deposited on conducting glasses by magnetron sputtering. The crystallinity of the annealed TiO_2 nanotube thin films was confirmed from XRD studies. The nonstoichiometry of the TNTA films due to bridging hydroxyl groups were proved by X-ray photoelectron spectroscopy. The band gap of the annealed TNTA measured by diffuse reflectance analysis was 3.36 eV indicating absorption capabilities in the ultra violet region.

N-doped TNTA corresponding to the compositions $TiO_{1.85}N_{0.115}$, $TiO_{1.813}N_{0.14}$ and $TiO_{1.84}N_{0.121}$ were synthesized in single step anodization in electrolyte containing different weight percent of urea. XRD and micro Raman analysis revealed the anatase phase crystallinity of the N-doped TNTA annealed at 400 ^{o}C. The XPS analysis confirmed nitrogen incorporation into TiO_2 matrix both in substitutional and interstitial form out of which major contribution arises from the substitutional states. A considerable shift in the band gap of the material was observed for the nitrogen doped samples and in the case of $TiO_{1.813}N_{0.14}$, introduction of an extra interband electronic state was observed.

References

---

[1] Paulose, M.; Mor, G. K.; K.Varghese, O.; Shankar K.; Grimes, C. A., *J Photochem. Photobiol. A: Chem.*, **2006,** *178*, 8-15

[2] Nagaveni, K.; Sivalingam, G.; Hegde, M. S.; Madras, G., *Environ. Sci. Tech.*, **2004,** *38*, 1600-1604.

[3] Tan, B.; Wu, Y., *J. Phys. Chem. B*, **2006,** *110*, 15932-15938.

[4] Choi, S. Y.; Mamak, M.; Coombs, N.; Chopra N.; Ozin, G. A., *Nano Lett.*, **2004,** *4*, 1231-1235.

[5] Mor, G. K.; Varghese, O. K.; Paulose, M.; Ong K. G.; Grimes, C. A., *Thin Solid Films*, **2006,** *496*, 42-48

[6] Nakade, S.; Kubo, W.; Saito, Y.; Kanzaki, T.; Kitamura, T.; Wada Y.; Yanagida, S., *J. Phys. Chem. B*, **2003,** *107*, 14244-14248.

[7] Zhu, Y.; Li, H.; Koltypin, Y.; Hacohen Y. R.; Gedanken, A., *Chemi. Comm.*, **2001,** *46*, 2616-2617.

[8] Wu, J. M., *J. Cryst. Growth*, **2004,** *269*, 347-355.

[9] Miao, Z.; Xu, D.; Ouyang, J.; Guo, G.; Zhao X.; Tang, Y., *Nano Lett.*, **2002,** *2*, 717-720.

[10] Su, C.; Hong, B. Y.; Tseng, C. M., *Catal. Today* **2004,** *96* (3), 119-126.

[11] Hayashi, H.; Torii, K., *J.Mater. Chem.y* **2002,** *12* (12), 3671-3676.

[12] Goossens, A.; Maloney, E.-L.; Schoonman, J., *Chem. Vap. Deposition* **1998,** *4* (3), 109-114.

[13] Zwilling, V.; Darque-Ceretti, E.; Boutry-Forveille, A.; David, D.; Perrin, M. Y.; Aucouturier, M., *Surf. Inter. Anal.* **1999,** *27* (7), 629-637.

[14] Gong, D.; Grimes, C. A.; Varghese, O. K.; Hu, W.; Singh, R. S.; Chen, Z.; Dickey, E. C., *J. Mater. Res.* **2001,** *16* (12), 3331-3334.

[15] Mor, G. K.; Varghese, O. K.; Paulose, M.; Ong, K. G.; Grimes, C. A., *Thin Solid Films* **2006,** *496* (1), 42-48.

[16] Zhu, Y.; Li, H.; Koltypin, Y.; Hacohen, Y. R.; Gedanken, A., *Chem. Comm.* **2001,** (24), 2616-2617.

[17] Macak, J. M.; Tsuchiya, H.; Ghicov, A.; Yasuda, K.; Hahn, R.; Bauer, S.; Schmuki, P., *Curr. Opinion. Solid State Mater. Sci.* **2007,** *11* (1–2), 3-18.

[18] Prakasam, H. E.; Shankar, K.; Paulose, M.; Varghese, O. K.; Grimes, C. A., *J. Phys. Chem. C* **2007,** *111* (20), 7235-7241.

[19] Narayanan, R.; Kwon, T.-Y.; Kim, K.-H., *Mater. Lett.* **2009,** *63* (23), 2003-2006.

[20] Macak, J. M.; Schmuki, P., *Electrochim. Acta* **2006,** *52* (3), 1258-1264.

[21] Paulose, M.; Shankar, K.; Yoriya, S.; Prakasam, H. E.; Varghese, O. K.; Mor, G. K.; Latempa, T. A.; Fitzgerald, A.; Grimes, C. A., *J. Phys. Chem. B* **2006,** *110* (33), 16179-16184.

[22] Cai, Q.; Paulose, M.; Varghese, O. K.; Grimes, C. A., *J. Mater. Res.* **2005,** *20* (01), 230-236.

[23] Wang, J.; Lin, Z., *Chem. Mater.* **2008,** *20* (4), 1257-1261.

[24] Macak, J. M.; Zlamal, M.; Krysa, J.; Schmuki, P, *Small* **2007,** *3* (2), 300-304.

[25] Macák, J. M.; Tsuchiya, H.; Schmuki, P., *Angew. Chem. Inter. Ed.* **2005,** *44* (14), 2100-2102.

[26] Taveira, L. V.; Macak, J. M.; Tsuchiya, H.; Dick, L. F. P.; Schmuki, P., *J. Electrochem. Soc.* **2005,** *152* (10), B405-B410.

[27] Wang, J.; Lin, Z., *J. Phys. Chem. C* **2009,** *113* (10), 4026-4030.

---

[28] Macak, J. M.; Tsuchiya, H.; Berger, S.; Bauer, S.; Fujimoto, S.; Schmuki, P., *Chem. Phy. Lett.***2006,** *428* (4–6), 421-425.

[29] Varghese, O. K.; Paulose, M.; Grimes, C. A., *Nat Nano* **2009,** *4* (9), 592-597.

[30] G. K. Mor, H. E. Prakasam, O. K. Varghese, K. Shankar and C. A. Grimes, *Nano Letters*, 7 (2007) 2356-2364.

[31] H. Zheng, A. Z. Sadek, M. Breedon, D. Yao, K. Latham, J. D. Plessis and K. Kalantar-Zadeh, *Electrochem. Comm.,* **2009,** *11*,1308-1311.

[32] J. M. Macak, H. Tsuchiya, S. Berger, S. Bauer, S. Fujimoto and P. Schmuki, *Chem. Phys. Lett*, **2006**, *428*, 421-425.

[33] Mor, G. K.; Shankar, K.; Paulose, M.; Varghese, O. K.; Grimes, C. A., *Nano Letters* **2006,** *6* (2), 215-218.

[34] Mor, G. K.; Varghese, O. K.; Paulose, M.; Grimes, C. A., *Adv. Func. Mater.* **2005,** *15* (8), 1291-1296.

[35] Allain, E.; Besson, S.; Durand, C.; Moreau, M.; Gacoin, T.; Boilot, J. P., *Adv. Func. Mater.* **2007,** *17* (4), 549-554.

[36] Borgarello, E.; Kiwi, J.; Graetzel, M.; Pelizzetti, E.; Visca, M., *J. Am. Chem. Soc.* **1982,** *104* (11), 2996-3002.

[37] Choi, W.; Termin, A.; Hoffmann, M. R., *J. Phys. Chem.* **1994,** *98* (51), 13669-13679.

[38] Asahi, R.; Morikawa, T.; Ohwaki, T.; Aoki, K.; Taga, Y., *Science* **2001,** *293* (5528), 269-271.

[39] Di Valentin, C.; Pacchioni, G.; Selloni, A.; Livraghi, S.; Giamello, E., *J. Phys. Chem. B* **2005,** *109* (23), 11414-11419.

[40] Lee, J.-Y.; Park, J.; Cho, J.-H., *App. Phys.s Lett.* **2005,** *87* (1), 011904.

[41] Finazzi, E.; Di Valentin, C.; Selloni, A.; Pacchioni, G., *J. Phys.Chem. C* **2007,** *111* (26), 9275-9282.

[42] Wang, H.; Lewis, J. P., *J. Phys.: Condensed Matter* **2006,** *18* (2), 421.

[43] Di Valentin, C.; Pacchioni, G.; Selloni, A., *Phys. Rev. B* **2004,** *70* (8), 085116.

[44] Yang, K.; Dai, Y.; Huang, B.; Han, S., *J. Phys. Chem. B* **2006,** *110* (47), 24011-24014.

[45] Henderson, M. A.; White, J. M.; Uetsuka, H.; Onishi, H., *J. Am. Chem. Soc.* **2003,** *125* (49), 14974-14975.

[46] Emeline, A.; Salinaro, A.; Ryabchuk, V. K.; Serpone, N., *Int. J. Photoenergy* **2001,** *3* (1), 1-16.

[47] Asahi, R.; Morikawa, T.; Ohwaki, T.; Aoki, K.; Taga, Y., *Science* **2001,** *293* (5528), 269-271.

[48] Sakthivel, S.; Kisch, H., *Angew. Chem. Int. Ed.* **2003,** *42* (40), 4908-4911.

[49] Fujishima, A.; Zhang, X.; Tryk, D. A., *Surf. Sci. Reports* **2008,** *63* (12), 515-582.

[50] Morikawa, T.;Asahi, R.;Ohwaki, T.;Taga, Y.;Aoki, K., Jpn. *J. Appl. Phys*. Part 2, **2001**, *40*, L561-L563

[51] Lindgren, T.; Mwabora, J. M.; Avendaño, E.; Jonsson, J.; Hoel, A.; Granqvist, C.-G.; Lindquist, S.-E., *J. Phys Chem. B* **2003,** *107* (24), 5709-5716.

[52] Wang, J.; Tafen, D. N.; Lewis, J. P.; Hong, Z.; Manivannan, A.; Zhi, M.; Li, M.; Wu, N., *J. Am. Chem.Society* **2009,** *131* (34), 12290-12297.

[53] Park, C. H.; Zhang, S. B.; Wei, S.-H., *Phys. Rev. B* **2002,** *66* (7), 073202.

[54] Qiu, X.; Burda, C., *Chem. Phys.* **2007,** *339* (1–3), 1-10.

[55] Irokawa, Y.; Morikawa, T.; Aoki, K.; Kosaka, S.; Ohwaki, T.; Taga, Y., *Phys. Chem. Chem. Phys.* **2006,** *8* (9), 1116-1121.

[56] Yin, S.; Aita, Y.; Komatsu, M.; Sato, T., *J. Europ. Cer. Soc.* **2006,** *26* (13), 2735-2742.

[57] Liu, M.; Fang, Q.; He, G.; Li, L.; Zhu, L. Q.; Li, G. H.; Zhang, L. D., *App. Phys. Lett.***2006,** *88* (19), 192904-3.

---

[58] Premkumar, J., *Chem.Mater.s* **2004,** *16* (21), 3980-3981.

[59] Lopez-Luke, T.; Wolcott, A.; Xu, L.-p.; Chen, S.; Wen, Z.; Li, J.; De La Rosa, E.; Zhang, J. Z., *J. Phys. Chem. C* **2008,** *112* (4), 1282-1292.

[60] Gang, L.; Feng, L.; Da-Wei, W.; Dai-Ming, T.; Chang, L.; Xiuliang, M.; Gao Qing, L.; Hui-Ming, C., *Nanotechnology* **2008,** *19* (2), 025606.

[61] Liu, X.; Liu, Z.; Zheng, J.; Yan, X.; Li, D.; Chen, S.; Chu, W., *J. Alloys. Comp.* **2011,** *509* (41), 9970-9976.

[62] Ghicov, A.; Macak, J. M.; Tsuchiya, H.; Kunze, J.; Haeublein, V.; Frey, L.; Schmuki, P., *Nano Letters* **2006,** *6* (5), 1080-1082.

[63] Lai, Y.-K.; Huang, J.-Y.; Zhang, H.-F.; Subramaniam, V.-P.; Tang, Y.-X.; Gong, D.-G.; Sundar, L.; Sun, L.; Chen, Z.; Lin, C.-J., *J. Hazard. Mater.* **2010,** *184* (1–3), 855-863.

[64] Su, Y.; Zhang, X.; Zhou, M.; Han, S.; Lei, L., *J.Photochem. Photobiol. A: Chem.* **2008,** *194* (2–3), 152-160.

[65] Karthik, S.; Kong Chhay, T.; Gopal, K. M.; Craig, A. G., *J. Physics D: Appl. Phys.* **2006,** *39* (11), 2361.

[66] Scherrer, 1918 P. Gottinger Nachrichte 2, 98**.**

[67] Nguyen, Q. A. S.; Bhargava, Y. V.; Devine, T. M., *J. Electrochem. Soc.* **2009,** *156* (3), E55-E61.

[68] Yasuda, K.; Macak, J. M.; Berger, S.; Ghicov, A.; Schmuki, P., *J. Electrochem. Soc.* **2007,** *154* (9), C472-C478.

[69] Jaszay, T.; Caprani, A.; Priem, F.; Frayret, J. P., *Electrochim. Acta* **1988,** *33* (8), 1093-1100.

[70] Roy, P.; Kim, D.; Lee, K.; Spiecker, E.; Schmuki, P., *Nanoscale* **2010,** *2* (1), 45-59.

[71] Varghese, O. K.; Gong, D.; Paulose, M.; Grimes, C. A.; Dickey, E. C., *J. Mater. Res.* **2003,** *18* (01), 156-165.

[72] Shannon, R. D., *J. App. Phys.* **1964,** *35* (11), 3414-3416.

[73] Zhang, H.; Banfield, J. F., *J. Mater. Res.* **2000,** *15* (02), 437-448.

[74] Gouma, P. I.; Mills, M. J., *J. Am. Ceramic Soc.* **2001,** *84* (3), 619-622.

[75] Hébrard, J.-L.; Nortier, P.; Pijolat, M.; Soustelle, M., *J. Am. Ceramic Soc.***1990,** *73* (1), 79-84.

[76] Ketteler, G.; Yamamoto, S.; Bluhm, H.; Andersson, K.; Starr, D. E.; Ogletree, D. F.; Ogasawara, H.; Nilsson, A.; Salmeron, M., *J. Phys. Chem. C* **2007,** *111* (23), 8278-8282.

[77] Shirley, D. A., *Phys. Rev. B* **1972,** *5* (12), 4709-4714.

[78] Tougaard, S., *J. Electron Spectroscopy and Related Phenomena* **1990,** *52* (0), 243-271.

[79] Bishop, H. E., *Surf. Inter. Anal.* **1981,** *3* (6), 272-274.

[80] C. D. Wagner, W. M. Riggs, L. E. Davis, J. F. Moulders and G. E. Mullenberg, G E Mullenberg (Ed), Hand book of Xray Photoelectron Spectroscopy, Perkin Elmer Cooperation, Eden Prairie, MN, 1979

[81] D. Briggs and M. P. Seah, Practical Surface Analysis, Vol. 1 Auger and X-ray Photoelctron Spectroscopy, 2nd ed. (Chichester: Wiley), 1990

[82] Kumar, P. M.; Badrinarayanan, S.; Sastry, M., *Thin Solid Films* **2000,** *358* (1–2), 122-130.

[83] Liu, H.; Yang, W.; Ma, Y.; Cao, Y.; Yao, J.; Zhang, J.; Hu, T., *Langmuir* **2003,** *19* (7), 3001-3005.

[84] Mahajan, V. K.; Misra, M.; Raja, K. S.; Mohapatra, S. K., *J. Physics D: Appl. Phys.* **2008,** *41* (12), 125307.

[85] Ketteler, G.; Yamamoto, S.; Bluhm, H.; Andersson, K.; Starr, D. E.; Ogletree, D. F.; Ogasawara, H.; Nilsson, A.; Salmeron, M., *J. Phys.l Chem. C* **2007,** *111* (23), 8278-8282.

---

[86] Wendt, S.; Sprunger, P. T.; Lira, E.; Madsen, G. K. H.; Li, Z.; Hansen, J. Ø.; Matthiesen, J.; Blekinge-Rasmussen, A.; Lægsgaard, E.; Hammer, B.; Besenbacher, F., *Science* **2008,** *320* (5884), 1755-1759.

[87] Yim, C. M.; Pang, C. L.; Thornton, G., *Phys. Rev. Lett.* **2010,** *104* (3), 036806.

[88] Habazaki, H.; Fushimi, K.; Shimizu, K.; Skeldon, P.; Thompson, G. E., *Electrochem. Comm.* **2007,** *9* (5), 1222-1227.

[89] Albu, S. P.; Ghicov, A.; Aldabergenova, S.; Drechsel, P.; LeClere, D.; Thompson, G. E.; Macak, J. M.; Schmuki, P., *Adv. Mater.* **2008,** *20* (21), 4135-4139.

[90] Jensen, H.; Soloviev, A.; Li, Z.; Søgaard, E. G., *App. Surf. Sci.* **2005,** *246* (1–3), 239-249.

[91] Simka, W.; Piotrowski, J.; Nawrat, G., *Electrochim. Acta* **2007,** *52* (18), 5696-5703.

[92] Ohsaka, T.; Izumi, F.; Fujiki, Y., *J. Raman Spectroscopy* **1978,** *7* (6), 321-324.

[93] Balaji, S.; Djaoued, Y.; Robichaud, J., *J. Raman Spectroscopy* **2006,** *37* (12), 1416-1422.

[94] Palgrave, R. G.; Payne, D. J.; Egdell, R. G., *J. Mater. Chem.* **2009,** *19* (44), 8418-8425.

Chapter 4

Photovoltaic, Field Emission and Surface Wetting Characteristics of Pristine and N-doped TiO_2 Nanotube Arrays

One dimensional nano-architectures of TiO_2, such as nano-tubes, nano-wires, nano-rods and nano-fibers with tailored geometry and surface complexity, in thin film form, are being investigated for various functional applications in energy, environment and electronics, where the advantages of tailored geometry combined with the intrinsic properties of nano-crystalline TiO_2 can be fully exploited. In applications like photovoltaics, large area electron field emission and smart surfaces where alignment, high aspect ratio, thin edges, surface roughness with long trapped air columns and directional electron transport properties are expected to play a major role in enhancing the efficiency of devices fabricated using the one dimensional nano-architectures, vertically aligned nanotube arrays are of great interest. The fabrication of Dye sensitized solar cells using TiO_2 nanotube arrays and their photovoltaic characteristics as well as electron field emission properties and wetting - dewetting characteristics of pristine and N-doped TiO_2 nanotube arrays are the highlights of this chapter.

Chapter 4

General Introduction

Dye sensitized solar cells (DSSCs), large area field emitters and super hydrophobic – super hydrophilic coatings are three areas in which self organized TiO_2 nanotube arrays (TNTA) are expected to play a major role. In the case of DSSCs; the vectorial electron transport properties of TNTA, because of the vertical alignment, enhances the electrode – electrical contact thereby decreasing the contact resistance. The large surface area of the nanotube arrays provide high surface area dye adsorption enhancing light harvesting and dye to electrode charge transfer. In addition, the filling of electrolyte in the intra and inter tubular spaces enhances the electrolyte – dye charge transfer, all contributing to the enhancement of overall cell efficiency. For large area field emitters; the directional electron transport, high aspect ratio and thin walls of the TNTA enhance electron emission from the tube tips. In addition, suitable anion doping of TiO_2 modifies the electronic energy band structure thereby shifting the Fermi level towards vacuum, which enhances electron tunneling leading to overall device efficiency. The increased pressure of trapped air inside the small diameter nanotubes as well as in the inter tubular spaces, of the closely packed high aspect ratio vertically aligned TNTA, render the nanotube array coated surfaces super / near super hydrophobic. While the small wall thickness, in the quantum confinement regime, will enhance photo induced surface restructuring enabling quick conversion to super hydrophilicity. Hence TNTA coatings can be used to make surfaces that are able to switch between super hydrophobic and super hydrophilic regimes and have potential application in micro-fluidic devices, smart membranes and sensors.

The present chapter deals with application studies of TNTA in the above three areas, and is divided in to three sections. Section one deals with fabrication of dye sensitized solar cells, using vertically aligned anatase TNTA grown on Ti foils and on transparent FTO coated glasses as described in chapter 3, along with their photovoltaic characteristics. Section two discusses the studies on electron field emission properties of pristine and N-doped anatase TNTA grown on Ti foils. Section three pertains to studies on wetting - dewetting properties of pristine and N-doped TNTA.

4.1. Photovoltaic Studies

4.1.1. Introduction

Different forms of TiO_2 nano architectures have been used as electrodes in third generation solar cells (dye sensitized solar cells, DSSCs) which includes quantum well, nanorods, nanowires, nanotubes and nanoparticles.[1-5] Among these one dimensional nanostructures, vertically aligned nanotube arrays offer distinct advantages such as high surface area for dye adsorption thereby enhancing light harvesting, readily accessible space for intercalation of redox electrolyte and easy electron transfer from the dye to the electrode and electrode to the electrical contact due to their vectorial nature.[6] However, the DSSCs fabricated using vertically aligned TNTA on Ti foils, as semiconducting electrodes[7,8] are limited by the need for illumination from the counter electrode side which reduces light intensity. In order to resolve this issue, several research groups synthesized transparent TNTA films by anodizing Ti thin films,[9-11] especially those deposited on FTO coated conducting glasses. In this case, the Ti films deposited on ITO/ FTO coated glasses are anodized to obtain TNTA thin films. The preparation method is challenging as the deposited Ti thin films are anodized at high positive potentials, which can lead to detachment of Ti film and degradation of the ITO/FTO coatings, thereby reducing the overall conductivity. Several reports discuss these issues and their effect on the photovoltaic performance.[12-15]

The photovoltaic characteristics of DSSCs fabricated using TNTA thin films on conducting glasses as well as TNTA on Ti foils were investigated and compared in this section.

4.1.2. **Experimental:**

4.1.2.1. Solar Cell Fabrication and testing

Vertically aligned TNTA were synthesized by anodizing Ti foils and Ti thin films deposited on FTO coated glasses at 40 V in ethylene glycol containing 0.5 wt% NH_4F and 2.5 wt% H_2O for 2 h at room temperature as described in chapter 3. The TNTA were then annealed at 400 ^oC to obtain anatase phase. The anatase TNTA were soaked in 0.5 mM Ruthenium I pyridyl, N-719, dye[16] (solaronix, Switzerland, which absorbs light in the wavelength up to 750 nm) in 3:1 volume ratio of acetonitrile and ethanol, for 12 hours. The dye adsorbed TNTA were then washed thoroughly with ethanol to remove the excess dye. The dye adsorbed film was then sealed with the Pt counter electrode using surlyn thermoplastic seal (Solaronix, Switzerland) of thickness 25 micrometers leaving a window area of 16 mm^2. The Pt counter electrode was fabricated by spin coating 3 mM aqueous H_2PtCl_6 followed by annealing at 400 ^oC for 10 mins. The iodolyte electrolyte (Solaronix, Switzerland) was injected into the cell through a small hole provided in the Pt counter electrode and the hole was sealed with a transparent tape. The device was tested under red LED light (LXHL-ND98 Red Luxeon) of 1.6 and 0.66 mW/cm^2 intensities. The photovoltaic characteristics of the device were obtained by applying an external potential bias to the cell and measuring the generated current using a potentiostat (Autolab PGSTAT302N).

4.1.3. Results and Discussions:

4.1.3.1. Photovoltaic studies

Solar cells were fabricated using anatase TNTA on Ti foils and on FTO coated glasses. The lengths of TNTA were 6.7 and 1.2 micrometer, for arrays grown on foils and conducting glasses, respectively. The efficiency η of the DSSC fabricated using TNTA films on Ti foils and FTO coated glasses were calculated, from the I-V characteristics, using the equation

$$\eta = \frac{J_{sc} V_{oc} FF}{P_{int}} \qquad (1)$$

where J_{sc} is the short circuit current density, V_{oc} the open circuit potential, FF the fill factor and P_{int} is the incident light intensity in mW/cm^2. The fill factor is calculated by the equation

$$FF = \frac{P_{max}}{I_{sc} V_{oc}} \qquad (2)$$

where I_{sc} is the short circuit current and P_{max} the maximum power obtained from the I-V plot. The incident photon to current conversion efficiency (IPCE) was calculated using the equation

$$IPCE = \frac{1239 J_{sc}}{P_{int} \lambda} \qquad (3)$$

where λ is the wavelength of the light energy used (λ = 625nm). For DSSCs fabricated using TNTA on foils, the incident light was probed from the counter electrode side (back side illumination) whereas, for those fabricated using transparent TNTA on FTO coated glasses, the incident light was probed from the working electrode side (front side illumination). Figure 4.1 shows the photocurrent-voltage characteristics of the fabricated DSSCs under red light illumination. Table 4.1 shows photovoltaic characteristics calculated from the I-V curves. The efficiency of the DSSC fabricated using TNTA on foils and FTO glasses, though matches with the results published in the early stages of DSSC studies,[14, 15] are low compared to the results published in a recent study by Oommen et al.[12] The fill factor (*FF*), which is defined as the ratio of maximum power (P_{max}) to the product of the short circuit current (I_{sc}) and the open circuit potential (V_{oc}), reflects the quality of the solar cell. The reduced efficiency can be ascribed to

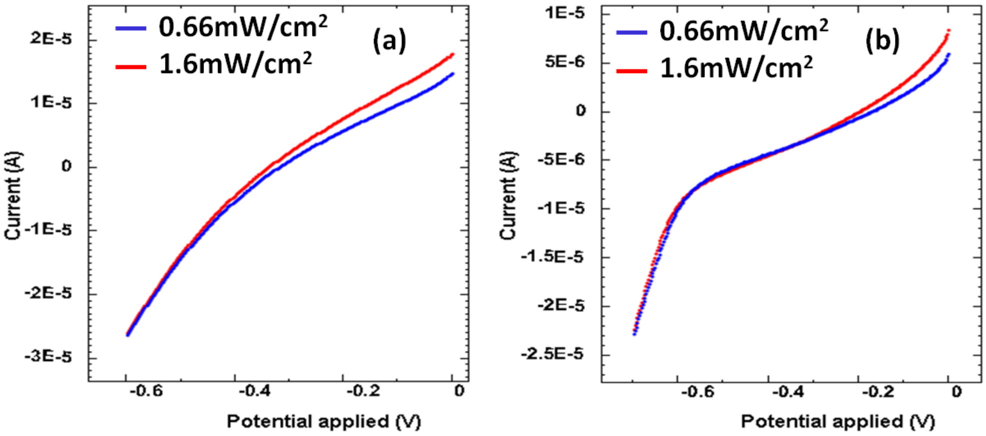

Figure 4.1a - b: The photocurrent-voltage characteristics of the TNTA on foils and thin films under red light illumination of different intensities.

Material	Film thickness (μm)	Light intensity (mW/cm^2)	J_{sc} (A/cm^2)	V_{oc} (V)	Maximum Power (P_{max})	FF	η (%)	IPCE(%)
TNTA on Ti foil	6.9	0.66	92.9x 10^{-6}	0.32	1.21x10^{-6}	0.26	1.2	28.7
		1.6	112.0x 10^{-6}	0.36	1.57 x10^{-6}	0.24	0.65	13.8
TNTA on FTO glass	1.2	0.66	37.3x 10^{-6}	0.34	6.5 x10^{-8}	0.033	0.07	11.5
		1.6	58.8x 10^{-6}	0.402	2.56x10^{-7}	0.076	0.11	7.2
Commercial TiO_2 on FTO glass	10	0.66	1.85x 10^{-4}	.550	5.5x 10^{-4}	0.6	9.2	55
		1.6	3.7.9x 10^{-4}	.596	11.6 x 10^{-4}	0.58	7.8	44.57

Table 4.1: The photovoltaic characteristics calculated from the I-V curves

the low *FF* value obtained in the present case. The very low efficiencies / FF values, obtained in the present study, can be attributed to the non optimized fabrication techniques, improper adsorption of the dye on to the TNTA, limited tube length in the case of TNTA on FTO coated glasses and inferior quality of the fabricated Pt counter electrode. In addition, reduction in the conductivity of the FTO coating due to its degradation by excess anodization and heat treatment at 400 ^oC for improving the TiO_2 crystallinity cannot be ignored. Also no scattering layer was introduced to increase the efficiency of the DSSC.

To ascertain the above said limitations of the cells, DSSCs were fabricated using TiO_2 coated FTO glasses and Pt counter electrodes procured from Solaronix, Switzerland, with the same dye and electrolyte employed before. The I-V characteristics of the cell fabricated using electrodes procured from Solaronix is given in Figure 4.2. Efficiencies of 9.2 and 7.8% were obtained at light intensities of 0.66 and 1.6 mW/cm^2, respectively. The difference in efficiency compared to those obtained from DSSCs based on TNTA electrodes indicates the inferior quality of the TNTA and Pt electrodes. This was further ascertained from the preliminary electrochemical impedance spectroscopic (EIS) studies. The impedance spectra obtained for the cells fabricated using indigenously made TNTA and Pt counter electrodes as well electrodes procured from Solaronix, under 0.66 and 1.6mW/cm^2 light intensities as well as in dark are given in Figure 4.3. From the figure it clear that the impedance of the cells fabricated, using TNTA and Pt counter electrodes made in house, are very high implying their inferior quality for application in DSSCs. Further studies are required to fabricate high efficiency DSSCs with TNTA electrodes with improved fabrication and assembly procedures.

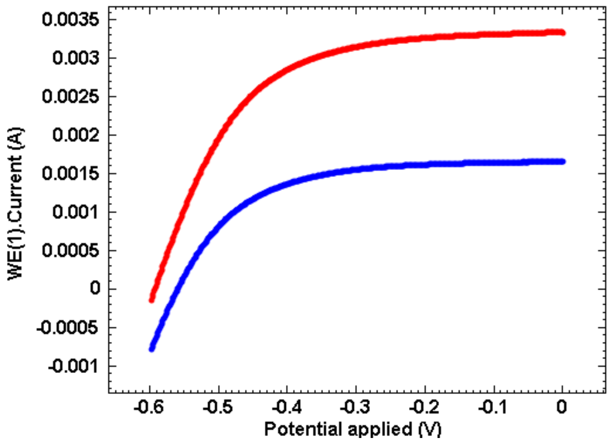

Figure 4.2: The photocurrent-voltage characteristics of the cell fabricated using electrodes procured from Solaronix under red light illumination, red line corresponds to the light intensity of 1.6 mW/cm^2 and blue corresponds to the light intensity of 0.66mW/cm^2.

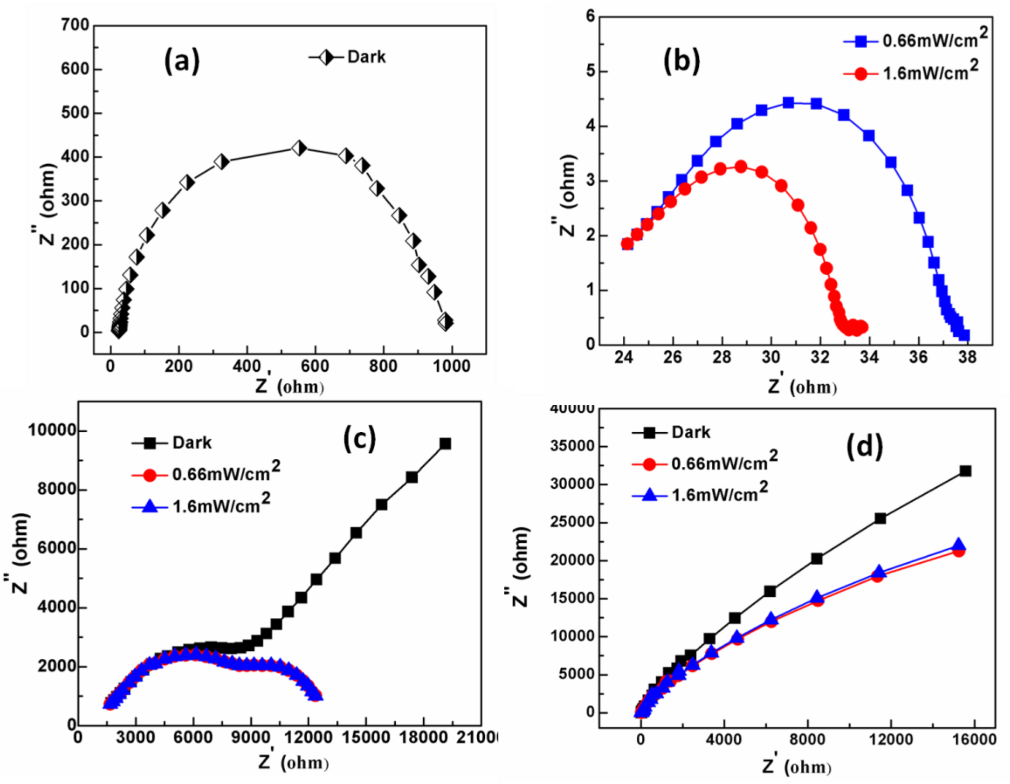

Figure 4.3a-d: Electrochemical Impedance spectra of (a) of the cell fabricated using electrodes procured from Solaronix in dark; (b) of the cell fabricated using electrodes procured from Solaronix under light illumination at different intensities, (c) and (d) of the cells fabricated using TNTA on foils and thin films.

4.2. Field Emission Studies of pristine and N-doped TiO_2 nanotube arrays

4.2.1. Introduction

Vertically aligned one dimensional nanostructures of semiconducting oxides are of much interest because of their possible application as efficient point electron sources in electron filed emitters. Generally carbon nanotube and nanowires has been widely explored due to its small tip radius of curvature, high aspect ratio and mechanical toughness. However, residual oxygen which is always present in the vacuum chamber can oxidize them causing reduction in the efficiency. Since properties of TiO_2 are not affected by the residual oxygen in the vacuum chamber, use of vertically aligned TiO_2 nanostructures is an alternative.

Field emission (FE) properties of TiO_2 are rarely investigated[17] prior to 2004, in spite of its low work function (4.5 eV) compared to other popular FE materials such as ZnO (5.3 eV), ZnS (7.0 eV) etc.[18] However, successful syntheses of self aligned quasi one dimensional TiO_2 nano-architectures with enhanced electrical properties, in thin film form, have attracted attention in investigating the FE properties of TiO_2. Field emission properties of aligned single crystalline TiO_2 nanowires grown on Ti, Si and Au doped TiO_2/Si substrates as well as that of self-aligned TNTA are reported in the literature.[19-24] Enhancement in FE properties on N doping are also reported[24, 25]. The study by Liu et al [24] is the only report on enhancement of FE properties of self-aligned TNTA on N-doping prior to 2010. The FE enhancement observed by Liu et al[24] after annealing the self aligned TNTA in ammonia atmosphere at 550 ^{o}C for 5 h was explained on the basis of introduction of donor states below the conduction band minimum (CBM), due to the presence of oxygen vacancies, and isolated localized N 2p state above the O- 2p dominant valence band. Both these effects induced by the partial substitution of oxygen atoms by nitrogen atoms in the anion sub-lattice. The chemical state of nitrogen in the doped sample was ascribed to N-Ti-O from the results of XPS. The N-1s BE obtained by them is 399.8 eV. Careful analyses of the XPS data, based on the results obtained by several researchers, reveal that the N-1s BE of 399.8 eV obtained by Liu et al corresponds to any one of the species viz. surface adsorbed N_2, surface adsorbed NO, bulk interstial NO^{2-}, interstitial N_2, interstitial N and interstitial NH. Detailed XPS analyses of single crystals of TiO_2 (110) annealed in ammonia atmosphere, by Diwald et al [26], showed an N-1s BE of 399.6 eV and has been assigned to interstitial NH. A recent XPS study, by Palgrave, Payne and Egdell [27] on TiO_2 (110) annealed in ammonia atmosphere at 550, 600 and 675 ^oC, and spectra acquired at 90^o and 10^o take off angles showed the presence of an N-1s peak at 399.8 eV. They have ascribed the N-1s peak to interstitial trapped nitrogen, N_i. Their study also concluded that the presence of N_i has little effect on the band gap of TiO_2 and the observed band gap narrowing is almost entirely due to substitutional nitrogen in the anion sub-lattice, N_O. In addition, several other researchers who have studied N-doping by annealing TiO_2 single crystals in ammonia atmosphere in the temperature range 300 to 700 ^oC, have identified the N-1s peaks obtained in the range ~399 to ~400 eV as belonging to interstitial nitrogen, N_i. [28-32]

In view of the above, the assignment of N-1s BE value of 399.8 eV, obtained by Liu et al from the XPS studies of vertically aligned TNTA annealed in ammonia atmosphere at 550 ^oC for 5 h, to substitutional nitrogen in the oxide ion lattice (N-Ti-O), and the explanation given for enhancement in electron FE on N-doping warrants further investigation.

The FE enhancement on N-doping can be explained clearly if one can synthesize N-doped TiO_2 corresponding to different N concentrations in the oxide ion lattice and study the electron FE variation with the N concentration. In the present study, the FE properties of pristine and N-doped TNTA corresponding to different concentrations of nitrogen in the oxide ion lattice are investigated.

4.2.2. **Experimental**

Pristine and N-doped anatase phase TNTA grown on Ti foils (size 10 mm x 20 mm) at 40 V for 2 h, as described in chapter 3, was mounted on a copper plate using silver paste. A flat cut mirror polished molybdenum rod of 3.0 mm diameter was used as the anode. The whole unit was housed in a vacuum chamber and pumped to 2 x 10^{-7} mbar. The positive terminal of a high voltage source (2 kV) has been connected to the anode and the other terminal to the copper plate. The gap between the anode and cathode was kept at 50 μm. The FE current was derived indirectly by measuring the voltage drop across the 500 kΩ resistor while applying the voltage to the anode in steps of 20V from 20V to 1650 V. The measured emission area was 0.07 cm^2. The schematic of the experimental set up is represented in Figure 2.8 of chapter 2.

4.2.3. **Results and Discussions**

Pristine and N-doped anatase phase TNTA grown on Ti foils at 40 V for 2 h and annealed at 400 ^{o}C, which has the best surface morphology as described in chapter 3, was chosen for the FE studies. The morphologies, crystal structure and composition of the samples used are given in the chapter 3. The nitrogen concentrations (as nitrogen substituting oxygen in the anion sub-lattice) of the doped samples, calculated from the XPS results, used for FE studies, are detailed in chapter 3 and are 3.88, 4.12 and 4.74 at% .

The variation in emission current density with field, obtained from the FE experiments, for $TiO_{2-\delta}$ and N-doped TNTA are shown in figure 4.4. From the plot, it is apparent that for $TiO_{2-\delta}$ nanotube arrays the electron emission is insignificant and is detected only beyond 20 V / μm. The N-doped samples exhibited an exponential-like behaviour which was found to be reproducible. For the N-doped TNTA, the electron emission was detected at much lower turn on fields (the field at which the current first increases from the background) viz., 12.5, 10.4 and 7.1 V / μm at 3.88, 4.12 and 4.74 at% of nitrogen doping, respectively. The corresponding current densities are greater than 33 μA / cm^2. The lower turn on values indicate that N-doping plays a significant role in enhancing the FE properties. The emission field corresponding to 1 mA / cm^2 for the N-doped TNTA of 3.88, 4.12 and 4.74 at% of nitrogen are 11.76, 14.61 and 20.43 V / μm, respectively. The electron FE current of the N-doped TNTA of 4.74 at% nitrogen was studied at 28 V / μm for 280 minutes and found to be stable.

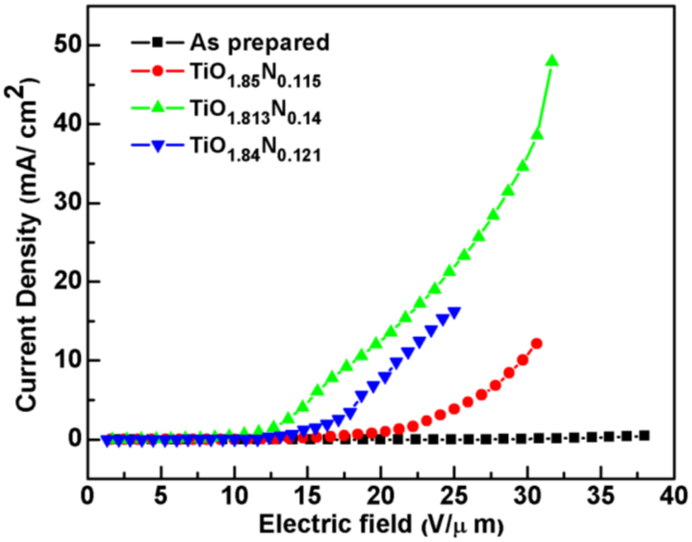

Figure 4.4: FE characteristics (current density Vs field plot) of the pristine as well as N-doped TNTA.

Liu et al obtained a turn-on field of 11.2 V / μm with current density of 10 μA / cm^2 for 9 at% nitrogen incorporated into TNTA. Though Liu et al did not observe N-1s BE values corresponding to substitutional nitrogen, (in the range 396 to 398 eV) they obtained enhancement in FE values. The enhancement can be attributed to oxygen vacancies generated on annealing of TNTA in NH_3 atmosphere as well as due to nitrogen incorporation into the interstitial locations.

At a temperature ≥ 550 °C, NH_3 is decomposed releasing H_2. This reducing atmosphere can cause partial reduction of TiO_2[27]. In addition the results by Palgrave[27] suggest that the presence of interstitial nitrogen has little effect on the electronic structure modification / band gap alteration in TiO_2. The generation of oxygen vacancies on annealing in NH_3 atmosphere is seen from the O-1s spectra of annealed samples, obtained by Liu et al. The O-1s BE obtained by them at 530 and 532 eV can be assigned to Ti^{4+}-O and Ti-$(OH)_2$-Ti bridge / $(Ti(OH)_xO_y$, respectively[33]. The oxygen vacancies modify the electronic structure by introducing band gap states, ~0.75 eV, below the conduction band minimum (CBM) and their population increases in direct proportion with the defect density[34]. This will enhance electronic FE.

The FE properties can be analyzed by the Fowler-Nordheim (F-N) tunneling model[35,36] given by the equation

$$ln\frac{j}{E^2} = ln\frac{A\beta^2}{\phi} + \frac{-B\phi^{3/2}}{\beta}\frac{1}{E} \qquad (4)$$

where *j* is the current density, *E* is the applied electric field, Φ is the work function and β is the field enhancement factor associated with the magnitude of the electric field at the emitting surface and is given by $\beta = E_{local} / E$, where E_{local} is the local electric field at the emitting surface.[37] *A* and *B* are constants with values of 1.54×10^{-6} (A eV / V^2) and 6.83×10^9 ($V\ m^{-1}\ eV^{-3/2}$), respectively. The work function Φ of TiO_2 is 4.5 eV.[38] Assuming the change in work function, on creating intrinsic oxygen deficiency and N-doping, to be negligible, the field enhancement factor β can be calculated from the F-N plot, ie; $(ln(j/E^2))$ against $(1/E)$. The F-N plots of N-doped TNTA, $(ln(j/E^2)$ vs $1/E)$, corresponding to the j-E characteristics obtained in this study (figure 4), above the turn-on field, are given in figure 4.5. The F-N plots show deviation from linearity signifying the semiconducting nature of N-doped TNTA.

The F-N plots for the 4.12 and 4.74 at% nitrogen doped samples can be divided in to three regions, two regions of linear behavior separated by an intermediate region of higher slope. In the case of sample with 3.88 at% N-doping, the intermediate region is still visible but not as clear as in the former cases, the data points here can reasonably be fit into a straight line. It is clearly seen that the intermediate region diminishes with decrease in nitrogen content. Different slopes are related to different states where electron can only be emitted beyond their critical fields.[39] From the slope of the fitted straight lines the enhancement factor β can be calculated. The enhancement factor β, of the N-doped samples is calculated from the respective slopes of the linear sections at low field value which is claimed to be FN effective.[39] The effective work function, Φ_{eff}, defined as $\Phi_{\mathrm{eff}} = \Phi/\beta^{2/3}$ is then calculated from β. The calculated β and Φ_{eff} values are given in Table 4.2. From Table 4.2 it is clear that the enhancement factor increases with increase in the nitrogen content. Also the effective work function decreases with increase in nitrogen doping. From the above observations, it can be concluded that the enhancement in the FE is due to the nitrogen doping. A comparison of emission field corresponding to emission current density of 1 mA / cm^2 obtained by various groups for different TiO_2 nano-architectures is given in reference.[25]

The enhancement in the FE property of the N-doped TiO_2 compared to the pristine one is ascribed to modification in the electronic structure resulting from N-doping. It is well known that titanium dioxide is oxygen deficient and in $TiO_{2-\delta}$ oxygen vacancies form localized donor states 0.75 – 1.18 eV below the CBM.[40-43] When oxygen vacancies are formed by the removal of neutral oxygen atoms from the anion sub-lattice, the excess electrons left over in the crystal lattice are redistributed among the nearest-neighbor Ti ions. This will increase the electron cloud density on the Ti ions (Ti 3d orbital) by reducing the valance state from Ti^{4+} to lower states

(Ti^{3+}). The populated localized donor states below the CBM, originated from the Ti 3d orbits, increase with increasing oxygen vacancies, and can even overlap with the conduction band in the case of highly oxygen deficient anatase TiO_2 thereby shifting the Fermi level to higher energy.[40,44]

In the case of $TiO_{2-3y}N_{2y}$, compared to $TiO_{2-\delta}$, there are additional oxygen vacancies due to N-doping. This increases the band width of the localized donor states and the energy gap between the localized donor states and CBM reduce to values below 0.75 eV (0.75 - Δ). It has been shown from experimental results and first-principle calculations that substitution of oxygen by nitrogen atoms in TiO_2 can create an isolated localized N-2p state above the O-2p dominant valence band maximum (VBM).[45-50]

From photo electrochemical studies, it has been shown that the localized N-2p state is located at ~0.75 eV above the VBM.[51] The presence of localized donor states located at (0.75- Δ) eV below the CBM and N-2p state at ~0.75 eV above the VBM will shift the Fermi level to higher energies as compared to TiO_2. Hence, compared to $TiO_{2-\delta}$, the Fermi level in $TiO_{2-3y}N_{2y}$ will be more close to the CBM. Since electron emission from a material to vacuum under the influence of an electric field take place by tunneling of electrons lying below the Fermi level through the potential barrier,[52,53] the rise in the position of the Fermi level will augment the FE properties consequent to lowering of work function.

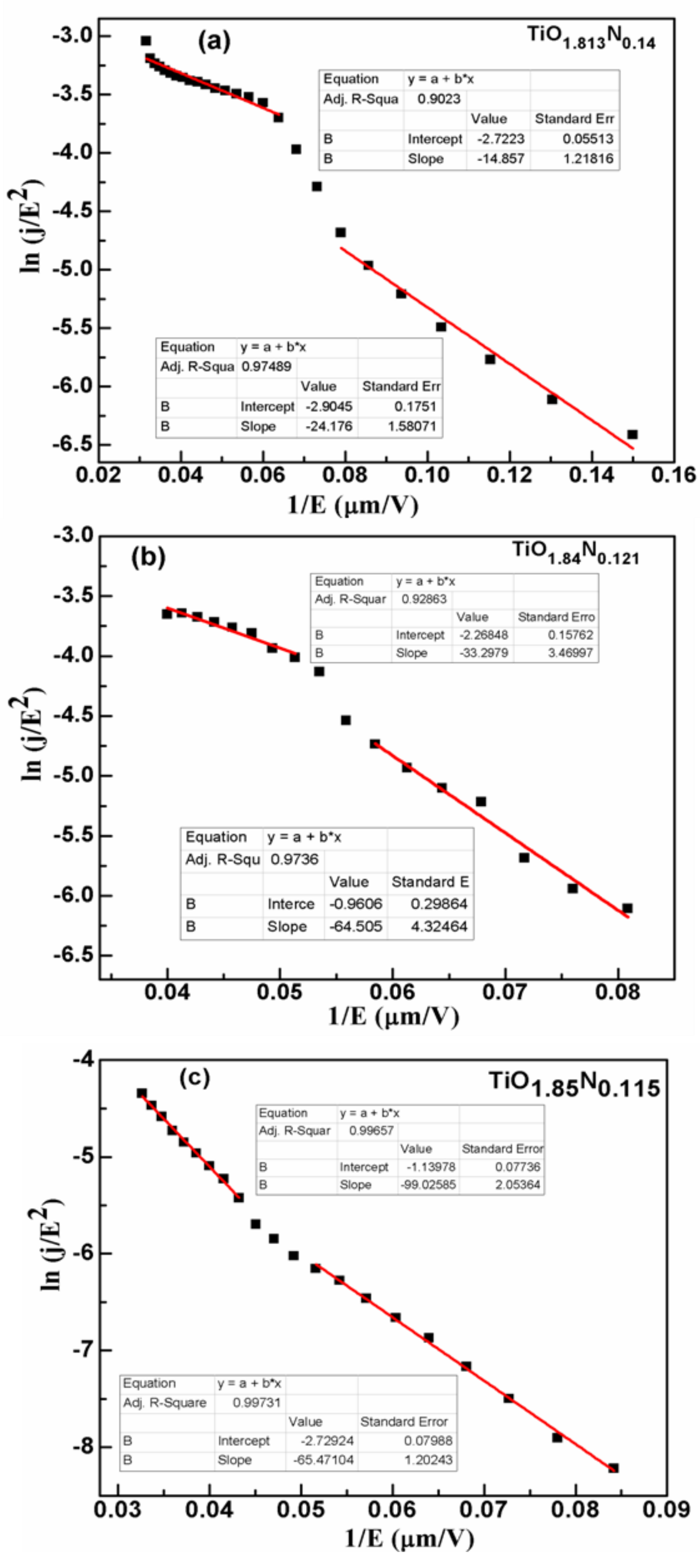

Figure 4.5: F-N plot of N-doped TNTA.

Sample	Turn on field (V/μm)	slope	Enhancement factor (β)	Effective work function (ϕ_{eff}) eV
Undoped TiO_2	20.25	-299.88	217.39	0.124
$TiO_{1.85}N_{0.115}$	10	-99.02 (high field) -65.47 (low field)	995.76	0.045
$TiO_{1.84}N_{0.121}$	9.21	-33.29 (high field) -64.50 (low field)	1010	0.045
$TiO_{1.813}N_{0.14}$	6.54	-14.85 (high field) -24.17 (low field)	2696.00	0.023

Table 4.2: The F-N slope, enhancement factor (β) and effective work function (Φ_{eff}) of pristine and N-doped TNTA thin films, calculated from the electron FE curves.

The F-N theory is strictly valid for metals when it was first derived in 1928.[36] For semiconductors, the theory of FE was deduced by R. Stratton in 1955.[54] An earlier publication by N. Morgulis have reported the effect of weak field penetration on electron emission from conduction band and the approximate estimate for the emission from the valence band.[55] Later a theoretical analysis of FE by Baskin et al was also published.[56] For large area FE, because of the high density of individual FE sites, the local field F at the tip of the individual emission sites is determined by its shape and size. In the case of one dimensional nanostructured semiconductors like vertically aligned nano-wires and nanotubes etc., the local field at the tip is greater than the applied field (E) and can be related to E_M (local field) by the following equation

$$E = \beta E_M \tag{5}$$

where the parameter β is called the "field enhancement factor" and is basically determined by the aspect ratio of the nanotube. It has been reported in the literature as well as observed in the present study that the F-N plots of vertically aligned one dimensional nano-structured semiconductors show non linear behavior which can be attributed to different factors. The aligned nanostructures have a strong local electric field at their tips due to their orientation parallel to the electric field direction. The effective work function, in these type of materials, depends on the applied electric field and surface states leading to non linear behavior. Taking this into consideration, the J-V relationship, according to the F-N theory which is applicable strictly for metals, is modified for semiconductors as given in the following:

$$J = \frac{A\beta^2 E^2}{\phi} + \frac{-B\phi^{3/2}}{\beta}\frac{1}{E} + \frac{(-\Delta W^s - \Delta W^P)}{2kT} \qquad (6)$$

where J is the emission current density, A and B are constant, φ is the work function, β is the field enhancement factor, E is the electric field, ΔW^s is the increase of surface barrier potential for semiconductor nanostructures due to surface states and ΔW^p is the decrease of surface barrier potential owing to field penetration.[36, 57] In the present case, because of the large surface area of vertically aligned TiO_2 nanotubes, the density of surface states will be high and the electrons from the conduction band are trapped in the surface states raising the surface potential barrier. At low fields the surface potential barrier dominates FE whereas at high electric fields the surface potential barrier will decrease because of field penetration. Hence, linear regions with different slopes are expected in the F-N plot. In the present study three regions could be observed. The low field region corresponds to surface states dominated FE. In the high field region, the field penetration breaks down the surface potential barrier increasing FE. In the intermediate region both these mechanisms compete resulting in a different slope. In each region, the F-N plot varies linearly and the corresponding slopes reflect the "β" value in that region. The effective work function corresponding to each region is related to the corresponding enhancement factor β.

From these studies it is clear that the electron FE of TiO_2 can be enhanced by substitutional N-doping, as it results in creation of interband electronic states below the CBM and above VBM thereby raising the Fermi level with consequent decline in work function.

4.3. Wetting properties

4.3.1. Introduction

Surface wetting is an important property of materials and plays an important role in nature and technology. The surface on which water droplets remain as almost perfect spheres (contact angles ≥ 150^o) and rolls off without leaving any residue are termed as superhydrophobic and the surfaces on which water droplets spreads completely (contact angles ≤ 5-10^o) are termed superhydrophilic.[58] Since the discovery of photo-induced hydrophobic to hydrophilic conversion in TiO_2 layers / thin film surfaces by Wang and co-workers in 1997[59], TiO_2 coatings/thin films have attracted wide attention as photo-functional materials for self-cleaning, antifogging, antibacterial and stain-proofing agents.[60,61] It has also been observed from contact angle measurements of water droplets on TiO_2 thin film surfaces that the reversible hydrophobic ↔ hydrophilic conversion can be achieved by keeping the irradiated samples in the dark[62-65]. The surfaces that are able to switch between superhydrophobic and superhydrophilic states are of importance[66] because of their potential application to enhance rapid water motion,[67] improve micro-fluidic devices[68] and create smart membranes[69] and sensors.[70]

Based on the experimental results, research groups across the world have proposed different mechanisms for the photoinduced superhydrophilicity of TiO_2. Among those, the three major ones are generation of surface oxygen vacancies, reconstruction of surface Ti-OH bond and photocatalytic organic decomposition on TiO_2 surface.[71] The mechanism for the photo induced hydrophobic ↔ hydrophilic conversion was first proposed by Wang et al.[63] In this mechanism, the photo-generated holes diffuse to the surface and create surface oxygen vacancies. The created surface oxygen vacancies cause reduction of Ti^{4+} to Ti^{3+} and this Ti^{3+} facilitates dissociative chemisorption of molecular water at the oxygen vacancies leading to the generation of surface hydroxyl groups. The generation of surface Ti-OH groups results in structural changes of the TiO_2 surface such that the intrinsically hydrophobic surface is converted to hydrophilic.[72-74] The reverse happens, as though slowly, when kept in dark due to dehydration process. The overall process can be represented as[75]

$$\equiv\text{Ti-O-T}\equiv \underset{dark}{\overset{\text{O2,h}\nu\geq\text{EBG}}{\rightleftarrows}} \equiv\text{Ti-OH}\ \ \text{HO-T}\equiv \qquad (7)$$

Sakai et al proposed another mechanism for Ti-OH generation in 2003[76], where the Ti-O bond is lengthened and weakened by the diffused holes. The adsorption of water causes the bond rupture. A proton is separated and a new OH group is built resulting in singly co-ordinated two OH groups. A different mechanism for photo induced hydrophilicity proposes the migration of photo-generated holes and electrons to the surface followed by destruction of very small amount of hydrocarbons, responsible for the hydrophobicity, present on the surface, by the reaction[76]

$$\text{Hydrocarbons} + O_2 \xrightarrow[h\nu\geq 3.2eV]{} \text{minerals (such as } CO_2 \text{ and } H_2O) \qquad (8).$$

Once the hydrophobic organics are removed, the surface turns hydrophilic. The slow reconversion to hydrophobic surface, when kept in the dark is explained on the basis of re-contamination of the hydrophilic surfaces by air-borne hydrophobic organics.[64] The ability of TiO_2 surfaces to photocatalytically degrade water and air pollutants coupled with its superhydrophilicity forms the basis for making self cleaning surfaces. To date there are only few reports on synthesis, characterization and reversible hydrophobic ↔ hydrophilic switching behavior of TiO_2 thin films.[60,62,63,77-79]

Recently, in 2009, Takahashi and Yui[80] analyzed the surface OH groups on the rutile TiO_2 surface by Polarization Modulation Infrared External Reflection Spectroscopy (PM-IER) under atmospheric conditions and proposed a mechanism for the surface wetting of TiO_2. Even though they could locate the surface hydroxyl groups on (110) and (100) surface (bridging oxygen sites) of rutile TiO_2, they didn't observe any increase in the surface hydroxyl groups after UV irradiation. They proposed that the observed hydrophilicity is not due to the generation of surface T-OH species but to the enhancement in hydrogen bonding between the water molecules / water molecules and OH species on TiO_2 surface due to the presence of intermediates such as hydrogen peroxide (H_2O_2) and hydronium ions (H_3O^+) produced by photo generated holes and / electrons.

Studies on photo induced hydrophilicity as well as reversible hydrophobic ↔ hydrophilic switching behaviour of TNTA were carried out by Patric Schmuki's group.[81-84] They have observed that the surface wetting properties of nanotube arrays is a strong function of tube diameter[82] and can be altered using organic monolayer coating coupled to UV irradiation.[83] Recently Kontos et al systematically correlated the morphological characteristics of electrochemically synthesized TNTA with UV-induced superhydrophilicity[81]. They have modeled the wetting and UV-induced superhydrophilicity by combining the Cassie-Baxter mode with Wenzel mode. Recently another report detailing synthesis as well as visible light assisted reversible hydrophobic ↔ hydrophilic switching behaviour of N-doped TiO_2 thin films has been reported[85].

The present section discusses photo-induced hydrophobic to superhydrophilic conversion of vertically aligned pristine and substitutional N-doped TNTA, correlation between morphology and photo-induced hydrophilicity as well as their reversible hydrophobic ↔ hydrophilic switching behaviour. The reversible hydrophobic to hydrophilic properties exhibited upon UV and sun light irradiation were studied and compared. Following the study by Kontos et al[81] the photo-induced superhydrophilicity was modeled by combining the Cassie-Baxter model with Wenzel model.

4.3.2. Experimental

Contact angle experiments were carried out on pristine and N-doped TNTA synthesized according to the procedures as explained in chapter 2, in an ambient environment, using a contact angle meter equipped with CCD camera (Holmarc, HO-IAD-CAM-01, India). An ultraviolet lamp (Philips, TUV, 8W) was employed as the UV light source. The intensity of the light incident on the film was 1.4 mW/cm^2. The intensity of the sunlight was 44 mW/ cm^2. Before contact angle measurements, the TNTA were stored in a vacuum desicator under dark. The sessile drop method was used for the contact angle measurements. Distilled water was used as the water source and the volume of the water droplets dispensed was approximately 2-3 μl. From the acquired images, the contact angles were measured using Image J software.

4.3.3. Results and Discussions

The FESEM images of the N-doped TNTA are given in figure 4.6(a-e). The inset in each micrograph shows the corresponding water contact angle. Figure 4.6f is the cross sectional micrograph of the N-doped TNTA revealing the tubular structure. The tube parameters evaluated from the FESEM images (figure 4a-e) using image analysis software is given in table 4.3. The water contact angles obtained, before light irradiation, for vertically aligned pristine and N-doped anatase TNTA are ~140 and ~125^0, respectively. These are high compared to those reported in the literature for pristine TNTA.[81-84] It can be seen from Table 4.3 that the aspect ratio of the nanotubes especially the tube diameter varies with the synthesis voltage.

No	Applied Voltage (V)	Diameter (D) nm	Wall thickness (w) nm	Height (h) nm	Intertubular distance (x) nm	surface density ρ (/μm^2)
1	20	47.7	4.23	2.39	13.67	193
2	30	71.45	4.9	2.69	22.26	93
3	40	97.41	7.9	6.8	29.8	62
4	50	105.88	8.46	8.3	38.5	50
5	60	128.68	10.8	13	31.76	30

Table 4.3: The tube parameters evaluated from the FESEM images using image analysis software. Surface density ‘ρ’ is the number of nanotubes per square micrometer of the anodized Ti surface

Figure 4.7 depicts the change in contact angle of N-doped TNTA with tube diameter. In the case of N-doped TNTA, with tube diameters in the range 45 to 100 nm, the observed contact angles are around 125^o. For arrays comprising of tube diameters of ~106 and ~130 nm, the observed contact angles are ~92 and ~53^o, respectively (Figure 4.6). The relatively high contact angle values despite the presence of very large porosity can be due to the cushion effect provided by air trapped in the vertically aligned nanotubes, which prevent the water droplet from penetrating into the tube. As tube diameter increases a decrease in cushion effect is expected and hence the reason for the low contact angle values observed in the case of nanotube arrays consisting of nanotubes of ~106 and ~ 130 nm diameters (nanotube arrays synthesized at 50 and 60 V, respectively). In addition, the formation of precipitates on the top surface, observed in samples synthesized at 50 and 60 V plays a role (Figure 4.8).

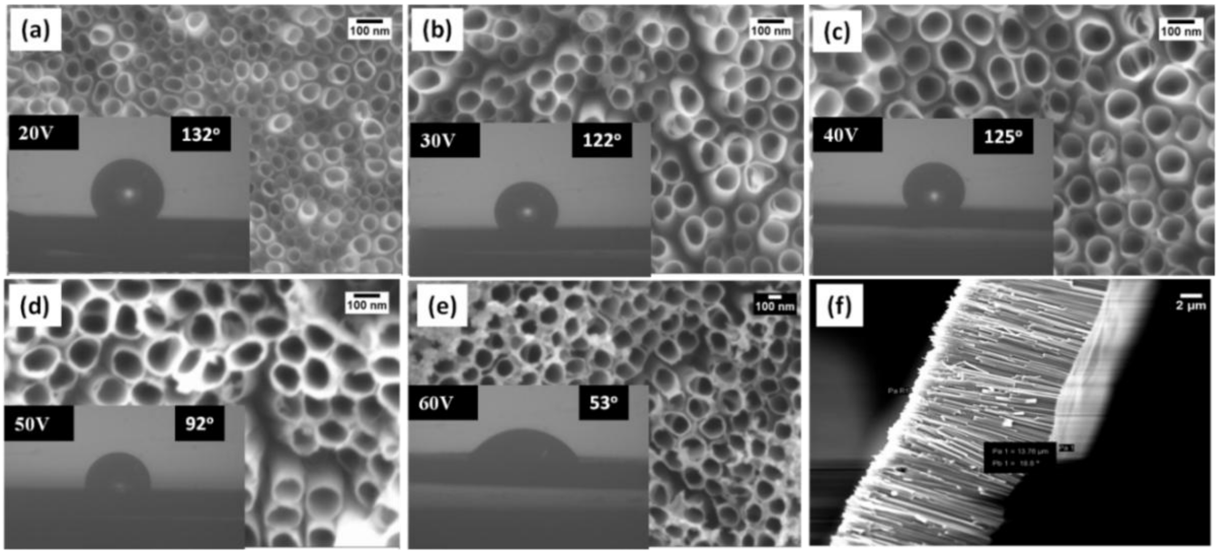

Figure 4.6a-e: The surface topography of the N-doped samples synthesized at (a) 20, (b) 30, (c) 40, (d) 50 and (e) 60 V and annealed at 400 ^oC for 2 h. inset shows image which reveals the water contact angle with increase in diameter and (f) Typical cross sectional FESEM image of the annealed sample.

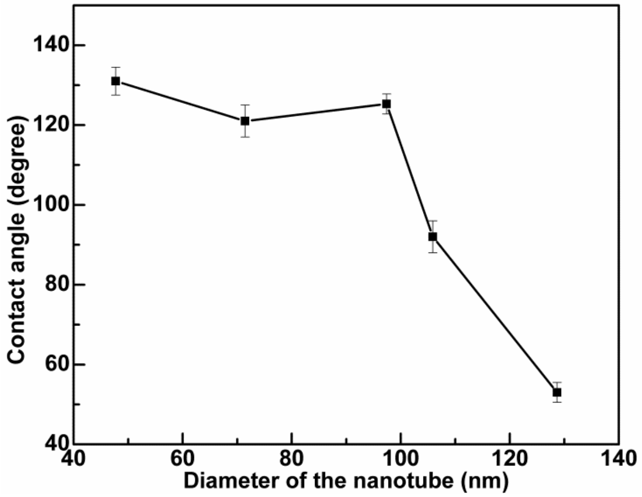

Figure 4.7: The variation in contact angle with tube diameter for N-doped TiO_2.

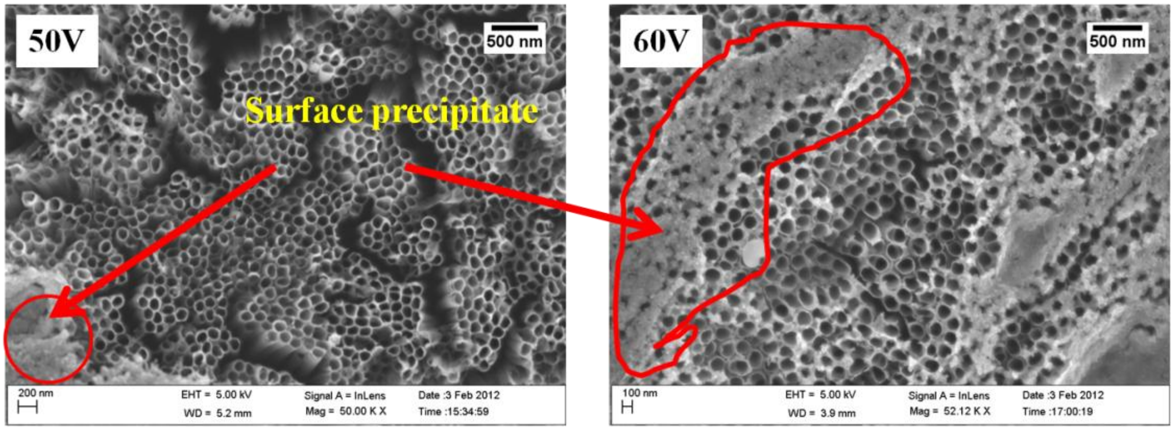

Figure 4.8: The FESEM micrographs of the samples anodized at 50 and 60 V (reveals the formation precipitates on the surface)

According to the Cassie and Baxter relation,[86, 87] the contact angle can be calculated using the equation:

$$Cos\ \Theta^* = f_s\ Cos\ \Theta - f_v \qquad (9)$$

where Θ^* is the real contact angle, Θ is the contact angle on surface of the smooth anatase TiO_2 (70^o)[61], f_s is the fraction of the surface area made up of solid TiO_2. This fraction corresponds to the TiO_2 surface area containing the nanotubes with respect to the total surface area of the sample including inter-tube voids and circular openings, f_v refers to surface fraction occupied by air and is equal to ($1-f_s$).

From the nanotube parameters obtained from FESEM images, f_s values were calculated using the equation:[81]

$$f_s = \frac{2\pi\ \omega(\omega + D)}{\sqrt{3}(D + 2\omega + x)^2} \qquad (10)$$

where ω, D and x are average tube wall thicknesses, inner diameters and spacing between tubes, respectively. The factor f_s can also be calculated using the expression[81]

$$* f_s = \pi\rho\ [(\frac{D}{2} + \omega)^2 - (\frac{D}{2})^2] \qquad (11)$$

where ρ is the tube density (number of tubes/unit area) obtained from FESEM images and $*f_s$ is the fraction of the surface area made up of solid TiO_2 obtained from tube density (eqn. 11) . The f_s and $*f_s$ values were obtained for the samples of different tube diameters (samples synthesized at different voltages), by using equations 10 and 11. The measured contact angles and contact angles calculated using the Cassie and Baxter relation (eqn. 9) employing the f_s and $*f_s$ values are given in table 4.4.

Applied Voltage(V)	CA measured (degree)	*fs*	**fs*	CA calculated using *fs*	CA calculated using **fs*
20	131	0.1634	0.1280	137.217	142.341
30	121	0.1266	0.1066	142.560	145.749
40	125.3	0.1479	0.1584	139.396	137.904
50	92	0.1299	0.1582	142.055	137.930
60	53	0.1648	0.1433	137.025	140.054

Table 4.4: The measured contact angles and those obtained from the Cassie and Baxter relation using the f_s and $*f_s$ values. Contact angles was calculated using the equation $Cos\ \Theta^* = f_s\ Cos\ \Theta - f_v$, Where Θ^* is the real (measured) contact angle, f_s is the fraction of the surface area made up of solid and is calculated from the equation, $f_s = 2\pi\ w(w + D) / 3^{1/2}\ (D + 2w + x)^2$ where $*f_s$ is calculated using the equation $*f_s = \pi\rho\ [((D/2) + w)^2 - (D/2)^2]$

The measured and calculated contact angle values for nanotube arrays of tube diameters 48, 71 and 97 are in good agreement. The deviation in contact angle values for arrays consisting of large diameter nanotubes (106 and 130 nm) can be due to the presence of precipitate on the surface (Figure 4.8) and reduction in air cushion effect because of large pore size.

Since in the present study, the nanotube arrays were synthesized in an organic medium, contamination of surfaces by organics is suspected even though the nanotube arrays were annealed in air at 400 ^oC for 2h. Hence, the samples were irradiated with high energy UV light (λ

= 250 nm, 1.4 mW/cm^2) for 10 h to remove the adsorbed organics responsible for hydrophobicity, if at all present in trace level. After 10 h of irradiation, the TNTA of different tube diameters showed superhydrophilicity (contact angle ≤ 5^o). The irradiated superhydrophilic samples were then stored in dark, in a vacuum desicator for weeks, intermittently taking out samples to measure the water contact angle. The investigations revealed that the initial hydrophobic state of the N-doped samples was recovered after 30 days. Whereas for the pristine samples, recovery of hydrophobic state was attained within 16 days. For further studies pristine and N-doped TNTA synthesized at 40 V and annealed in air at 400 ^{o}C for 2 h were chosen. The rationale behind the selection of samples synthesized at 40 V is that, out of all the samples synthesized at various voltages, the samples synthesized at 40V have the maximum surface uniformity and homogeneity in terms of tube diameter, inter tube spacing and tube wall thickness.

The images of water droplets and variation in contact angle with time left in dark, after 10 hours of UV irradiation, for pristine and N-doped TNTA are shown in Figure 4.9 and 4.10. The recovery rate calculated from the plots, for the pristine and doped samples are 0.144 and 0.053^o per day, respectively. The variation of water contact angles of the pristine and doped samples were measured with irradiation time till all the samples reached the superhydrophilic state. Figure 4.11 shows the change in contact angle with UV irradiation time. From figure 4.11 it is clear that both pristine and N-doped samples attained superhydrophilic state in 15 minutes. The contact angle decay depicts two distinct regimes viz. hydrophobic and hydrophilic. In the hydrophobic regime the variation is almost linear and change in contact angle is minimum, whereas it is exponential in the hydrophilic region. The change in contact angle in the hydrophobic regime is much less pronounced and its variation remains almost linear.

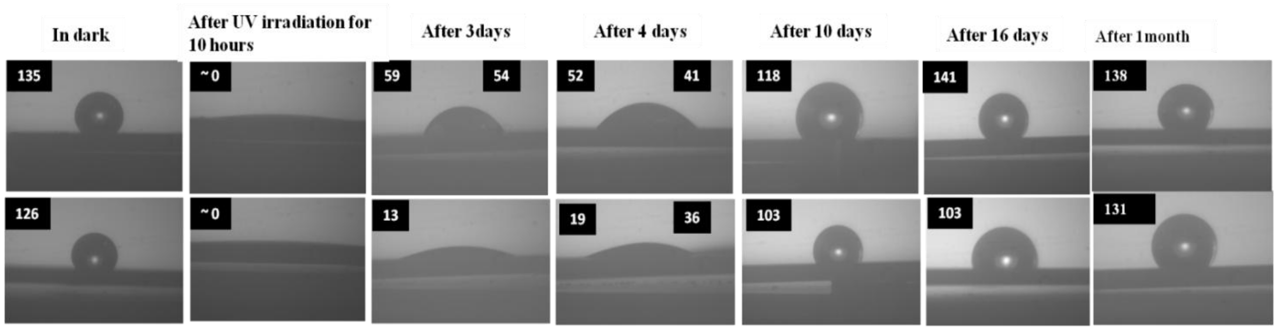

Figure 4.9: Images of water droplets, on pristine and N-doped TNTA, showing increase in contact angle with time nanotube arrays left in dark.

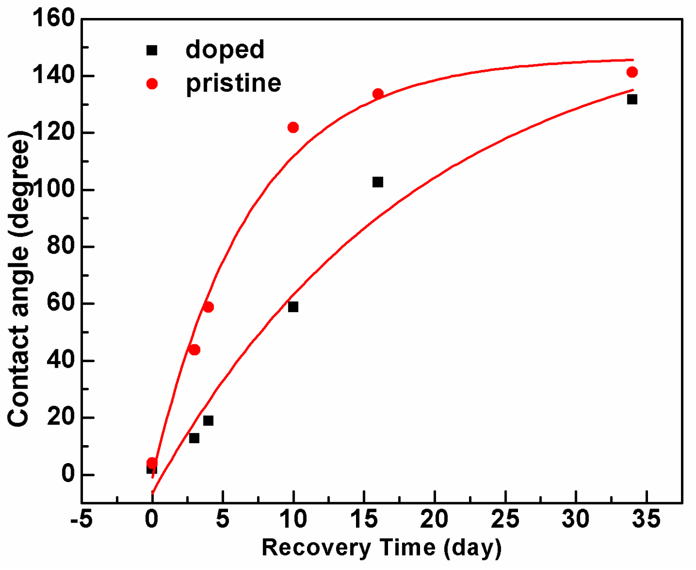

Figure 4.10: Increase in contact angle with time left in dark (after UV irradiation for 10h), for pristine and doped samples.

Thereafter it is not considered for kinetics study. The kinetics of the contact angle decay in the hydrophilic regime can be fitted using an exponential expression.[62,88]

$$\Theta = \Theta_0 \; e^{-kt} \qquad (12)$$

The value of the kinetic constant, *k*, for the contact angle decay under UV irradiation obtained for pristine and N-doped samples, from the plots (figure 4.11), are 0.57° min^{-1} and 0.67° min^{-1} respectively.

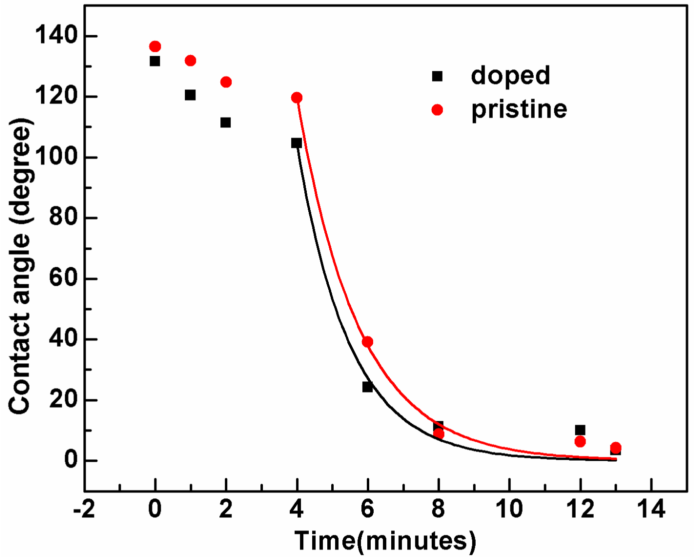

Figure 4.11: The variation of contact angle with UV irradiation time for pristine and N-doped TiO_2.

After attaining the superhydrophilic state, the samples were kept under dark condition and contact angles were measured intermittently to study the recovery to the initial hydrophobic state. The contact angles slowly increased with time, and the pristine and N-doped TNTA regained its hydrophobic state within 2 and 4 days, respectively. The increase in contact angle with time kept under dark can be fitted to an exponential function:

$$\Theta = \Theta_0 + Ae^{-k_{rec}t} \qquad (13)$$

as shown in Figure 4.12. The value of the kinetic recovery constant, k_{rec}, obtained from the plot, for the pristine and N-doped samples are 1.07 x 10^{-3} and 1.01 x 10^{-6} min^{-1}, respectively. The reversible hydrophobic ↔ superhydrophilic transition was studied several times to establish the reversible hydrophobic ↔ superhydrophilic switching capability of pristine and N-doped samples. The observed switching pattern is given in Figure 4.13.

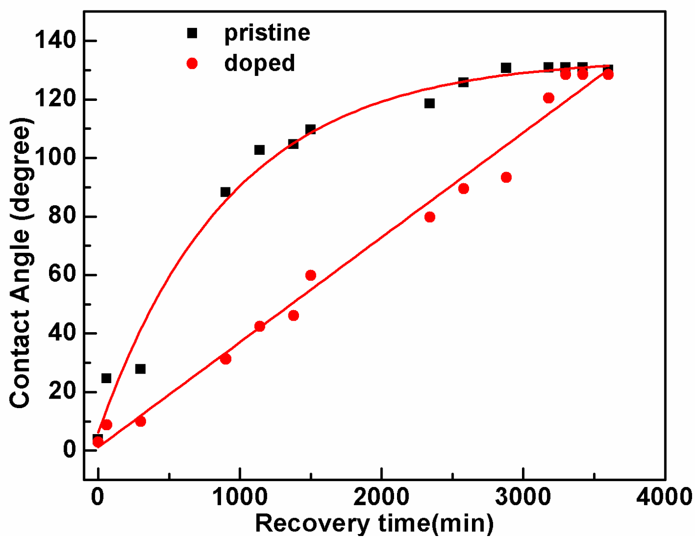

Figure 4.12: The increase in contact angle with time kept under dark after 15 minutes of UV irradiation for pristine and N-doped TiO_2.

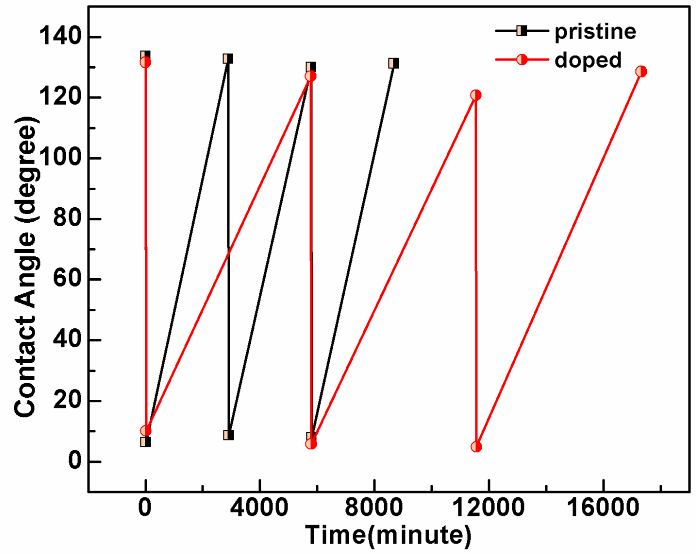

Figure 4.13: The reversible hydrophobic ↔ super hydrophilic switching capability of pristine and N-doped samples under UV/ dark

Since the results of diffuse reflectance spectroscopic studies (chapter 3) indicated visible light absorption by N-doped samples, the sun light induced hydrophobic – superhydrophilic transitions and reversible hydrophobic ↔ superhydrophilic switching behavior of N-doped samples were studied. The N-doped sample attained superhydrophilic nature in 90 minutes of sun light irradiation and recovered its initial hydrophobicity in two and a half days, when kept in dark. Figure 4.14 depicts the variation of water contact angle with time of sun light irradiation and increase in contact angle with time left in dark (after sun light irradiation for 90 minutes), respectively. The contact angle decay under sun light and recovery with time kept under dark can be fitted with exponential functions

$$\Theta = \Theta_0 \, e^{-k_{sun} t} \qquad (14)$$

$$\Theta = \Theta_0 + A e^{-k_{dark} t} \qquad (15)$$

respectively. The value of the kinetic decay constant (k_{sun}) and recovery constant (k_{dark}) obtained from the plots are 0.06 and 1.01 x 10^{-6} min^{-1}, respectively. Figure 4.15 shows the reversible hydrophobic ↔ superhydrophilic switching behaviour on exposure to sunlight / dark. The reversible hydrophobic to superhydrophilic switching behaviour, upon sun light irradiation followed by storage in the dark, indicate their potential use as visible light active smart membranes. The mechanism behind the hydrophobic ↔ superhydrophilic switching can be explained on the basis of the various mechanisms given in the literature. As mentioned in the introduction, no single mechanism is capable of explaining all the experimental results. Hence, a combination of mechanisms (photocatalytic decomposition of adsorbed organics and photo induced surface reconstruction) are considered.[89,90]

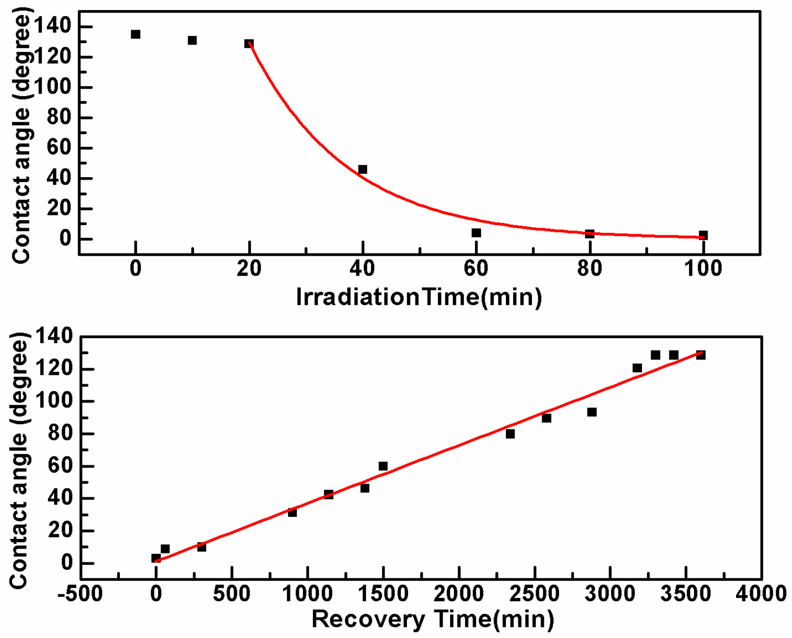

Figure 4.14: (a) the variation of water contact angle with time of sun light irradiation and (b) increase in contact angle with time left in dark (after sun light irradiation for 90 minutes).

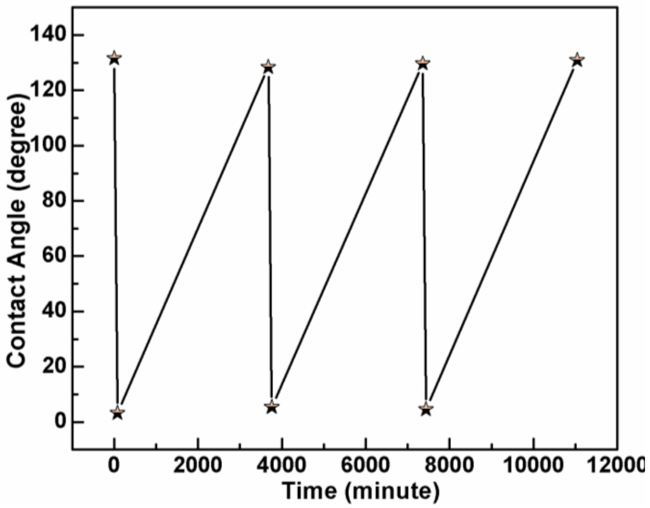

Figure 4.15: The reversible hydrophobic ↔ super hydrophilic switching behavior of N-doped TiO_2 on exposure to sunlight / dark.

In the case of stoichiometric TiO_2 and TiO_2 with negligible oxide ion vacancies, it is quite appropriate to state that, the photo generated holes after migrating to the surface take part in the destruction of adsorbed organics and reaction with oxide ions generating surface O^{2-} ion vacancies. The generated oxygen vacancies at the surface take the form of missing oxide ions in the bridging oxygen row (bridging oxygen vacancies i.e. Ti - V_O – Ti) leading to the formation of coordinatively unsaturated Ti^{3+} ions. These Ti^{3+} ions constitute distorted coordination geometry because of adjacent oxide ion vacancies. These have a tendency to form additional coordination and therefore, the oxygen vacancies act as adsorption sites for water molecules. The water molecules adsorbed at the bridging oxygen vacancies are dissociated into OH and H. The OH group fills the oxygen vacancy to form Ti – OH – Ti / Ti-OH HO-Ti. The surface reconstruction along with increase in number of the surface OH groups enhances hydrophilicity. In short, upon irradiation with photons of suitable wave-length, the adsorbed organics are photocatalytically destroyed and TiO_2 surface structure gets reconstructed with increased number of hydroxyl groups, resulting in hydrophobic to superhydrophilic conversion.

In the case of TiO_2 having considerable oxide ion vacancies, for example reduced TiO_2 and N-doped TiO_2, water dissociatively chemisorbs in the bridging oxygen vacancies creating hydroxyls, as described above. Hydroxylation at the bridging oxygen vacancies was elucidated by Wendt et al from the results of scanning tunneling microscopic studies and density functional theory calculations carried out,[91] on reduced rutile TiO_2 (110) surfaces which were not subjected to photo irradiation. That means, in case of reduced or suitably doped TiO_2, the surface is already hydroxylated, and upon irradiating with photons of suitable wave length, the resulting increase in number of hydroxyl groups and surface reconstruction due to the photo generated holes may not be the major contributing factor towards the hydrophobic to hydrophilic conversion. A recent study by Takahashi and Yui on the analysis of OH groups on TiO_2 single crystal surfaces (110), (100) and (001) with polarization modulation infrared external reflection spectroscopy (PM-IER) did not detect any remarkable increase in the number of surface OH groups to account for the increase in observed hydrophilicity.[80] Based on their results of PM-IER studies on (110), (100) and (001) surface before, during and after UV irradiation, they explained the photo induced hydrophilicity owing due to the generation of intermediates such as hydrogen peroxide (H_2O_2) and oxonium ions (H_3O^+), by the photo generated holes and / or electrons, which enhance hydrogen bonding between adsorbed water molecules, leading to an increase in the amount of adsorbed water and enhancement of wettability.[80]

In view of the above discussions, it can be stated that, photocatalytic destruction of adsorbed organics and the surface reconstruction due to the generation of bridging hydroxyl groups, and enhancement of hydrogen bonding between the adsorbed water molecules due to the generation of intermediates such as H_2O_2 and H_3O^+ by the photo generated electrons/holes contribute to the hydrophobic to hydrophilic conversion.

Based on the results of present investigation, it is inferred that in the case of pristine and N- doped TNTA a combination of the above mentioned mechanisms play a vital role. It is well understood that, compared to pristine TiO_2, N-doped TiO_2 samples have higher oxygen vacancy fraction and hence greater fraction of surface OH group. This was confirmed from the analysis of the O-1s peak of pristine and N-doped TiO_2, obtained from the X-ray photoelectron spectroscopic studies (Table 4.5). Because of the presence of more number of surface OH groups, the enhancement in hydrogen bonding between adsorbed water molecules and the surface hydroxyl groups as well as the bonding between the adsorbed molecules, due the photogenerated intermediates (H_2O_2 and H_3O^+), play a role in the enhancement of wettability and therefore a low contact angle.

Element	Chemical environment of each element	Binding Energy (eV)	Doped TiO_2 Atom fraction	Pristine TiO_2 Atom fraction
O	O-Ti(+4)	530.5	0.126	0.090
	O-Ti (+3)	530.9	0.354	0.430
	HO-Ti(+3,+4)	531.9	0.152	0.113
Ti	Ti (+4)-O	459.4	0.204	0.254
	Ti (+3)-O	458.0	0.081	0.062
	Ti (+3)-OH	456.9	0.032	0.018
	Ti (+2)-O	455.6	0.012	0.007

Table 4.5: Atomic fractions of each element in different oxidation states

The plots (Figure 4.11 and Figure 4.14a) representing the contact angle variation with light irradiation, for the pristine as well as N-doped samples, consist of two regimes viz. a hydrophobic to hydrophilic and a hydrophilic to superhydrophilic regimes. The first regime can be ascribed to the effect of surface reconstruction because of the generation of bridging hydroxyl groups, and enhancement of hydrogen bonding between the adsorbed water molecules. In this regime the variation of water contact angle with irradiation time is very slow. The second regime can be ascribed to the effect of photocatalytic organic decontamination (air born pollutants). In the case of N-doped TNTA because of the presence of more number of surface hydroxyl (Ti-OH) groups due to doping generated oxygen vacancies, the major contribution towards initial hydrophilicity can be considered to be from enhancement of hydrogen bonding between the adsorbed water molecules / water molecules and surface OH groups. The recovery of the initial hydrophobic state when kept in dark is due to the adsorption of air borne organics and desorption of intermediate species / molecular water.

4.4. Conclusion

In summary, the solar cell performance of the TNTA on Ti foils and FTO coated glasses were investigated. The deterioration of the FTO film upon anodization resulted in the incomplete anodization of Ti thin film and therefore limited length of the nanotubes (~1 micron). In addition, the annealing of anodized samples at 400 ^{o}C deteriorated the film transmittance. A low fill factor due to improper dye attachment was also observed. These shortcomings limited the photovoltaic performance of the TNTA on FTO glass. Whereas in the case of TNTA on Ti foils, the low fill factor, inferior quality of the Pt counter electrode and reduction in light intensity due to illumination from the counter electrode side contributed to the inferior photovoltaic performance. Once all these limitation are overcome, it is expected that TNTA will be a promising candidate material for the third generation solar cells.

The enhancement in electron FE of TNTA with N-doping and variation of electron emission with concentration of substitutional nitrogen was studied. The emission current was found to be stable over a duration extending to 5 hours. Systematic variation in electron emission with increase in N-doping confirms the role played by substitutional nitrogen in FE enhancement. The enhancement of FE properties on N-doping arises due to the presence of localized donor states, with higher band width, located at energy levels close to CBM compared to that of TiO_2 and N-2p state above the VBM leading to a shift in Fermi level to higher energies compared to TiO_2.

Nearly superhydrophobic pristine (contact angle = ~140^{o}) and N-doped TNTA (contact angle = ~125^{o}) were synthesized electrochemically. The hydrophobic to superhydrophilic conversion of the N-doped nanotube arrays of different tube diameters under UV as well as sun light were studied and compared with pristine TNTA synthesized under similar conditions. The doped nanotube array surfaces were more hydrophilic. The hydrophobic to super hydrophilic conversion was found to be faster for doped samples. Whereas, the time taken for reverting to the initial hydrophobic state when left in dark was less for pristine TiO_2 samples. The results confirm the superiority of N-doped TiO_2 over pristine TiO_2 for use as antifogging / self cleaning coatings.

References:

---

[1] Lee, Y.-L.; Lo, Y.-S., *Adv. Func. Mater.* **2009,** *19* (4), 604-609.

[2] Adachi, M.; Murata, Y.; Takao, J.; Jiu, J.; Sakamoto, M.; Wang, F., *J. Am. Chem. Soc.* **2004,** *126* (45), 14943-14949.

[3] Mor, G. K.; Shankar, K.; Paulose, M.; Varghese, O. K.; Grimes, C. A., *Nano Letters* **2006,** *6* (2), 215-218.

[4] Muduli, S.; Lee, W.; Dhas, V.; Mujawar, S.; Dubey, M.; Vijayamohanan, K.; Han, S.-H.; Ogale, S., *ACS App. Mater. Inter.* **2009,** *1* (9), 2030-2035.

[5] Tan, B.; Wu, Y., *J. Phys. Chem. B* **2006,** *110* (32), 15932-15938.

[6] Maggie, P.; Karthik, S.; Oomman, K. V.; Gopal, K. M.; Craig, A. G., *J. Phys. D: Appl. Phys.* **2006,** *39* (12), 2498.

[7] Karthik, S.; Gopal, K. M.; Haripriya, E. P.; Sorachon, Y.; Maggie, P.; Oomman, K. V.; Craig, A. G., *Nanotechnology* **2007,** *18* (6), 065707.

[8] Shankar, K.; Bandara, J.; Paulose, M.; Wietasch, H.; Varghese, O. K.; Mor, G. K.; LaTempa, T. J.; Thelakkat, M.; Grimes, C. A., *Nano Lett.* **2008,** *8* (6), 1654-1659.

[9] Mor, G. K.; Varghese, O. K.; Paulose, M.; Grimes, C. A., *Adv. Func. Mater.* **2005,** *15* (8), 1291-1296.

[10] Zheng, H.; Sadek, A. Z.; Breedon, M.; Yao, D.; Latham, K.; Plessis, J. d.; Kalantar-Zadeh, K., *Electrochem. Comm.* **2009,** *11* (6), 1308-1311.

[11] Macak, J. M.; Tsuchiya, H.; Berger, S.; Bauer, S.; Fujimoto, S.; Schmuki, P., *Chem. Phys. Lett.* **2006,** *428* (4–6), 421-425.

[12] Varghese, O. K.; Paulose, M.; Grimes, C. A., *Nat Nano* **2009,** *4* (9), 592-597.

[13] Kim, J. Y.; Noh, J. H.; Zhu, K.; Halverson, A. F.; Neale, N. R.; Park, S.; Hong, K. S.; Frank, A. J., *ACS Nano* **2011,** *5* (4), 2647-2656.

[14] Sadek, A. Z.; Zheng, H.; Latham, K.; Wlodarski, W.; Kalantar-zadeh, K., *Langmuir* **2008,** *25* (1), 509-514.

[15] Weickert, J.; Palumbiny, C.; Nedelcu, M.; Bein, T.; Schmidt-Mende, L., *Chem. Mater.* **2010,** *23* (2), 155-162.

[16] Nazeeruddin, M. K.; De Angelis, F.; Fantacci, S.; Selloni, A.; Viscardi, G.; Liska, P.; Ito, S.; Takeru, B.; Grätzel, M., *J. Am. Chem. Soc.* **2005,** *127* (48), 16835-16847.

[17] Znamirowski, Z.; Pawlowski, L.; Cichy T.; Czarczynski, W. *Surf. Coat. Tech.*, **2004**, *187*, 37-46.

[18] Fang, X. S.; Bando, Y.; Shen, G. Z.; Ye, C. H.; Gautam, U. K.; Costa, P. M. F. J.;. Zhi, C. Y; Tang C. C.; Golberg, D. *Adv. Mater*, **2007**, *19,* 2593-2596.

[19] Huo, K.; Zhang, X.; Fu, J.; Qian, G.; Xin, Y.; Zhu, B.; Ni, H.; Chu, P. K. *J. Nanosci. Nanotechnol.* , **2009**, *9*, 3341-3346.

[20] Xiang, B.; Zhang, Y.; Wang, Z.; Luo, X. H.; Zhu, Y. W.; Zhang, H. Z.; Yu, D.P. *J. Phys. D: Appl. Phys*., **2005**, *38*, 1152-1155.

[21] Wu, J. M.; Shih, H. C.; Wu, W. T. *Chem. Phys. Lett*., **2005**, *413*, 490-494.

[22] Miyauchi, M.; Tokudome, H.; Toda, Y.; Kamiya, T.; Hosono, H. *Appl. Phys. Lett*., **2006**, *89*, 43114.

[23] Chen, J. B.; Wang, C. W.; Ma, B.H.; Li, Y.; Wang, J.; Guo, R. S.; Liu, W. M. *Thin Solid Films,* **2009**, *517*, 4390-4393.

---

[24] Liu, G.; Li, F. Wang, D. W.; Tang, D. M.; Liu, C.; Ma, X.; Qing Lu, G.; Cheng, H. M. *Nanotechnology*, **2008**, *19*, 025606.

[25] Raut, N. C.; Mathews, T.; Panda, K.; Sundaravel, B.; Dash S.; Tyagi A. K. *RSC Adv*, **2012**, *2*, 812-815.

[26] Diwald, O.; Thompson, T. L.; Zubkov, T.; Goralski, E. G.; Walck S. D.; Yates, J. T. *J. Phys. Chem. B*, **2004**, *108*, 6004- 6008.

[27] Palgrave, R. G.; Payne D. J.; Egdell, R. G. *J. Mat. Chem*, **2009**, *19*, 8418-8425.

[28] Wang, J.; Tafen, D. N.; Lewis, J. P.; Hong, Z.; Manivannan, A.; Zhi, M.; Li, M.; Wu, N.*J. Am. Chem. Soc.*, **2009**, *131*, 12290-12297.

[29] Valentin, C. D.; Finazzi, E.; Pacchioni, G.; Selloni, A.; Livraghi, S.; Paganini M. C.; Giamello, E. *Chemical Physics*, **2007**, *339*, 44.

[30] Oropeza, F. E.; Harmer, J.; Egdell, R. G.; Palgrave, R. G. *Phys. Chem. Chem. Phys*., **2010**, *12*, 960-969.

[31] Takahashi, I.; Payne, D. J.; Palgrave R. G.; Egdell, R.G. *Chem. Phy.s Lett*, **2008**, *454*, 314-317

[32] Okato, T.; Sakano T.; Obara, M. *Phys. Rev. B*., **2005**, *72*, 115124.

[33] Ketteler, G.; Yamamoto, S.; Bluhm, H.; Andersson, K.; Starr, D. E.; Ogletree, D. F.; Ogasawara, H.; Nilsson A.; Salmeron, M. *J. Phys. Chem. C*, **2007**, *111*, 8278-8282.

[34] Yim, C. M.; Pang C. L.; Thornton, G. *Phys. Rev. Lett*., **2010**, *104*, 036806.

[35] Nordheim, L.W. *Proc. R. Soc. A*, **1928**, *121*, 626-639.

[36] Fowler, R. H.; Nordheim, L. W. *Proc. R. soc. A*, **1928**, *119*, 173-181.

[37] Das, S.; Ahmed, S.F.; Mitra, M. K.; Chottopadhyay, K. K. *Appl. Phys. A: Mater. Sci. Process*, **2008**, *91*, 429-433.

[38] Pascual, J.; Camassel, J.; Mathieu, H. Phys. Rev. B, **197**8, *18*, 5606.

[39] Al-Tabbakh, A. A.; More, M. A.; Joag, D. S.; Mulla, I. S.; Pillai, V. K. *ACS Nano*, **201**0, *4*, 5585-5590.

[40] Nakamura, I.; Negishi, N.; Kutsuna, S.; Ihara, T.; Sugihara S.; Takeuchi, K. *J. Mol. Catal. A*, **200**0, *161*, 205-212.

[41] Ihara, T.; Ando M.; Suguhara, S. *Photocatalysis*, **2001**, *5*, 19 (in Japanese).

[42] Justicia, I.; Ordejon, P.; Canto, G.; Mojos, J. L.; Fraxedas, J.; Battiston, G. A.; Gerbasi, R.; Figueras, A. *Adv. Mater.*, **2002**, *14*, 1399-1402.

[43] Ihara, T.; Miyoshi, M.; Iriyama, Y.; Matsmoto, O.; Sugihara, S. *App. Catal. B*, **2003**, *42*, 403-409.

[44] Oertzen G.U.; Gerson, A.R. *J. Phys. Chem. Solids*, **2007**, *68*, 324-330.

[45] Lin, Z.; Orlov, A.; Lambert, R. M.; Payne, M. C. *J. Phys. Chem. B*, **2005**, *109*, 20948-20952.

[46] Irie, H.; Watanabe, Y.; Hashimoto, K. *J. Phys. Chem. B*, **2003**, *107*, 5483-5486.

[47] Lindgren, T.; Mwabora, E.; Avendano, J.; Jonsson, J.; Hoel, A.; Granqvist, C.G.; Linduist, S. E. *J. Phys. Chem. B* , **2003**, *107*, 5709-5716.

[48] Sakthivel S.; Kisch, H. *Chem. Phys. Chem*., **2003**, *4*, 487-490.

[49] Irie, H.; Watanabe, S.; Yoshino N.; Hashimoto, K.; *Chem. Comm.* , **2003**, *11*, 1298-1299.

[50] Valentin, C.D.; Pacchioni, G.; Selloni, A. *Phys. Rev. B*, **2004**, *70*, 085116.

[51] Nakamura, R.; Tanaka, T.; Nakato, Y. *J. Phys. Chem. B*, **2004**, *108*, 10617-10620.

[52] Modinos, A. Thermionic and Secondary Electron Emission spectroscopy (Newyork: Plenum) **1984**.

[53] Murphy E. L.; Good, R. H. *Phys. Rev.*, **1956**, *102*, 1464.

---

[54] Stratton. R.; *Proc. Phys. Soc. B,* **1955**, 68, 746-757.

[55] Morgulis. N.; *J. Tech. Phys.,* **1947**, 17, 983.

[56] Baskin. L. M.; Lvov. O. I.; Fursey. G. N., *phys. stat. sol.(b)*, **1971,** 47, 49-62

[57] Linn. S. Q.; Liang. Y. X; Wang. T. H, *App. Phys. Lett.*, **2006,** 88, 053107.

[58] Drelich, J.; Chibowski, E., *Langmuir* **2010,** *26* (24), 18621-18623.

[59] Wang, R.; Hashimoto, K.; Fujishima, A.; Chikuni, M.; Kojima, E.; Kitamura, A.; Shimohigoshi, M.; Watanabe, T., *Nature* **1997,** *388* (6641), 431-432.

[60] Fujishima, A.; Hashimoto K,; Watanabe, T., BKC, Inc: 1999

[61] Fujishima, A.; Rao, T. N.; Tryk, D. A., *J. Photochem. Photobio. C* **2000,** *1* (1), 1-21.

[62] Stevens, N.; Priest, C. I.; Sedev, R.; Ralston, J., *Langmuir* **2003,** *19* (8), 3272-3275.

[63] Wang, R.; Sakai, N.; Fujishima, A.; Watanabe, T.; Hashimoto, K., *J.Phys. Chem. B* **1999,** *103* (12), 2188-2194.

[64] Sakai, N.; Wang, R.; Fujishima, A.; Watanabe, T.; Hashimoto, K., *Langmuir* **1998,** *14* (20), 5918-5920.

[65] Miyauchi, M.; Nakajima, A.; Fujishima, A.; Hashimoto, K.; Watanabe, T., *Chem. Mater.* **1999,** *12* (1), 3-5.

[66] Wang, J.; Mao, B.; Gole, J. L.; Burda, C., *Nanoscale* **2010,** *2* (10), 2257-2261.

[67] Daniel, S.; Chaudhury, M. K.; Chen, J. C., *Science* **2001,** *291* (5504), 633-636.

[68] Beebe, D. J.; Moore, J. S.; Yu, Q.; Liu, R. H.; Kraft, M. L.; Jo, B.-H.; Devadoss, C., *Proceedings of the National Academy of Sciences* **2000,** *97* (25), 13488-13493.

[69] Zhai, G.-Q.; Ying, L.; Kang, E. T.; Neoh, K. G., *Surf. Inter. Anal.* **2004,** *36* (8), 1048-1051.

[70] Samuel, J. D. J. S.; Ruther, P.; Frerichs, H. P.; Lehmann, M.; Paul, O.; Rühe, J., *Sensors and Actuators B.* **2005,** *110* (2), 218-224.

[71] Zhang, L.; Dillert, R.; Bahnemann, D.; Vormoor, M., *Energy. Environ. Sci.* **2012,** *5* (6), 7491-7507.

[72] Zeman, P.; Takabayashi, S., *J. Vac. Sci. Tech. A.* **2002,** *20* (2), 388-393.

[73] Miyauchi, M.; Kieda, N.; Hishita, S.; Mitsuhashi, T.; Nakajima, A.; Watanabe, T.; Hashimoto, K., *Surf Sci.* **2002,** *511* (1–3), 401-407.

[74] Zubkov, T.; Stahl, D.; Thompson, T. L.; Panayotov, D.; Diwald, O.; Yates, J. T., *J. Phys. Chem. B* **2005,** *109* (32), 15454-15462.

[75] Mills, A.; Crow, M., In Situ, *J. Phys. Chem. C* **2007,** *111* (16), 6009-6016.

[76] Sakai, N.; Fujishima, A.; Watanabe, T.; Hashimoto, K., *J. Phys. Chem. B* **2003,** *107* (4), 1028-1035.

[77] Sakai, N.; Fukuda, K.; Shibata, T.; Ebina, Y.; Takada, K.; Sasaki, T., *J. Phys. Chem. B* **2006,** *110* (12), 6198-6203.

[78] Hashimoto, K.; Irie, H.; Fujishima, A., *Jpn. J. Appl. Phys,* **2005**, 44, 8269-8285.

[79] Watanabe, T.; Nakajima, A.; Wang, R.; Minabe, M.; Koizumi, S.; Fujishima, A.; Hashimoto, K., *Thin Solid Films* **1999,** *351* (1–2), 260-263.

[80] Takahashi, K.; Yui, H., *J. Phys. Chem. C* **2009,** *113* (47), 20322-20327.

[81] Kontos, A. G.; Kontos, A. I.; Tsoukleris, D. S.; Likodimos, V.; Kunze, J.; Schmuki, P.; Falaras, P., *Nanotechnology* **2009,** *20* (4), 045603.

[82] Balaur, E.; Macak, J. M.; Tsuchiya, H.; Schmuki, P., *J. Mater. Chem.* **2005,** *15* (42), 4488-4491.

---

[83] Balaur, E.; Macak, J. M.; Taveira, L.; Schmuki, P., *Electrochem.y Comm.* **2005,** *7* (10), 1066-1070.

[84] Doohun, K.; Jan, M. M.; Felix, S.-S.; Patrik, S., *Nanotechnology* **2008,** *19* (30), 305710.

[85] Wang, J.; Mao, B.; Gole, J. L.; Burda, C., *Nanoscale* **2010,** *2* (10), 2257-2261.

[86] Feng, X.; Zhai, J.; Jiang, L., *Angew. Chem. Int. Ed.* **2005,** *44* (32), 5115-5118.

[87] Cassie, A. B. D.; Baxter, S., *Trans. Farad.Soc.* **1944,** *40*, 546-551.

[88] Borrás, A.; López, C.; Rico, V.; Gracia, F.; González-Elipe, A. R.; Richter, E.; Battiston, G.; Gerbasi, R.; McSporran, N.; Sauthier, G.; György, E.; Figueras, A., *J. Phys. Chem. C* **2007,** *111* (4), 1801-1808.

[89] Langlet, M.; Permpoon, S.; Riassetto, D.; Berthomé, G.; Pernot, E.; Joud, J. C., *J.Photochem. Photobio. A.* **2006,** *181* (2–3), 203-214.

[90] Yan, X.; Abe, R.; Ohno, T.; Toyofuku, M.; Ohtani, B., *Thin Solid Films* **2008,** *516* (17), 5872-5876.

[91] Wendt, S.; Sprunger, P. T.; Lira, E.; Madsen, G. K. H.; Li, Z.; Hansen, J. O.; Matthiesen, J.; Rasmussen, A. B.; Laegsgaard, E.; Hammer, B.; Besenbacher, F. *Science*, **2008**, *320*, 1755-1758.

Chapter 5

Synthesis of Pristine, N and C co-doped TiO_2 nanotube powders by Rapid Break down Anodization Technique and their characterization

Self aligned nanotube arrays are advantageous because of their vectorial electron conduction compared to nanotube powders. However, in certain applications like hydrogen generation by photolysis of water, destruction of organics and microbes in water, powders are advantageous as these can be suspended in the media facilitating better light harvesting capability and superior reaction kinetics. In addition, the powders can be doctor bladed / screen printed on to suitable substrates for various applications. The present chapter discusses electrochemical synthesis of pristine and doped TiO_2 *nanotubes in the powder form and their subsequent characterization.*

5.1. Introduction

Nanostructured TiO_2 is an important candidate material for fabricating functional devices for various applications in energy and environment. Hence its production in a cost effective, tunable and easily controllable manner is of scientific and technological interest. Classical methods to produce nanoporous and nanoparticulates of TiO_2 include sol-gel and hydrothermal synthesis. As detailed in chapter 3 and the references mentioned therein, electrochemical anodization is an excellent technique to synthesize self aligned TiO_2 nanotubes. These self aligned nanostructures have limitations in photocatalytic applications such as organic degradation and hydrogen generation where large area exposure is needed for light absorption and reactant adsorption. Therefore, nanotubes in the powder form, which can be dispersed in the medium containing the reactants, are generally preferred. It is a common practice to synthesize self aligned TiO_2 nanotubes by anodizing Ti in fluoride ion containing electrolytic medium. Extending this synthesis method in chloride ion containing medium, Hahn et al synthesized nanotube powders of TiO_2 and WO_3 in sodium per chlorate and perchloric acid media.[1] In 2009, Fahim and Sekino synthesized nanotubes of TiO_2 in powder form by electrochemical anodization technique using Ti foils in perchloric acid and sodium chloride / sodium phosphate media and this electrochemical approach was termed as rapid break down anodization technique.[2] They obtained X-ray amorphous TiO_2 nanotube powders, which on heating crystallized into anatase phase in a temperature range 300 – 500 ^oC. Heating beyond 500 ^oC resulted in anatase to rutile phase transformation.

It has been reported recently that the visible light activity of TiO_2 can be enhanced by nitrogen doping which is already explained in chapter 3. The enhancement in photocatalytic activity can be further improved by C and N co-doping.[3-5] Chen et al reported that TiO_2 shows an efficient photocatalytic activity by substitutional doping of carbon and nitrogen in the oxygen lattice. The carbonaceous species formed at the TiO_2 surface during C-doping are potential sites for adsorption of organic molecules.

The present study describes the synthesis of high surface area TiO_2 nanotube powders, having wall thickness, pore diameter as well as particle size less than those reported by Fahim and Sekino[2]. In this study anatase - TiO_2 nanotube powders were obtained in as prepared state. Anodization was carried out at 10 and 20 V in perchloric acid medium at room temperature. Structure, morphology and optical properties of the as prepared and annealed samples as well as the annealing temperature limit for maintaining the tubular morphology and phase purity were investigated. Further, synthesis of C and N- co-doped anatase TiO_2 nanotube powders were carried out by anodizing Ti foil in a highly oxidative electrolyte (0.1 M $HClO_4$) containing urea as C and N source.

5.2. Experimental details

5.2.1 Synthesis of TiO_2 nanotube powders

Preparation of electrodes (Ti and Pt) was carried out according to the procedures mentioned in chapter 3. Reagent grade perchloric acid was chosen as the electrolyte. The titanium foils and the platinum cathode were connected to electrical leads by means of crocodile clips and dipped into the electrolyte solution (0.1 M perchloric acid). Two anodization experiments, one at room temperature (10 and 20V) and the other at ~ 2 ^oC (20V) were carried out. The variation of current with time, during anodization, was recorded using a computer controlled digital multimeter. Anodization was continued until the Ti foil completely transformed into TiO_2 powder. The white powders obtained after anodization at 10 V (26 ^oC), 20 V (26 ^{o}C) and 20 V (2 ^{o}C) were named as NP1, NP2 and NP3, respectively. These powders were washed several times with de-ionized water, centrifuged and dried overnight at 50 ^{o}C in a Petri dish. The samples were then annealed at 400, 500, 600 and 700 ^{o}C, at a heating rate of 3^{o} per minute, for two hours and then cooled slowly. For the synthesis of C and N co-doped TiO_2 nanotube powders Ti foils are anodized in 0.1 M perchloric acid containing 3.75 wt% urea. These powders were washed several times with double distilled water, centrifuged and kept in a Petri dish over night for drying. The undoped and doped TiO_2 samples were analyzed using different microscopic and solid state characterization techniques.

5.2.2. Characterization

Field Emission Scanning Electron Microscopic, XRD, micro Raman, Diffuse reflectance, XPS analyses of the pristine and doped TiO_2 nanotube powders were carried out as described in chapter 2. The surface areas of the samples were measured by Brunauer Emmet Teller (BET) adsorption method (Sorptomatic 1990, Thermo Electron Corporation, US), using nitrogen gas as an adsorbate. The transmission electron microscopic (TEM) analyses of the samples were carried out TEM equipment, make Philips, Netherlands. The samples for TEM studies were prepared by placing a drop of nanotube powder suspension in methanol on a carbon coated copper grid and allowing it to dry. The crystal structure of the nanotube powders were obtained from Selected Area Electron Diffraction (SAED) pattern. The photoluminescence (PL) measurements were carried out using the Jobin Yvon-Spex make Spectrofluorometer (Fluorolog version-3; Model FL3-11) with 450 W high pressure xenon arc lamp as an excitation source. PL excitation and emission spectra were acquired at room temperature for a spectral resolution of 0.2 nm and slit width of 0.25 mm.

5.3. Results and Discussions

5.3.1. Synthesis and characterization of Pristine TiO_2 nanotube powders

5.3.1.1. Potentiostatic transient and nanotube formation

The variation of current with time during the electrochemical processes is shown in Figure 5.1. During initial stages of anodization, formation of a white layer of titanium dioxide was observed on the surface of the Ti metal, which started breaking down into the electrolytic solution as white powders. The anodization reaction can be represented as

$$2Ti + 2H_2O \longrightarrow 2TiO_2 + 4e + 4H^+ \qquad (1)$$

The rate of oxide formation is faster in the initial stage. The initial white TiO_2 layer formed on the metal surface started dissolving because of electrochemical etching by chlorine species giving rise to the formation of pits. The subsequent inward migration of oxide ions resulted in the formation of a thick porous layer of TiO_2 leading to reduction in current. In addition, the chlorine species etched the Ti metal causing dissolution of Ti as $[TiCl_6]^{2-}$. The electrochemical etching of Ti metal facilitated the easy breakdown of the oxide layer. Because of the high mechanical stress existing between the metal and metal oxide interface, originating from mismatch in crystal volume, a small disturbance is good enough to remove the metal oxide layer. This disturbance was provided by chemical reactions in the electrolyte, strong bubbling in the solution due to hydrogen evolution at the cathode and local turbulence arising from magnetic stirring of the solution. The periodic release of oxide layer continued until the complete conversion of Ti metal to TiO_2. The current – time profile of the room temperature anodization performed at 10 and 20 V (Figure 5.1) are similar except for the current magnitude and time duration at each stage. The differences can be attributed to the change in kinetics with applied potential. During room temperature anodization at 20 V, the electrolyte bath temperature increased by ~15-18 °C whereas, the rise in temperature was only ~3 °C at 10 V. The relatively large rise in temperature, at 20 V, led to increase in current. In addition, the breakdown of titanium oxide layer started within minutes of anodization exposing fresh metal surface, whereas the onset as well as rate of oxide layer breakdown was slow at 10 V.

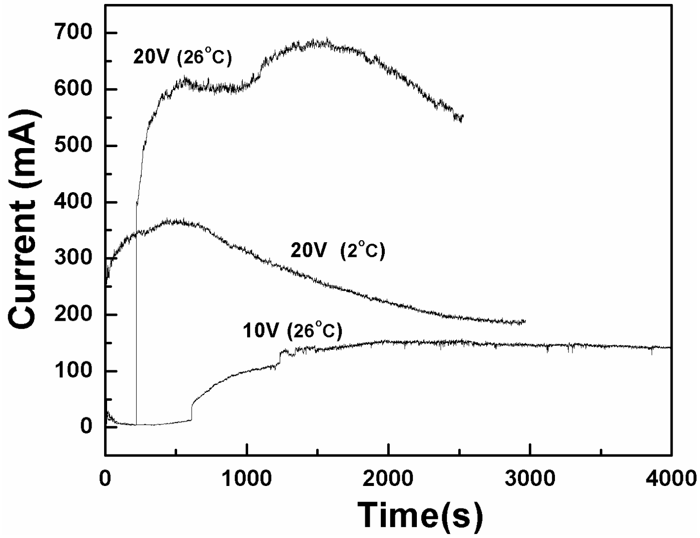

Figure 5.1: Variation of current with time during anodization

In the case where applied voltage and electrolyte temperature were 20 V and ~2 °C, respectively, the current increased slowly and then decreased very slowly until the Ti metal was completely oxidized to TiO_2. The slow change in current with time is because of the slow reaction kinetics at low temperature. The surface area of the sample calculated from BET adsorption plot is 155 g/m^2.

5.3.1.2. Field emission scanning electron microscopic studies

The FESEM images of the TiO_2 powder samples NP1, NP2 and NP3 are shown in Figure 5.2. The images reveal clusters of nanotubes of high aspect ratio. The SEM images indicate that changes in the experimental conditions did not change the morphology but the growth rate.

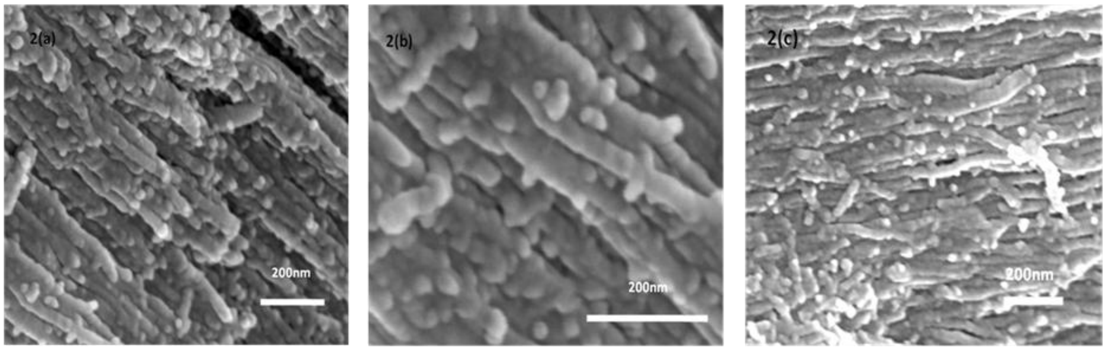

Figure 5.2a-c: FESEM images of the TiO_2 nanotube powders synthesized at different conditions (a) 10V and ~26 °C (NP1) (b) 20V and ~26 °C (NP2) and (c) 20V ~2 °C (NP3)

The growth rate diminished with decrease in temperature as well as applied potential. The outer diameter of the nanotube was about 18 nm and the length was approximately 5 to 10 μm. Though the tube walls appear smooth with nanoparticles sitting on it, a close observation of the micrograph reveals that the walls consist of nanograins. The diameter of the tube increases in the order NP1 (10 V, 26 °C) < NP3 (20 V, 2 °C) < NP2 (20 V, 26 °C). Figures 5.3 and 5.4 show the typical FESEM images of the nanotube powders annealed at different temperatures. An increase in particulate like morphology was seen after annealing and the particle size increased with increase in annealing temperature. The nanograins / nanoparticles that constitute the nanotube walls became conspicuous on annealing.

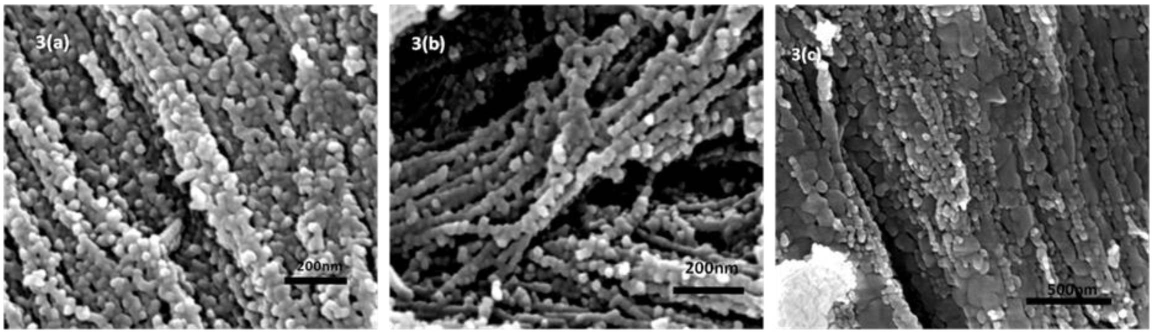

Figure 5.3a–c: FESEM images of NP1 samples annealed at different temperatures. (a) 400 °C, (b) 500 °C, (c) 600 °C

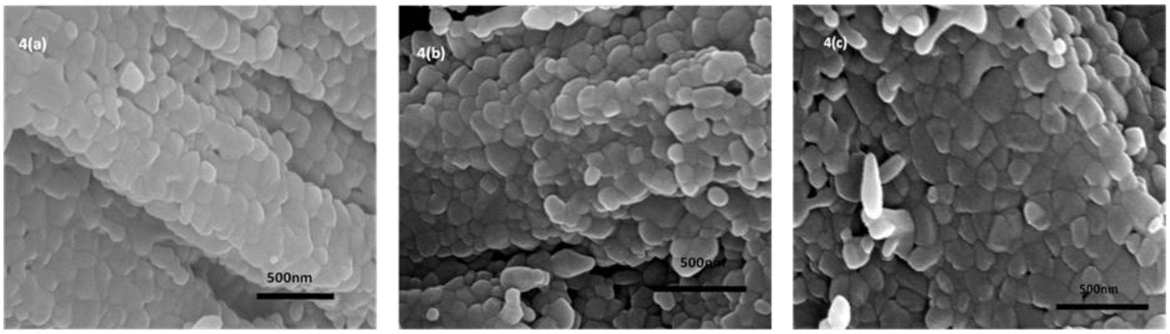

Figure 5.4a–c: FESEM images of NP1, NP2 and NP3 samples annealed at 700 ^{o}C.

The SEM images of the samples (NP1) annealed at 400 ^{o}C and 500 ^{o}C reveals that the overall morphology of the samples is retained, although the nanograins which constitute the tube walls are clearly visible (Figure 5.3a and 5.3b). The SEM image of the samples (NP1) annealed at 600 ^{o}C shows that the nanotubes start to disintegrate to particles resulting in a morphology having both nanotubes and nanoparticles (Figure 5.3c). Similar features are seen in the case of NP2 and NP3 samples annealed at 400, 500 and 600 ^{o}C. Figure 4 depicts the SEM images of the samples (NP1, NP2, NP3) annealed at 700 ^{o}C. An increase in disintegration of tubular morphology in the ascending order NP1 < NP2 ≤ NP3 is discernible.

5.3.1.3. Transmission electron Microscopic studies

The TEM image of the as prepared sample (NP1) revealing the tubular microstructure of the powders is shown in figure 5.5a. The tubes are of uniform width measuring about 15 to 18 nm in diameter. The inner diameter of the tubes varies from 5 to 8 nm and the wall thickness is about 5 nm. Similar images were obtained for NP2 and NP3 samples. Figure 5.5b shows the SAED pattern of sample NP1, the different (hkl) planes were identified as (101), (103), (105), (204) and (116) of anatase phase. TEM studies were also carried out for the annealed samples of nanotube powders synthesized at 10V (NP1). The tubular nature as observed in the case of as prepared samples were not clearly seen in the case of annealed samples.

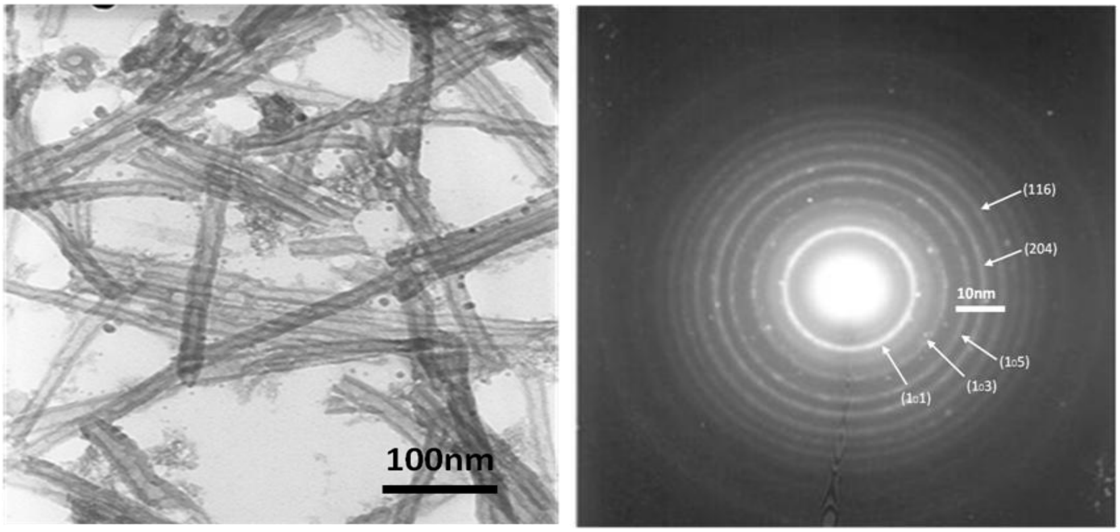

Figure 5.5a-b: (a) TEM image of the TiO_2 nanotube powders synthesized at 10V (~26º C). (b) SAED pattern of NP1 (as prepared)

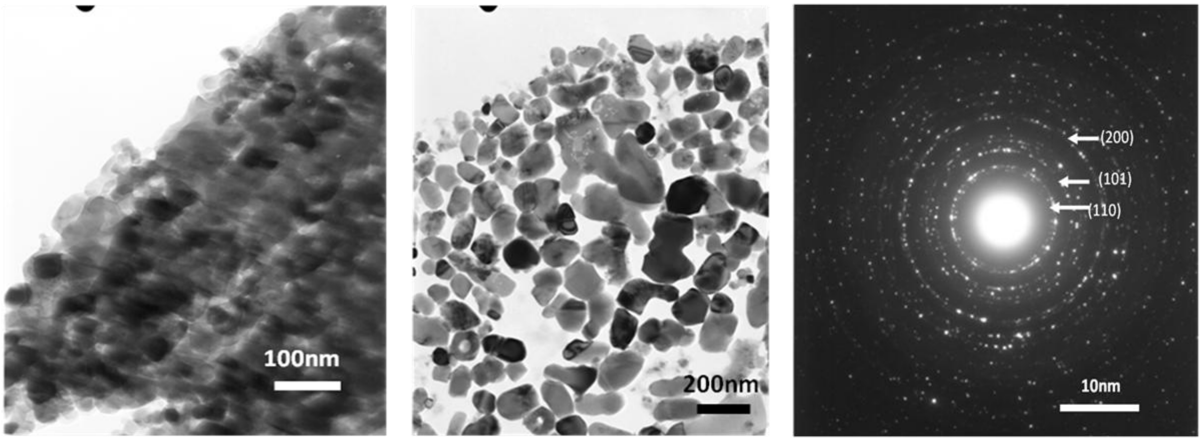

Figure 5.6a–b: TEM images (a) NP1 annealed at 600 ^oC (b) NP1 annealed at 700 ^oC (shows complete destruction of tubular morphology). Figure 6b: SAED pattern of the NP1 annealed at 700 ^oC

The TEM image of sample annealed at 600 ^oC (Figure 5.6a) shows linear array of nanograins indicating tube collapse. At 700 ^oC, the tubular morphology is completely lost resulting in the formation of nanograins distributed in random, as shown in Figure 5.6b. The results obtained from the TEM results are in agreement with the SEM observations. The SAED pattern (Figure 5.6c) of the sample annealed at 700 °C reveals that the sample is comprised of rutile phase in agreement with the XRD results given below.

5.3.1.4. Powder X-ray diffraction studies

The crystalline nature of the as prepared samples is further confirmed by XRD. Figure 5.7 depict the XRD pattern of the as prepared samples. The pattern matches well with that of anatase phase. The presence of broad peaks indicates that the crystallite size is in the nanometer regime. The crystallite size calculated for the samples NP1, NP2 and NP3, using Scherer formula, are 10, 13 and 12 nm, respectively. The microscopic and XRD studies confirm the formation of anatase phase of nanotube powders by electrochemical synthesis, without any additional post annealing requirement. The XRD patterns of the as prepared and annealed NP1 samples are shown in Figure 5.8. From the XRD patterns, it is clear that the anatase phase is stable up to a temperature of 500 °C. XRD pattern of the sample annealed at 600 °C shows the presence of both rutile and anatase phases. At 700 °C complete transformation to rutile phase occurs. Figure 5.9 shows the variation of crystallite size with annealing temperature.

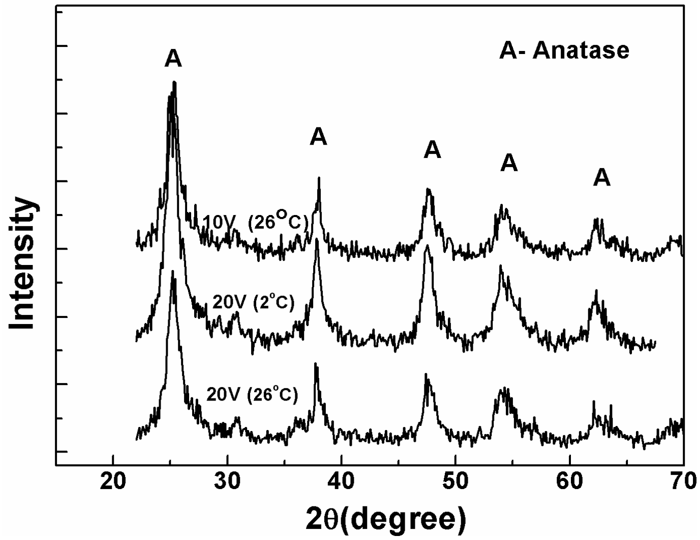

Figure 5.7: XRD pattern of the as prepared samples (NP1, NP2 and NP3)

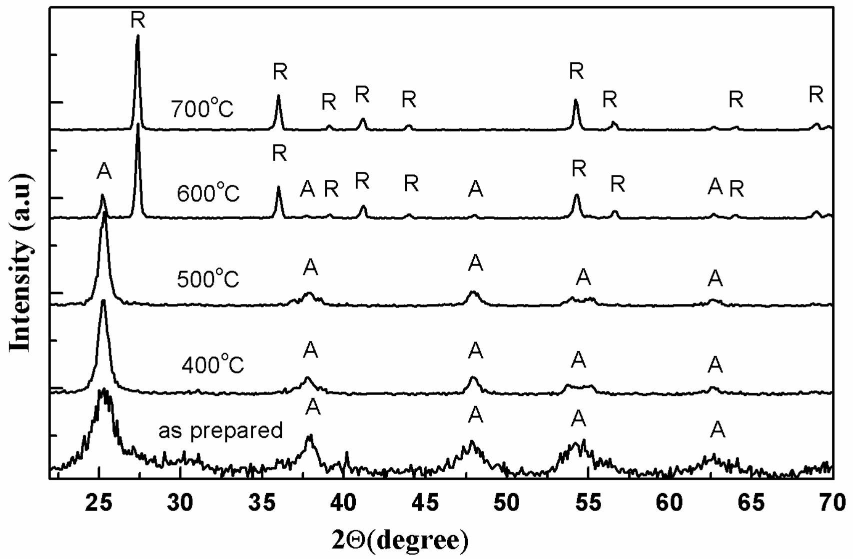

Figure 5.8: XRD patterns of NP1 samples (as prepared and annealed at various temperatures)

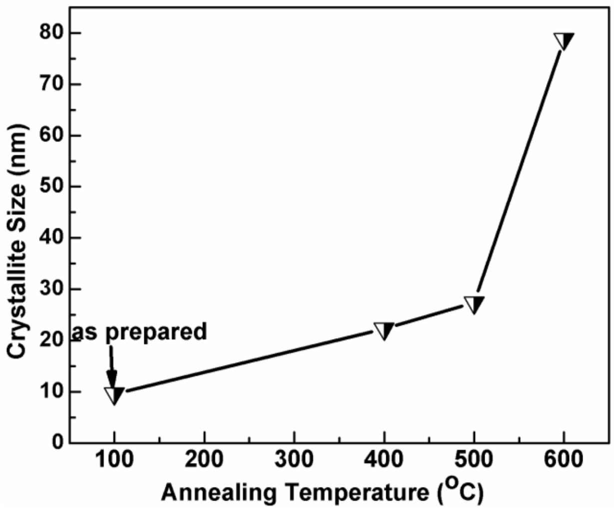

Figure 5.9: Variation of crystallite size, of the NP1 samples, with annealing temperature.

The curve represents a linear change in crystallite size until a temperature of 500 °C. Beyond this a sharp increase in crystallite size is observed. The rapid atomic diffusion accompanying phase transformation and grain growth are the underlying reasons for this sharp rise. It is further evident from the FESEM, TEM and XRD results that the anatase phase stability lasts only up to

500 ^{o}C. These results indicate that from application point of view where the anatase-TiO_2 is more efficient, the sample should preferably be annealed below 500 ^{o}C.

5.3.1.5. Raman Spectroscopy analysis

Figure 5.10 shows the Raman spectra of the as prepared TiO_2 nanotube powders. The crystal structure of anatase-TiO_2 is tetragonal (space group D^{19}_{4h} ($I4_1/amd$)) with two TiO_2 formula molecular units in the primitive cell giving rise to six Raman active phonons in the vibrational spectra: three Eg (144, 197 and 639 cm^{-1}), two B_1g (399 and 519 cm^{-1}) and one A_1g (513 cm^{-1}). For rutile TiO_2 there are four active modes: 144 cm^{-1}(B_{1g}), 448 cm^{-1} (E_g), 613 cm^{-1} (A_{1g}) and 827 cm^{-1} (B_{2g}).[6-8] Four peaks appear at around 149, 396, 517 and 638 cm^{-1} and these peaks are assigned to E_g, B_{1g}, B_{1g}/A_{1g} and E_g modes, respectively. The intense low frequency band at 149 cm^{-1} arises from the O – Ti - O bending vibrations and is a characteristic feature of the anatase phase of TiO_2. All the four peaks correspond to the Raman active phonon modes of tetragonal anatase phase of TiO_2.[6] It can be seen that the intense Raman peak corresponding to the E_g mode of TiO_2 (144cm^{-1} for standard bulk samples) has shifted towards higher wave number and the FWHM is high compared to those of standard microcrystalline samples. The shift and broadening of the Raman peaks observed in this study suggest the presence of size effects and can be attributed to the optical phonon confinement effect in agreement with the literature where quantum confinement effect in TiO_2 nanoparticles giving rise to blue shift is reported.[9,10] The broadening of Raman line can be attributed to gross structural disorder in nanocrystalline phase. The peak positions and FWHM of the Raman peaks of the as prepared samples (NP1, NP2 and NP3), obtained by fitting to Lorenzian, are shown in Table 5.1. In addition to the shift and broadening an asymmetry is seen on the peak (149 cm^{-1}) which can be attributed to the contribution from the less intense Raman peak at 197 cm^{-1}(E_g). No other peaks corresponding to rutile or any other TiO_2 polymorphs are seen in the spectra, which is in good agreement with XRD results.

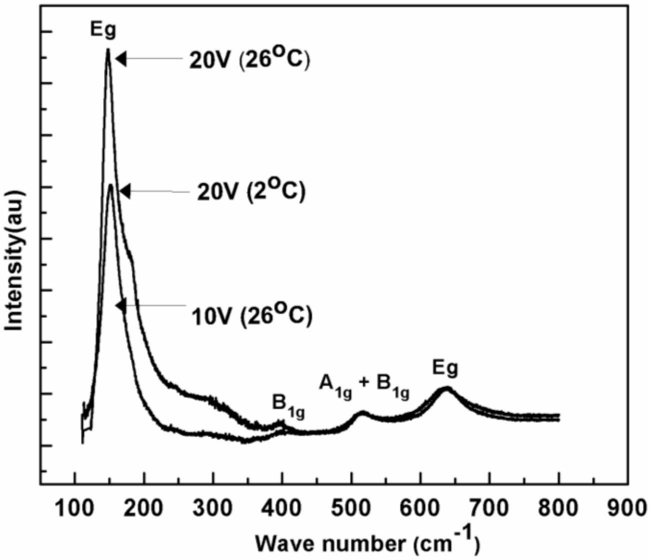

Figure 5.10: Raman spectra of the as prepared samples (NP1, NP2 and NP3).

Sample	Eg (cm^{-1})	B_1g (cm^{-1})	A_1g +B_1g(cm^{-1})	Eg (cm^{-1})
10V (26 K)/ NP1	153.05(30.59)	401.83(40.06)	514.51(86.18)	639.68(111.59)
20V (26 K) / NP2	149.11(23.04)	398.95(31.23)	516.13(10.59)	639.49(76.04)
20V (2 K) / NP3	153.12(38.97)	401.74(40.98)	516.62(38.97)	639.34(52.32)

Table 5.1: The wave number and the FWHM (in parentheses) of Raman spectra of the samples

5.3.1.6. Photoluminescence studies

The photoluminescence spectroscopy is a useful technique to reveal the efficiency of charge carrier trapping and transfer in semiconducting materials.[11] Figure 5.11 shows the PL spectra of the as prepared and annealed NP1 samples. Broad, asymmetric PL bands, tailing towards low photon energies and peaking around 3.1 eV and 3.0 eV are observed for NP1 as well as NP1 annealed at 400 °C and 500 °C and for NP1 annealed at 600 °C and 700 °C, respectively. The band gaps of the samples evaluated from the peak positions of the PL spectra as fitted to Gaussian are 3.12, 3.13, 3.13, 3.02, and 3.01 for NP1, NP1 annealed at 400 ^{o}C, 500 ^{o}C, 600 ^{o}C and 700 ^{o}C respectively. The spectra on deconvolution revealed the presence of three main PL bands. The bands around 3.1 eV (in the case of NP1, NP1 annealed at 400 ^{o}C and 500 ^{o}C) and 3.0 eV (NP1 annealed at 600 ^{o}C and 700 ^{o}C) are attributed to the indirect transitions.

For TiO_2 nanotubes, because of high surface to volume ratio, substantial number of Ti ions are exposed at the surface. As evident from FTIR studies, sufficient numbers of these atoms exist as O-Ti-OH. The presence of Ti-OH bonds distort the TiO_6 octahedra and introduce localized energy states within the band gap. These charge-carrier trapping surface states with different energy levels become luminescent centers. The PL bands observed around 2.85 eV and the flat bands around 2.65 eV (440 to 480 nm) with several sharp peaks can be ascribed to luminescence from these surface states that are present on the distorted TiO_6 octahedra (excitons trapped at shallow-trap and medium-trap surface states). It is seen from the spectra that the PL intensity increases as the sample is annealed at 400 ^{o}C and then starts decreasing on annealing at 500^{o}C. The temperature dependence of the PL data may be attributed to the different structural phases and microstructures of the annealed samples. The rise in PL intensity (at 400 ^{o}C) can be attributed to annealing of defects and thereby causing scattering elimination if scattering centers are present in the as prepared sample. The rise in intensity is also accompanied with the reduction in the FWHM signifying reduction in disorder. Further increase in annealing temperature to 500 ^{o}C causes reduction in spectral intensity. The PL spectra of the as prepared and annealed samples (400 and 500 ^{o}C) are very similar except for the small difference in intensity. Whereas the spectra of the samples annealed at 600 and 700 ^{o}C are different and are accompanied with enhanced broadening, decrease in spectral symmetry and intensity. This is because the as prepared and 400 and 500 ^{o}C annealed samples are of anatase phase whereas the

600 ^{o}C annealed sample is a mixture of anatase and rutile phases and the sample annealed at 700 ^{o}C is completely rutile. The presence of rutile phase enhances the broadening and reduces the PL intensity because of its poorer photo-reactivity compared to anatase. The observed gradual red shift indicates anatase to rutile phase transformation in agreement with the XRD and SAED results. The red shift observed in the case of NP1 annealed at 600 ^{o}C (mixture of rutile and anatase) is induced by charge transfer from anatase to rutile. As the conduction band energy level of anatase is higher than that of rutile some electrons in the anatase particles that are excited from the valence band to the conduction band transfer to the conduction band of rutile, and the photo-induced electrons and holes recombine to give luminescence.

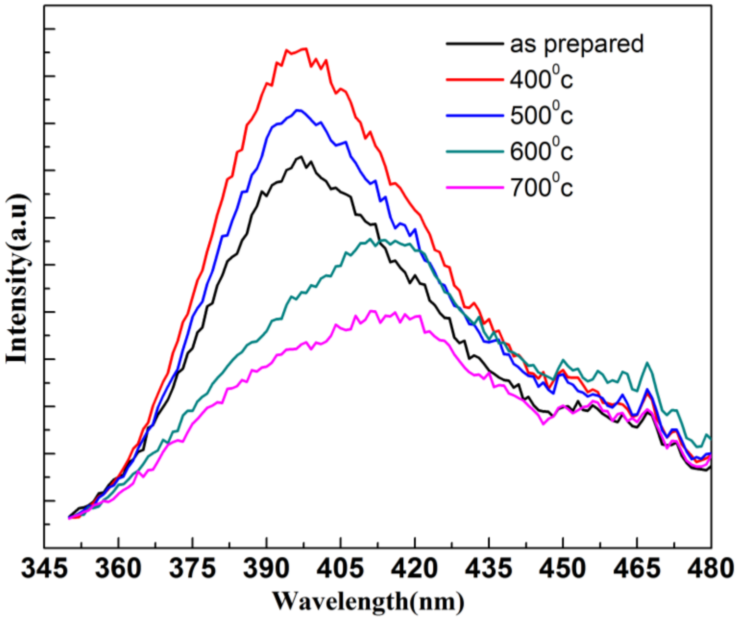

Figure 5.11: Photoluminescence spectra of the annealed samples of NP1

5.3.1.7. Optical Characterization

The optical absorption studies were carried out by taking the diffuse reflectance spectra of the powder samples. The optical band gap, obtained by extending the line, from the slope of the linear part of the Tauc plot, to x = 0, is 3.07, 3.05 and 2.95 eV for NP1, NP2 and NP3, respectively. Whereas the band gap reported in the literature for anatase TiO_2 is 3.2 eV. The reflectance spectra and the Tauc plot of the as prepared samples are depicted in Figures 5.12a and 5.12b respectively. Similar plots were obtained for NP1 samples annealed at different temperatures and the band gap values evaluated from the plots are given in Table 5.2. In the case of NP1 samples annealed at different temperatures, there is a declining trend in band gap with increase in annealing temperature. This reflects anatase to rutile phase transformation. The lower band gap of the rutile phase makes the absorption edge appear around visible region. The decrease in band gap values of the nanotubes compared to those reported can be attributed to the presence of oxygen vacancies. The broad peak in the PL spectra also gives evidence of oxygen vacancies, which creates a decrease in the band to band transition energy. Band gaps obtained from both PL and DRS studies are given in table 5.2. The mechanism of absorption of light in semiconducting materials involves the use of photon energy to excite the electrons from valence band to the conduction band. In the present case, the absorption is in the visible range close to UV. Therefore, the TiO_2 nanotubes could find active use in photocatalytic applications.

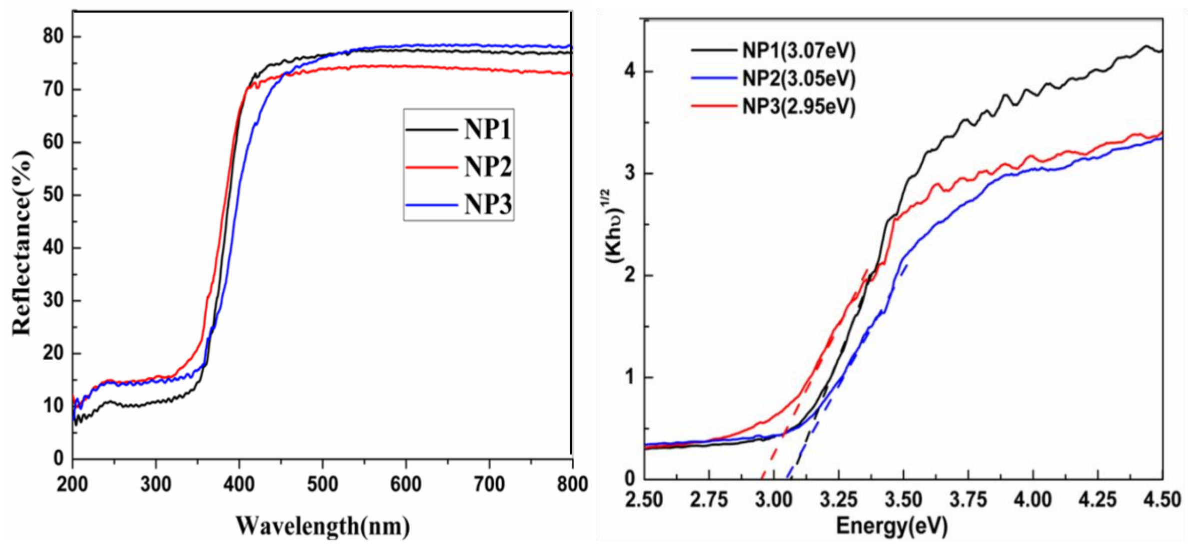

Figure 5.12a-b: (a) Diffuse reflectance spectra of the as prepared samples (NP1, NP2 and NP3), (b) Tauc plot of the as prepared samples (NP1, NP2 and NP3). The band gaps are 3.07, 3.05 and 2.95 for NP1, NP2 and NP3 samples respectively.

Sample Details	Band gap (Eg) calculated from PL(eV)	Band gap (Eg) calculated from DRS(eV)
NP1	3.12	3.07
NP2	-	3.05
NP3	-	2.95
annealedNP1(400 °C)	3.13	2.85
annealedNP1(500 °C)	3.13	2.91
annealedNP1(600 °C)	3.02	2.87
annealedNP1(700 °C)	3.01	2.88

Table 5.2: Band gap of the TiO_2 nanotubes obtained from photo luminescent and diffuse reflectance studies

5.3.1.8. Fourier transform infrared spectroscopic analysis

The FTIR spectra of the as prepared sample NP1 as well as the annealed NP1 samples are shown in Figure 5.13. The spectra show strong absorption bands at 3200-3600 and 1630 cm^{-1}, for the as prepared samples. These are attributable to the stretching mode of the OH group and the deformation mode of the molecular water, respectively. This characteristic mode reveals that there are chemisorbed as well as physisorbed hydroxyl species on the surface of TiO_2

nanotubes.[12] The same features were present in the FTIR spectra of the samples annealed at 400 and 500 °C.

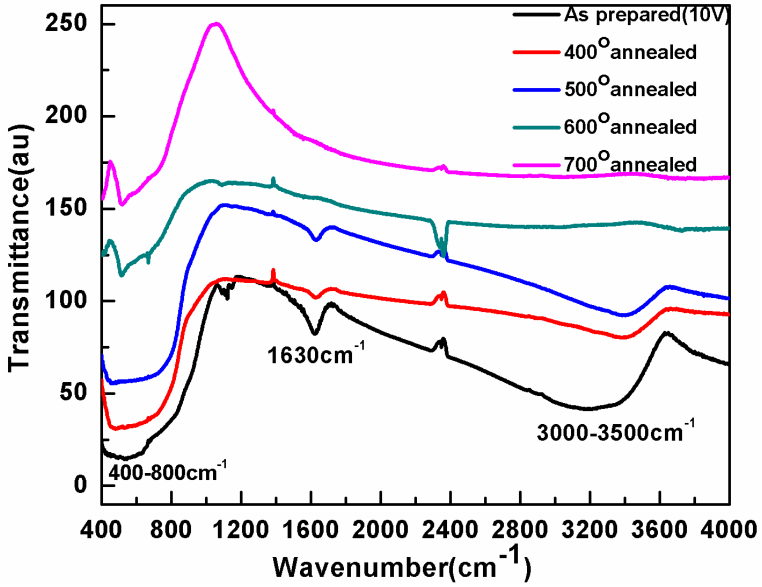

Figure 5.13: FTIR spectra of the NP1 samples annealed at various temperatures

However, in the case of samples annealed at 600 and 700 °C the characteristic vibrational modes corresponding to the OH groups were absent. There is an additional broad band over the range of 400-800 cm^{-1} that corresponds to the characteristic peak of TiO_6 octahedra.[13,14] As the annealing temperature increases this band becomes sharper suggesting that the Ti-OH bonds converts to a strong network of Ti-O-Ti in TiO_2 framework. The present data obtained agrees well with the reported values.[12,15]

5.3.2. Synthesis and characterization of N & C co-doped TiO_2 nanotube powders

5.3.2.1. Synthesis

The current density variation with time during anodization of Ti foil in 0.1 M $HClO_4$ and 0.1 M $HClO_4$ + urea is shown in Figure 5.14. The observed transients are similar confirming similar mechanism as described in earlier section.

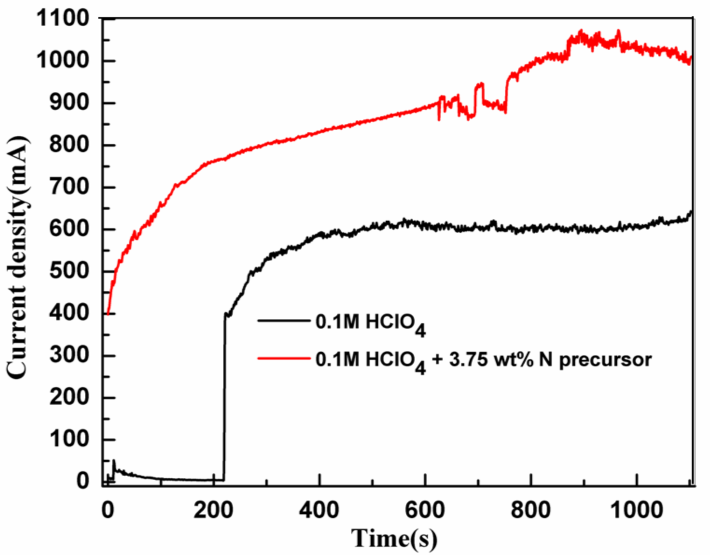

Figure 5.14: Potentiostatic transients during anodization.

5.3.2.2. Scanning and Transmission Electron Microscopic Analysis

The morphology of the samples synthesized in urea containing electrolyte were investigated by FESEM and TEM. The micrographs obtained are given in Figure 5.15. The nanotubular morphology observed in the case of samples synthesized in electrolyte without urea could not be seen in the case of samples synthesized in urea containing electrolyte. Disintegration of tubular morphology could be discerned from the SEM (Figure 5.15a) and TEM images (Figure 5.15b).

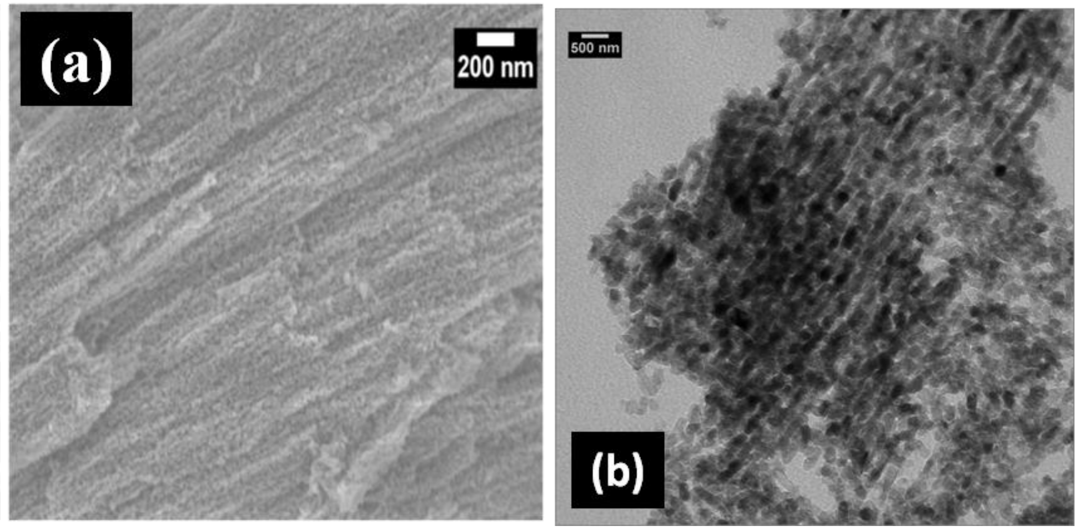

Figure 5.15a-b: (a) FESEM images of doped TiO_2 nanotube powders, (b) TEM images of doped TiO_2 nanotube powders

5.3.2.3. X-ray photoelectron spectroscopic studies

Since urea was used as a precursor for doping C and / N- doping was expected. Hence the N1s and C1s high resolution photoelectron spectra of the doped samples were taken and analyzed in detail. Figure 5.16 shows the N 1s spectrum corresponding to doped TiO_2. The deconvoluted N 1s spectrum shows peaks at 404.62, 402.76, 401.10 and 399.79 eV. In the present study, no peaks were observed, at ~397 eV, corresponding to N-Ti-O, indicating absence of oxygen substitution by nitrogen in the oxygen sub-lattice. The peak at 399.79 eV is assigned to the interstitial nitrogen ie; Ti-O-N type of chemical linkage. Figure 5.17 shows the C 1s deconvoluted spectrum of doped TiO_2. The deconvoluted C1s spectra reveal five peaks positioned at 289.25, 286.53, 284.96, 281.79 and 280 eV. The peak at 284.96 eV indicates presence of adventitious carbon. The peaks corresponding to 281.79 and 280 eV can be assigned to carbon in the oxygen sub-lattice (C-Ti-O). The peaks at 289.53 and 286.53 eV belong to Ti $(CO_3)_2$ and Ti $(CO_3)_n$, because the carbon atom diffuses through the Ti matrix and substitute the Ti or occupies the interstices in the lattice.[16] The above results indicate formation of C and N- co doped TiO_2 nanotubes, where nitrogen occupies the interstitial position resulting in the formation of Ti-O-N bond species and carbon substitutes oxygen in the oxygen sub-lattice.

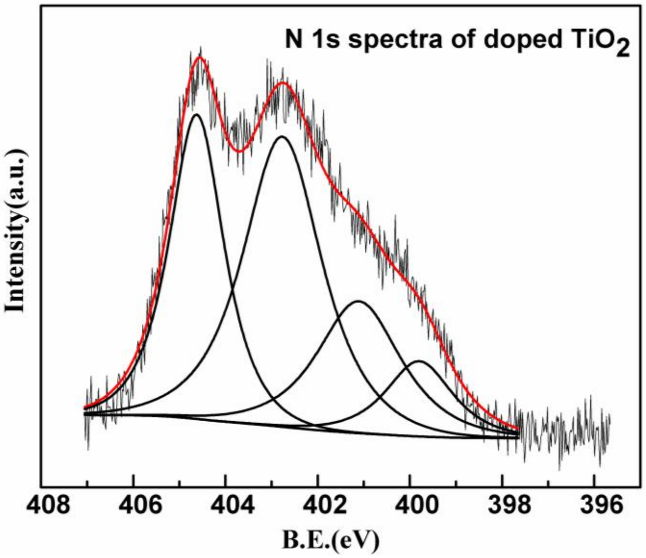

Figure 5.16: High resolution N 1s spectra of the doped TiO_2 sample.

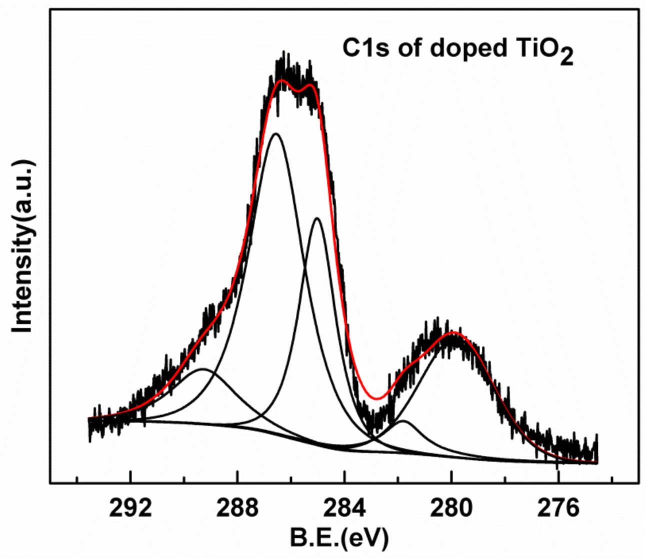

Figure 5.17: High resolution C 1s spectra of the doped TiO_2 sample.

5.3.2.4. X-ray Diffraction Studies

The XRD pattern of the sample is given in Figure 5.18. The XRD pattern of the pristine sample is also shown for comparison. The pattern matches well with that of anatase phase. No peaks corresponding to rutile TiO_2 are observed. The presences of broad peaks indicate that the crystallite sizes are in the nanometer regime. No changes in d spacing (101), could be observed. Thus doping does not change the crystallinity of the TiO_2 and is consistent with the earlier reports.[3,4,5] The crystallite sizes of the pristine and doped samples were calculated from the Scherrer formula. It was observed that the crystallite size of TiO_2 has increased from 10 to 13 nm when the doping was carried out. This change is also reflected in the BET surface area of the doped samples. The surface area decreased with doping (155 m^2/g to 124 m^2/g).

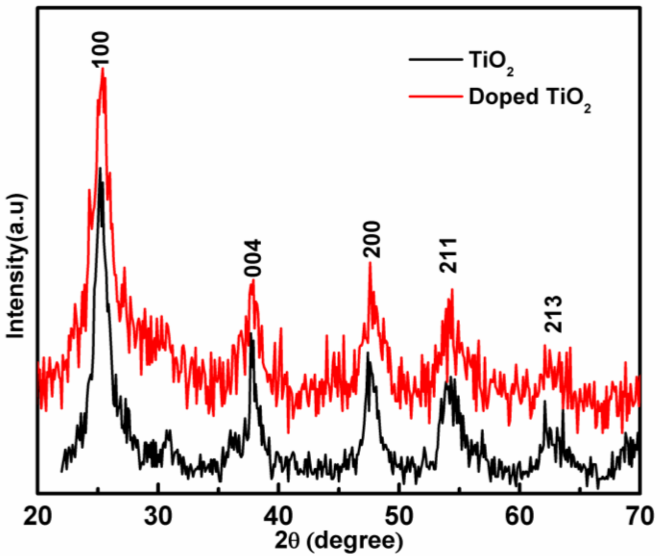

Figure 5.18: XRD patterns of undoped and doped TiO_2 nanotubes

5.3.2.5. Optical Characterization

The diffuse reflectance spectra of the powders are shown in Figure 5.19a. The reflectance spectra of the undoped samples are also shown for comparison. From the reflectance spectra of the samples (Figure 5.19a), it is clear that there is a small red shift in the absorbance of the doped TiO_2 sample. Figure 5.19b represents the variation of $(F*E)^{1/2}$ against E. The observed band gap from the Tauc plot (Figure 5.19b) for pristine and doped TiO_2 samples are 3.1 eV and 3.06 eV, respectively. The observed is very small red shift and lies within the error within limit.

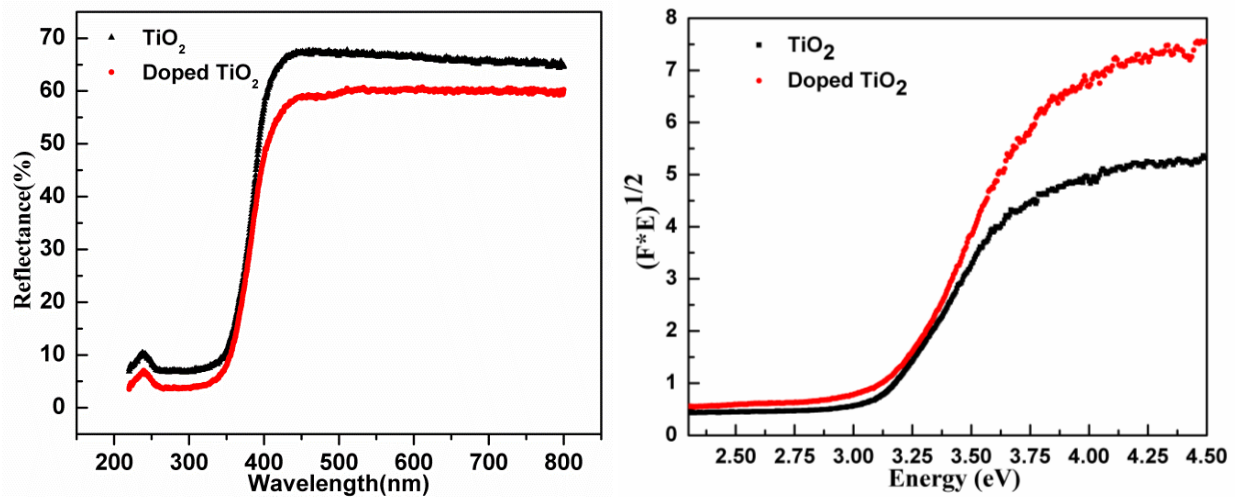

Figure 5.19a-b: (a) Diffuse Reflectance plots of the undoped and doped TiO_2 nanotubes, (b) Tauc plot of the undoped and doped TiO_2 nanotubes

Figure 5.20a shows the PL spectra of the doped samples (PL spectra of the pristine samples are given for comparison). The spectra on deconvolution revealed the presence of three main PL bands. The main peak around 3.10 eV for doped TiO_2 samples is attributed to the indirect transition. The PL bands observed around 2.80 eV and 2.19 eV can be ascribed to luminescence arising from the surface states that are present on the distorted TiO_6 octahedra (excitons trapped at shallow-trap and medium-trap surface states). The rise in PL intensity in the case of doped TiO_2 can be attributed to the higher density of defects. These defects state can act as the electron-hole recombination centres, thereby reducing the photocatalytic efficiency. Figure 5.20b shows the Raman spectra of pristine (shown for comparison) as well as doped TiO_2. In the case of doped TiO_2, in addition to the 7 bands, a band at 859.91 cm^{-1} is observed. Compared to the peak positions of pristine TiO_2, the peaks of doped TiO_2 are shifted to higher wave numbers.

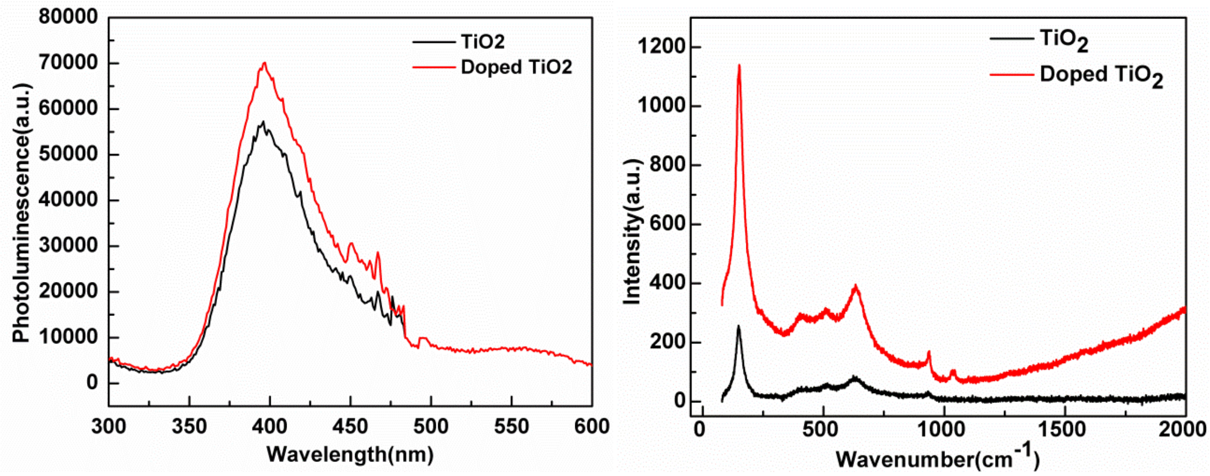

Figure 5.20a-b: (a) Photoluminescence spectra of the undoped and doped TiO_2 nanotubes, (b) micro Raman spectra of the undoped and doped TiO_2 nanotubes.

The Raman features at 149.71, 204.1, 515.67 and 630.33 can be attributed to the E_g, E_g, B_{1g} and E_g vibrational modes of anatase phase, respectively. An additional peak at 859.91cm^{-1} is assigned to the B_{2g} mode of rutile and can be attributed to the presence of rutile phase in the doped samples. So the sample contains a very low percent of rutile phase which could not be resolved in X-ray diffraction pattern. Similar observations are reported by Okato et al., where interstitial N- doping hindered the growth of anatase phase, giving rise to evolution of rutile phase.[17]

From the results of diffuse reflectance and PL studies, it is clear that there is no significant difference between the band structures of pristine and doped TiO_2, even though presence of substitutional carbon and interstitial nitrogen could be discerned from the XPS results. Hence, an enhancement in photocatalytic properties cannot be expected. In turn, deterioration in photocatalytic property is possible due to the generation of defect states, arising upon doping, which acts as electron-hole recombination centres. Indeed, this has been observed and is presented in the succeeding chapter.

5.4. Conclusion

High aspect ratio anatase phase TiO_2 nanotube powders were synthesized by employing rapid breakdown anodization technique. The method is simple, cost effective and easy. The yields of the TiO_2 nanotube powders were high as compared with other synthesis techniques. Even though potentiostatic anodization was employed, the transient was completely different from the expected one. This may be attributed to the periodic release of the TiO_2 formed on surface. Change in the applied potential and temperature did not have much effect on the sample morphology. However, the growth rate variation was noticed while changing experimental condition. The asprepared powders were confirmed to have tubular morphology with ~8 nm inner diameter and ~5 nm wall thickness as revealed from FESEM and TEM analysis. The SAED, XRD and Raman spectral studies revealed that these nanotubes are polycrystalline and is of anatase phase having crystallite size varying from 9 to 13 nm. The morphology and phase changes of the samples annealed at different temperatures, revealed by various techniques, enabled fixing of annealing temperature to confine to a specific morphology and phase, depending on the type of application. The photoluminescence of the nanotube powders have shown a temperature dependence that can be attributed to the change in crystallinity and microstructure which occurs with variation in annealing temperature. The as prepared samples showed good optical properties, where the band gaps varied from 2.95 to 3.07 eV. Compared to TNTA, even though self organized property of the material was lost in the present case, the nanotubes were of smaller diameter and wall thickness, and exhibited quantum confinement effects. While the TNTA are amorphous, as is the case in the asprepared condition, the nanotube powders consist of anatase phase. Simultaneous C and N-doping was attempted using urea in the electrolyte as precursor for C and N. XPS analysis revealed the incorporation of nitrogen into the

TiO_2 matrix as interstitials and carbon substituting oxygen in the anion sub-lattice. XRD and TEM analysis revealed the samples to be of anatase phase and 12 nm – 14 nm crystallite sizes. Diffuse reflectance measurements revealed very small red shift of 0.04 eV in the band gap of doped TiO_2 indicating no significant reduction in the band gap.

References

---

[1] Hahn, R.; Macak, J. M.; Schmuki, P., *Electrochem. Comm.* **2007,** *9* (5), 947-952.

[2] Fahim, N. F.; Sekino, T., *Chem.Mater.* **2009,** *21* (9), 1967-1979.

[3] Chen, D.; Jiang, Z.; Geng, J.; Wang, Q.; Yang, D., *Indus. Eng. Chem. Res.* **2007,** *46* (9), 2741-2746.

[4] Zhou, A.; Wang, X.; Qu, J.; Wang, Y.; Li, Y.; Wang, G., *Adv. Mater. Res*., **2011,** 148-149, 1007-1010.

[5] Yin, S.; Komatsu, M.; Zhang, Q.; Saito, F.; Sato, T., *J. Mater. Sci.* **2007,** *42* (7), 2399-2404.

[6] Hu, M.; Lai, P.; Bhuiyan, M.; Tsouris, C.; Gu, B.; Parans Paranthaman, M.; Gabitto, J.; Harrison, L., *J. Mater. Sci.* **2009,** *44* (11), 2820-2827.

[7] Ohsaka, T.; Izumi, F.; Fujiki, Y., *J. Raman Spec.* **1978,** *7* (6), 321-324.

[8] Tang, H.; Prasad, K.; Sanjines, R.; Schmid, P. E.; Levy, F., *J. App. Phys.* **1994,** *75* (4), 2042-2047.

[9] Xu, C. Y.; Zhang, P. X.; Yan, L., *J. Raman Spec.y* **2001,** *32* (10), 862-865.

[10] Pottier, A.; Cassaignon, S.; Chaneac, C.; Villain, F.; Tronc, E.; Jolivet, J.-P., *J. Mater. Chem.* **2003,** *13* (4), 877-882.

[11] Li, X. Z.; Li, F. B.; Yang, C. L.; Ge, W. K., *J.Photochem. Photobiol. A.* **2001,** *141* (2–3), 209-217.

[12] Jensen, H.; Soloviev, A.; Li, Z.; Søgaard, E. G., *App. Surf. Sci.* **2005,** *246* (1–3), 239-249.

[13] Zeitler, V. A.; Brown, C. A., *J.Phys. Chem.* **1957,** *61* (9), 1174-1177.

[14] Mauritz, K. A.; Jones, C. K., Kumar, P. M.; Badrinarayanan, S.; Sastry, M., *Thin Solid Films* **2000,** *358* (1–2), 122-130.

[15] Mauritz, K. A.; Jones, C. K., *J. App. Polym. Sci.* **1990,** *40* (7-8), 1401-1420.

[16] Rengifo-Herrera, J. A.; Mielczarski, E.; Mielczarski, J.; Castillo, N. C.; Kiwi, J.; Pulgarin, C., *App. Catal. B.* **2008,** *84* (3–4), 448-456.

[17] Okato, T.; Sakano, T.; Obara, M., *Phys. Rev. B* **2005,** *72* (11), 115124.

Chapter 6

Photocatalytic Hydrogen generation and dye degradation studies using Pristine and C and N co-doped TiO_2 nanotube powders

Various nano-architectures of TiO_2, with tailored geometry having high surface area are being studied for various functional applications in energy and environment. In applications like green-energy hydrogen generation by splitting of water and photocatalytic decomposition of organic pollutants in water, suspensions of large surface area particles like nanotubes are preferred as the configuration has better light harvesting capability and hence superior efficiency. The present chapter deals with the studies on hydrogen generation by photo assisted water splitting using Pt loaded TiO_2 nanotubes suspended in water-organic mixture and photo-assisted destruction of organics in water by pristine and C and N co-doped TiO_2 nanotube powder suspensions in water.

6.1. Introduction

Presently, the major source of energy for industrial and economic purposes is fossil fuels. Depletion of fossil fuel reserves and pollution caused by combustion of fossil fuels is a major concern. Hydrogen, an effective energy carrier, is considered as a possible alternative to reduce the strong dependence on fossil fuels and environmental pollution. When H_2 becomes the primary energy carrier the hydrocarbon economy (oil economy) will be replaced by hydrogen economy. Currently 95% of the H_2 production is from steam reforming of natural gas, which has an indirect dependence on fossil fuels. Hydrogen generation by photo splitting of water, being an environmentally friendly and economically viable process, is being considered as the best alternative. The first report on photocatalytic splitting of water on TiO_2 electrode by Fujishima and Honda created a new paradigm in energy conversion and environmental remediation using solar photons.[1] Currently, various research groups are working on H_2 generation by water splitting using solar energy. The principle behind photolysis of water using TiO_2 is that, when TiO_2 is in contact with water the photo excited conduction band electrons can reduce water, to generate hydrogen, if the conduction band level is more negative with respect to the H^+/H_2 reduction potential. Compared to bulk, nano-structured TiO_2 have enhanced photocatalytic properties due to quantum confinement and heightened reactivity associated with their molecular electronic structure and phenomenal increase in surface to volume ratio. When the size of the particles become comparable with the de-Broglie wave length of the charge carriers, which lies between 5 and 25 nm for oxide semiconductors like TiO_2, the wave function of charge carriers get spread over the entire particle do not need to diffuse anymore to accomplish reactions with species present at the surface, thereby increasing the quantum yield[2]. However, the photocatalytic efficiency of TiO_2 is limited due to the high recombination rate of photo generated electron - hole pairs. To resolve this issue and enhance the photocatalytic activity, methods like deposition of noble metals and their oxide particles and chemical surface modification have been proposed[3-11]. Noble metals like Pt, Au, and Pd have been reported to be very effective in enhancing the photocatalytic efficiency, when loaded onto TiO_2[12]. Since the Fermi levels of the noble metals are lower than the TiO_2 conduction band, when loaded onto TiO_2, the photo excited TiO_2 electrons move to the noble metal Fermi levels leaving the holes in the valence band[13], reducing the electron – hole recombination and thereby enhancing the photocatalytic efficiency. As the number of electrons on the noble metal particles increases, the Fermi level shifts more and more close to the conduction band of the TiO_2 causing more energy levels for electron transfer. The Fermi level of the TiO_2-noble metal composite photocatalyst should be more negative than the H_2 evolution level ($E_{H2/\,H2O}$)[14,15] to enable effective transfer of the accumulated electrons to the protons adsorbed on the noble metal-TiO_2 interfaces and noble metal surfaces. Among the noble metals, Pt is found to be more effective and acts as a catalyst for the hydrogen evolution, by reducing the activation energy for water reduction.[16] Various techniques such as evaporation, irradiation, thermal decomposition and chemical reduction have been adopted for Pt loading.[17-20] Chemical reduction technique has advantages over other techniques in terms of high yield and narrow particle size distribution etc.[21]

Heterogeneous photocatalysis in which the photo generated holes and electrons are involved have found interest to solve environmental pollution. When a TiO_2 photocatalyst absorbs a photon with energy equal to or greater than its band-gap an electron/hole pair is generated. The generated free electron and free hole ``walk randomly" towards the surface of the photocatalyst. The electrons react with surface adsorbed oxygen molecule to form superoxide ion (O_2^-) and the holes react with adsorbed hydroxyl groups (OH^-) to produce $^{\cdot}OH$ radicals. These species then coupled to form H_2O_2. These intermediate species along with the holes were found to play a major role in photocatalytic destruction of organics. Generally heterogeneous photocatalytic degradation mechanism follows Langmuir Hinshelwood mechanism[22-24] in which the rate of reaction '*r*' is proportional to the surface coverage, θ_I, of the reactants. In a bimolecular reaction, rate of reaction can be expressed as

$$r = k\theta_A\theta_B = \frac{kK_AK_Ba_Aa_B}{(1+K_Aa_A)(1+K_Ba_B)} \qquad (1)$$

where k is the actual rate constant, K_A and K_B are the adsorption constants of the reactants A and B and a_A and a_B are either activities in the liquid phase or partial pressures in the gas phase. Generally one of the reactants is taken in excess or kept constant and therefore the equation reduces to

$$r = k\theta_A\theta_B = k'\theta_A = \frac{k'K_Aa_A}{(1+K_Aa_A)} \qquad (2)$$

In the liquid phase the activities can be approximated to concentration and the equation assumes the form

$$r = \frac{k'K_AC_A}{(1+K_AC_A)} \qquad (3)$$

Where k' ($k' = k\theta_B$) is the pseudo rate constant and C_A the concentration of the reactant. When C becomes very less ie; dilute solutions ($< 10^{-3}$ M) , θ_A will approximately equal to $K_A C_A$ and therefore the pseudo rate constant becomes apparent rate constant 'k_{app}'.

The present chapter discusses the heterogeneous photocatalytic efficiency of the TiO_2 nanotube powders synthesized by rapid breakdown anodization technique, with respect to hydrogen generation by water splitting and destruction of organic pollutants in water. The studies concentrate on the utilization of photo generated electrons and holes for the reactions. The chapter is divided into two sections. The first section deals with photocatalytic hydrogen generation studies using pristine and Pt loaded TiO_2 nanotube powders. The H_2 generation efficiency with respect to different weight percent of Pt loading is discussed. The second part of the chapter emphasizes the dye destruction capability of the pristine and N and C co-doped TiO_2 nanotube powders under sun light illumination. Rhodamine 6G dye is taken as a model pollutant and the visible light degradation kinetics is elucidated.

6.2. Experimental

6.2.1. Preparation of Platinum supported TiO_2 Nanotubes

Anatase TiO_2 nanotube powders were synthesized and characterized according to the procedure described in chapter 5, by potentiostatic rapid breakdown anodization technique. The Pt/TiO_2 photocatalyst was prepared by adding excess of $NaBH_4$ to a colloidal suspension of 0.20 g TiO_2 nanotube powder in about 80 ml of aqueous H_2PtCl_6 of varying concentrations (0, 25, 50, 75, 100, 150 and 200 ppm of Pt), under stirring. After the chemical reduction, the Pt loaded suspension was centrifuged and washed repeatedly with distilled water and ethanol, followed by drying at 50^oC for 6 hours. The weight percentage of Pt deposited on TiO_2 was estimated assuming complete reduction of H_2PtCl_6. The as prepared photocatalyst's color varied from white to black with increase in Pt loading. The pH of the H_2PtCl_6 solution, TiO_2 dispersed H_2PtCl_6 solution and solution after $NaBH_4$ reduction was monitored using a pH meter. The Pt concentrations in the H_2PtCl_6 solution before and after $NaBH_4$ reduction were measured using an Inductively Coupled Plasma Optical Emission Spectrometer (ICP-OES).

6.2.2. Characterization of Platinum Supported Titania Nanotubes

Surface area of the as prepared TiO_2 nanotubes was measured by BET adsorption method using surface area analyzer. The chemisorbed surface area (CSA) of both as prepared TiO_2 nanotubes and Pt loaded nanotubes were measured by pulse chemisorption technique using a temperature programmed desorption reduction oxidation (TPDRO) equipment. For chemisorption surface area measurement, the sample was weighed, carefully placed in the quartz reactor of the TPDRO equipment and degassed at 120^o C in a flowing argon-8 volume% hydrogen mixture to remove any sorbed gases and moisture. Further heat treatment was carried out, in the same environment, at 400^oC to remove chemisorbed reducible species. This will ensure that the loaded Pt is in pure elemental form. The system was then brought back to room temperature. Pulse chemisorption measurement was carried out by introducing known amount of pure hydrogen to the reactor containing the sample and measuring the residual hydrogen coming out after chemisorption. Chemisorption surface area was estimated from the amount of chemisorbed hydrogen, mass of the sample and Pt loading. The morphological analyses of the samples were carried out by FESEM and TEM imaging. The composition of the samples was analyzed by EDAX attached to the FESEM equipment. The crystalline phases of the as prepared and Pt loaded samples were identified using XRD. Photoluminescence studies were recorded using a Micro Raman Spectrometer (Renishaw, UK), equipped with a confocal microscope with an “argon ion laser” operating at 514.5 nm at a power level of 200 mW.

6.2.3. Photocatalytic hydrogen generation

The photocatalytic hydrogen generation experiments were performed in a 150 ml quartz flask at ambient temperature. Schematic of the experimental set-up is shown in chapter 2. A 120 W lamp (λ = 380 nm), positioned 50 mm away from the reactor, was used as the UV light source. In a typical experiment, 20 mg of the photocatalyst (Pt/TiO_2) was suspended in a mixture of 80 ml ethanol and water, (ethanol to water ratio of 1:3) and irradiated from the bottom of the reactor. Before the commencement of the experiment, the catalyst in the quartz flask was dispersed well by placing inside an ultrasonic bath, for ten minutes. The quartz flask was then connected to the experimental set-up and argon gas was bubbled through the reaction mixture for

15 minutes to remove dissolved oxygen and to ensure that the reaction system is under anaerobic condition. Argon flow was stopped and the quartz vessel was isolated from the gas flow line by closing the inlet and outlet valves. After this, the quartz vessel was isolated and irradiated with UV light for 30 minutes. After the 30 minutes irradiation, the gas generated over the reaction mixture was carried to the polymer electrolyte membrane based H_2 meter (PEMHM) for H_2 analysis[25, 26]. Any H_2 generated produces a peak and the amount of H_2 generated was estimated from the peak area. The measurements were carried out repeatedly. The experiment was conducted in the absence of the photocatalyst and no H_2 generation was observed with photoirradiation. The sensor was calibrated prior to the measurements using standard Ar + H_2 gas mixtures. A second set of measurements were carried out using a 64 W UV source, with an incident photon wavelength of 254 nm. The set-up was made by positioning four 16 W UV lamps around the reacting vessel, at a vessel to lamp distance of 50 mm. The reactor temperature was maintained at 298 ± 2 K by means of a cooling fan. The H_2 generation efficiency was then calculated and compared.

6.2.4. Photocatalytic dye degradation studies.

A known mass of Rhodamine 6G dye was dissolved in double distilled water and subjected to visible light irradiation in a beaker with TiO_2 nanotube powder loading of 0.6g/L. The photocatalytic reaction was carried out using both, pristine and C and N-doped TiO_2. The experiments were performed for 3 h (from 10 AM to 1 PM) at room temperature under normal day sunlight (44 mW/cm^2 light intensity). Prior to these experiments, the suspension was magnetically stirred for 10 minutes. At different time intervals aliquots were taken out with the help of a micropipette. The absorption spectra were recorded and the rate of decolourization was observed in terms of change in intensity at λ_{max} (526 nm) of Rhodamine 6G dye. The absorption spectra were collected by scanning from 200 nm to 900 nm at a scan rate of 200 nm/min. The intensity change of the absorption spectrum before and after sun light irradiation indicates the degradation of dye. The concentration of dye was quantified by a calibration procedure based on Beer-Lambert's law.

6.3. Results and Discussion

6.3.1. Photocatalytic Hydrogen Generation

6.3.1.1. Preparation of platinum supported photo catalyst

Rapid addition of excess $NaBH_4$ in to the TiO_2 nanotube suspension in H_2PtCl_6 solution resulted in color change due to Pt precipitation. It was observed that the color of the suspension, after reduction, varied from pale grey to black with increase in H_2PtCl_6 concentration, indicating increased Pt loading with H_2PtCl_6 concentration. The probable reactions are[21]

$$NaBH_4 + H_2PtCl_6 + 3H_2O \rightarrow Pt + H_3BO_3 + 5HCl + NaCl + 2H_2 \qquad (4)$$

$$NaBH_4 + H_2O \rightarrow H_2 + \ boron\ hydrolysis\ products \qquad (5)$$

The pH of the pure H_2PtCl_6 solutions corresponding to various concentrations of Pt varied from 2.5 to 3.5. The pH increased slightly after dispersing TiO_2 nanotubes in the solution. When the reducing agent was added, the solution became alkaline. The pH of the solution measured after each stage is given in Table 6.1.

No	Percentage of Pt loading in TiO_2 (200mg)	Concentration of Pt in the solution (ppm).		pH of the solution		
		Before reduction	After reduction	Before reduction		After reduction
				Before dispersing TiO_2 nanotube powder	After dispersing TiO_2 nanotube powder	
1	1.25	20	<0.5	3.42	2.73	9.65
2	2.5	47	1.3	3.39	2.8	9.63
3	3.75	93	<0.5	2.94	2.44	9.57
4	5	120	0.6	2.88	2.35	9.61
5	7.5	180	1.7	2.8	2.28	9.44
6	10	270	2.6	2.79	2.26	9.66

Table 6.1: Platinum concentration and pH of the solution before and after reduction

6.3.1.2. Microstructure and phase analysis of Pt loaded TiO_2

Figure 6.1a shows the FESEM image of the TiO_2 after Pt loading. Even though the Pt nanoparticles deposited on the TiO_2 nanotubes are not visible in the SEM image, partial destruction of the tubular morphology is quite evident. A similar observation was made by Baiju et al[27] in the case of TiO_2 nanotubes synthesized by hydrothermal method, for Pt loadings above 1 mol%. Even though the tubular structure gets destructed, the alignment of the TiO_2 particles along the tube length is maintained.

TEM images of 1.25 and 5 wt% Pt loaded TiO_2 are shown in figures 6.1b and 6.1c. The Pt particles in the electron micrograph appear as black dots as the electron density of Pt is high compared to that of TiO_2. From Figure 1b it is clear that, for 1.25 wt% loading, the Pt particles are of very fine nature and well dispersed. Figure 6.2a shows the histogram of the particle size distribution. The sample population is 130. The mean diameter calculated by the image analysis is 1.978 ± 0.349 nm. Similar results are obtained for 2.5 wt % Pt loaded samples. The presence of Pt was also confirmed by energy dispersive X-ray spectrometry (not shown). At 5 wt% Pt loading, clustering of Pt nanoparticles is observed (Figure 6.1c). The average Pt cluster size calculated from the image analysis is 74 ± 23 nm. The particle size distribution is shown in Figure 6.2b.

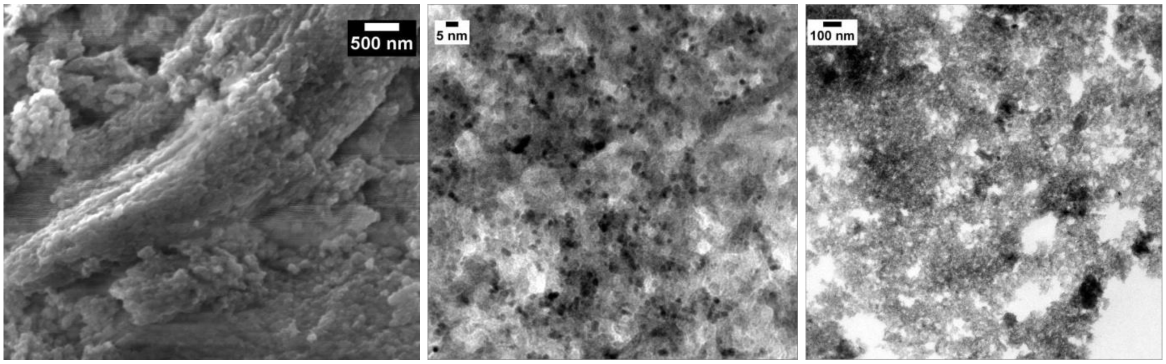

Figure 6.1a-c: (a) FESEM image of the Pt loaded TiO_2. (b) TEM image of the Pt nanoparticles dispersed in the TiO_2 matrix (1.25 wt% loading). (c) TEM image of 5 wt% Pt loaded TiO_2 (reveals clustering of platinum nanoparticles at high loading)

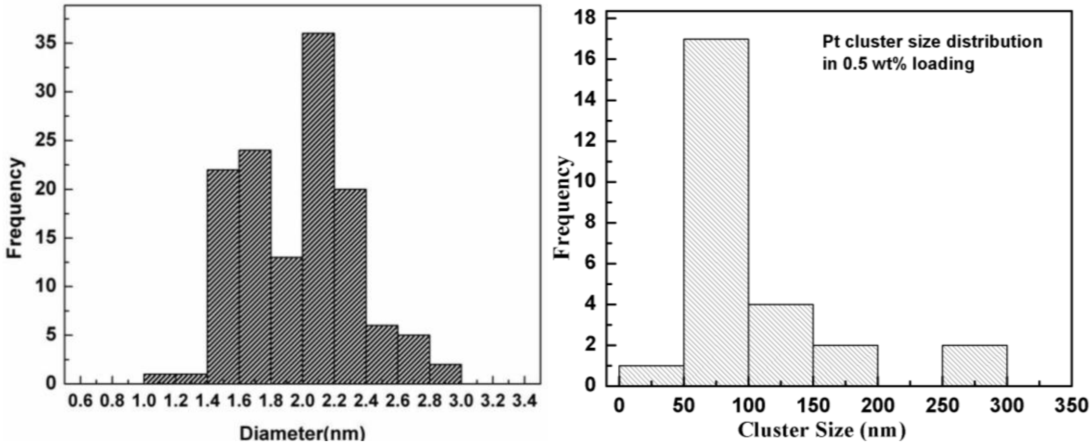

Figure 6.2a-b: (a) Platinum particle size distribution for 1.25 wt% Pt loaded TiO_2 (obtained by image analysis of the TEM image) and (b) Platinum particle size distribution for 5 wt% Pt loaded TiO_2 (obtained by image analysis of the TEM image)

The crystal structure of the photocatalysts prepared at various conditions was revealed by XRD. Figure 6.3 shows the XRD patterns of 0.0, 2.5 and 5.0 wt% Pt loaded TiO_2 samples. The pattern reveals that the photocatalyst in which Pt loading is low (≤2.5 wt %) is of anatase phase.

The XRD pattern of 5 wt% Pt loaded TiO_2 shows the presence of rutile and anatase phases, indicating phase transformation during Pt deposition. The phase transformation observed is akin to structural transformation, stimulated by changes in surface environment in ZnS, reported by Gilbert et al[28]. The broad XRD pattern of the anatase TiO_2 particles obtained in the study indicate that the crystallites are of fine size and have substantial lattice strain. The strain and associated distortion in crystal structure will be higher at the surface. Binding of Pt nanoparticles onto the TiO_2 surface relieves the strain resulting in phase transformation.

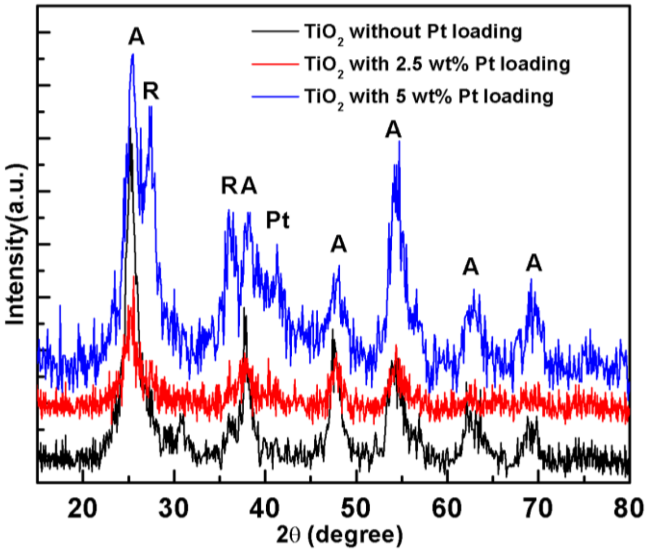

Figure 6.3: XRD pattern of as prepared TiO_2 and Pt loaded TiO_2 samples (Pt loading ≥ 5 wt% reveal anatase to rutile phase transformation)

6.3.1.3. Surface area measurements

Surface area of the as prepared TiO_2 nanotubes powder estimated by BET adsorption isotherm method was found to be 155 g/m^2. The high specific surface area of the nanotube powders points towards the availability of large number of adsorption sites on the nanotube powder. The mean chemisorption surface area (CSA) of as prepared as well as Pt/TiO_2 samples measured by TPDRO technique and dispersion of Pt are summarized in Table 6.2. From Table

6.2 it is clear that the CSA of the catalyst decreases with increase in Pt loading in the range of 1.25 to 10 wt%. The reduction in active surface area is caused by the agglomeration of the Pt nanoparticles observed at higher loadings and as revealed by the TEM imaging.

No	Weight percentage of Platinum in TiO_2	Chemisorbed Surface area (m^2/g)	Degree of dispersion (%)
1	0	-	-
2	1.25	259.3	94.37
3	2.5	157.4	57.30
4	5	148.7	54.11
5	7.5	116.7	42.46
6	10	82.6	30.03

Table 6.2: Variation of the active surface area and degree of dispersion of the platinum with loading

6.3.1.4. Photoluminescence studies

In order to reveal the charge carrier trapping, transfer and the fate of the electron - hole pair in TiO_2 because of Pt loading, PL studies of as prepared and Pt loaded samples were carried out. The PL emission spectra mainly results from the recombination of the free carriers.[29] The spectra were examined in the range of 1.8 eV to 3.5 eV. Figure 6.4 shows the PL spectra of the as prepared as well as the Pt loaded samples. It can be observed that the emission intensity decrease with Pt loading. This can be ascribed to the transfer of photo generated electron from TiO_2 to Pt metal. It also reveals the good contact between Pt nanoparticles and TiO_2.[30] All the samples show five peaks at about 2.25, 2.53, 2.75, 2.95 and 3.18 eV which correspond to wave length of 551, 490, 451, 420 and 390 nm, respectively. Among these, the peak at 390 nm corresponds to the band gap of TiO_2 and the 2.95 eV emission peak to the lowest indirect $\Gamma_{1b} - X_{1a}$ transition.[31] All other low energy peaks correspond to the defects and nonstoichiometry in TiO_2. These defects and nonstoichiometry are generated due to the presence of oxygen vacancies in the case of anatase phase, and intrinsic defects in the case of rutile phase.[32]

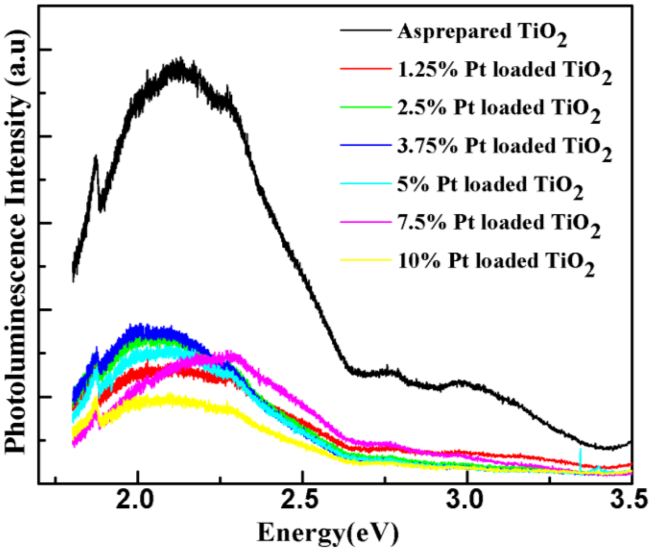

Figure 6.4: Photoluminescence spectra of the as prepared and Pt loaded TiO_2 samples

The PL property of the Pt loaded TiO_2 can be correlated with the photocatalytic activity. Pt particles on the TiO_2 surface acts as sinks for the photogenerated conduction band electrons and forms a barrier facilitating interfacial electron migration thereby enhancing electron - hole separation. The electron migration continues until the Fermi levels are aligned.[33] The resultant Fermi level of the TiO_2 – Pt composite will be closer to the TiO_2 conduction band. When there are no electron sinks on the TiO_2 surface, the photo excited electrons are de-excited through recombination centers as seen from the PL spectra of as prepared TiO_2. This effect is also reflected in the hydrogen generation rate of as prepared TiO_2 nanotubes.

6.3.1.5. Photocatalytic hydrogen generation

The typical signal of H_2 produced by photo dissociation of ethanol - water mixture, using 120 W UV lamp emitting photons of ~380 nm wavelength, obtained from PEMHS which can measure H_2 comfortably down to 10 ppm, is shown in Figure 6.5. When the experiment was carried out in the absence of the photocatalyst (Pt/TiO_2) no H_2 generation could be observed and the H_2 concentration measured by the hydrogen sensor remained at the background level. The experiments performed using asprepared TiO_2 nanotubes (photocatalyst without Pt loading) did not show any significant hydrogen generation (< 80 µ mol / hr / g of TiO_2). This can be attributed to the fast recombination of electrons and holes. Photo induced H_2 generation was high at Pt loading of 1 to 2.5wt%, but decreased with further increase in platinum loading. This can be due to various reasons. From the TEM images it is clear that at low Pt loading, the Pt nanoparticle size gets restricted to ~2 nm with narrow size distribution and is homogeneously distributed. Hence, the available surface area is high. Since reduction of proton to hydrogen on Pt is a surface reaction, H_2 generation increases with increase in CSA. If the active sites for H_2 generation are located at the Pt-TiO_2 interface rather than on isolated Pt and/or TiO_2 nanoparticles, a decrease in H_2 generation rate at higher Pt loading can be expected as higher Pt loading beyond a certain concentration leads to agglomeration of Pt nanoparticles resulting in interface area shrinkage. This will manifest as sharp drop in H_2 generation rate, as observed in the present study (Figure 6.6). In addition, the reduced size of Pt particles brings its Fermi level at optimal level with respect to conduction band location of TiO_2 facilitating enhanced electron harvesting. Because of the presence of discrete energy levels in Pt nanoparticles, the shift in energy level of accommodated electrons will be higher for smaller size nanoparticles and therefore, the Fermi level of the Pt-TiO_2 composite will be more close to the TiO_2 conduction band. This will increase the reductive power of the electrons leading to enhanced photocatalytic activity.[34]

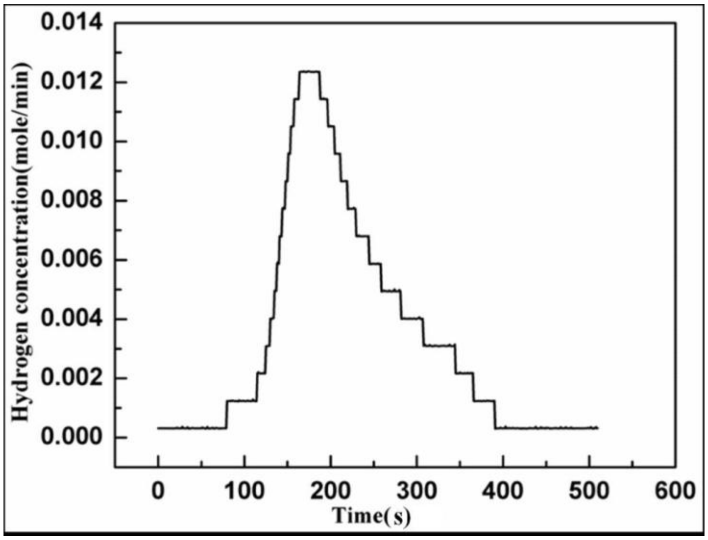

Figure 6.5: Signal obtained from the hydrogen sensor revealing hydrogen generation from ethanol - water system by photocatalysis

Figure 6.6 shows the variation of CSA and H_2 production (at 120 W, $\lambda = 380$ nm) with Pt loading. The hydrogen CSA of Pt/TiO_2, measured using TPDRO technique shows a maximum value at 1.25 wt% Pt and a decrease thereafter. The highest photocatalytic activity observed (at 120 W, $\lambda = 387$ nm) was for 1.25 and 2.5 wt% Pt loaded TiO_2 samples and are 777.3 and 927.9 μ moles / h / g of Pt/TiO_2, respectively. Experiments carried out under similar conditions with 1.25 and 5 wt% of Pt loaded TiO_2 photo-catalysts, using 64 W UV source radiating photons of 254 nm wavelength, resulted in H_2 generation of 0.030 and 0.010 moles / hr / g of Pt/TiO_2, respectively.

The turn over frequency (TOF) of the Pt surface area was calculated from the results of H_2 generation studies carried out at 120 W ($\lambda = 380$ nm) radiation using the formula

$$\text{TOF} = \text{rate of } H_2 \text{ generation (mols } s^{-1}) / \text{moles of surface Pt atoms present} \quad (6)$$

The number of moles of surface Pt atoms was calculated from the dispersion of Pt obtained from TPDRO studies. Taking into account the complete reduction of $HPtCl_6$, as confirmed by ICPOES measurements, the calculated TOF values of Pt/TiO_2 corresponding to 1.25, 2.5, 3.75, 5, 7.5 and 10 wt% Pt loadings are 0.0035, 0.0035, 0.0011, 6.644×10^{-5}, 7.99×10^{-5} and 15.27×10^{-5} s^{-1}, respectively.

The decrease in TOF values with increase in Pt loading indicates changes in chemical environment of Pt atom. The Pt dispersion can also be calculated from the size of the Pt nanoparticles obtained from the TEM studies. The Pt particle size obtained for the 1.25 wt% Pt loading is 1.99 nm and the calculated dispersion value is 57%. The TOF value obtained using this dispersion is 0.0059 s^{-1}. For photocatalytic H_2 generation the TOF value also depends on incident light energy. Hence, TOF value for H_2 generation from 1.25 wt% Pt loaded sample suspensions irradiated using 64 W ($\lambda = 254$ nm) source was calculated and found to be 13.69 s^{-1}. A table depicting the hydrogen generation rates obtained by various groups using different photo catalysts is given in the reference[35] and is represented in Table 6.3.

In the present study, a phase transition from anatase to rutile was observed at higher Pt loadings (≥5 wt %) as revealed by XRD patterns. Anatase and rutile phases differ by the distortion in the octahedra and by the assembly pattern of the octahedral structures.[36] Each Ti^{4+} ion is surrounded by an octahedron of six O^{2-} ions. In the rutile structure, each octahedron is surrounded with 10 neighboring octahedra (two edge sharing octahedra and eight corner sharing octahedra), while in anatase structure, each octahedron is in contact with eight neighbors (four sharing an edge and four sharing a corner).[36] Due to this difference, these coordinations differ in their structures (lattice parameters), electrical and optical properties.[37, 38] Also the crystalline structure determines the luminescence center for the material. The luminescence center changes from oxygen vacancies to intrinsic defects, when the phase is changed from anatase to rutile.[31] Pt on the TiO_2 inhibits the electron/hole recombination at oxygen vacancies of anatase whereas it has little control on the recombination at the intrinsic defect in rutile.[31] In these studies, the photo activity of low Pt loaded TiO_2 (anatase phase) was high compared to that of high Pt loaded TiO_2 (which is a mixture of anatase and rutile phases). From the above, it can be said that the decrease in H_2 production with increase in Pt loading is because of the synergetic effect of decrease in CSA and phase change of TiO_2. In all the hydrogen generation measurements, it was observed that the amount hydrogen produced for a given time of irradiation did not vary when repeated, using the same Pt/TiO_2 – ethanol/water system (Figure 6.7). Figure 6.7 shows the plot of the hydrogen signal obtained from the sensor.

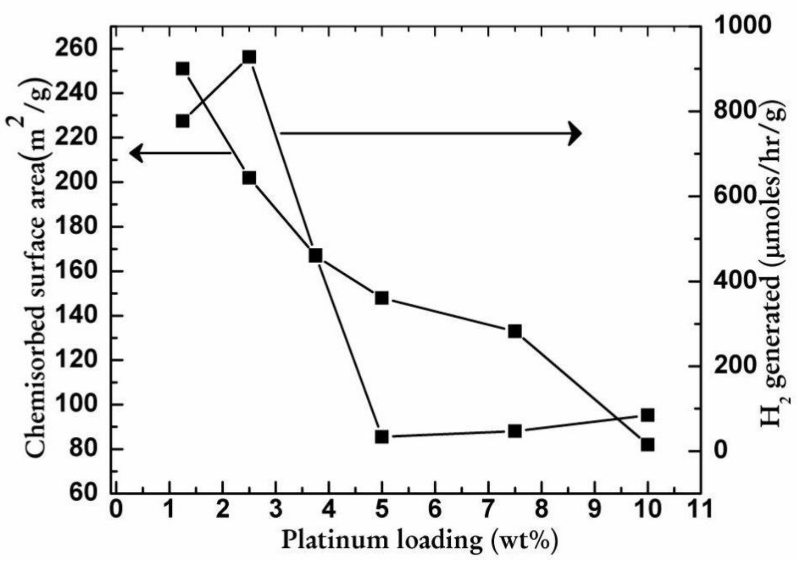

Figure 6.6: Variation of chemisorptions surface area as well as hydrogen generation rate with Pt loading

No	Photocatalyst	Preparation method	Sacrificial agent	Hydrogen generation rate μmol h^{-1} g^{-1} catalyst	Reference
1	10 mol% CuO-TiO_2, TiO_2: anatase nanoparticle	Wet impregnation	1:1 methanol/water	675	[39]
2	1.2 wt% Cu-TiO_2, TiO_2: anatase nanoparticle	Incipient-wetness	1:1.4methanol/water	2400	[40]
3	1.5 wt% CuO-TiO_2 1 wt% PdO-TiO_2 2 wt% Au-TiO_2 0.6 wt% Pt-TiO_2 TiO_2: mesoporous nanoparticle	Single step sol-gel	1:10 methanol/water	1800 2100 2800 6900	[41] [42]
4	1.0 wt% Pt-TiO_2 TiO_2: mesoporous nanoparticle	Photo deposition	1:10 methanol/water	6000	[43]
5	Eosin-1.0 wt% CuO-TiO_2 TiO_2: P25	Wet impregnation	1:5.7 diethanolamine/H2O	540	[44]
6	7 wt% CuO-TiO_2 TiO_2: P25	Wet impregnation	1:19 methanol/water	4300	[45]
7	0.3 wt% Pt-TiO_2 19.2 [7] TiO_2: P25	Dry impregnation	1:40 methanol/water	25,560	[46]
8	0.5 wt% Pt-TiO_2 TiO_2: P25	Wet impregnation	1:30 ethanol solution	27,750	[47]
9	9.1 mol% CuO-TiO_2 TiO_2: P25	Wet impregnation	1:9 methanol/water	18,500	[35]
10	1.25wt% Pt- TiO_2 TiO_2 nanotube powders	Chemical reduction	1:3 ethanol/water	33,000	Present study

Table 6.3: Represent the hydrogen generation rates obtained by various groups using different photo catalysts as given in reference.[35]

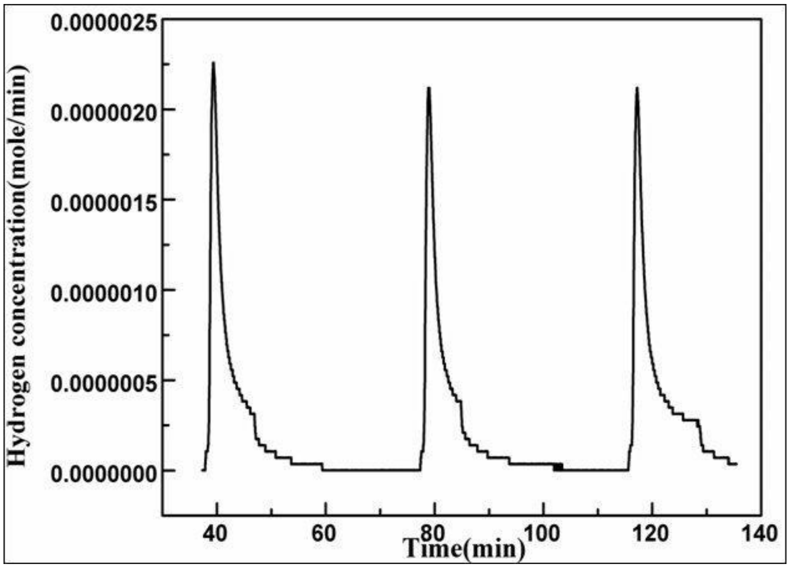

Figure 6.7: Signal from the hydrogen sensor revealing the constant hydrogen generation rate (see text). The time scale corresponding to each peak is the duration of irradiation (20 minutes) and measurement.

The first peak corresponds to the amount of hydrogen generated during the first irradiation, for 30 minutes. The second and third peaks correspond to the amount of hydrogen generated for the subsequent irradiations of 30 minutes duration, after a ~20 min break, using the same Pt/TiO_2 – ethanol/water system.

6.3.2. Photocatalytic degradation studies of Rhodamine 6G using pristine and C&N doped TiO_2 nanotube powders

6.3.2.1. UV Visible absorption studies

The Rhodamine 6G dye has a Xanthene group. The main absorption band of R6G in visible region appears at 526 nm (λ_{max}). It corresponds to a transition moment largely parallel to the long axis of the molecule which in turn is because of $\pi - \pi^*$ transition. A shoulder at 499 nm is also observed which indicates the presence of dimerized species. The band at 526 nm is attributed to the monomeric entity.[48] At high concentrations, R6G exists as a dimer. The absorption spectrum obtained at low concentrations (Figure 6.8) with λ_{max} located at 526 nm indicates that the molecule exists as monomer.

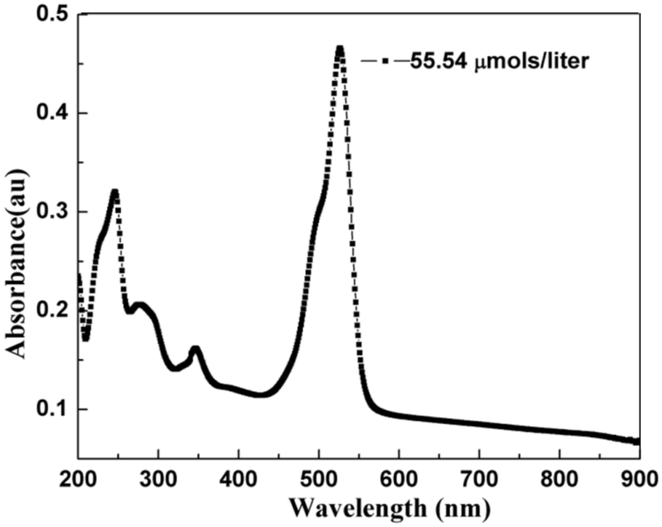

Figure 6.8: Absorption spectra of Rhodamine 6 G solution at a concentration of 55.54 μ mol / litre.

The concentration of the dye solution used for photodegradation studies was quantified by calibration based on Beer-Lambert's law and was found out to be 55.54 μmole / l. During the calibration process, the peak position was fixed at 526 nm which is the λ_{max} of R 6G. The photodegradation experiments were carried out using pristine and C and N co-doped TiO_2. The concentration of degraded dye solutions collected after different time intervals was quantified by the same calibration method. The absorption spectrum of R 6G during the course of reaction, when doped TiO_2 was used as photocatalyst, is given in Figure 6.9. The plots in Figure 6.10a and 6.10b show time dependent concentration change of R6G during irradiation in the presence of pure and doped TiO_2, respectively. Experiments performed under sun light without the addition of photocatalyst did not show any significant change in concentration (Figure 6.10c).

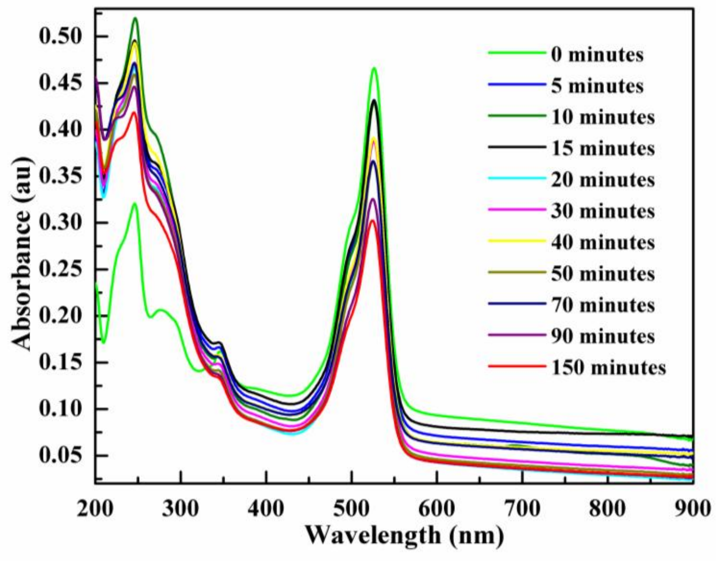

Figure 6.9: Absorption spectra of Rhodamine 6G during the course of the reaction when doped TiO_2 was used as the photocatalyst.

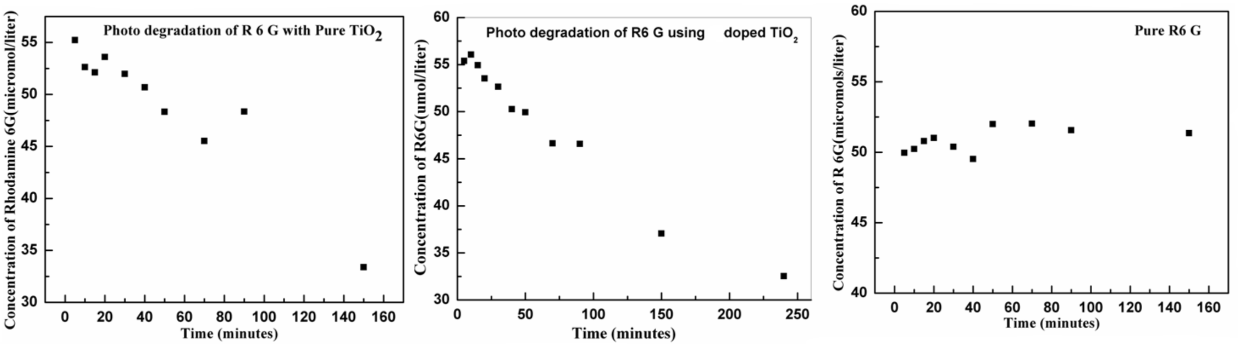

Figure 6.10a-c: Variation of Rhodamine 6 G concentration with time using (a) pure TiO_2 nanotubes, (b) doped TiO_2 nanotubes and (c) without the TiO_2

The degradation of R 6G is visible from the plot in terms of decrease in intensity of the absorbance spectrum. Photocatalytic degradation can happen in two different manners either photocatalytic oxidation[49-52] or photosensitized oxidation.[53-59] In photocatalytic oxidation, TiO_2 is irradiated and excited in a near UV energy creating electron-hole pairs, whereas, dyes are excited by visible light and thereby electron injection into TiO_2 conduction band, in photosensitized oxidation. In general it is difficult to tell which will dominate. It is reported that under visible light, photosensitizing mechanism will help to improve the overall efficiency of the dye degradation.[60,61] The mechanism of photocatalytic degradation can be explained as follows. There are mainly two species responsible for decomposition of organic molecules namely holes, h^+_{vb}, and hydroxyl radical. The higher oxidation potential of the holes, generated by photoexcitation, allows direct oxidation of the dye to reactive intermediates. Based on the two main reports on the photocatalytic dye degradation kinetics of different dyes[62,63], the general photocatalytic dye destruction can be represented by the following equations:

$$TiO_2 + h\nu \rightarrow TiO_2\ (e^-_{CB} + h^+_{VB}) \qquad (7)$$

The electron and hole generated can also recombine and the equation can be represented as

$$e^-_{CB} + h^+_{VB} \rightarrow heat \qquad (8)$$

The hydroxyl radical is generated by the decomposition of surface adsorbed water and / or hydroxide species:

$$h^+_{VB} + S - H_2O \rightarrow H^+ + S - OH^{\cdot} \qquad (9)$$

$$h^+_{VB} + S - OH^- \rightarrow S - OH^{\cdot} \qquad (10)$$

The hydroxyl radical can also be formed by the electron pathway

$$e^- + O_2 \rightarrow O_2^{-\cdot} \qquad (11)$$

$$O_2^{-\cdot} + e^- + 2H^+ \rightarrow H_2O_2 \qquad (12)$$

$$O_2^{-\cdot} + 2H^+ \rightarrow O_2 + H_2O_2 \qquad (13)$$

$$H_2O_2 + e^- \rightarrow OH^{\cdot} + OH^- \qquad (14)$$

Mobile species (dyes and hydroxyl radical) can be absorbed on the substrate and these can be represented as

$$S + D \leftrightarrow S - D \qquad (15)$$

$$S + OH^{\cdot} \leftrightarrow S - OH^{\cdot} \qquad (16)$$

Dye adsorbed on the substrate reacts with holes and hydroxyl radicals and undergoes degradation and the equation can be represented as:

Hole reaction

$$S - D + h_{VB}^{+} \rightarrow S - D^{0+} \rightarrow end\ species \qquad (17)$$

$$D + h_{VB}^{+} \rightarrow D^{+} \rightarrow end\ species \qquad (18)$$

Hydroxyl reaction

$$S - D + S - OH^{\cdot} \rightarrow S + S - D'^{o} \rightarrow end\ species \qquad (19)$$

$$D + S - OH^{\cdot} \rightarrow S + D'^{o} \rightarrow end\ species \qquad (20)$$

$$S - D + OH^{\cdot} \rightarrow S - D'^{o} \rightarrow end\ species \qquad (21)$$

$$D + OH^{\cdot} \rightarrow D'^{o} \rightarrow end\ species \qquad (22)$$

Since the hydroxyl radical is a strong nonselective oxidant ($E^0 = 3.06$ eV) which decomposes the organic molecules,[64, 65] it is expected that the hydroxyl radical plays the major role.

6.3.2.2. Kinetic study

Figure 6.11a and 6.11b depict kinetics of photodegradation of Rhodamine 6G solution of initial concentration 55.4 micromoles in presence of pure and doped TiO_2. It is reported in several literatures that the photocatalytic degradation of various dyes by TiO_2 follows Langmuir Hinshelwood (LH) kinetics model[22,48,60,62,65,66]. When the concentration of the dye is in the millimolar range, LH kinetic equation simplifies to an apparent first order equation[48,60,61]. The photocatalytic degradation of the Rhodamine dye, therefore, in both the cases follows pseudo first order kinetics.

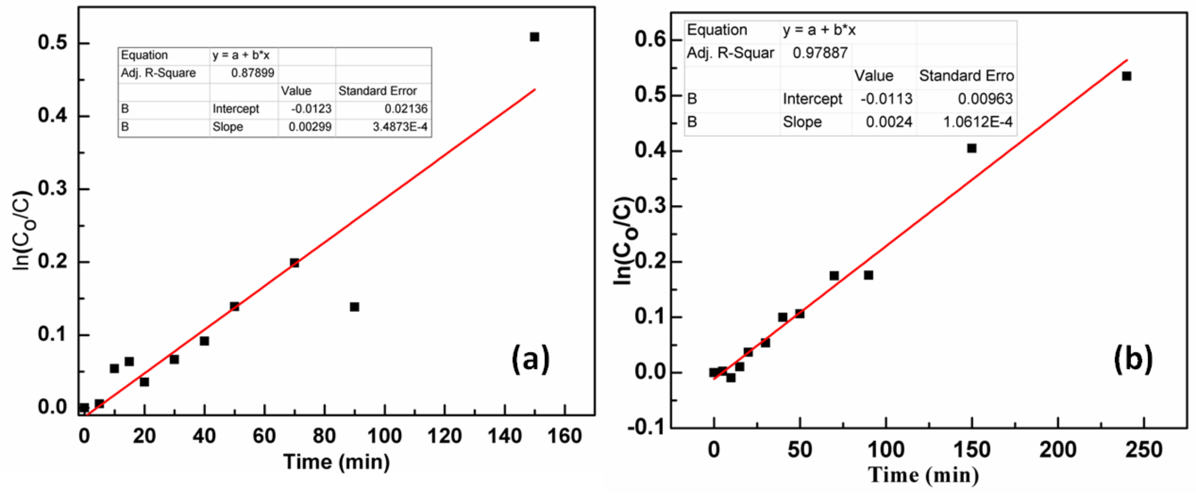

Figure 6.11a-b: ln (Co/C) vs time graph, showing kinetics of photodegradation using (a) undoped TiO_2 nanotubes (b) doped TiO_2 nanotubes.

The rate expression for pseudo first order reactions is

$$\ln \frac{C_0}{C} = kt \qquad (23)$$

where C_0 is the initial concentration, C is the concentration at any time t and k is the rate constant. The plot of $ln\ (C_0/C)$ versus time gives a straight line, the slope of which gives the rate of the reaction. The correlation constant for the fitted line was calculated to be R_2 = 0.88 and R_2 = 0.98 for pure and doped TiO_2 respectively. The corresponding rate constants were calculated to be $4.99 \times 10^{-5}\ s^{-1}$ ($2.99 \times 10^{-3}\ min^{-1}$) and $3.99 \times 10^{-5}\ s^{-1}$($2.4 \times 10^{-3}\ min^{-1}$) respectively.

The photo assisted decolourization of Rhodamine 6G using pure and doped TiO_2 was also studied. The dye destruction efficiency efficiency was calculated using the equation

$$Dye\ destruction\ efficiency = \frac{(C_o - C)}{C} \times 100\% \qquad (24)$$

where C_0 is the initial concentration and C is the concentration after photoirradiation. Figure 6.12 shows the plot of dye destruction efficiency of pure and doped TiO_2 as a function of time.

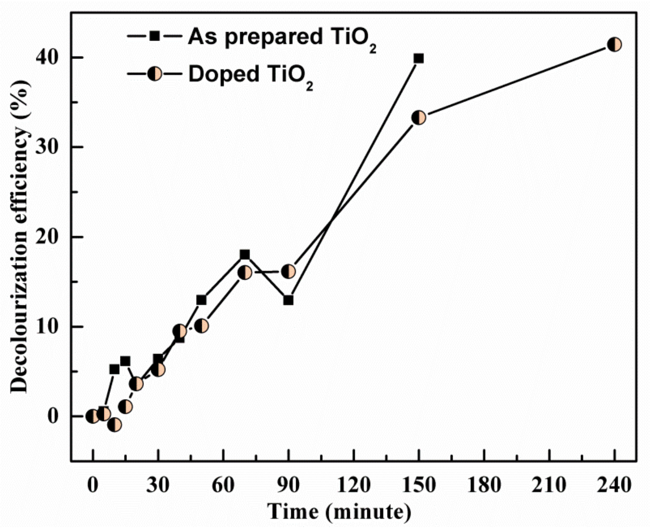

Figure 6.12: Plot of decolourization efficiency of pure and doped TiO_2 as a function of time.

The decolourization efficiency was approximately 40% in 150 minutes for pure and 42% in 240 minutes for doped TiO_2. In the present study, with doped samples, it was observed that a slight decrease in the photocatalytic activity occurs. This can be attributed to the charge recombination centers expected to be generated due to doping.

6.4. Conclusion

Pt/TiO_2 photocatalyst was synthesized by depositing Pt nanoparticles, by chemical reduction of H_2PtCl_6 solution using $NaBH_4$, on to TiO_2 nanotubes obtained by rapid break down anodization technique. The highest photocatalytic activity was observed at 1.25 and 2.5 wt% of Pt loading. An anatase to rutile phase transformation was observed at ≥ 5 wt% Pt loadings, which can be ascribed to the significant removal of lattice strain due to binding of platinum particles onto the TiO_2 surface. Also increased Pt loading resulted in clustering of Pt nanoparticles thereby reducing the chemically active surface area leading to reduced hydrogen generation. The photoluminescence characteristics of Pt loaded TiO_2 samples were investigated and the spectral features were correlated with the photocatalytic hydrogen generation properties of different Pt loaded samples. From these results the critical role of particle size of Pt and resultant enhancement of CSA in the photocatalytic hydrogen generation was clearly established. For incident light of 254 nm wave length and 1.25 wt% Pt on TiO_2, the hydrogen generation rate obtained were 0.030 moles / hour / g of Pt/TiO_2. The photocatalysts are promising candidates for fuel cells, photocatalysis, solar cells and sensors.

Photodegradation studies of Rhodamine 6G were carried out using the pristine and doped samples and their photocatalytic effect were compared. From these results it is clear that both pure and doped samples show almost similar photocatalytic property. Kinetic study revealed that photodegradation reaction follows pseudo first order kinetics. The dye destruction efficiencies of pristine and doped samples were 40% in 150 minutes and 42% in 240 minutes, respectively, even though there is a slight decrease in the band gap of doped TiO_2. This can be attributed to generation of recombination centres on doping. Further studies are required to confirm it.

References:

---

[1] Fujishima, A.; Honda, K., *Nature* **1972,** *238* (5358), 37-38.

[2] Carp, O.; Huisman, C. L.; Reller, A., *Prog. Solid State Chem.* **2004,** *32* (1–2), 33-177.

[3] Bamwenda, G. R.; Tsubota, S.; Nakamura, T.; Haruta, M., *J. Photochem. Photobiol. A.* **1995,** *89* (2), 177-189.

[4] Sreethawong, T.; Yoshikawa, S., *Int. J. Hyd. Energy* **2006,** *31* (6), 786-796.

[5] Wilke, K.; Breuer, H. D., *J. Photochem. Photobio. A. Chem* **1999,** *121* (1), 49-53.

[6] Asahi, R.; Morikawa, T.; Ohwaki, T.; Aoki, K.; Taga, Y., *Science* **2001,** *293* (5528), 269-271.

[7] Khan, S. U. M.; Al-Shahry, M.; Ingler, W. B., *Science* **2002,** *297* (5590), 2243-2245.

[8] Park, H.; Choi, W., *J. Phys. Chem. B* **2004,** *108* (13), 4086-4093.

[9] Choi, W., *Catalysis Surveys from Asia* **2006,** *10* (1), 16-28.

[10] Li, Y.; Lu, G.; Li, S., *J. Photochem. Photobio. A: Chem.* **2002,** *152* (1–3), 219-228.

[11] Tachikawa, T.; Tojo, S.; Fujitsuka, M.; Majima, T., *J. Phys. Chem. B* **2004,** *108* (30), 11054-11061.

[12] Seery, M. K.; George, R.; Floris, P.; Pillai, S. C., *J.Photochem. Photobio. A: Chem.* **2007,** *189* (2–3), 258-263.

[13] Priya, R.; Baiju, K.; Shukla, S.; Biju, S.; Reddy, M.; Patil, K.; Warrier, K., *Catal. Lett.* **2009,** *128* (1), 137-143.

[14] Kowalska, E.; Mahaney, O. O. P.; Abe, R.; Ohtani, B., *Phys. Chem. Chem. Phys.* **2010,** *12* (10), 2344-2355.

[15] Subramanian, V.; Wolf, E. E.; Kamat, P. V., *J. Phys. Chem. B* **2003,** *107* (30), 7479-7485.

[16] Baba, R.; Nakabayashi, S.; Fujishima, A.; Honda, K., *J. Phys. Chem.* **1985,** *89* (10), 1902-1905.

[17] M. Jakob, M.; Levanon, H.; Kamat, P. V., *Nano Lett.* **2003,** *3* (3), 353-358.

[18] Granqvist, C. G.; Buhrman, R. A., *Solid State Comm.* **1976,** *18* (1), 123-126.

[19] Charvolin, J.; Froidevaux, C.; Taupin, C.; Winter, J. M., *Solid State Comm.* **1966,** *4* (7), 357-359.

[20] Benson, J. E.; Boudart, M., *J. Catal.* **1965,** *4* (6), 704-710.

[21] Van Rheenen, P. R.; McKelvy, M. J.; Glaunsinger, W. S., *J. Solid State Chem.* **1987,** *67* (1), 151-169.

[22] Eklund, S. E.; Cliffel, D. E., *Langmuir* **2004,** *20* (14), 6012-6018.

[23] Hoffmann, M. R.; Martin, S. T.; Choi, W.; Bahnemann, D. W., *Chem. Rev.* **1995,** *95* (1), 69-96.

[24] Song, Y.; Garcia, R. M.; Dorin, R. M.; Wang, H.; Qiu, Y.; Coker, E. N.; Steen, W. A.; Miller, J. E.; Shelnutt, J. A., *Nano Lett.* **2007,** *7* (12), 3650-3655.

[25] Guo, J. W.; Zhao, T. S.; Prabhuram, J.; Wong, C. W., *Electrochim. Acta* **2005,** *50* (10), 1973-1983.

[26] Ramesh, C.; Murugesan, N.; Krishnaiah, M.; Ganesan, V.; Periaswami, G., *J. Solid State Electrochem.* **2008,** *12* (9), 1109-1116.

[27] Vijayan, B. K.; Dimitrijevic, N. M.; Wu, J.; Gray, K. A., *J. Phys. Chem. C* **2010,** *114* (49), 21262-21269.

[28] Gilbert, B.; Zhang, H.; Huang, F.; Finnegan, M. P.; Waychunas, G. A.; Banfield, J. F., *Geochem.Trans.* **2003,** *4* (4), 20-27.

[29] Yu, J. C.; Yu; Ho; Jiang; Zhang, *Chem. Mater.* **2002,** *14* (9), 3808-3816.

[30] Cheng, B.; Le, Y.; Yu, J., *J. Hazard.Mater.***2010,** *177* (1–3), 971-977.

[31] Daude, N.; Gout, C.; Jouanin, C., *Phys. Rev. B* **1977,** *15* (6), 3229-3235.

[32] Shi, J.; Chen, J.; Feng, Z.; Chen, T.; Lian, Y.; Wang, X.; Li, C., *J. Phys. Chem. C* **2006,** *111* (2), 693-699.

---

[33] Korzhak, A. V.; Ermokhina, N. I.; Stroyuk, A. L.; Bukhtiyarov, V. K.; Raevskaya, A. E.; Litvin, V. I.; Kuchmiy, S. Y.; Ilyin, V. G.; Manorik, P. A., *J. Photochem. Photobio A: Chem.* **2008,** *198* (2–3), 126-134.

[34] Subramanian, V.; Wolf, E. E.; Kamat, P. V., *J. Phys. Chem. B* **2003,** *107* (30), 7479-7485.

[35] Xu, S.; Sun, D. D., *Int. J. Hyd. Energy* **2009,** *34* (15), 6096-6104.

[36] Chen, X.; Mao, S. S., *Chem. Rev.* **2007,** *107* (7), 2891-2959.

[37] Diebold, U., *Surf. Sci. Rep.* **2003,** *48* (5–8), 53-229.

[38] Chaves, A.; Katiyar, R. S.; Porto, S. P. S., *Phys. Rev. B* **1974,** *10* (8), 3522-3533.

[39] Choi, H.-J.; Kang, M., *Int. J. Hyd. Energy* 2007, *32* (16), 3841-3848.

[40] Wu, N.-L.; Lee, M.-S., *Int. J. Hyd. Energy* 2004, *29* (15), 1601-1605.

[41] Sreethawong, T.; Yoshikawa, S., *Catal. Comm.* 2005, *6* (10), 661-668.

[42] Sreethawong, T.; Puangpetch, T.; Chavadej, S.; Yoshikawa, S., *J.Power Sources* 2007, *165* (2), 861-869.

[43] Yi, H.; Peng, T.; Ke, D.; Ke, D.; Zan, L.; Yan, C., *Int. J. Hyd. Energy* 2008, *33* (2), 672-678.

[44] Jin, Z.; Zhang, X.; Li, Y.; Li, S.; Lu, G., *Catal. Commun.* 2007, *8* (8), 1267-1273.

[45] Bandara, J.; Udawatta, C. P. K.; Rajapakse, C. S. K., *Photochem. Photobio. Sci.* 2005, *4* (11), 857-861.

[46] Galińska, A.; Walendziewski, J., *Energy & Fuels* 2005, *19* (3), 1143-1147.

[47] Patsoura, A.; Kondarides, D. I.; Verykios, X. E., *Catal. Today* 2007, *124* (3–4), 94-102.

[48] Toptygin, D.; Packard, B. Z.; Brand, L., *Chem. Phys. Lett*, **1997**, *277*, 430-435.

[49] Houas, A.; Lachheb, H.; Ksibi, M.; Elaloui, E.; Guillard, C.; Herrmann, J.-M., *App. Catal. B: Env.* **2001,** *31* (2), 145-157.

[50] Bianco Prevot, A.; Baiocchi, C.; Brussino, M. C.; Pramauro, E.; Savarino, P.; Augugliaro, V.; Marcì, G.; Palmisano, L., *Env. Sci. Tech.* **2001,** *35* (5), 971-976.

[51] Tanaka, K.; Padermpole, K.; Hisanaga, T., *Water Res.* **2000,** *34* (1), 327-333.

[52] Galindo, C.; Jacques, P.; Kalt, A., *J. Photochem. Photobio. A: Chem.* **2000,** *130* (1), 35-47.

[53] Bandara, J.; Mielczarski, J. A.; Kiwi, J., *Langmuir* **1999,** *15* (22), 7680-7687.

[54] Zhang, F.; Zhao, J.; Shen, T.; Hidaka, H.; Pelizzetti, E.; Serpone, N., *App. Catal. B: Env.* **1998,** *15* (1–2), 147-156.

[55] Liu, G.; Wu, T.; Zhao, J.; Hidaka, H.; Serpone, N., *Env. Sci. Tech.* **1999,** *33* (12), 2081-2087.

[56] Chen, F.; Xie, Y.; Zhao, J.; Lu, G., *Chemosphere* **2001,** *44* (5), 1159-1168.

[57] Epling, G. A.; Lin, C., *Chemosphere* **2002,** *46* (4), 561-570.

[58] Vinodgopal, K.; Bedja, I.; Hotchandani, S.; Kamat, P. V., *Langmuir* **1994,** *10* (6), 1767-1771.

[59] Vinodgopal, K.; Wynkoop, D. E.; Kamat, P. V., *Environ. Sci. Tech.* **1996,** *30* (5), 1660-1666.

[60] Konstantinou, I. K.; Albanis, T. A., *App. Catal. B: Environ.* **2004,** *49* (1), 1-14.

[61] Tang, W. Z.; Huren, A., *Chemosphere* **1995,** *31* (9), 4157-4170.

[62] Sivalingam, G.; Nagaveni, K.; Hegde, M. S.; Madras, G., *App. Catal. B: Environ.* **2003,** *45* (1), 23-38.

[63] Aarthi, T.; Madras, G., *Ind. Eng. Chem. Res.* **2006,** *46* (1), 7-14.

[64] Legrini, O.; Oliveros, E.; Braun, A. M., *Chem. Rev.***1993,** *93* (2), 671-698.

[65] Kuo, W. S.; Ho, P. H., *Chemosphere* **2001,** *45* (1), 77-83.

[66] Xu, Y.; Langford, C. H., *Langmuir* **2001,** *17* (3), 897-902.

Chapter 7

Summary and Scope for Future Research

The thesis encompasses synthesis, characterization and selected applications of pristine and doped TiO_2 nanotube arrays and powders. The applications were selected based on the characteristics of the synthesized TiO_2 nanoarchitectures, that will enhance the efficiency of respective devices fabricated using them. For selected application studies such as dye sensitized solar cells, large area field emitters and near superhydrophobic ↔ superhydrophilic switching surfaces, vertically aligned TiO_2 nanotube arrays are preferred because of their high aspect ratio, directional electron transport properties and surface roughness with long trapped air columns. Whereas, in applications like green-energy hydrogen generation by water photolysis and photocatalytic destruction of organic pollutants in water, suspensions of large surface area particles like nanotubes are preferred as the configuration has large number of reactant adsorption sites and better light harvesting capability. Synthesis of C and N-doped TiO_2 nanoarchitectures were also carried out as these were found to modify the electronic energy band structure resulting in photon absorption in the visible region, which constitutes 45% of solar radiation spectrum. Major results of the present investigations are summarized below.

7.1. Conclusions

7.1.1. Synthesis and Characterization of Pristine and N-doped TNTA by Potentiostatic Anodization

The electrochemical process parameters such as applied voltage, time of anodization and electrolyte composition for the synthesis of smooth walled high aspect ratio TiO_2 nanotube arrays (TNTA) were optimized with the support of current density versus time plots obtained during anodization and subsequent FESEM analysis of the anodized samples. The optimized process parameters, for synthesis of nanotube arrays on Ti foils are 30 to 50 V applied potential, anodization time of 2 to 3 hours and electrolyte composition of 0.25 to 0.5 wt% of NH_4F + 2 to 3 wt% of H_2O in ethylene glycol, and those for transparent nanotube arrays upon FTO coated glass are same electrolyte composition, 40 V applied potential and anodization for 2 hours. The as prepared nanotube arrays were amorphous in nature and on annealing at 400 ^oC yielded anatase phase. With increase in annealing temperature, the nanotube arrays underwent phase transformation from anatase to rutile and at 800 ^oC complete phase transformation occurred leading to the formation of thick rutile TiO_2 layers. The tubular structure of TiO_2 nanotube arrays is retained up to 700 ^oC. A compositional analysis by XPS revealed the presence of surface and subsurface defect states such as bridging oxygen vacancies (Ti - V_O – Ti), Ti – OH – Ti / Ti-$(OH)_2$-Ti bridge and surface terminating Ti - OH. The water molecules and organic species present in the ambient are adsorbed in the bridging oxygen vacancies and undergo dissociation and oxidation, respectively, upon light irradiation and therefore has immense influence on photocatalytic activity. The band gap calculated from the results of diffuse reflectance spectroscopy was around 3.3 eV implying absorption in the near UV region.

N-doped TNTA were fabricated by single step anodization technique using urea in different weight percentage as a nitrogen precursor in ethylene glycol medium containing 0.5 wt% ammonium fluoride and 2.5wt% of water. The XPS analysis confirmed nitrogen incorporation in TiO_2 matrix both in substitutional and interstitial forms, of which major contribution arises from the substitutional states. The calculated compositions are $TiO_{1.85}N_{0.115}$ (3.88 at% of N), $TiO_{1.813}N_{0.14}$ (4.12 at% of N) and $TiO_{1.84}N_{0.121}$ (4.74at% of N) for 0.1, 0.2 and 0.3 wt % of urea in the electrolyte, respectively. The as prepared samples were amorphous in nature and upon annealing at 400 ^{o}C, it transformed to anatase phase. The optical band gap values were found to shift to lower values with N-doping. The band gap values obtained are 3.22, 2.75 and 2.77 eV for $TiO_{1.85}N_{0.115}$, $TiO_{1.813}N_{0.14}$ and $TiO_{1.84}N_{0.121}$, respectively. In the case of $TiO_{1.813}N_{0.14}$, introduction of interband state could be discerned from the absorption spectrum. The observed shifts in the band gap energy for $TiO_{1.85}N_{0.115}$, $TiO_{1.813}N_{0.14}$ and $TiO_{1.84}N_{0.121}$ from that of the pristine TiO_2 are 0.05, 0.52 and 0.5 eV, respectively. The extra state introduced in the case of $TiO_{1.813}N_{0.14}$ is located 0.68 eV above the valence band.

7.1.2. Photovoltaic, Field Emission and Surface Wetting Characteristics of Pristine and N-doped TNTA

Selected application studies such as dye sensitized solar cell (DSSC) studies using pristine TNTA on Ti foil and FTO coated glasses, field emission and photoinduced surface wetting-dewetting properties of pristine and N-doped TNTA on foil were carried out.

The photovoltaic performance of DSSCs fabricated using pristine TNTA on Ti foil and FTO coated glasses were found to be inferior to those reported in literature, which could be attributed to the non optimized process parameters. The drawbacks were identified as improper dye attachment to the TNTA, low conductivity of the in-house made Pt counter electrode, limited length of the TiO_2 nanotubes on FTO glass, decrease in conductivity of the FTO glass due to excess anodization as well as high temperature annealing and the counter electrode side light illumination for the DSSCs fabricated using TNTA on foils. All the above mentioned issues resulted in low fill factor (FF) values which resulted in the poor efficiency of the fabricated DSSCs. This was further confirmed by the higher V_{oc}, I_{sc}, FF, efficiency and IPCE values obtained for the DSSC fabricated in-house using commercially available TiO_2 and Pt coated conducting glasses. In addition, the high electrochemical impedance obtained for the cells fabricated using TNTA confirmed the identified shortcomings.

The field emission (FE) properties of pristine and N-doped anatase TNTA corresponding to different concentrations of nitrogen were studied to understand their potential for application in large area electron field emitters. An enhancement in FE was observed with N-doping. The FE was found to increase with increase in the nitrogen concentration in the anion sublattice. From the Fowler Nordheim (FN) plot, the turn on fields obtained for 3.88, 4.12 and 4.74 at% of N-doping were 12.5, 10.4 and 7.1 V / μm, respectively. The low turn on values of doped TNTA compared to pristine ones indicate that N-doping plays a very significant role in enhancing the FE properties. The enhancement of FE properties on N-doping can also be ascribed to the presence of localized donor states, with higher band width, located at energy levels close to CBM compared to that of TiO_2 and N-2p state above the VBM, leading to a shift in Fermi level to higher energies and consequent reduction in work function. The nonlinearity in the FN plot of the N-doped TNTA revealed different mechanisms for field emission at high and low fields. In the present study, three regions were observed and identified in the FN plot, a low field region, an intermediate region and a high field region. The low field region corresponds to surface states dominated FE. In the high field region, the field penetration breaks down the surface potential barrier increasing FE. In the intermediate region both mechanisms compete resulting in a different slope.

The hydrophobic ↔ hydrophilic switching behavior of pristine and N-doped anatase TNTA was studied, under UV and sun light illumination, to understand their potential for application as smart membranes. Surface wetting investigations on pristine and N-doped anatase TNTA revealed near superhydrophobic nature of pristine and N-doped TNTA, in which the N-doped ones were found to be more hydrophilic. The photo induced near superhydrophobic ↔ superhydrophilic switching was observed for both pristine and doped TNTA under UV (1.4 mW/cm^2) / dark conditions. In the case of N-doped samples, in addition to UV light, the switching behavior was observed under sun light ($10mW/cm^2$). The kinetic analyses of contact angle decay with photo irradiation time as well as the recovery with time in dark carried out for the pristine and N-doped TNTA revealed faster near superhydrophobic to superhydrophilic conversion rate and slow reverse process rate for N-doped TNTA. The near superhydrophobic to superhydrophilic conversion rate for the N-doped TNTA, under sun light was less pronounced compared to that under UV light and the recovery to the initial hydrophobic state was fast. The visible light induced super hydrophilicity of N-doped TNTA indicates their potential use as visible light active smart membranes.

7.1.3. Synthesis and Characterization of Pristine and N and C co-doped TiO_2 nanotube powders by Rapid Break down Anodization Technique.

High surface area anatase TiO_2 nanotube powders were synthesized by anodizing Ti foils in 0.1M perchloric acid. FESEM and TEM analysis confirmed the tubular architecture. The as prepared TiO_2 nanotubes were of ~8 nm inner diameter, ~5 nm wall thickness, 5 to 10 μm tube length and 9 to 13 nm crystallite size, as revealed by XRD and TEM analysis. Destruction of tubular morphology and phase transformation from anatase to rutile were observed for the TiO_2 nanotubes when annealed above 500°C. The asprepared samples showed good optical properties where the band gaps varied from 2.95 to 3.07 eV as revealed by PL and diffuse reflectance spectroscopic measurements. The BET surface area of the samples was 155 m^2/g. An effort to synthesize C and N-doped TiO_2 nanotube powders using urea as the precursor in the electrolyte resulted in the destruction of tubular structure. XRD and micro Raman analysis showed anatase phase crystallinity as in the case of pristine TiO_2 nanotube powders. XPS studies showed presence of interstitial N-doping and substitutional C-doping. Peaks corresponding to substitutional nitrogen (~397 eV) could not be observed. Diffuse reflectance spectroscopy did not show any appreciable change in the band gap with doping.

7.1.4. Photocatalytic Hydrogen generation and dye degradation studies using Pristine and C and N co-doped TiO_2 nanotube powders

Hydrogen generation by water photolysis using Pt loaded TiO_2 nanotube powders were studied to understand their potential as efficient catalyst for green energy based hydrogen generation. Sodium borohydride reduction of chloroplatinic acid in which TiO_2 powders are dispersed was employed for synthesizing Pt loaded TiO_2. Platinum was loaded in different amounts varying from 1 to 10 wt%. An anatase to rutile phase transformation was observed at higher Pt loadings (> 5wt %). The highest H_2 generations under near UV light (~380 nm and 120 W) was observed at 1.25 and 2.5 wt% of Pt loadings and the respective quantities liberated are 777.3 and 927.9 μ moles of H_2 / h / g of Pt-TiO_2 respectively. Also, increased Pt loading resulted in clustering of Pt nanoparticles thereby reducing the chemically active surface area leading to reduced hydrogen production. The photoluminescence characteristics of Pt loaded TiO_2 samples revealed photo-generated electron transfer from TiO_2 to Pt. From the results of this study the critical role of particle size of Pt and resultant enhancement of CSA in the photocatalytic hydrogen generation was clearly established. This was further confirmed by turn over frequency calculation. An enhancement in the H_2 generation rate was observed with increase in incident light frequency. For incident light of 254 nm wave length (64 W) and 1.25 wt% Pt loading, the hydrogen generation rate obtained was 0.030 moles / hour / g of Pt/TiO_2.

Photocatalytic dye degradation studies using pristine as well as N and C co-doped TiO_2 nanotube powders were investigated taking Rhodamine 6 G (R6G) as a model pollutant under sun light illumination. The change in concentration of R6G with irradiation time was quantified by UV-visible absorption studies and it was observed that the pristine as well as N and C co-doped TiO_2 nanotube powders showed similar photocatalytic activity. Degradation of the dye in presence of TiO_2 followed apparent first order kinetics based on L-H mechanism and the rate constant calculated were $4.99 \times 10^{-5}\ s^{-1}$ ($2.99 \times 10^{-3}\ min^{-1}$) and $3.99 \times 10^{-5}\ s^{-1}$($2.4 \times 10^{-3}\ min^{-1}$) for pristine and doped TiO_2 nanotube powders, respectively. The slight decrease in dye destruction efficiency of the doped TiO_2 can be ascribed to the generation of charge recombination centres on doping.

7.2. Scope for Future Research

Fabrication of various nano-architectures of TiO_2, their characterization and application in specific areas based on their morphology and associated characteristics, is quite time consuming. Only a beginning has been made to synthesize selected quasi one dimensional nano-architectures of high surface area, such as vertically aligned nanotube arrays and nanotube tube powders and study their applications in chosen areas where the specific architectures are expected to enhance the efficiencies of devices fabricated using these nanoscale materials. The selected studies pertain to the basic aspects of applications of TNTA and TiO_2 nanotube powders in areas such as photo-voltaic, field emission, self cleaning surfaces, photo-induced H_2 generation by water splitting and destruction of organic pollutants. Much work is needed to optimize the properties of the quasi one dimensional TiO_2 nano-architectures to enhance the efficiencies pertaining to above mentioned applications. It is hoped that the present thesis would form the foundation of the future research work in this direction.

7.2.1. Recommendations

a. The TNTA fabricated on FTO coated glasses in the present investigations posed difficulties in DSSC applications because of their limited tube length, less transparency and decrease in conductivity after anodization followed by annealing. Preliminary results obtained in the fabrication and photovoltaic studies are inconclusive. Therefore careful fabrication steps are needed to get high aspect ratio anatase TNTA on FTO glasses. Since N-doped TNTA have better electrical and optical properties, compared to the pristine ones, it is worthwhile to fabricate DSSCs using transparent N-doped TNTA on conducting glasses and study their photovoltaic characteristics. In addition, synthesis of increased surface area nanotube arrays, by modifying the inner and outer surface morphologies of individual nanotubes (creating ripples and ridges) by tuning the electrochemical parameters and studies on their effect in DSSC's performance is worth pursuing.

b. Substitutional N- doped TNTA was fabricated by anodizing Ti in urea containing electrolytes. These studies can be broadened to fabricate other anion (C, B, S and F) doped TNTA by employing suitable precursor in the electrolyte. Co-doping (like C&N, C&S, F&N and B&N) of the TNTA can be tried out by modifying or varying the precursor in the electrolyte medium. Careful compositional analysis can shed light on the effect of doped elements in the electronic energy band structure of TiO_2. The effect of doping and co-doping on the photocatalytic, field emission and antifogging characteristics can also be investigated.

c. Present studies indicated enhancement in FE on N-doping as well as aspect ratio tuning by varying the applied voltage. More detailed investigations on the effect of tube length, diameter and wall thickness of the N-doped TNTA on the FE, can be explored which could provide a rational basis for the development of large area field emitters employing quasi one dimensional nano architectures of $TiO_{2..}$

d. High surface area anatase TiO_2 nanotube powders in high yield, synthesized using rapid break down anodization technique in this study, will provide the basis for the fabrication of DSSCs, by coating the nanotube powders onto suitable transparent conducting substrates like FTO/ ITO coated glasses by spin coating, dip coating and doctor blading technique. The thickness of the TiO_2 coating can be tuned to obtain efficient DSSC device.

e. Platinum loaded nanotube powders when used as photocatalysts for hydrogen generation by photolysis of water, under UV light, gave generation rates as high as 0.03 moles of H_2 /g of catalyst in one hour. It is worthwhile to carry out the studies with more cost effective metal and metal oxide, such as Ag, Cu, Cu_2O, loaded TiO_2 nanotubes to make the process more cost effective. Hydrogen generation studies of the catalysts under sun light is another area worth pursuing.